Geophysical Study of Historical Landfill at Wishingwell Park, St. John's, Newfoundland and Labrador, Canada.

By
Tshering Dendup

A Thesis Submitted to the School of Graduate Studies in partial fulfillment of the requirements for the degree of Master of Science in Geophysics

Department of Earth Sciences

Memorial University of Newfoundland

May 2025.

St. John's, Newfoundland and Labrador

Abstract

The Empire Avenue landfill, approximately 3 km from downtown St. John's, was used as the city's official landfill from approximately 1947 until its official closure in 1963. The highly mixed waste, evidenced via photo records, was reported to be covered by soil every day in trenches. Following its abandonment, the area was eventually transformed into the present day Wishingwell Park. However, there are no detailed records about the landfill. Consequently, a thorough integrated geophysical investigation was carried out using magnetic, geoelectrical, electromagnetic and ground penetrating radar surveys to map and investigate the possible locations and extent of the buried waste.

A magnetic survey was carried out over the entire park. The data clearly suggest the presence of metallic waste underneath much of the study area. There are four linear magnetic features representative of the axes of buried trenches. Six resistivity profiles were measured over the entire park. The geoelectrical results revealed numerous conductive anomalies (75-190 mS/m), mostly observed where the profiles crossed the magnetic linear features. These geoelectrical anomalies could indicate the vertical extents of the trenches with their depths ranging from about 4 m (top) to 12 m (bottom). The spatially coincidental anomalies in both methods help conclude that these anomalies are due to metallic waste, although some conductive anomalies could be from leachates and increased ground water contents in loose till.

A frequency-domain electromagnetic survey was conducted over the soccer and rugby fields in the western part of the park. The lowest frequency data show significant inphase responses mostly from those regions where the anomalies were recorded for magnetic and geoelectrical surveys. A ground penetrating radar survey was conducted over almost the same area as the electromagnetic survey, with a penetration depth of about 1-1.5 m. The data indicated the existence of near-surface layers and a dipping layer in the vicinity of the strongest magnetic anomaly, likely depicting the top of the ground surface before

construction of the playing fields.

Thus, this integrated geophysical study found evidence of buried waste, including significant metal, over the extent of Wishingwell Park. The waste is buried in subparallel, covered trenches occurring at a depth of approximately 4 m (top) to 12 m (bottom) below the current ground surface.

Acknowledgement

The work of this magnitude necessitates assistance and guidance of a multitude of people. This work has received unwavering support and timely guidance from many personnel throughout the last two years. I would like to wholeheartedly and sincerely mention the following people without whom this work would not have been possible.

First and foremost, immense thanks are due to my two wonderful and resourceful supervisors, Dr. Colin G. Farquharson and Dr. Alison Leitch. They have been pivotal from the very beginning, through all the field works, analyses and interpretations, to the final preparation of the manuscript. Their indispensable involvements in this work are beyond words to express.

Dr. Charles A. Hurich for his guidance and assistance with the ground penetrating radar method. Dr. Mehrdad Darijani of Geotexera Inc. for his guidance and assistance with the 3D inversion of magnetic data. Additionally, my sincere thanks to Geotexera Inc. for providing me with unhindered access to their in-house 3D inversion software.

I would also like to sincerely express my gratitude to those colleagues, especially the people who kindly assisted me in acquiring the humungous amount of geophysical data, namely; Dr. Xushan Lu, Dr. Yee Lee, Dr. Aliyu Saley, Feng Lee and Passang Dorji amongst many others. I thank my professors throughout my graduate career, whose teachings have provided me with the required knowledge to take up this work. Thanks are due to the Royal University of Bhutan for providing me with the prestigious scholarship.

Finally, I owe my sincerest thanks to my wife and parents who have played unimaginable roles in achieving success as a student, as a person and as a professional. All who played both minor and major roles are equally thanked for your contribution in this pursuit.

Table of Contents

List of Figures

List of Tables

Chapter 1: Study Area

1.1 Introduction

It is a matter of fact that any human settlements, dense or sparse, are bound to inflict some degree of environmental pollution primarily from wastes and their mismanagement (Dawson et al., 2002). It was not a big problem a few decades ago and disposal of waste was rarely monitored and regulated around the world (Adewuyi & Oladapo, 2011). However, the problems are increasing especially in central places and major cities around the world with rapidly increasing populations (Voukkali et al., 2017). Authorities in many parts of the world delayed adopting standardized and well-regulated measures to manage waste. Consequently, many places, especially in the outskirts of cities, became illegal dumping sites. In recent years, municipalities or city authorities across the globe have realized the urgency of the problem and sought solutions. One of the preferred solutions was landfilling — an environmentally conscious and economically viable resolution — to address the ever-increasing rate of waste production. However, the majority of these landfills are neither properly reclaimed nor remediated upon reaching the projected carrying capacity (Dawson et. al., 2002). A large proportion of these landfills are merely abandoned, at the end of their lifespan, by simply covering them with earth, with little or no efforts to monitor for any adverse impacts resulting from the buried waste (Cochran & Dalton, 1995; Bernstone & Dahlin, 1997; Dawson et al., 2002; Khalil, 2016; Appiah et al., 2018). The environmental impact of landfills, particularly concerning groundwater contamination and land use, have become a growing concern (Loke et a., 2013). Moreover, most of these landfills lack authentic historical records making them more problematic research targets.

The Empire Avenue landfill, now covered by Wishingwell Park, is one such case in the city of St. John's, Newfoundland. The landfill was primarily used to accommodate highly mixed waste. The landfill is considered significant from an environmental standpoint due to its location over areas previously occupied by headwaters of Kelly's Brook, which ran

through residential areas. Given its nature and its location in the city, Wishingwell Park is a good target for study of its present-day subsurface conditions and its likelihood of contributing to environmental pollution. Such an endeavor necessitates understanding certain critical aspects of the landfill such as its spatial extent (boundary), reclamation technique implemented, distribution of trenches and approximate depths, types of waste and remediation measures implemented, if any. However, none of these crucial aspects of the landfill can be traced from the rather vague records available either as archived images or news (Garland, 2006). Consequently, this area received no research interest from the scientific community, except for a seismic refraction tomography study in 2006. Further, the area is entirely occupied by soccer, rugby, tennis and baseball fields which likely precluded public awareness of its previous existence as a dump site or research interest involving applications of invasive techniques especially like well-monitoring and destructive geotechnical in-situ tests.

Accordingly, this thesis aims to resolve these information gaps by conducting a comprehensive integrated geophysical study in Wishingwell Park. This study integrates magnetic, geoelectrical, frequency-domain electromagnetic and ground penetrating radar surveys to investigate the area non-destructively (Benson et al., 1984). Particularly, this study focuses on assessing the spatial distribution of the wastes, unveiling the landfill reclamation technique deployed, if any, and understanding the nature of remnant waste in the area. Given the limited prior research conducted in this region and no official accounts, this thesis intends to offer an important first step toward understanding aspects of the landfill and environmental challenges which may result from it. The results of this study will also provide insights for the municipal authorities and policymakers in the region to act on any challenge promptly and to approach challenges in similarly under-researched regions.

This work consists of seven different chapters. Chapter 1 includes discussion of the study area and its historical overview and introduction to the work. Chapter 2 encapsulates

literature reviews and Chapters 3 through Chapter 6 discuss each of the geophysical methods used. Chapter 3 covers aspects of magnetic method subdivided into three sections: basic principles, field survey methods and analyses and interpretations. Chapters 4 through 6 cover similar ground on the geoelectrical, electromagnetic and ground penetrating radar methods, respectively. Finally, Chapter 7 summarizes and integrates important observations and results from all the four geophysical methods and, hence, provides the final conclusions of the study.

1.2 Historical Overview

The present-day city of St. John's was once a sparsely inhabited area with its major settlements centered around the harbor until the last quarter of the 19th century. Over the next few decades, the city saw significant growth in population leading to rapid expansion of settlements into regions circumferentially away from the harbor. Consequently, like for the majority of cities around the globe, managing waste became challenging tasks facing the general population in St. John's. Wicks in his report 'Down in the Dumps: Garbage Disposal in St. John's (1892-1930)' affirmed that most regions in the vicinity of the city limits of the day were dumping sites. According to his report, areas like Newtown Road, Quidi Vidi Lake, Old Pennywell Road, Anderson Avenue, Merrymeeting Road, Freshwater Road and Empire Avenue, shown in Figure 1.1, were predominant illegal dumping sites, although a few sites were authorized under the purview of the then municipal council. People with fallow, vacant lands would offer them to the city council to use as a dump site in return for some nominal offers from the city (Wicks, n.d). The council used to designate some dump sites for summer seasons and others for harsh winter seasons (Wicks, n.d). Scott Osmond (2021) mentioned that expansion of the road networks far from the harbor region, such as Topsail Road, Waterford Bridge Road, Torbay Road, Portugal Cove Road and Freshwater Road (see Figure 1.1), led to predominantly ribbon developments in other areas. He also asserted that the construction of the Newfoundland Railway in 1881, in a location now known as Empire Avenue, further brought more settlements outward from the otherwise dominant harbor settlement. This rapid expansion and growth of population contributed immensely to illegal dumping problems on the land as well as along the sides of Kelley's Brook and Rennies River.

With the increasing rate of immigration, housing demand rose and there was a rapid expansion of settlements into areas along streams/rivers for farming, fishing and rearing domestic animals. Moreover, in 1882, the Colonial Cordage Company was established

along Ropewalk Lane, and settlements in the Mundy Pond region started growing rapidly (Collier, 2011; O'Neill, 2008). According to Bland (1946), the houses in the Mundy Pond area were built with insufficient space for the distribution of the effluents, and septic tanks were used without sewers; this contributed indirectly to the pollution of Kelly's Brook. Scott Osmond (2021) inferred that the expanding settlements in late 1940s in between Freshwater Road and Empire Avenue, Mundy Pond and Ropewalk Lane, and housing developments around Churchill Park necessitated the municipal council to rethink the location of a dumping area to curb waste problems in these areas.

Scott Osmond (2021) asserted that the council of the day chose the location of present-day Wishingwell Park, at latitude 47°33'37" north and longitude 52°44'24" west, and then known as the Empire Avenue landfill (in archived photo records), as the official landfill. The site is indicated as the green polygon in the present day-day map of the area in Figure 1.1. This decision from the council was made as it was marshy wetland with a few ponds, the headwaters for Kelly's Brook, unsuitable for residential or commercial businesses, and it was conveniently located alongside the Newfoundland railway and in the vicinity of the then city limits (Wicks, n.d). The city council considered the landfill area as a modern and environmentally-conscious approach as it was based on the concept of sanitary landfill. Daily News (1959a and 1961a), as cited by Scott Osmond (2021), reported that waste was placed in trenches with 18-24 inches of top cover every evening, with occasional use of disinfectant or crude oil, in an attempt to curb undesirable runoff infiltration into the waste in the trenches. The city of St. John's land use maps of 1922 and 1945 depicting the location of the landfill are shown in Figure 1.2.

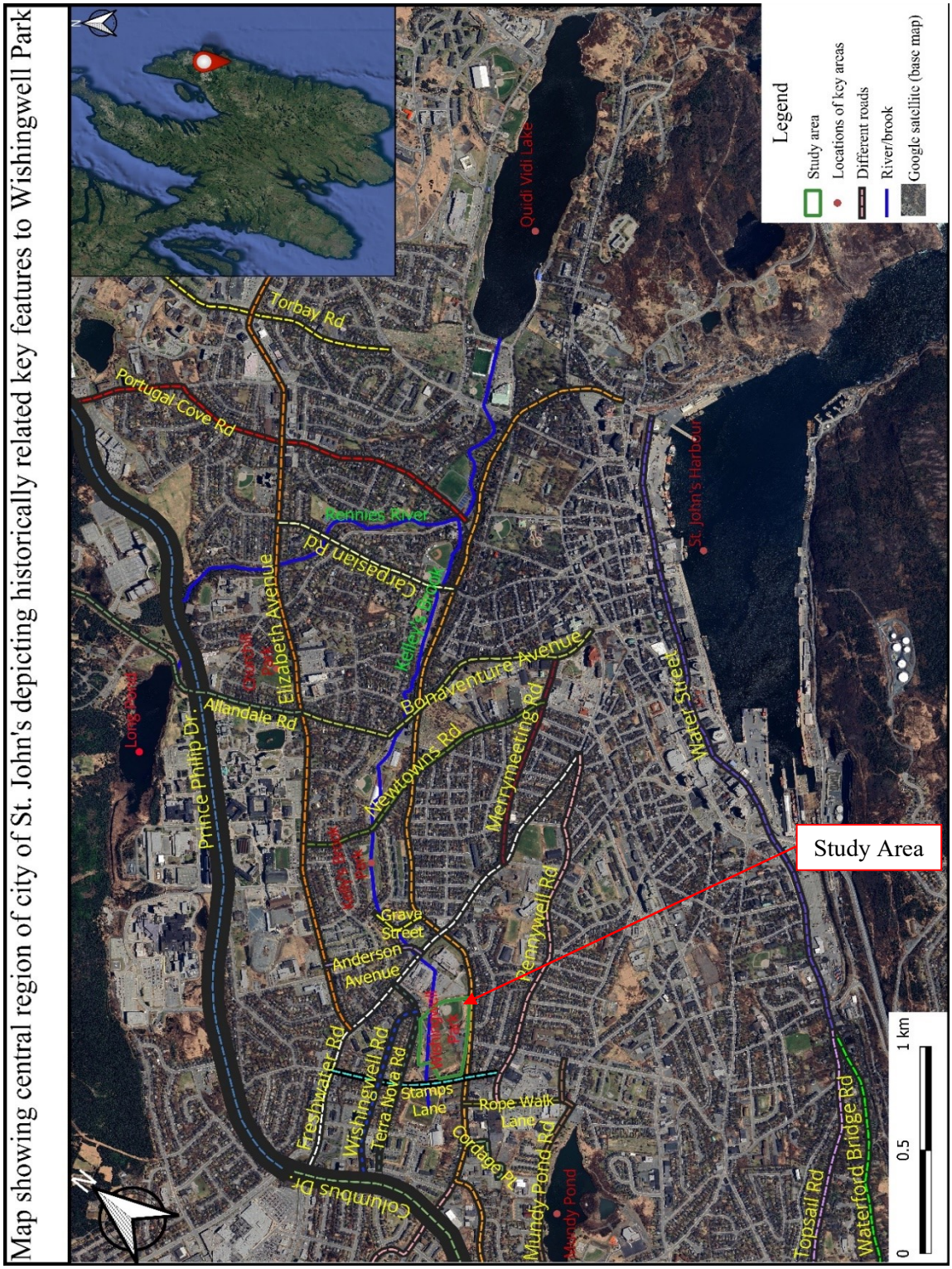

Figure 1.1: Map of central region of St. John's depicting roads and rivers mentioned in the text as sites of illegal dumping. The location of Wishingwell Park is outlined by a green polygon.

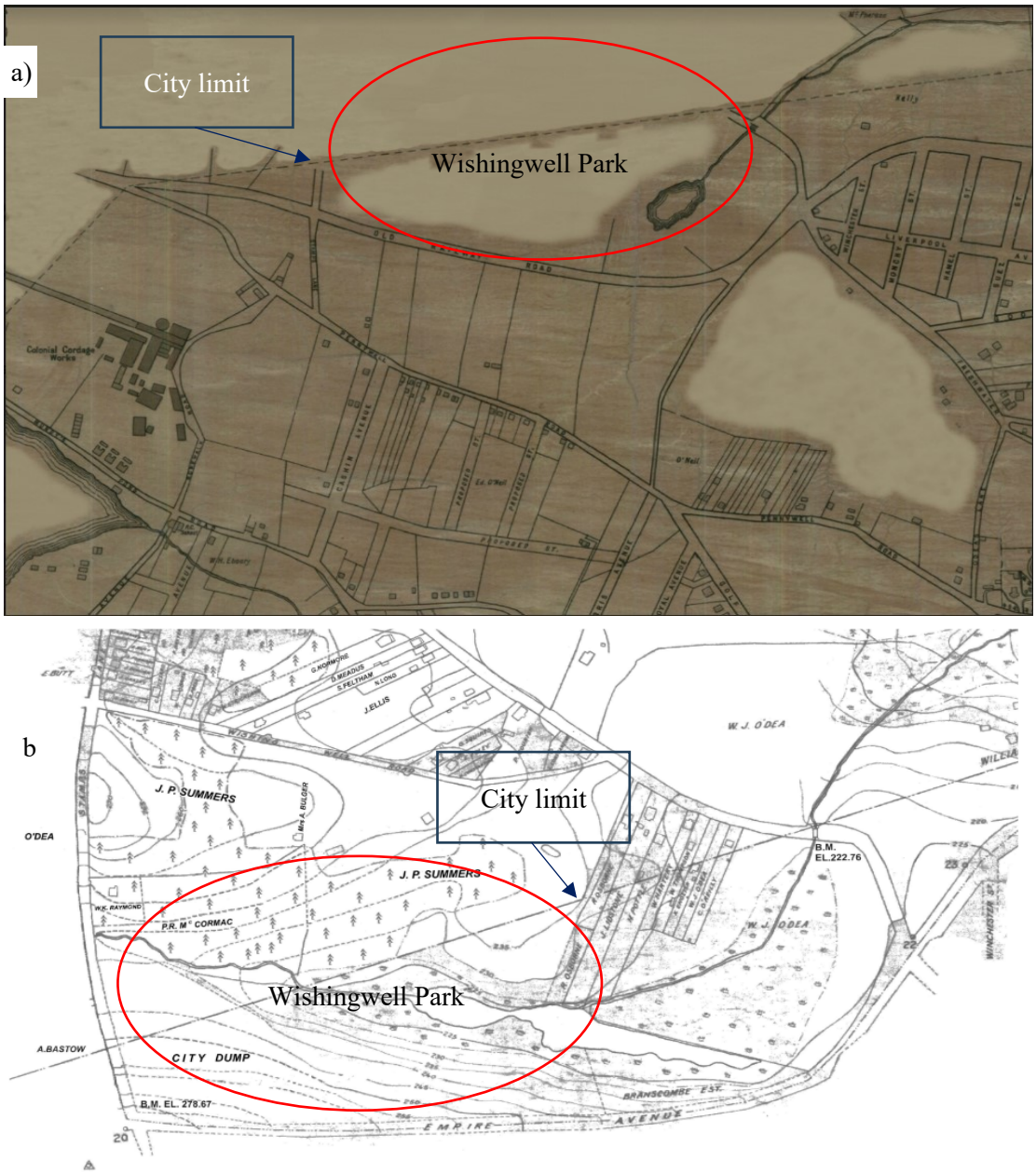

Figure 1.2: Land use land cover maps of Wishingwell Area of 1922(a) and 1945(b) showing study area enclosed in red ellipses. (Modified from Elliott, n.d.)

The city of St. John's is known for strong winds; consistent fires at the landfill deteriorated the quality of air in the surroundings with waste blown out everywhere, water quality worsened and foul odours polluted the community nearby, forcing people to leave their houses and take refuge in the houses of family members in other parts of St. John's (Osmond, 2021; Daily News, 1961b).

In 1959 (Daily News, 1959a), a formal complaint was lodged to the municipal council about these nuisances by the locals, however, it was not considered. This led to frustration amongst the residents who demanded the immediate closure of the landfill. The council then conducted a feasibility and cost benefit study to replace the landfill with incinerators. However, this plan did not materialize as the study concluded that having a landfill was the more economical solution. However, the council assured the community that the area would be provided with a park upon its closure in the next 7 years (Osmond, 2021; Daily News, 1962). This led to further extensive public outcry and protests for a couple of years. An aerial photo of the area depicting the existence of waste in the landfill is shown in Figure 1.3.

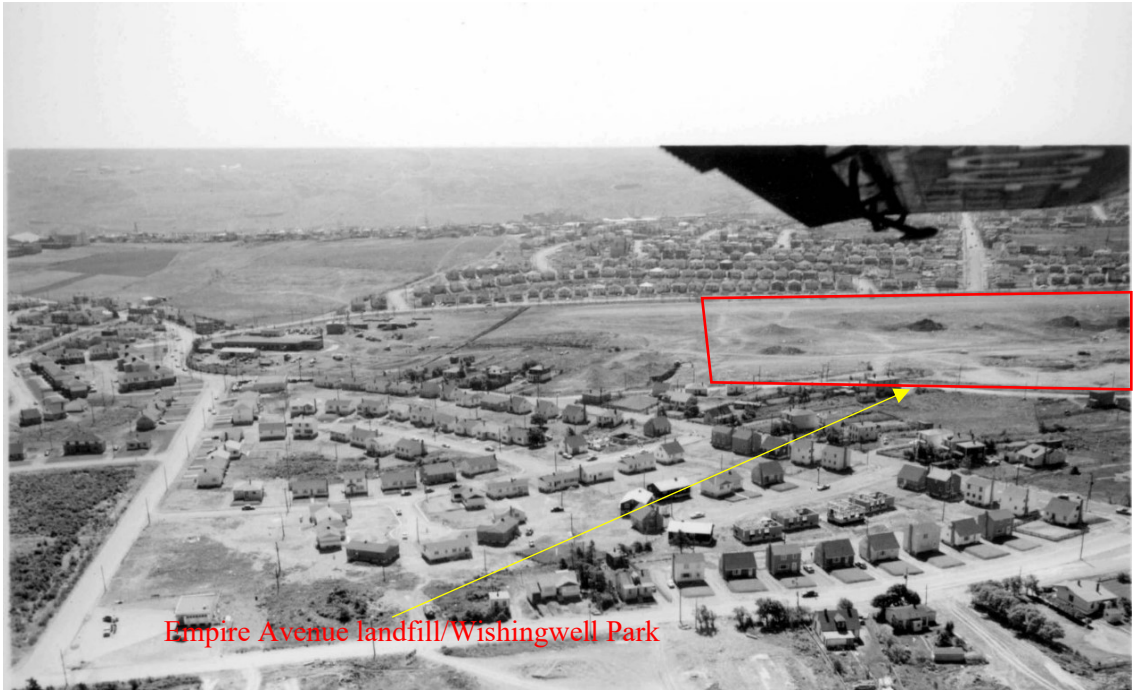

Figure 1.3: Oblique aerial photo of Empire Avenue, Freshwater Road, Terra Nova Road and Anderson Avenue taken in 1960s, looking to the southeast. (Modified from City of St. John's Archives, n.d.)

The landfill at this area was publicly buried and sealed on 17th June, 1963, after selecting the former U.S military dump site in Robin Hood Bay as the next site (Osmond, 2021; Daily News, 1963). Although officially closed, there is no official record of any remediation done at the abandoned site. Seymour (1963) described this area as “the dunes

of a geographically distant desert" entirely enclosed by chain-link fences.

The council's plan to construct city hall over the area was withdrawn and the area was eventually transformed into a park which today is known as Wishingwell Park. According to Scott Osmond (2021), who cited Buchanan & QVRRDF (1991) (I could not access the original document), it was the council's decision to culvert two small ponds and contributing wetland in the headwater region prior to opening the landfill as a countermeasure to protect Kelly's Brook from infiltrating pollutants from the landfill as shown in Figure 1.4.

Figure 1.4: Chronology of culverting Kelly's Brook and the Empire Avenue landfill (shaded yellow).

(After Osmond, 2021.)

Bland (1946) in their recommendations to the city of St. John's commission suggested that this river would best serve as a green belt between industrial and residential areas. However, rapid growth of residential dwellings in Churchill Park, Anderson Avenue and Grave Street aggravated pollution in the brook thereby forcing the council to culvert the remaining stretch of the brook by the end of 1959. This was celebrated by the residents with the slogan 'Pollution is Gone Forever' (Daily News, 1959b). According to Daily

News (1959b), it was done by council in a desperate attempt to curtail further pollution of murky Kelly's Brook and resolve the issue of foul odors from it. The following year (1960), council spent $60,000 to culvert Kelly's Brook from Hoyle's Avenue to Newtown Road, from Newtown Road to Allandale for about $14,000 and later that same year from Allandale to Carpasian Road costing council around $43,000. The final stretch from Carpasian road to Rennie's River was culverted in 1961 using steel tubes of varying diameters (Osmond, 2021). According to the City of St. John's archive record, under Michael O'Dea's arbitration for Wishingwell area, the then municipal council used a few areas in William J. O'Dea's estate as dump sites without formal agreement between them. Micheal O'Dea in 1960 submitted arbitration against the city council which led to council's expropriation of lands, shown in Figure 1.5, in 1965 having paid Mr. O'Dea about $15,000.

The whole stretch of Kelly's Brook remained buried for at least 30 years. Over time, environmental consciousness has improved across the world and within this city as well. In the late 1970s, a few conservational groups were formed, especially Quidi Vidi-Rennie's River Development Foundation (QVRRDF) which played a key role in petitioning the City of St. John's to carry out extensive pollution assessments of Kelley's Brook (Osmond, 2021). This led to an elaborative study done by Elliot & Elliot Limited in 1988 with the key recommendations to daylight the culverted brook (Osmond, 2021). In the subsequent year, the QVRRDF commenced the work of restoring a 215m stretch of Kelly's Brook from Rennies River; the work was completed on June 5, 1991 (Callahan, 1991; Osmond, 2021).

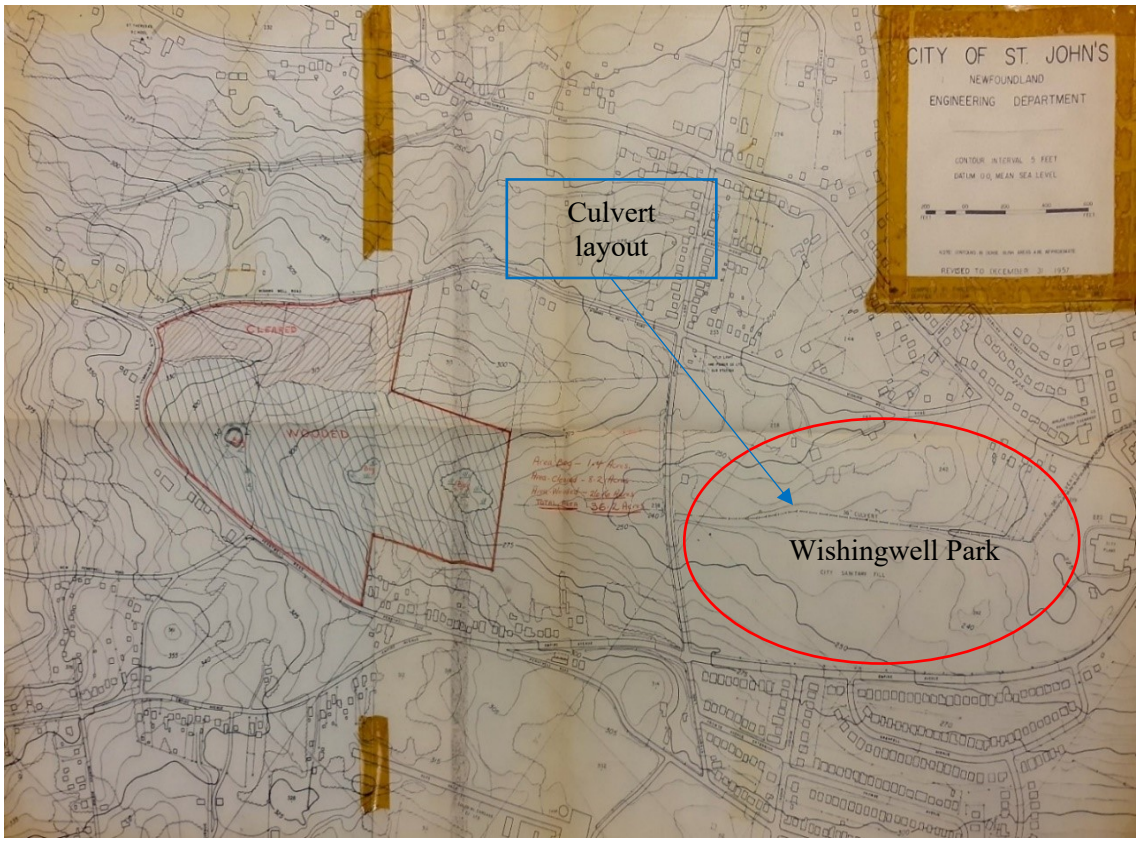

Figure 1.5: O'Dea's property (shaded), landfill (red ellipse) and culvert outline for Kelly's Brook (dashed line). (Modified from City of St. John's archive, 1957.)

An extensive survey was conducted in 1992 of the estimated remaining 6.2 kilometres of reclaimable stretch of the brook (Osmond, 2021). The most critical portion of this was the 600 m stretch in between Bonaventure Avenue and Carpasian Road on account of odor, and a high concentration of dissolved chemicals and contaminants from the long-abandoned Empire Avenue landfill. However, the city of St. John's commission did not approve the project in 1999, thus, ending the efforts of daylighting the remaining culverted stretch of the brook.

From photo records in the City of St. John's archive centre, it is clear that there was no enforcement of segregation of waste at the landfill. Thus, waste was highly mixed in nature with metallic scraps and vehicular wreckages clearly visible in mechanically dug

trenches, as shown in Figure 1.6.

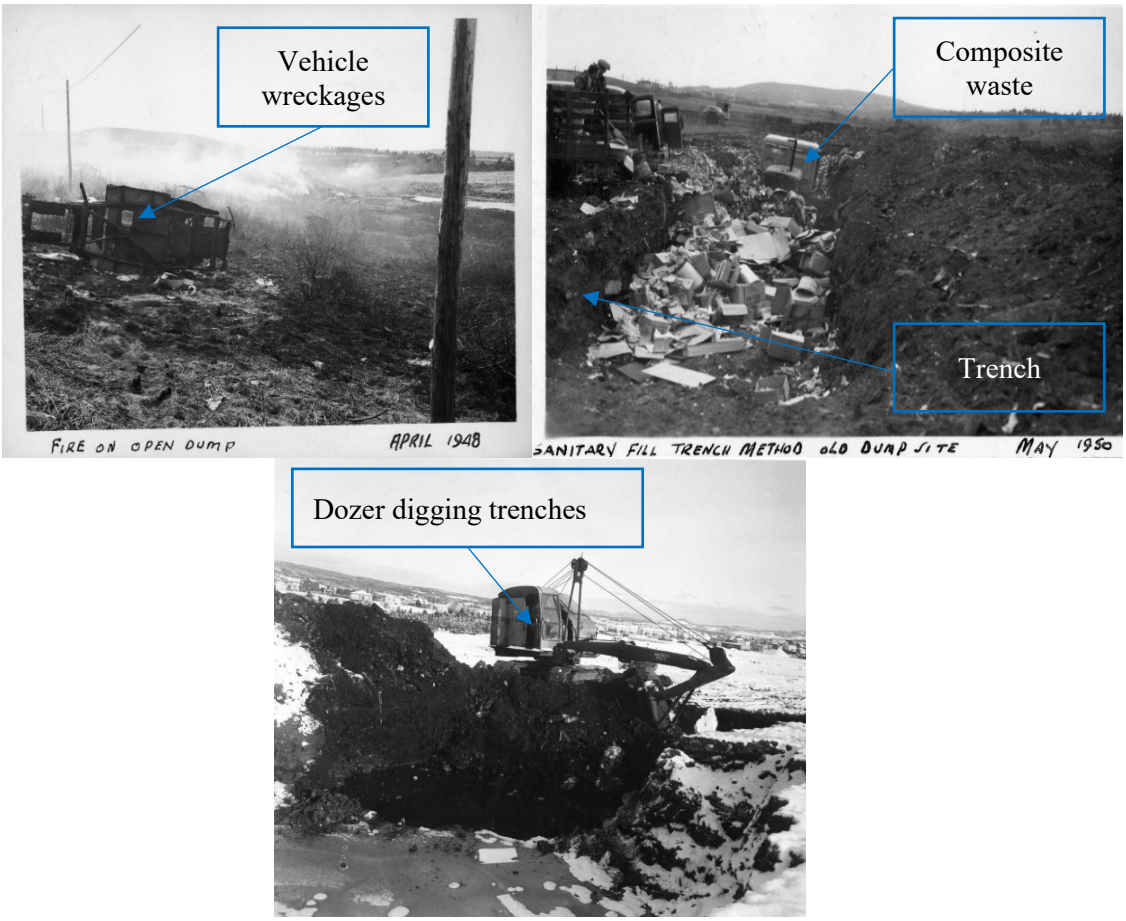

Figure 1.6: Mixed types of wastes, open fire, and trenches at the sanitary landfill.

(Modified from Building Department, city of St. John's archive, 1948 &1950.)

There are no traceable records of any remediation efforts dedicated to evaluating the conditions of the abandoned landfill at Wishingwell Park once it was buried in 1963. Despite the few environmental organizations' efforts in the 1990s to study the area in relation to Kelly's Brook, no action was taken. The majority of the landfill is now occupied by some playing fields such as rugby, soccer and baseball as shown in Figure 1.7. This may be one of the reasons limiting any studies being done in the area (Garland, 2006). The area at present is busy public playgrounds during summers, and largely unused throughout cold winters, and potential environmental impacts are unknown.

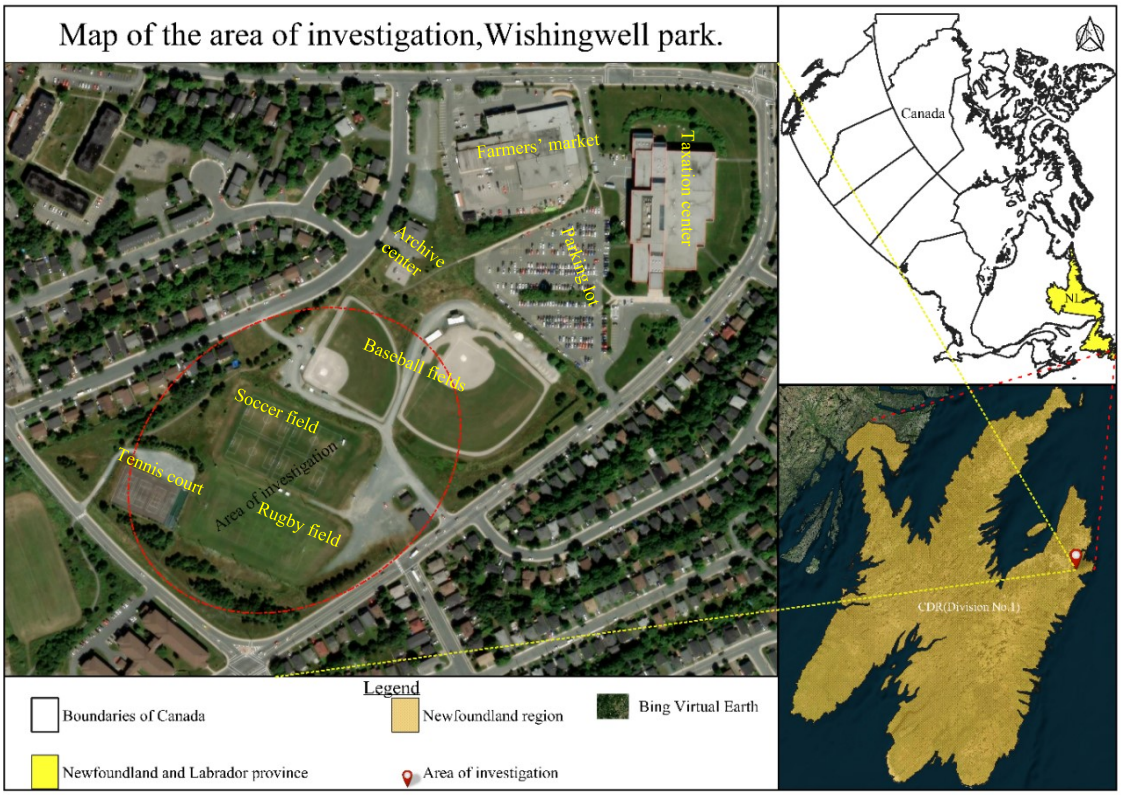

Figure 1.7: Map of the study area showing current features (red-ellipse = extent of area covered by this work).

Garland (2006) conducted a seismic refraction tomography study within Wishingwell Park. He concluded that there was a dipping contact between disturbed tills (fill) and undisturbed tills occurring at depths of about 10 m in the south and 16 m in the north of the area with much seismic scattering events observed towards the north. This scattering was interpreted to be due to the presence of an anthropogenic trench dug during its closure to hosting remnant waste, with its long axis running roughly S85E as depicted in Figure 1.8. He identified the area of dumping as crossing Stamp's Lane (see Figure 1.8), under land now occupied by Swiler's Rugby Park. Garland also concluded that surficial geology of the area consists of disturbed tills transitioning into undisturbed tills likely underlain by bedrock. However, the local geological details still remain very vague and limited for the area.

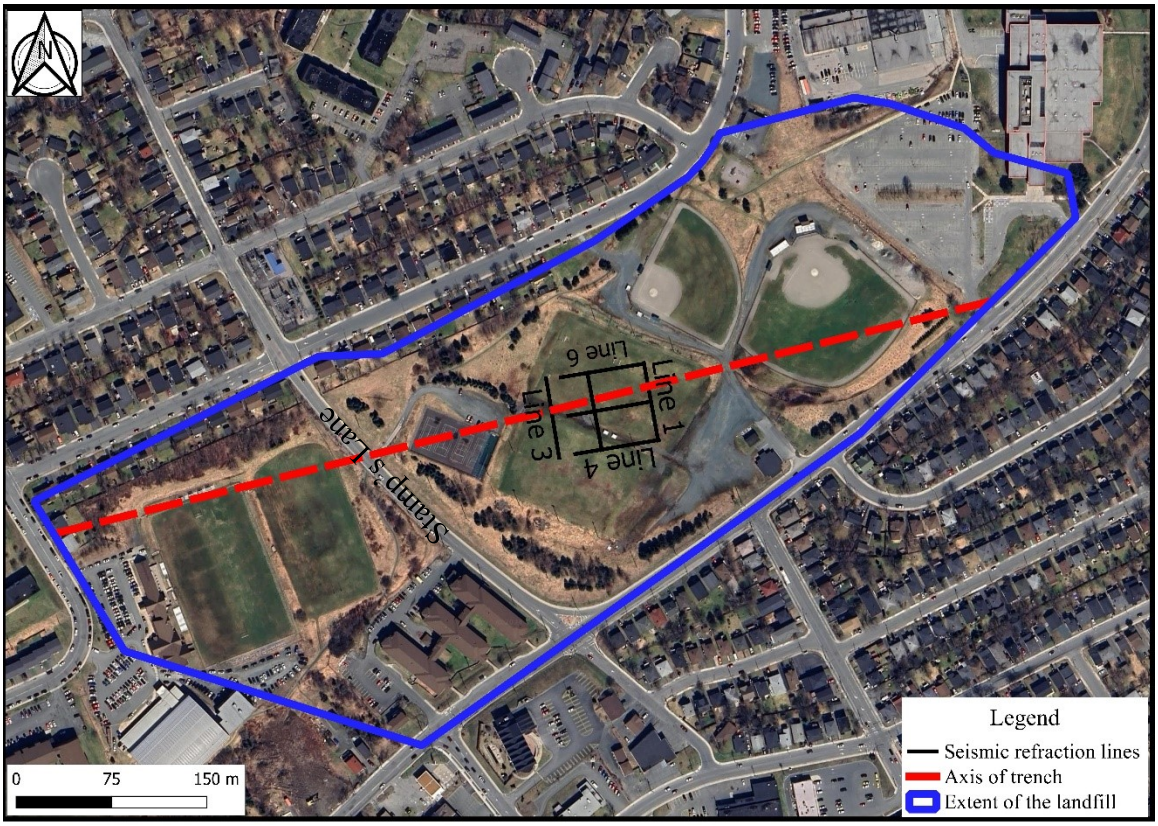

Figure 1.8: Tentative orientation of axis of a trench at Wishingwell Park and seismic refraction lines. (After Garland, 2006.)

Chapter 2: Literature Reviews

2.1 Overview

Rapid development, increasing populations and fast changing lifestyles around the world have brought about increased challenges in waste management paradigms. Landfills are one of the most common methods of managing waste practiced across the globe (Idris et al., 2004; Scott et al., 2007; Hart, 2013). However, most landfilling operations pose significant environmental challenges in relation to such issues as groundwater contamination, subsurface instability and soil degradation (Appiah et al., 2018). These inevitably undesirable impacts from landfilling have led to significant research and studies, much of which have involved expensive drilling, hydrochemical and geochemical analyses of samples (Hart, 2013). These approaches are costly, slow, localized, invasive and do not provide true representations of pollution across the entire extent of landfills (Benson et al., 1984; Hart, 2013). Thus, application of geophysical methods provides a rapid, non-invasive and cost-effective alternative for better characterization of covered landfills through mapping of the spatial distribution of characteristic physical properties of constituent waste and recovery of plausible subsurface models (Kearey and Brooks, 1991; Loke et al., 2013).

With the recent advancements in geophysics—improved cost-efficiency, high-density data logging, digitalization, improved precision and advancement in processing techniques—the spectrum of its applications has broadened beyond classic applications such as mineral exploration, mining and hydrocarbon exploration (Telford et al., 1990; Nabighian et al., 2005). Geophysical investigations to understand and monitor environmental impacts and plan remediation efforts have become an important aspect of environmental studies of landfills and numerous other applications such as water-resource assessments, archaeological mapping (Smith et al., 2000) and engineering applications such as locating buried pipelines (McConnell et al., 1999).

Landfills are of a highly heterogeneous nature (Idris et al., 2004; Scott et al., 2007; Appiah et al., 2018). For the majority of the studies done on landfills, especially of municipal origin, discarded ferromagnetic objects like tools, drums, and other metallic waste constitute significant proportions (Prezzi et al., 2005). Importantly, landfills are severely prone to production of leachate predominantly driven by decomposition and biodegradation of disposed waste mixing with infiltrating water, moisture in the subsurface or surface runoff (Prezzi et al., 2005; Hajar et al., 2013; Carpenter et al., 1990). Baedecker and Apgar (1984) suggested that chloride is a good indicator of leachate as it undergoes very little chemical or biological change in the groundwater system even though leachate can be of highly variable compositions. Abdel-Shafy et al. (2024) found that leachates are composed of soluble organic matters, inorganic components, heavy metals and xenobiotic organic compounds. These factors can alter and complicate geophysical properties within landfills in comparison to the surrounding areas. Consequently, much of the geophysical investigations on landfills involve integration of two or more complimentary geophysical methods or opting for multidisplinary approaches as these are challenging targets to be thoroughly investigated using a single geophysical technique (Fenning & Williams, 1997; Bernstone and Dahlin, 1997). A few of the most commonly applied methods include magnetic, electromagnetic, geoelectrical, seismic and ground penetrating radar which are integrated to address different research objectives concerning the target landfills (Green et al., 1999).

2.2 Magnetometry

The magnetic method is generally the first and obvious choice amongst geophysicists to investigate municipal landfills for landfill mining and remediation purposes owing to its capability to detect discarded metallic objects (Marchetti et al., 2002; Prezzi et al., 2005; Vollprecht et al., 2019). The first such application was reported by Cochran and Dalton (1995) over an abandoned landfill using high-density magnetic data. It was concluded that the resolution of anomaly maps and their ability to correctly detect buried waste depend largely on data density, grid size used, target size and depth. Dawson et al. (2002) demonstrated that the magnetic gradient data was preferred over total magnetic intensity data (TMI) as gradiometers help suppress noise from long-wavelength features, suffer no diurnal variations and enhance the resolution of near-surface anomalies. The success of magnetic surveys to characterize landfills depends on the measure of bulk (volume) susceptibility in addition to the relative proportion and spatial distribution of magnetic waste (Marchetti et al., 2002; Vollprecht et al., 2019). Vollprecht et al. (2019) studied a municipal landfill, in Austria, using a magnetic survey to assess its feasibility for landfill mining. Here, the authors implemented an approach of modelling the field TMI observations for bulk susceptibility distributions and compared the modeled values against laboratory measured susceptibility values of samples collected from the landfill. It was reported in the study that a model constructed by inversion of magnetic data for the area exhibited a range of bulk susceptibility (0.06 SI to 0.11 SI), with a significant deviation from those of samples (0.01 to 0.05 SI).

Appiah et al. (2018) applied a magnetic survey integrated with a magnetic susceptibility survey, at Sunyani municipal landfill in Ghana, and successfully mapped the overall boundaries, probable waste compositions and the depth of the landfill. Ibraheem et al. (2021) studied a covered landfill, in Germany, using a magnetic survey, in which they mapped ferromagnetic waste using total magnetic intensity and vertical gradient data which were then corroborated using geoelectrical inversion results and borehole data.

Khalil and Hassan (2016) detected leachate contaminations/leakages for a landfill in Egypt using a magnetic survey. They also estimated the depth of magnetic anomalies applying some carefully chosen filtering techniques such as analytical signal and Euler 3D deconvolution.

Vollprecht et al. (2019) observed that complex remanent magnetization can significantly affect magnetic inversion results thus complicating the modelling approaches. This usually leads to a simplified version of the actually complicated scenario hidden within the measured magnetic responses (Dentith and Mudge, 2014; Telford et al., 1990; Vollprecht et al., 2019). Further, numerous magnetic data processing techniques like reduction to the pole and apparent susceptibility, based on an assumption of only induced magnetizations, are rendered ineffective and often erroneous (Dentith and Mudge, 2014; Khalil and Hassan, 2016).

Deng et al. (2020) studied the applicability of magnetometry in detecting buried firearms in Toronto, Canada. The authors succesfully demonstrated the efficacy of high data-density magnetic surveys in detecting buried ferromagnetic firearms at much greater depth than electromagnetic and ground penetrating radar methods through the use of reasonably good agreement between forward models and actual field measurments at the test site using a GSM-19GW Overhauser magnetometer from GEM System Inc.

2.3 Geoelectrical Surveys

Landfills are principal sources of leachate resulting in altered subsurface physical properties such as electrical conductivity (or resistivity) which is related to total dissolved salts and ions (such as chloride) in groundwater (Baedecker and Apgar, 1984; Abdel-Shafy et al., 2024). More generally, these properties are related to geological parameters such as the mineral and fluid content, porosity and degree of water saturation in the rock/soils (Loke, 2015; Dentith and Mudge, 2014). Consequently, geoelectrical surveys are one of the best methods at enabling geophysicists to study landfills, predominantly characterized by a highly altered resistivity distribution in contrast to its surrounding environment, and leachate plumes (Meju, 2000; Kearey et al., 2002; Dentith and Mudge, 2014).

It is worthy to note, however, that the measured resistivities are 'apparent' values, with complex relations to the true resistivity distribution in the subsurface, largely influenced by the geometry of the applied array which affects sensitivities, resolutions, signal strength and depth of investigation (Haber et al., 2000; Seaton and Burbey, 2002; Loke, 2015). Thus, the nature of heterogeneity to be mapped, background noise levels at the site, the sensitivity required to resolve structures of interest and the expected resolution of the image dictate the choice of the arrays (Loke, 2001; Griffiths and Barker, 1993; Dahlin and Zhou, 2004). Hesse et al. (1986) suggested the use of more than one array, simultaneously, to map different features of the subsurface contributing to better interpretations.

On account of the time and resources implications, most commonly applied geoelectrical landfill investigations involve using 2D resistivity and pseudo-3D imaging approaches constrained with other data and complementary methods (Meju, 2000). Meju (2000) also constructed subsurface resistivity models and predicted appropriate geochemical parameters such as total dissolved solute (TDS) and chloride using empirical relations

derived using the data from three landfills. Genelle et al. (2012) applied the geoelectrical method augmented by spontaneous potential data to investigate possible damage to landfill cover in order to prevent infiltration and leachate accumulation in the landfill. Dahlin et al. (2002) showed that a 3-D electrical survey can resolve complex trends of leachate flow in a sludge disposal area in Sweden. In their study, the authors recovered lower values of resistivity in contaminated zones in comparison to non-contaminated zones and this was attributed to the existence of abundant ions or charged molecules in the groundwater. Similarly, Park et al. (2016) conducted groundwater contamination investigation by carefully mapping contaminated zones and landfill leachate flow from an uncontrolled landfill using 3D resistivity imaging.

2.4 Electromagnetic Surveys

According to McNeill (1980), electromagnetic surveys can be applied to delineate conductive anomalies such as buried metallic objects, ore bodies, fractures filled with fluids and landfill leachate or saltwater intrusion. Of two major classes under electromagnetics, the frequency-domain (FD) technique has been employed mostly in shallow engineering and environmental studies (Frischknecht et al., 1991; Dentith and Mudge, 2014). It is more sensitive to the absolute conductivity of a medium rather than the relative contrast and hence could be a better detector of conductive targets than the geoelectrical method (Dentith and Mudge, 2014). However, Benson et al. (1988) stated that, though it can be used to map anomalies, the measured absolute values of conductivity should not be taken as a diagnostic parameter. Hence, electromagnetic surveys are widely used for landfill investigations to detect and map metallic waste and leachate plumes.

Hutchinson (1994) investigated a landfill containing solid waste of a putrescible nature where conductive leachate in landfill was easily mapped using a frequency-domain electromagnetic survey. Primarily, this method is chosen for landfill boundary detection, mapping leachate plumes and finding the approximate thickness and volume of waste (Stenson, 1988; Hutchinson, 1994). Frischknecht et al. (1991) demonstrated the applicability of the electromagnetic sounding technique to study landfills. Hajar et al. (2013) applied the electromagnetic method as a non-intrusive approach to image the spatial distribution of conductive subsurface structures, i.e., the buried waste or contaminated regions using either conductivity value maps or phase maps.

Huang and Won (2000) successfully applied a broadband electromagnetic technique to study two landfills and a defunct gas plant in the USA. They used low frequency data to compute apparent magnetic permeability and with these and other data, they estimated the apparent conductivity and apparent susceptibility. The authors also compared gridded

electromagnetic results at a few sites to gridded magnetic intensity data and concluded that an electromagnetic survey could resolve shallower anomalies better with good resolution while the magnetic method was better at delineating anomalies at deeper depth. Huang and Fraser (2000) proposed algorithms for using inphase-quadrature or amplitude-phase to analytically compute desired parameters, specifically permeability and resistivity from broadband low induction number electromagnetic surveys and successfully applied the algorithms to a few cases of landfills.

Belmonte-Jiménez et al. (2014) studied possible aquifer contamination due to leachate infiltration from a landfill hosting municipal solid waste using a low induction number system (EM-31) combined with a very low frequency (VLF) survey. Here, the authors applied the Fraser filtering technique (Fraser, 1969) on inphase VLF data and 2D conductivity inversion for EM-31 data and found the methods corroborated each other very well. Johnson et al. (2012) showed the effectiveness of time-lapse measurements using frequency-domain electromagnetic surveys, employing a GEM2 system over a landfill in Connecticut over 5 years duration to closely monitor changes in geoelectrical conditions of the landfill following remediation efforts to curb leachate amount. The time-lapse responses at the site saw reductions in electrical conductivities over time indicating the success of the remediation work at the site. Furthermore, Johnson et al. (2012) concluded that electromagnetic data from GEM2, when inverted for conductivity at various depths, corroborated well with inversion models of a geoelectrical survey.

Won et al. (1996), Huang and Won (2000) and Crook et al. (2016) described cases where the simple contouring (gridding) of inphase and quadrature components acquired using a GEM2 system, in parts part million (ppm), could clearly depict the spatial distributions of the probable anomalous responses without needing complicated computations, thereby facilitating fast reconnaissance operations over landfills.

2.5 Ground Penetrating Radar Survey

The aforementioned methods are generally ineffective to resolve certain aspects of landfills like internal structures and layering (Benson et al., 1984). For standard landfills, it is important to monitor internal structure and the structural integrity of the containment walls to prevent any mishaps. This could be achieved using ground penetrating radar (GPR) surveys based on reflections due to contrasts in either electrical or magnetic properties. Benson et al. (1984) stated that GPR and seismic refraction can be best integrated to map the layering nature of the landfills. In addition to using GPR surveys to understand structures and stratigraphy, Splajt et al. (2003) argued that they can be applied to delineate the depth of waste, waste-leachate interfaces reinforced by drill logs and other data. They also suggested the use of multi-frequency GPR data to resolve highly varying dielectric properties in the landfills. Júnior et al. (2016) investigated the probable slip surface passing through the landfill using GPR, in Brazil, and concluded the existence and extent of the slip surface based on the contrast in properties of air and waste at the site.

Daniels (2006) used ground penetrating radar surveys to detect buried explosive mines, buried ordnance, concealed tunnels, buried bodies, archaeological objects, and contaminated waste. Cassidy (2009) and Annan (2002) asserted that the presence of highly conductive materials/media in the subsurface highly attenuate the electromagnetic signals thereby limiting or completely stopping the propagation of radio waves any deeper into the subsurface, which is usually the case for municipal landfills (Green et al., 1999). Also, Schultz (2012) conducted ground penetrating radar surveys to locate graves and burial sites. Splajt et al. (2003) studied landfill using borehole information and chemical analyses of surface samples supplementing a ground penetrating radar survey. The GPR method can be used as a rapid reconnaissance survey to delineate and map the existence of illegally buried waste in the abandoned landfills without much prior information as well (Massarelli et al., 2021).

Zhang et al. (2022) used shielded GPR over a landfill consisting of construction waste and estimated the volume of waste through the application of GPR inversion using a complex refractive index model and spatial interpolation achieved using the kriging method. According to Yochim et al. (2013), in their study over two landfills in Canada titled “Determining Water Content in an Active Landfill with the Aid of GPR”, the overall effectiveness of GPR imaging showed improvement when the site of investigation possessed high water content although the moisture content largely varied spatially. One added advantage of applying a GPR survey for landfill delineation and mapping over its EM counter-part is attributed to a very high-resolution imaging capability of shallow targets which are common in landfill studies (Yochim et al., 2013). Similarly, numerous authors (Yochim et al., 2013; Dawrea et al., 2021) have studied landfills for their potential to generate landfill gas and they found GPR was the most effective method for simply detecting and delineating the landfill extent and its constituents. Ferrier et al. (2009) demonstrated in their study of monitoring two landfills in the United Kingdom that GPR could be used as a complementary technique to validate a probabilistic risk-based modeling technique. The authors also demonstrated that GPR interpretations could be enhanced and made more physically realistic by incorporating as many prior data as possible during its processing. These data could include information such as water table height, detailed local geology and waste disposal records. Wu and Huang (2006) used GPR as an effective tool to detect and delineate illegal dump sites as the replacement for the traditional investigation of using soil gas or soil sampling which was proven inefficient both in terms of cost and time.

2.6 Integrated Methods

Landfills being highly heterogenous, composite and complex geophysical targets necessitate careful integration of several surveys, thus limiting the use of a single survey, to characterize them fully (Green et al., 1999). Adewuyi and Oladapo (2011) carried out a landfill study using integrated geoelectrical and VLF- electromagnetic methods. They found that the electrical method depicted several layers of contrasting properties, however, electromagnetic data did not show this. In a landfill study, Mack (1993) concluded that the low-resistivity anomalies were well mapped by electrical and inductive terrain conductivity surveys due to an increase in ground-water specific conductance in the landfill affected regions. Pellerin (2002) also concluded that integrated electromagnetic and resistivity methods could detect plumes of contaminants in groundwater, thereby helping in ground water contamination studies. A pseudo-3D resistivity survey, integrated with magnetics and frequency-domain electromagnetic surveys, was used in imaging landfill extent, leachate plume and a few isolated landfill anomalies in Sweden (Bernstone and Dahlin, 1997). Khalil (2012) studied a landfill in Cairo, Egypt, using magnetic and geoelectrical surveys supported by ground water and soil quality analyses. Crook et al. (2016) carried out a geophysical investigation at Nazareth landfill, Mexico, using an electromagnetic survey (GEM2) combined with magnetic and geoelectrical methods and successfully demarcated the landfill boundary, depth of waste and the aerial extent of the landfill. Also, Soupios et al. (2007) conducted an integrated geophysical study over a large landfill to study the geometry of the landfill (depth and extent) and showed that the results of shallow electromagnetic measurements agreed well with electrical tomography results for delineating the spatial extent of the landfill. The authors also correlated high conductivity zones with zones with the highest waste thickness and maximum leachate accumulation due to bedrock relief at the landfill.

Numerous authors have applied ground penetrating radar carefully integrated with other techniques to study landfills given their complex nature (Green et al., 1999; Bievre and

Garambois, 2023). One such case is reported by Porsani et al. (2004) where GPR was integrated with vertical electrical sounding (VES) and successfully delineated contamination plumes indicated by the absence of reflectors or presence of very weak signals that are known as shadow zones due to the existence of high conductivity regions. Loperte et al. (2010) used the GPR method in conjunction with magnetic survey to map medieval buried structures. Reyes-López et al. (2008) successfully investigated a landfill in Mexico for spatial distribution of leachate plumes and probable direction of flow using GPR and VES with traditional chemical analyses. Khalil and Hassan (2016) carried out a landfill investigation by integrating ground penetrating radar (100 MHz) with magnetic and direct current resistivity surveys. They concluded that regions with higher concentrations of waste correspond to significant scattering of GPR energy, thereby corroborating the observations in other methods though there remained a few areas of disagreement. Pujari et al. (2007) studied possible contaminations to groundwater from a nearby landfill, in India, using integration of GPR and direct current survey. The authors also depicted the case where migration of the GPR data, in addition to normal processing, led to the better resolvability of features because of the scattering phenomenon expected in such areas.

Fenning and Williams (1997) applied a combination of ten geophysical methods namely; magnetic, geoelectrical (resistivity and VES), electromagnetic (inductive conductivity and VLF), GPR, seismic (refraction and reflection) and gravity surveys to successfully delineate the spatial extent and margins of a landfill in southern England. Green et al. (1999) also integrated five effective geophysical methods namely, magnetics, geoelectrical, electromagnetic and ground penetrating radar, along with both seismic reflection and refraction techniques, and successfully studied a few critical aspects of a landfill, in Switzerland, such as its spatial extent (boundaries), regions of different waste compositions, approximate depth extent and the host-surrounding contrast with very limited ground truths. Marchetti et al. (2002) reported effectiveness of using magnetic, geoelectrical, GPR and multi-frequency electromagnetic surveys to investigate landfills

in Italy, where buried waste was predominantly discarded steel drums. Dumont et al. (2017) applied integration of magnetic, electromganetic, geoelectrical and seismic methods. They concluded that the magnetic method was significant in delineating the extent of landfill against the host formation in the area. Dawson et al. (2002) demonstrated that iron-rich leachate plumes at landfill sites could also be detected using magnetic surveys along with inductive terrain-conductivity, geoelectrical, seismic reflection and borehole electromagnetic induction and gamma logging. Dawson et al. (2002) extensively investigated Winthrop landfill, Maine, using 2D electrical resistivity, inductive terrain conductivity, borehole electromagnetic, seismic reflection, and magnetic surveys to map leachate flow direction. Missiaen and Feller (2008) used a unique combination of seismic, sonar and magnetic surveys and successfully mapped and characterized chemical munitions (waste) from World War I in the Baltic Sea and also identified a few buried shiprecks.

Therefore, based on the extensive literature studies on landfills of similar nature and the limited prior information on the likely nature of waste at the site, this study chooses a combination of four different geophysical surveys namely, magnetic, geoelectrical, electromagnetic and GPR to study the present-day conditions of Wishingwell Park.

Chapter 3: Magnetic Survey

3.1 Basic Principles

A magnetic survey is a passive and non-invasive geophysical technique. Typically, for geological or geotechnical surveys, the total magnetic field intensity (TMI) is measured, and anomalies relative to the Earth's (geomagnetic) field are identified. Magnetic anomalies are due to materials that are magnetized either due to the present geomagnetic field or to some past field. The total magnetic field intensity is a measure of only magnitudes (resultants) of the sum of Earth's field, the induced field and the remanent field at a specific time and location. Figure 3.1 shows typical working principle of magnetic survey.

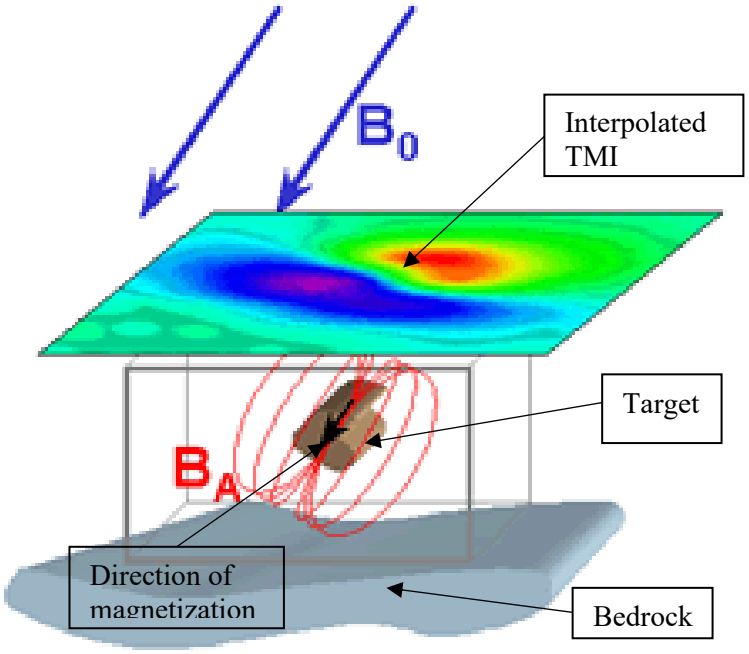

Figure 3.1: Diagram showing working mechanism of magnetic survey with a susceptible body. (Modified from eoas.ubc.ca, 2016.)

The intensity of the geomagnetic field is commonly measured in nanotesla ($1nT=10^{-9}$ Tesla, T), the small unit is used because the magnitude of measured magnetic anomalies is generally very small in geophysical exploration (e.g., Dentith and Mudge, 2014). Rather than $\mathbf{B_0}$, geophysicists sometimes prefer to use **H**, which has units of Ampères per metre (A/m). The relationship between them is given by:

$$\boldsymbol{B} = \mu_0(\boldsymbol{H} + \boldsymbol{M}) \tag{3.1}$$

where:

B is magnetic flux density (nT),

μ_0 is the permeability of free space ($4\pi \times 10^{-7}$ H/m), and

M is the magnetization (magnetic dipole moment per unit volume).

Surveys measure the magnetic field outside of magnetized materials (usually in air) where **M** is 0, so measurements of the fields $\mathbf{B_0}$ and **H** differ only in their units. Materials which generate magnetic anomalies are magnetized based on a physical property of the material known as magnetic susceptibility (K) and permeability (μ or μ_0). The magnetic susceptibility is a dimensionless ratio between the induced magnetization, $\mathbf{M} = \mathbf{B_A}$, in the material to that of the inducing magnetic field, **H** (Telford et al., 1990). Here, the inducing magnetic field refers to the Earth's geomagnetic field ($\mathbf{B_0}$) whose strength and orientation vary spatially and temporally in different parts of the world. The induced magnetization, expressed in the same units as **H**, refers to the magnetic dipole moment per unit volume as a result of alignment of atomic dipoles or of magnetic domains in mineral grains. Thus, from the definition above:

$$\boldsymbol{M} = \text{K}\boldsymbol{H}. \tag{3.2}$$

Magnetic susceptibility is a measure of how easily can different materials be magnetized and helps to categorize them into various magnetic classes such as diamagnetic, paramagnetic and ferromagnetic amongst others. The most common geophysical targets include paramagnetic, ferrimagnetic and ferromagnetic materials. From equations 3.1 and 3.2,

$$\mathbf{B} = \mu_0(\boldsymbol{H} + \boldsymbol{M}) = \mu_0(\boldsymbol{H} + \text{K}\boldsymbol{H}) = \mu_0(1 + \text{K})\boldsymbol{H} \tag{3.3}$$

and the magnetic permeability (μ) of a material is given by:

$$\mu = \mu_0(1 + \text{K}). \tag{3.4}$$

The equations above are for ideal cases of magnetization due to the present inducing geomagnetic field (see Figure 3.1). However, paleomagnetic studies have proven the existence of a magnetic phenomenon called remanent magnetization. It is due to irreversible changes in the magnetic properties of a material after the removal of an inducing field. The occurrence of remanent magnetization depends on the strength of the inducing field, polarity of field, magnetic mineral contents, magnetic grain sizes, microstructures, re-magnetization and tectonic processes amongst others (Dentith and Mudge, 2014). The strength and orientation of remanent magnetization will be the vector sum of all permanent magnetizations commonly known as Natural Remanent Magnetization (NRM). Thus, it can have either an additive or subtractive effect towards the overall measured magnetic responses. Thus, this phenomenon can render the measured magnetic data complex and problematic for inversion and filtering processes principally due to the ambiguous nature of its contribution to the measured data. This is the prevalent observation specifically for ferrimagnetic, where the magnetic domains are non-uniform with weaker magnetization potential, and ferromagnetic materials.

In the ideal cases of magnetization (or with remanent magnetization parallel to the inducing field), the TMI data at magnetic poles, equator and mid-latitudes are understood to have characteristic shapes (without remanent effect) which are well documented provided the dip and shape of the anomalous body is known. A TMI profile across an isolated magnetic source at the magnetic poles is typically with the positive TMI peak vertically above the anomaly with two smaller symmetrical lobes of TMI lows, one each on either side of the peak. A TMI profile over a similar source at the equator has a negative peak over the anomaly and positive lobes on either side. At mid-latitudes, there are dipolar signatures, with relatively higher positive peak towards the north and south of the source in the southern and northern hemisphere, respectively (Dentith and Mudge, 2014). The typical magnetic profiles for a few ideal cases are shown in Figure 3.2.

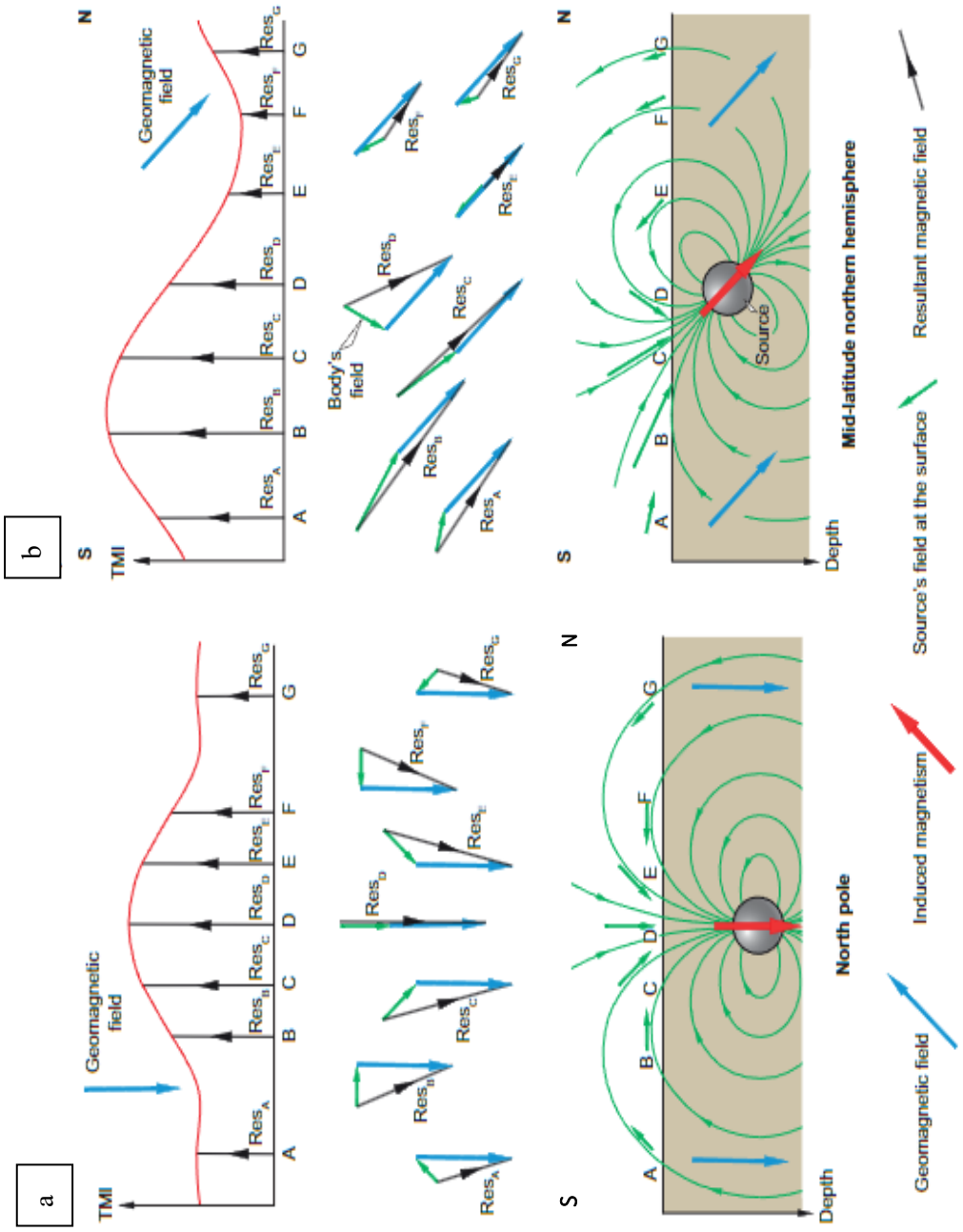

Figure 3.2: Standard TMI profiles over a spherical body at North Pole (a) and mid-latitudes in northern hemisphere (b). (Modified from Dentith and Mudge, 2014.)

3.2 Field Survey Methods

A magnetic survey uses a highly sensitive instrument called a magnetometer, with at least a rover and a base, to record the resulting magnetic field responses due to interactions between the Earth's field and target(s). The measured magnetic data may be total magnetic intensity (TMI), TMI and gradients or all the three vector components through either an aeromagnetic, surface or downhole deployment. The best choice is dictated by the objectives of the study, targets, availability of instruments, survey coverage and budgets amongst many others. Afterwards, the data should be accordingly processed, analyzed and interpreted.

In this study, a GEM Overhauser magnetometer (gradiometer- GEM-WG 19) from GEM System Inc. was used to collect the data. It is a type of proton precession magnetometer except that it has greater sensitivity than the ordinary proton precession magnetometer, i.e., a resolution of 0.01nT and absolute accuracy of 0.1nT. The magnetometer, GEM-WG 19, operates based on the principle of the Overhauser effect (Overhauser, 1953). The Overhauser effect is a transfer of energy from large electron magnetic moments (of a special liquid with unpaired unbound electrons) to protons (hydrogen atoms) combined in the same sample which, when exposed to secondary polarization from a radio frequency magnetic field, results in free precession frequency of the protons (Hrvoic, 1989; Ripka and Arafat, 2019). Thus, the precession frequency, also known as Larmor frequency, is electronically measured and the external magnetic field, which is directly proportional to the precession frequency, is subsequently computed using a well-established relationship in quantum mechanics.

Here, two GEM-WG 19 consoles (a base and a rover) and three sensors were deployed during the field work. The base, located at the periphery of the study area, recorded the time-synchronized Earth's field every 4 seconds. This data is essential to monitor and correct magnetic responses of diurnal variations and magnetic storms which may contaminate the data. The rover was mounted with two sensors, 0.25 m apart, and a geographic positioning system which was time-synched to both the base and rover. The final assembly is shown in Figure 3.3.

Figure 3.3: Overhauser magnetometer assembly deployed at the site.

The assembly was used to survey the entire study area, in walk-grad mode, thereby measuring the total magnetic intensity and vertical gradient data. In order to achieve high-density magnetic data, a point data was recorded every second, while walking with the assembly, with its geographic location being simultaneously recorded using a global positioning system antenna attached vertically above the sensors. Detailed images of

various components of the magnetometer are shown in Appendix A.

For this work, the overall magnetic survey involved irregular grids of roughly parallel lines, spaced about 5 m apart, across the rugby, soccer and baseball fields with tie lines covering the entire area as depicted in Figure 3.4. All of these data were collected in three different phases: phase I on 2nd September 2022, phase II on 25th May 2023 and phase III on 8th November, 2023.

Figure 3.4: Map of magnetic survey layout and its coverage.

3.3 Data Analyses and Interpretations of Magnetic Survey

Following the data acquisition, firstly, the raw total magnetic intensity data was carefully examined for quality control by examining base measurements visually as well as using an algorithm from GEM link software. However, no significant external interference was observed during the surveys and hence no separate correction was necessary.

Subsequently, the total magnetic intensity data were further processed using gridding techniques implemented in Oasis Montaj from Seequent. Gridding is the process of spatially interpolating input data onto equally spaced cells forming a uniform grid (Seequent, 2022). Of numerous gridding algorithms available in Oasis Montaj, the 'Minimum Curvature' algorithm was chosen for this work. It is the best gridding technique to handle smoothly varying, randomly distributed data, which is the case with our magnetic measurements. The algorithm interpolates any XYZ data by solving an optimization problem of fitting a two-dimensional surface to the raw data (Briggs, 1974), by iteratively minimizing the curvature of the surface (Seequent, 2022). Using a grid cell size of 2.5 m, a search radius of 5 m and setting the maximum number of iterations to 100, the TMI data was successfully interpolated achieving the required tolerance limit of 5% (as the stopping criterion) as shown in Figure 3.5.

Clearly in Figure 3.5, there are a number of linear and continuous regions with high TMI responses across the study area. These features align roughly WSW-ENE with TMI values higher than 50,800 nT.

The area has numerous existing anthropogenic features which are essential amenities associated with the several different types of playing fields. A map showing all these features superimposed on the TMI map is given in Figure 3.6. Some of these surficial metallic features, such as chain-link fences, catcher's box fences, rugby and soccer posts,

baseball plates and openly lying metal pieces, are the principal sources of magnetic noise in the area.

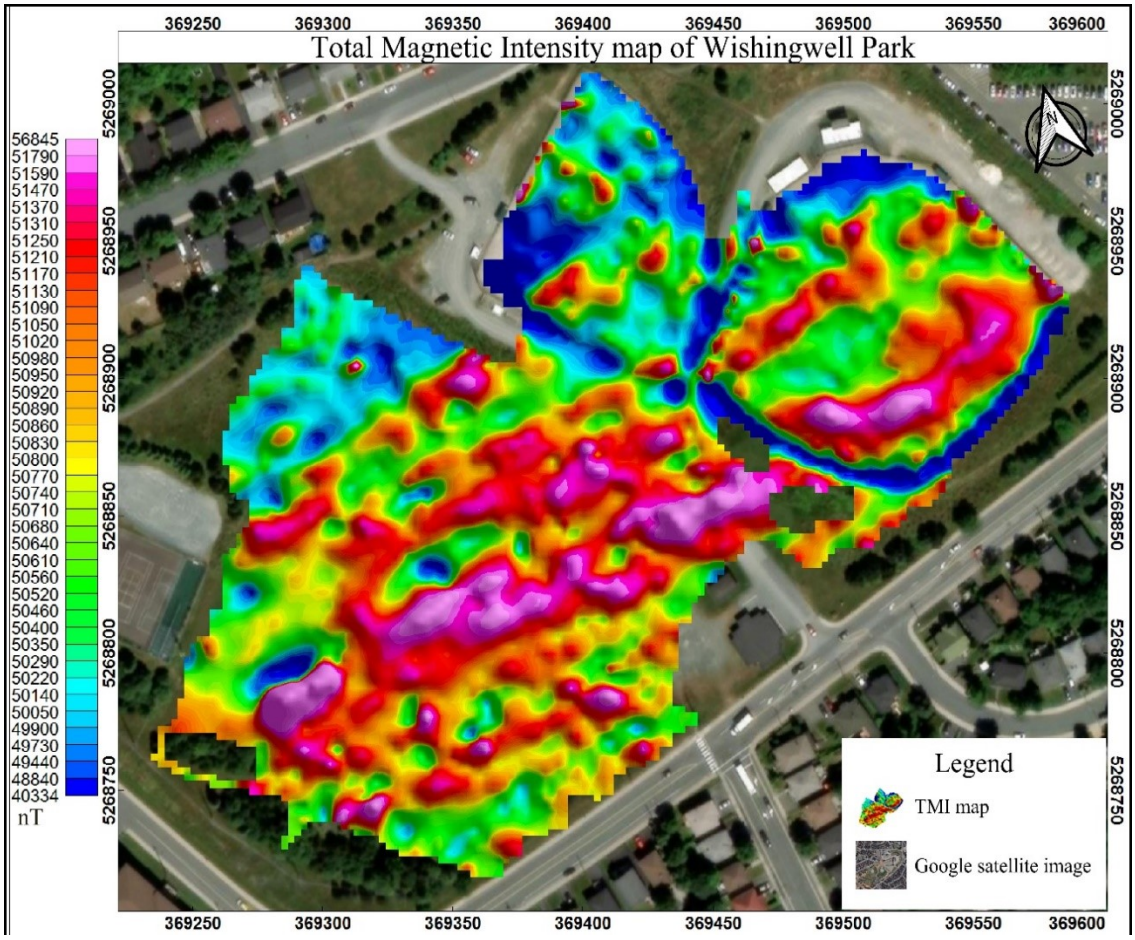

Figure 3.5: Total magnetic intensity map of the study area.

(Colour method =histogram equalization, cell extended beyond data = 0 and north arrow= magnetic north.)

A detailed survey was conducted with approximately 1 m line spacing around soccer goals using two different layouts in the area to understand their influence on the recorded magnetic responses. This data was gridded and compared against the broader scale survey data as shown in Figure 3.7. Clearly, these metallic, presumably iron, goals (approx. width 3.7 m, height of 2.1 m) have a strong influence on the measured data as shown by the low TMI values in the immediate vicinity of the goals in the highlighted patches in Figure 3.7. However, their effects are not particularly significant when compared to the magnetic intensity of many of the other anomalies recorded in the area.

Also, it can be observed that the extent of the negative anomalies from these goals is very limited and that the general north-east trend of magnetic anomalies for the detailed survey and the overall survey is the same.

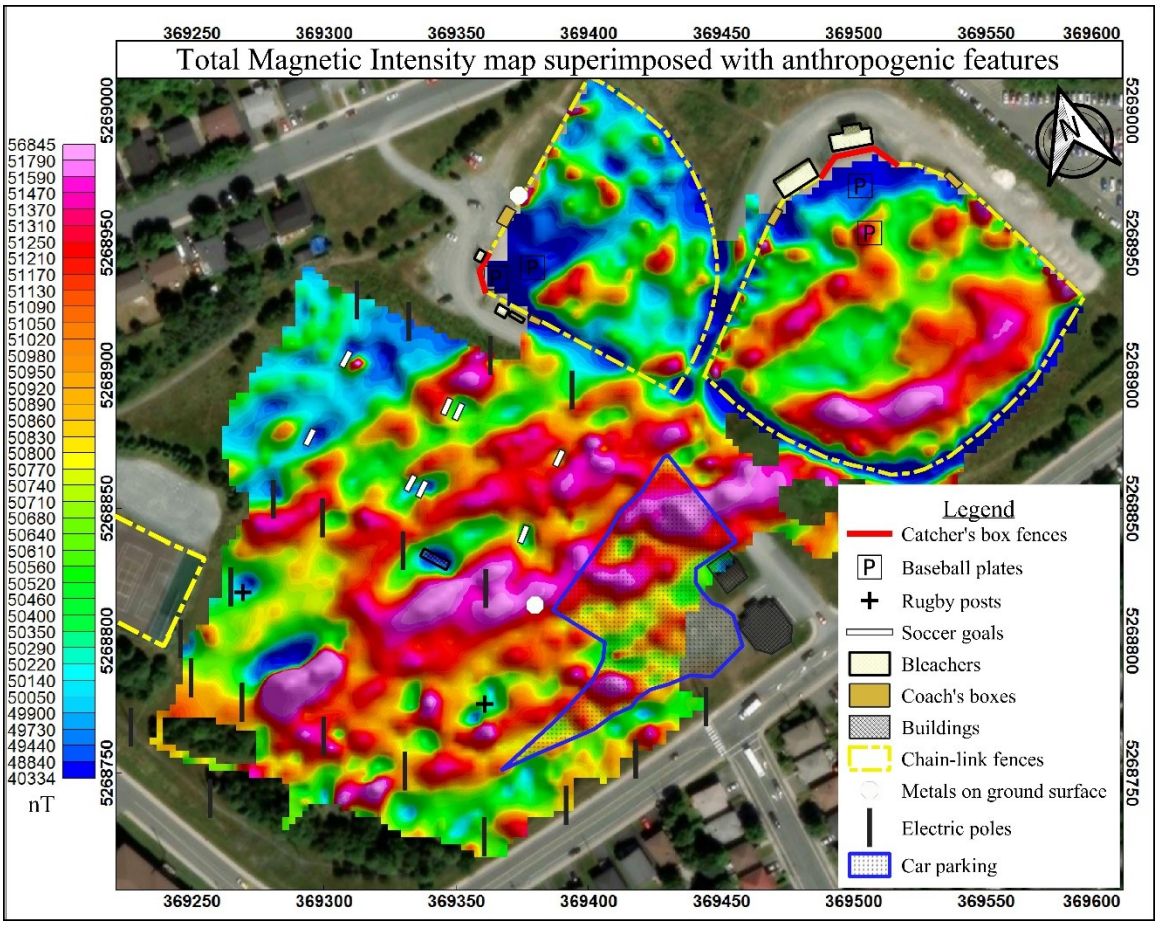

Figure 3.6: Map showing existing anthropogenic features in Wishingwell Park superimposed on the TMI map. (Colour method =histogram equalization, cell extended beyond data = 0 and north arrow= magnetic north.)

On the other hand, it is clear that the magnetic responses around the two baseball fields are strongly influenced by anthropogenic features like the chain-link fences, catcher's box fences and baseball plates which are highly magnetic in nature. Due to the extreme and rapidly changing gradients in these areas, the magnetometer was unable to obtain stable readings and gave TMI responses closest to these anthropogenic features as zero: hence these values were removed. These zones with strongest negative troughs of magnetic responses in the vicinity of those features can be clearly attributed to the

influence of these anthropogenic features existing on the surface.

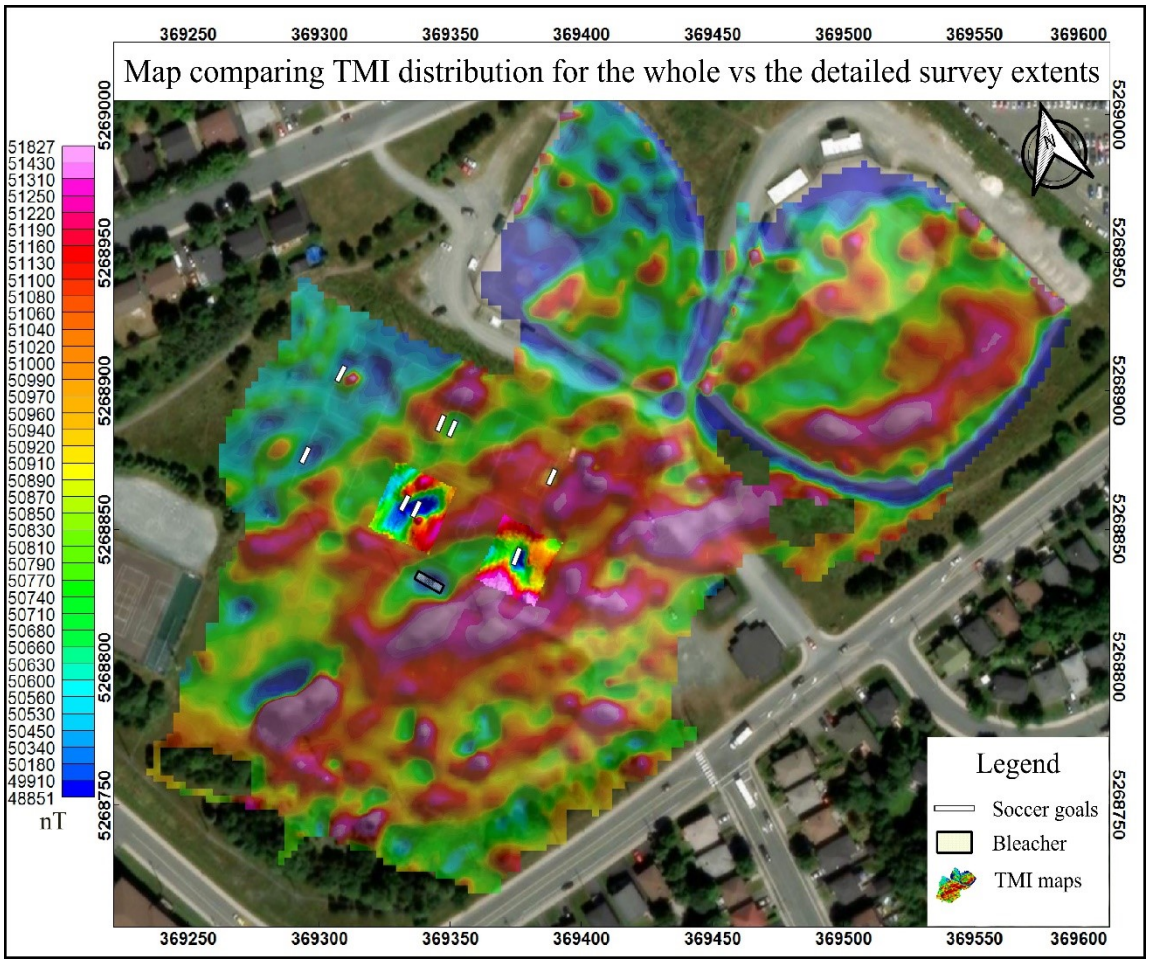

Figure 3.7: Map showing comparison of TMI responses of soccer goals against whole extent of study area. (Colour method =histogram equalization, cell extended beyond data = 0 and north arrow= magnetic north.)

Using the International Geomagnetic Reference Field (IGRF), model (1950-2024) based on the gufm1 model after Jackson et al. (2000), the averaged reference Earth's field in the area is approximately 50,700 nT (at inclination ≈ 66.6˚ and declination ≈ -16.7˚). It is straightforward to expect higher TMI responses in regions with magnetic anomalies than just the Earth's that would occur field over regions without any anomalies (Telford et al., 1990). However, the magnetic anomalies are complex for straightforward visualization everywhere on the Earth except for the two geomagnetic poles and equator (Dentith and Mudge, 2014; Rajagopalan, 2003). Thus, detailed magnetic data interpretation involves

application of several mathematical techniques called filters, to simplify the responses.

Reduction to the Magnetic Pole

One of the most common filtering methods is to mathematically convert complex magnetic responses from different locations on the Earth's surface into their polar or equatorial equivalent using respectively the reduction to the magnetic pole (RTP) or reduction to the magnetic equator (RTE) techniques (Baranov and Naudy, 1964). Rajagopalan (2003) concluded that the RTP technique worked best when it was applied for places with inclination higher than mid-latitudes. Therefore, for this study, based on the steep inclination of the study area, the RTP method was chosen. Fundamentally, this filter works correctly and effectively only if the recorded magnetic data are purely induced, without remanent magnetization at all or remanent magnetization being parallel to Earth's field (Dentith and Mudge, 2014; Rajagopalan, 2003).

Here, the TMI grid, Figure 3.5, was used to perform RTP filtering by providing parameters such as the magnetic inclination of 66.6 degrees and the magnetic declination of -16.7 degrees for the area. The resulting polar equivalent magnetic data, with a grid size of 2.5 m, is shown in Figure 3.8. This figure depicts the magnetic responses which are more localized over the sources than the more smudged magnetic responses observed in the TMI map in Figure 3.5.

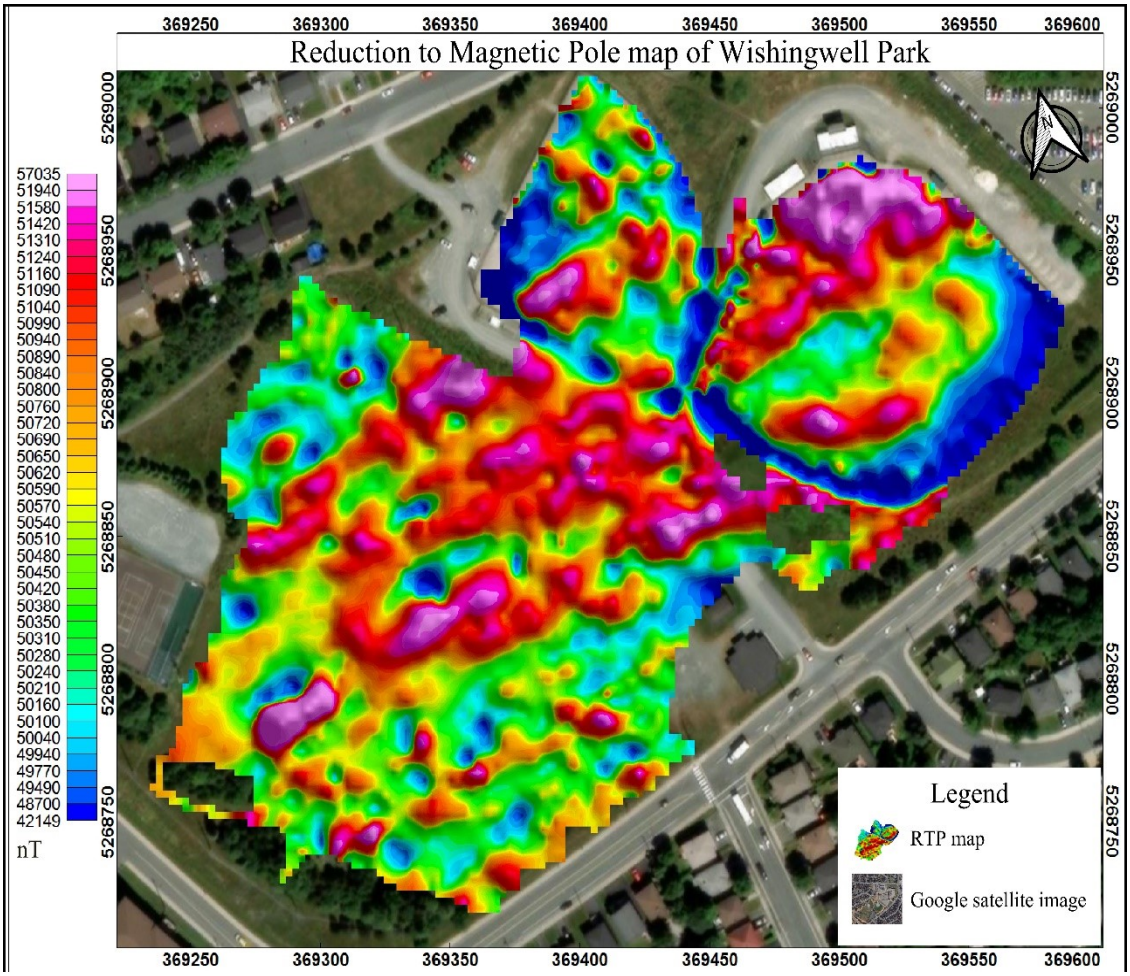

Figure 3.8: Reduction to pole magnetic intensity map. (Colour method =histogram equalization, cell extended beyond data = 0 and north arrow= magnetic north.)

Anomalous Magnetic Intensity

Anomalous magnetic intensity data (magnetic residuals) were computed manually by subtracting the average Earth's field of 50,700 nT from the corrected TMI data. This data provides good estimates of the magnetic responses as a consequence of the existing anomalies in the area. The residual data-set was gridded using the minimum curvature algorithm with the grid size of 2.5 m as shown in Figure 3.9. This figure clearly depicts linear trends of magnetic anomalies in the area predominantly trending WSW-ENE with substantial magnetic anomalous intensity ranging from -10366 to 6145 nT. These linear

magnetic features are interpreted as the likely axes of artificial trenches, trending roughly WSW-ENE, hosting waste in the area as shown in Figure 3.10.

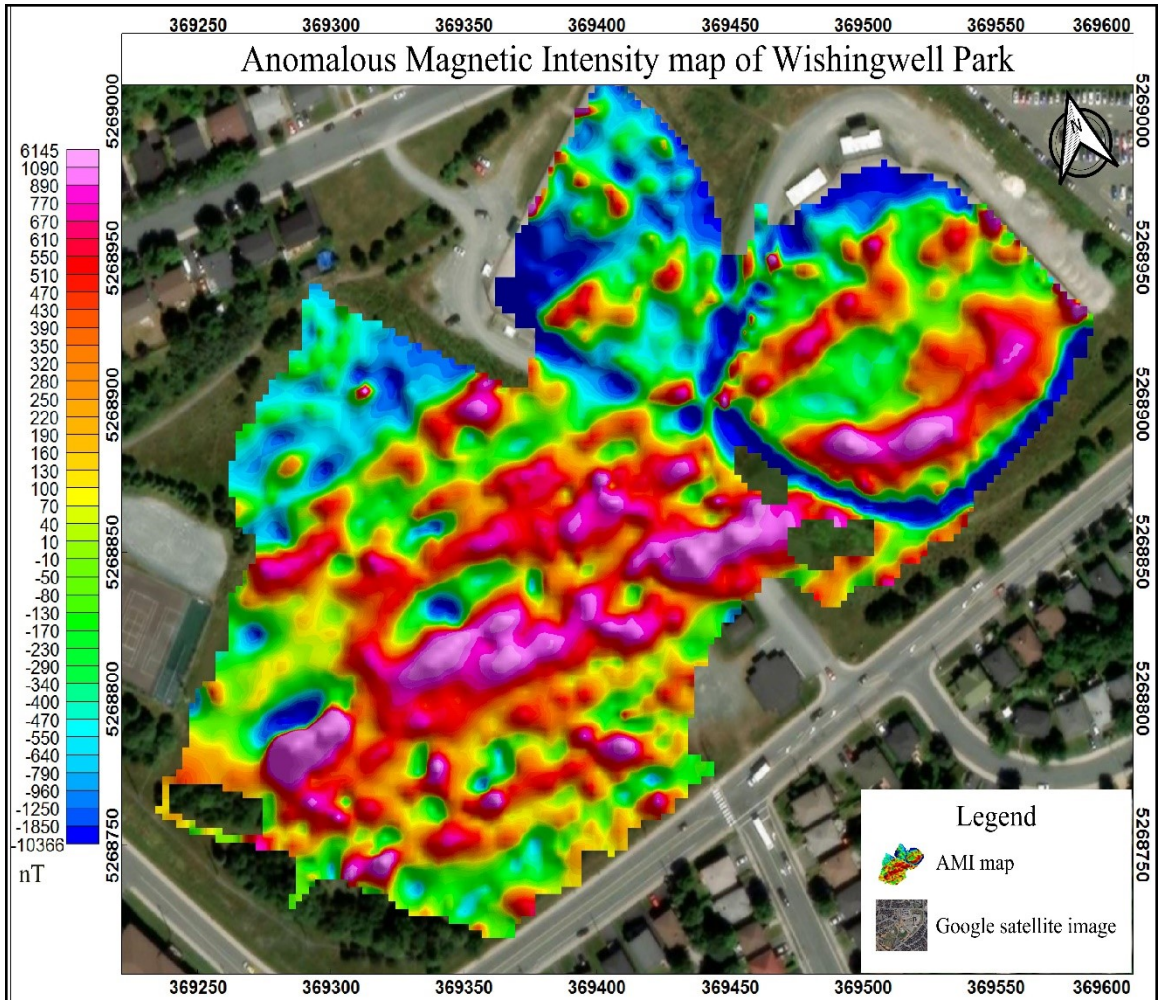

Figure 3.9: Anomalous magnetic intensity map. (Colour method =histogram equalization, cell extended beyond data = 0 and north arrow= magnetic north.)

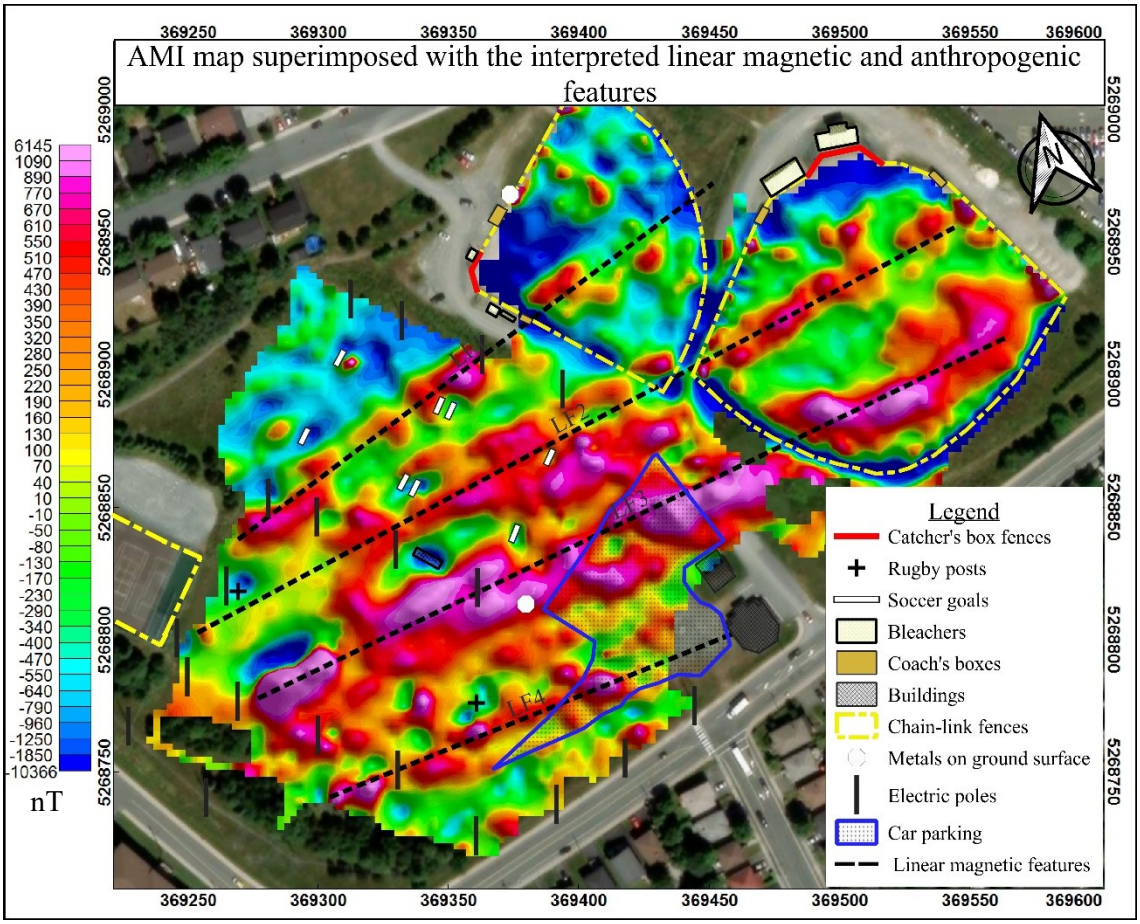

Figure 3.10: Interpreted magnetic linear features representing axes of trenches and the anthropogenic features superimposed on the AMI map.

Despite very strong influence from the anthropogenic features in the north-eastern corner of the area, the anomalous magnetic intensity recorded in the entire area is very high compared to the typical ranges reported in similar studies (e.g. Cochran and Dalton, 1995).

Gaussian High-Pass Filter

With the crude understanding of likely magnetic anomalies and their trends in the area, one crucial step is to comprehend how deep or shallow are these anomalies buried. Here, the Gaussian High-Pass filter in Oasis Montaj is used. This filter preferentially emphasizes features that have a narrow width, which is characteristic of features due to shallow sources. It operates in the Fourier domain by specifying a cut-off central

wavelength. The Gaussian high-pass filter was applied to compute magnetic residual responses using the TMI grid and a cut-off central wavelength of 75 m corresponding to shallower magnetic sources. Khalil and Hasan (2016) applied central wavelength longer than 56 m to filter the deeper sources using the radially averaged power spectrum principle of Spector and Grant (1970). For this study, the wavelengths of 75 m and shorter are understood to represent the shallower sources through fitting different depths to the radially averaged power spectrum plot of the TMI data. A cut-off wavelength shorter than 75 m (e.g. 35 m and below) leads to very shallow source depth and noisier data which are much lower (3x) in magnitude than the AMI data. The resulting magnetic data with the cut-off wavelength of 75 m have very good agreements with magnetic anomalies, in terms of magnitude and the linear trends, observed in the AMI map. The resulting magnetic residuals grid is shown in Figure 3.11. It is clear from this figure that the magnetic residuals, i.e. responses from shallower sources, have very high intensity (>5000 nT) which are similar in range to that of the anomalous magnetic intensity. Thus, from these observations, it is clear that the waste is buried at moderately shallower depths in linear trenches in the area.

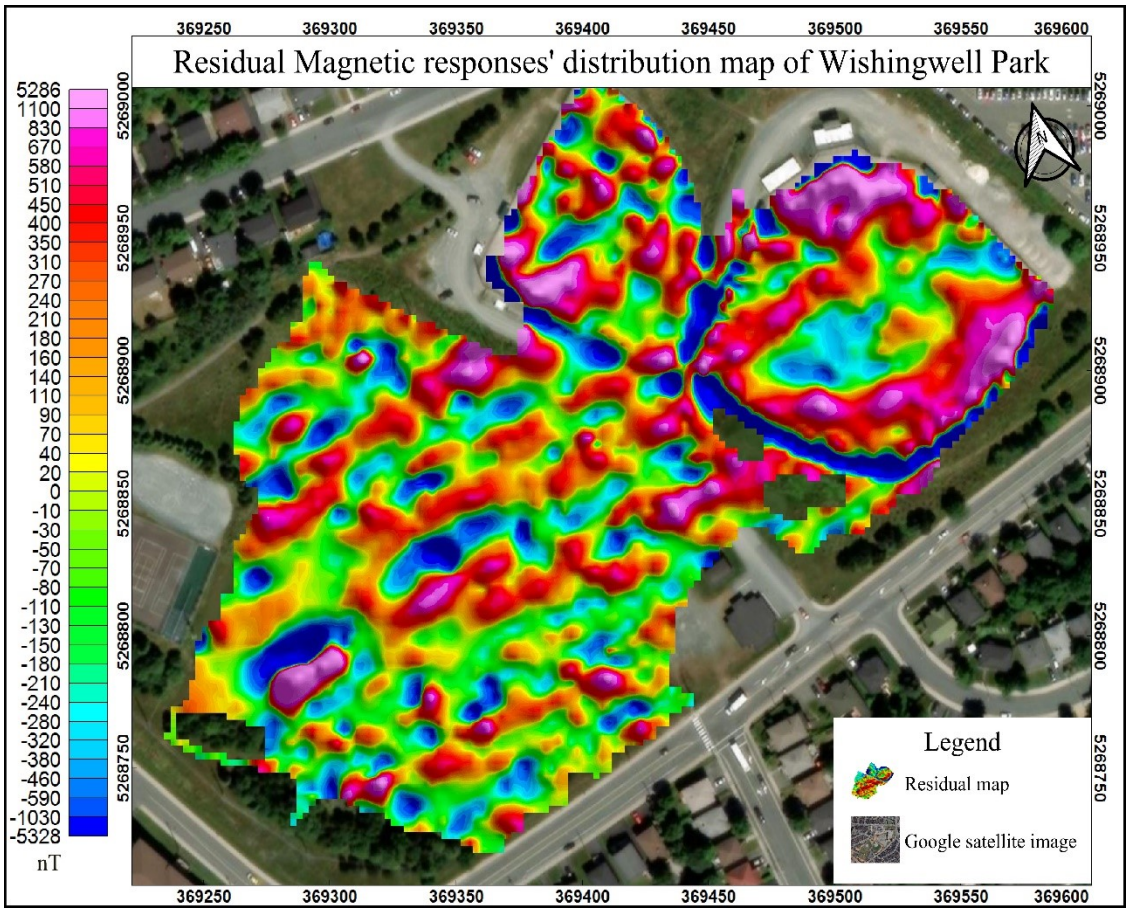

Figure 3.11: Residual magnetic map after the application of a Gaussian high-pass filter, cut-off wavelength of 75 m. (Colour method =histogram equalization, cell extended beyond data = 0 and north arrow= magnetic north.)

Vertical Magnetic Gradient

According to Khalil (2012) and Ibraheem et al. (2021), the vertical gradient measurements are key to understanding shallower anomalies as this data is inherently free of diurnal variations and also suppresses the regional effects. This data is more sensitive to shallow magnetic sources as the gradient falls off more quickly with distance than does the magnetic field. It is obtained by taking the differences between the TMI measurements made by two vertically separated magnetic sensors (with the exact same instrumental settings) and normalized by the constant separation distance between them (0.25 m for this work). Here, the vertical gradient measurements are spatially interpolated

using the minimum curvature technique with the 2.5 m square grid as shown in Figure 3.12.

From this figure, it is evident that the vertical gradient anomalies are distributed across the area. It can be clearly observed that the shallower anomalies are linearly trending over the soccer and the baseball fields whereas they are more of random and rounded in the rugby field. The intensity of the vertical gradient responses ranges from 7906 nT/m to -12159 nT/m which is very high when compared with the typical ranges of vertical gradient responses reported in literature on landfill investigations of a similar nature (Ibraheem et al., 2021; Vollprecht et al., 2019; Dumont et al., 2017). Also, very strong negative troughs can be seen in the vicinity of the metallic anthropogenic features in the baseball fields. Upon comparing Figure 3.8, Figure 3.9, Figure 3.11 and Figure 3.12, clearly the dominant trends of magnetic anomalies remain predominantly linear along WSW-ENE direction in the area as interpreted in Figure 3.10 although the shallow anomalies in the rugby field appear more random and rounded.

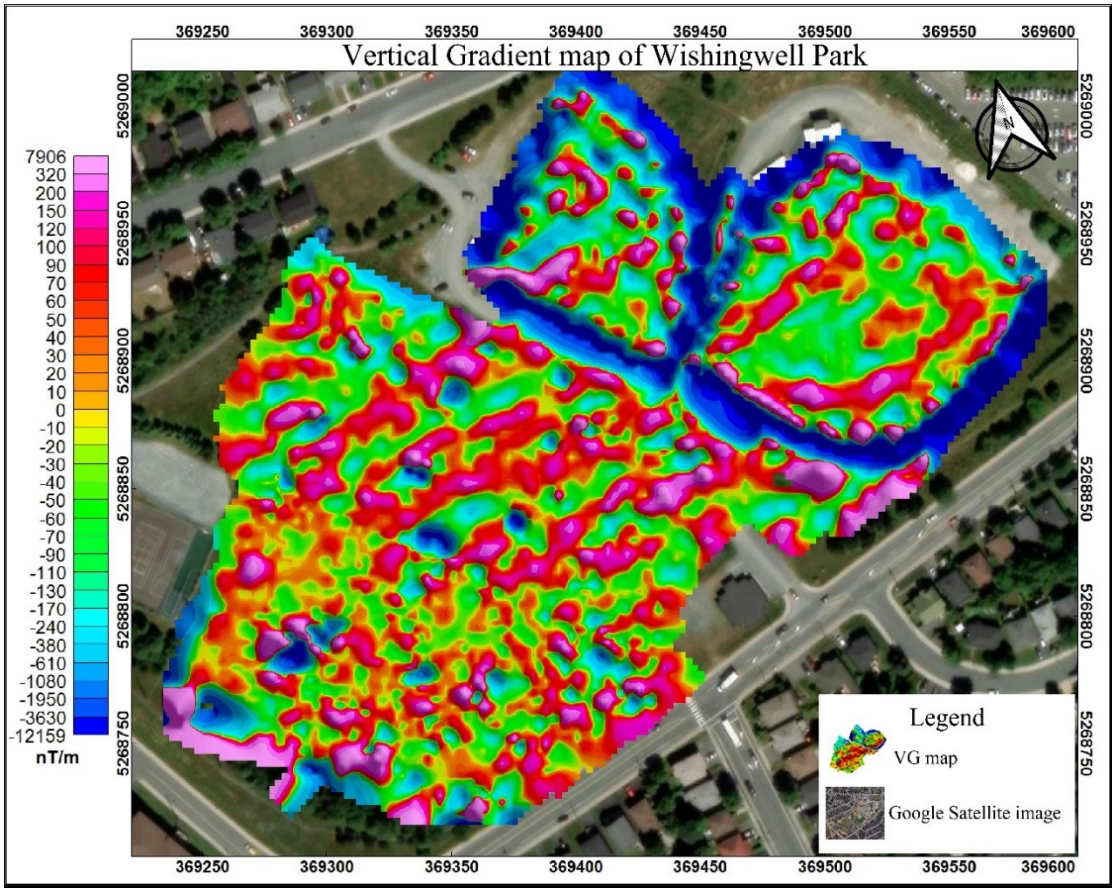

Figure 3.12: Vertical gradient map of the magnetic survey. (Colour method =histogram equalization, cell extended beyond data = 0 and north arrow= magnetic north.)

Analytical Signal

Based on the understanding of the spatial distribution and relative strength of anomalies in the area, an attempt was made to further understand likely source-locations and their distributions in the area. To this end, an analytical signal filter was applied to the data. Analytical signal is the mathematical technique in which total gradients of magnetic data are computed from the first-order spatial derivatives (Dentith and Mudge, 2014). It has the form of a ridge located above a magnetic source, independent of the direction of magnetization (Rajagopalan, 2003; Dentith and Mudge, 2014).

Here, the analytical signal amplitude is computed from the TMI grid using Oasis Montaj.

The gridded result is shown in Figure 3.13. There are numerous magnetic sources which are detected almost all over the area. The magnetic sources are appearing more linear over the soccer and baseball fields while they are more randomly distributed in the rugby field like in the case of the vertical gradient data. A few of the most prominent/strong magnetic sources are marked in the figure as **MA1** through **MA7** in Figure 3.13. Clearly, as expected, the analytical signal around the chain-link fences and the catcher's box fences are observed to be due to the direct influence of these metallic features as discussed earlier.

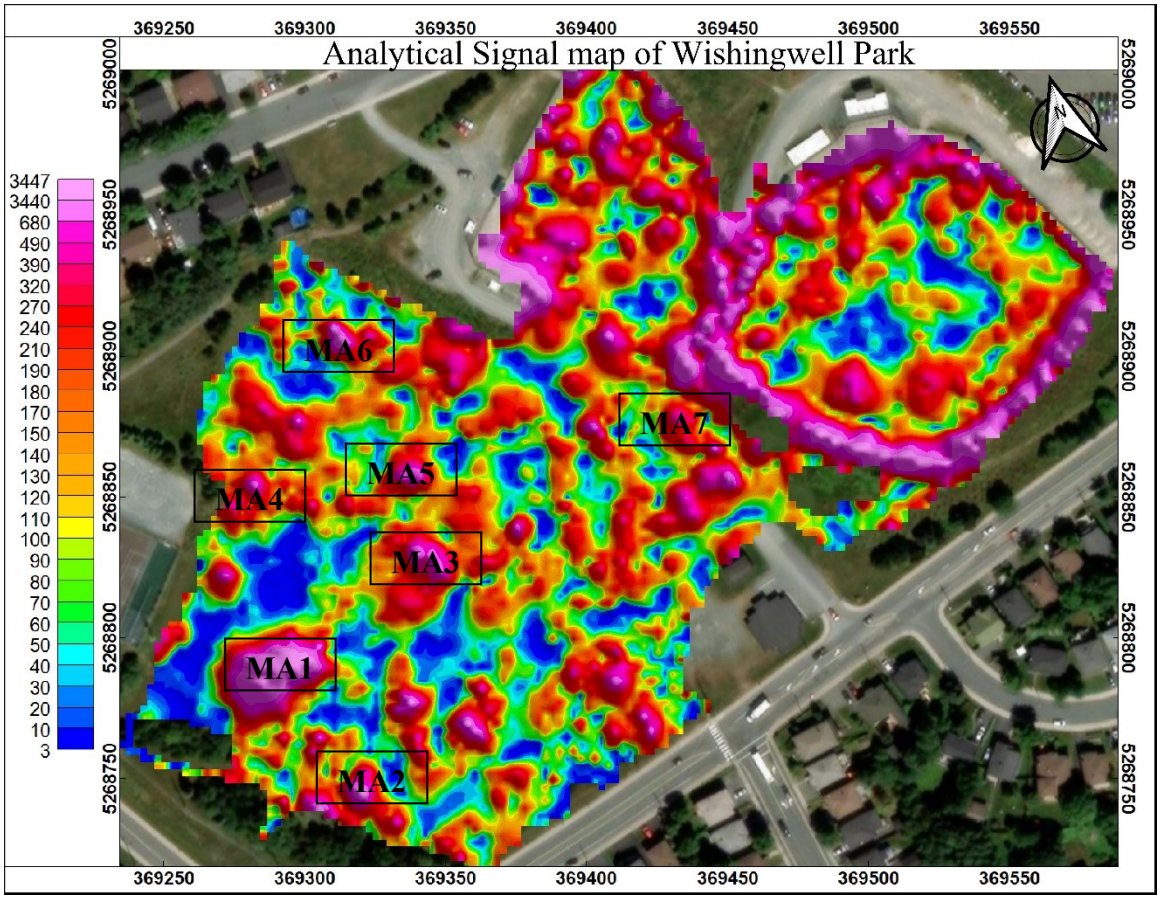

Figure 3.13: Analytical signal map showing magnetic sources' distribution. (Colour method =histogram equalization, cell extended beyond data = 0 and north arrow= magnetic north.)

Euler's 3D Deconvolution (Depth to Source)

Following the previous discussions, one of the ultimate goals here is to understand how

deep these magnetic sources are buried in the area. To this end, a simple depth-to-source estimation can be achieved using a semi-automated depth-to-source estimation inversion technique known as Euler's 3D deconvolution for magnetic data (Zhang et al., 2000; Dentith and Mudge, 2014).

Euler's deconvolution connects the magnetic field and its gradient components to their respective locations and depths to the sources. The degree of homogeneity, known as the structural index (N), is an important parameter here and must be defined carefully based on the assumed nature of the magnetic sources to account for the decrease in amplitude of the magnetic field with respect to the distance from the sources. In this work, the structural index of N=3, corresponding to spherical source, and N=2, corresponding to horizontal pipe/cylinder, were computed and compared. N =3 was chosen for this work as the results have similar range of depth estimates (Khalil and Hassan, 2016; Dentith and Mudge, 2014). Euler's solutions were obtained using the TMI data, with the 2.5 m grid, and the resulting depth-to-source estimates are accordingly superimposed on a TMI map which is downward continued to 2 m (to ground surface), approximately the height of the sensor above the ground, as shown in Figure 3.14. The downward continuation is the filtering technique in which the measured magnetic responses at a given height is used to compute responses at lower heights closer to the magnetic sources. Here, the downward-continued responses represent the magnetic responses which will be measured on the actual ground surface in the area.

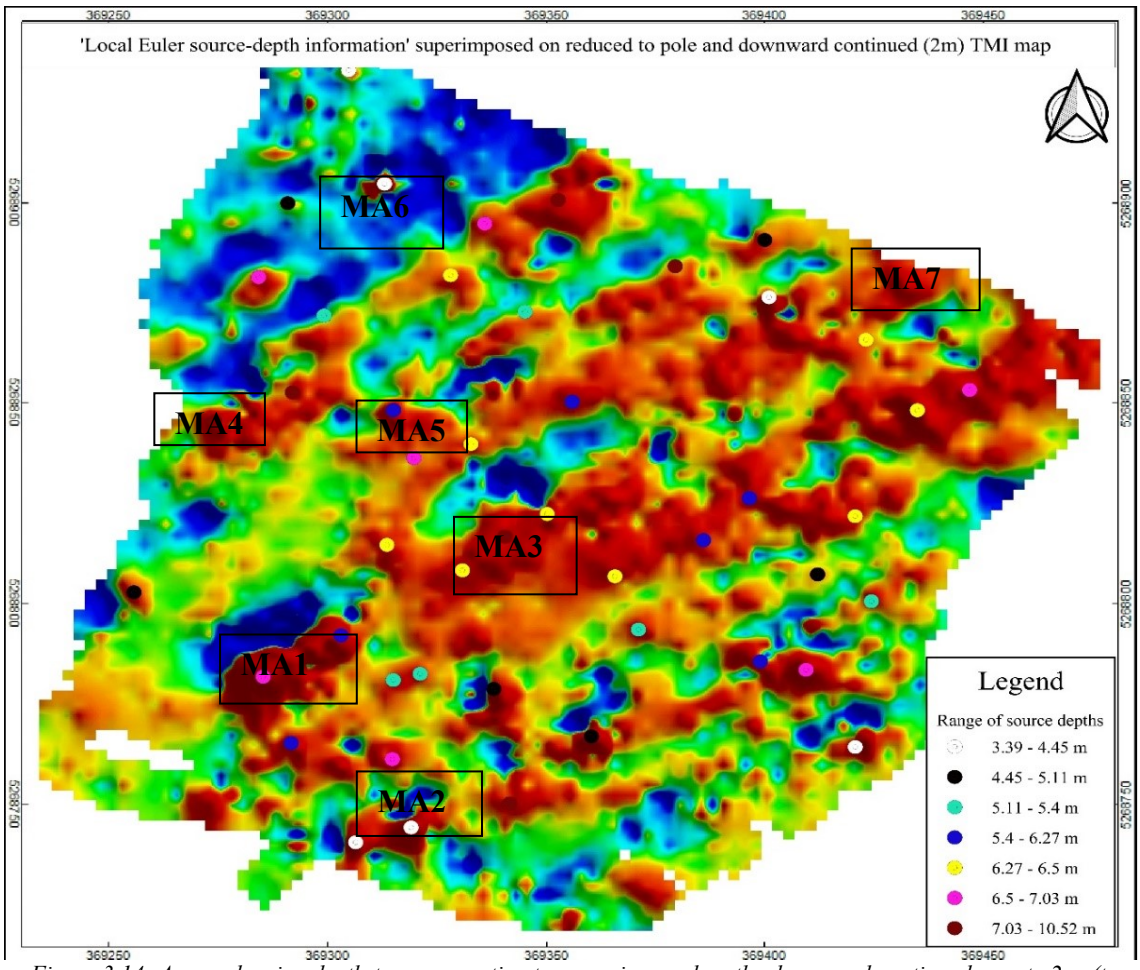

Figure 3.14: A map showing depth-to-source estimates superimposed on the downward continued map to 2 m (to ground surface).

From Figure 3.14, the depth estimates of magnetically susceptible waste range from 3.5 m to 10.5 m, with an average depth of burial being about 6 m. The depth information helps to infer the depths of artificial trenches in the area hosting the waste.

*Magnetic Anomaly 1 (**MA1**)*

Amongst numerous magnetic anomalies observed in the area, the strongest and the most extreme anomaly is the one labelled '**MA1**' in Figure 3.15. It is further examined for its characteristic TMI and RTP profiles to help understand whether or not its magnetic response is influenced by remnant magnetizations (Dentith and Mudge, 2014) which is

common in landfills of such nature owing to the presence of significant amount of magnetic waste (Vollprecht et al., 2019). The TMI and RTP profiles are examined using 4 parallel lines, using the TMI and the RTP grids, with the line spacing of about 6.5 m running over the anomaly as shown in Figure 3.16.

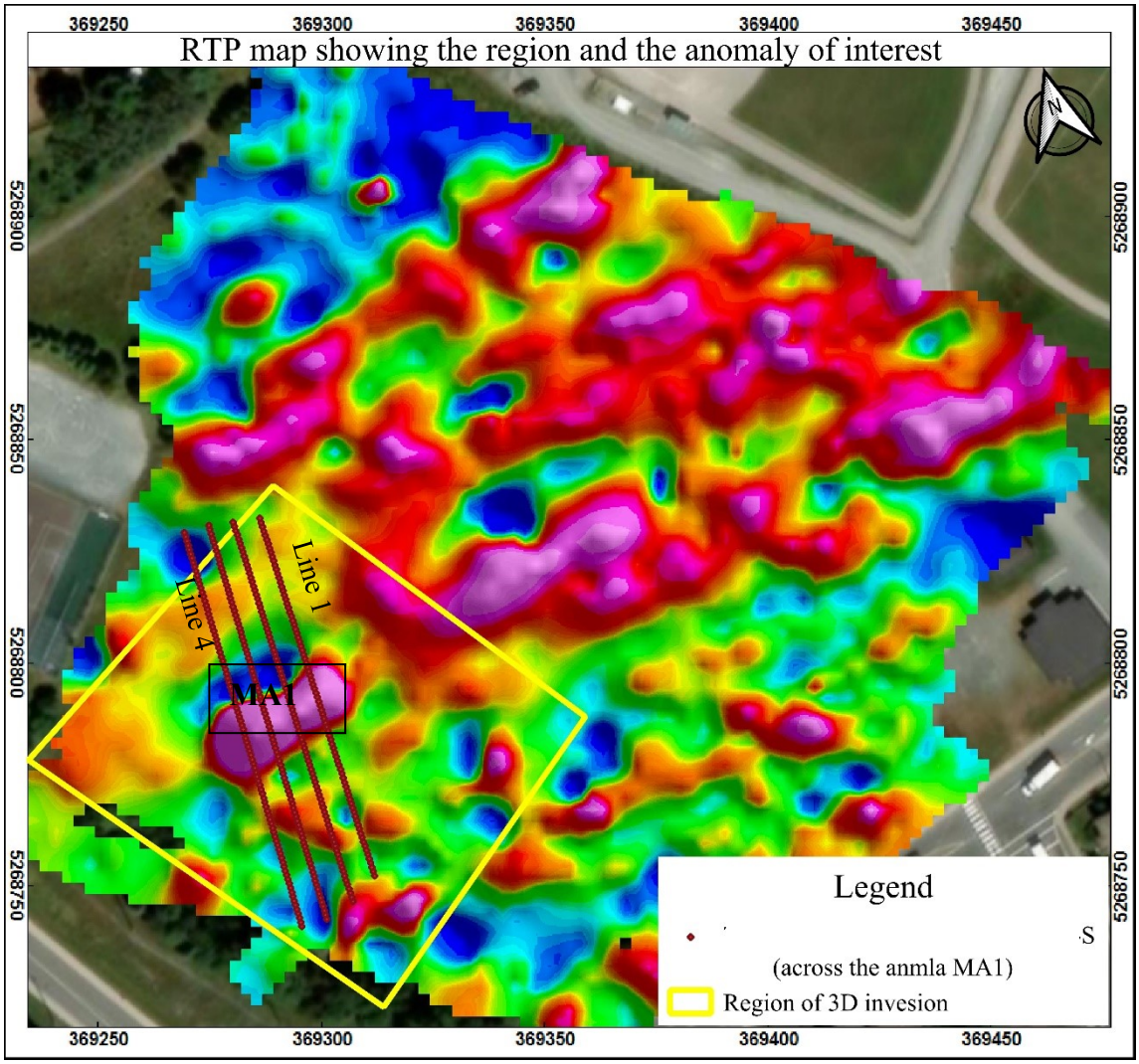

*Figure 3.15: Map showing the region of interest enclosing the anomaly, **MA1**, used for profiling and 3D magnetic inversion.*

From the discussion in Section 3.1, it is clear that in the northern hemisphere, the characteristic shape of the TMI profiles should have lows towards the north and highs in the south under no effect of remnance phenomenon (Dentith and Mudge, 2014). Figure 3.16 clearly depicts the dipolar TMI profiles with TMI-highs and TMI-lows towards the

south and north, respectively, which are the characteristic shape as a consequence of only the induced fields or the remnant magnetizations parallel with the Earth's field, if any, observed in the area. Hence, the magnetic responses in the area are consistent with being dominantly induced or parallel to the Earth's field.

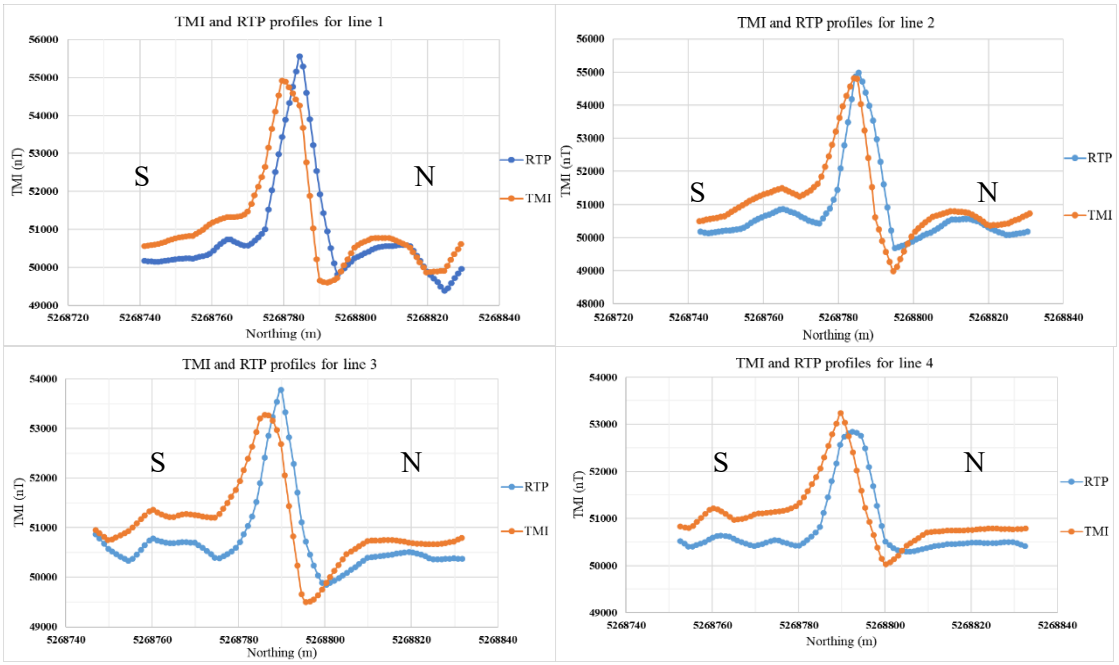

*Figure 3.16: The TMI and RTP profiles from east (Line 1) to west (Line 4) over the anomaly, **MA1**, in north-south direction.*

3D Susceptibility Modelling

According to Dentith and Mudge (2014), magnetic modelling, 2D or 3D, is the best approach to understand magnetic anomalies' shapes, susceptibility variations and anomaly depth. Magnetic modelling is the computational process of recovering subsurface distribution of magnetic property of interest which could best explain the measured field data (Blakely, 1996; Dentith and Mudge, 2014). Vollprecht et al. (2019) attempted to correlate the laboratory measured magnetic susceptibility values to that of the modelled values for a few landfill cases and concluded that the recovered magnetic susceptibility models exhibited very large deviations from that of the laboratory results. However, it is observed that the regions with high recovered magnetic susceptibilities

correspond well to the areas with higher iron contents which was corroborated using borehole information. For this work, the physical property of interest is the magnetic susceptibility and its 3D distribution in the study area. Here, a mesh-based inversion scheme, called *Vidi*, from Geotexera Inc., was used for 3D magnetic susceptibility inversion (Geotexera Inc., 2022; Darijani, 2019; Lelièvre et al., 2012). The program (software) uses tetrahedral unstructured meshes, and susceptibility inversion method was chosen for the 3D magnetic susceptibility inversion using available magnetic data. This method is the minimum structure inversion technique (Lelièvre et al., 2012) and the final model is achieved through the iterative minimization of the objective function using the Gauss-Newton method.

The TMI data within the yellow-rectangular bound around the magnetic anomaly, **MA1**, shown in Figure 3.15, is converted to magnetic residual data (shown in Appendix A) and are modelled using inversion parameters such as tetrahedral meshes of volume 5 m^3, geomagnetic inclination of ≈ 66.6°, declination angle of ≈ -16.7°, model type as susceptibility model and maximum iterations of 100 with a normalized target misfit of 1 as the convergence criterion (Darijani, 2019; Lelièvre, 2023). The final susceptibility model was constructed upon achieving the normalized data misfit value of 1.01 at the 19^{th} iteration and is shown in Figure 3.17 (difference of input vs. inverted map is given in Appendix A). The magnetic source of anomaly **MA1** is depicted as a localized area of high magnetic susceptibility.

The range of bulk susceptibility values in the model for the anomaly **MA1** ranges from 0.1 to 0.6 SI which is slightly higher than the ranges of volume susceptibility of buried steel drums or storage tanks reported in Barrows and Rocchio (1999). Further, the 2D sections, one each along x and y axes, are obtained from the 3D model as shown in Figure 3.18 and Figure 3.19 respectively. From these two 2D-sections, it is clear that the top of the anomaly is located roughly at the depth of about 4-5 m with the main susceptible bodies lying within 6-12 m underneath the existing ground surface. This

recovered depth compared very well with the depth-to-source estimates over the anomaly, **MA1**, obtained using Euler's 3D deconvolution algorithm (see Figure 3.14).

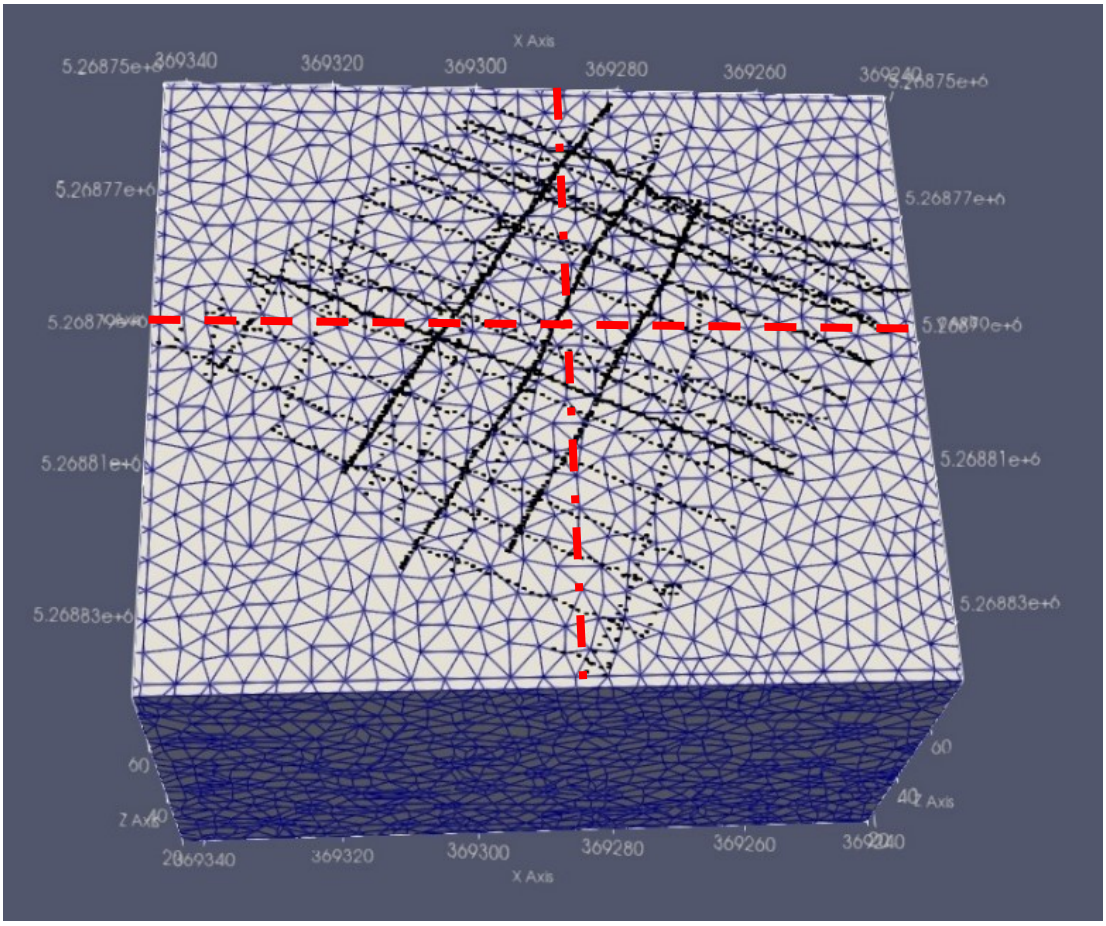

*Figure 3.17: Recovered 3D susceptibility model for anomaly **MA1** (Black dots= survey points and red dashed lines=axis of 2D sections.)*

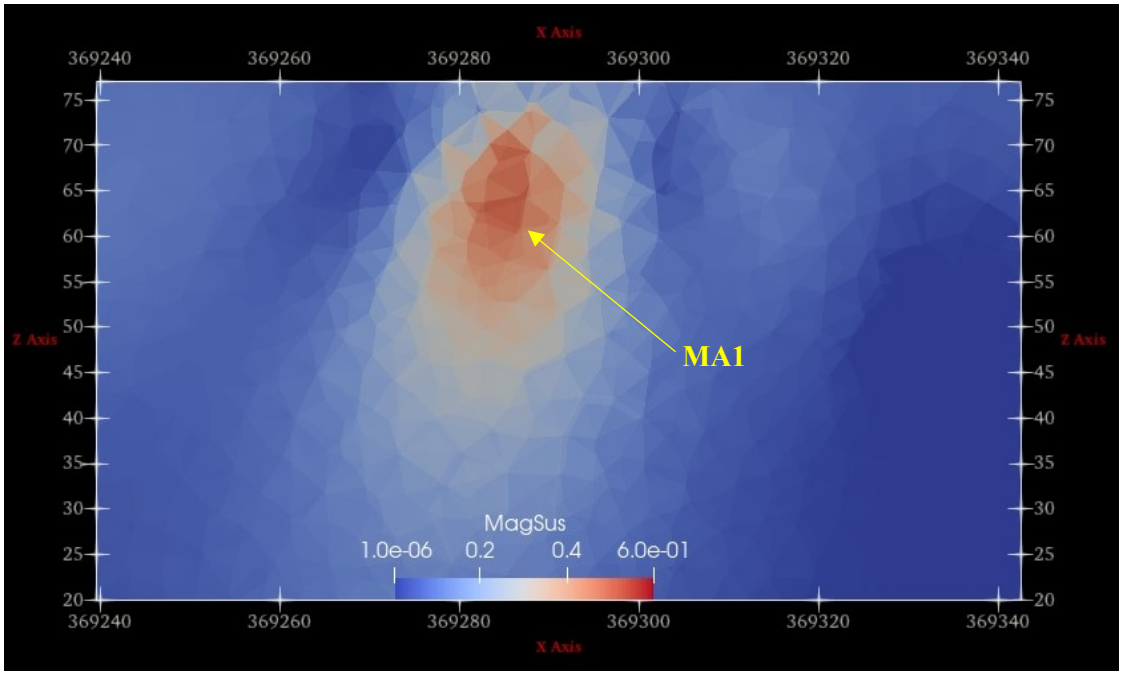

*Figure 3.18: 2D section of the anomaly, **MA1**, cut through middle of the anomaly along x-axis.*

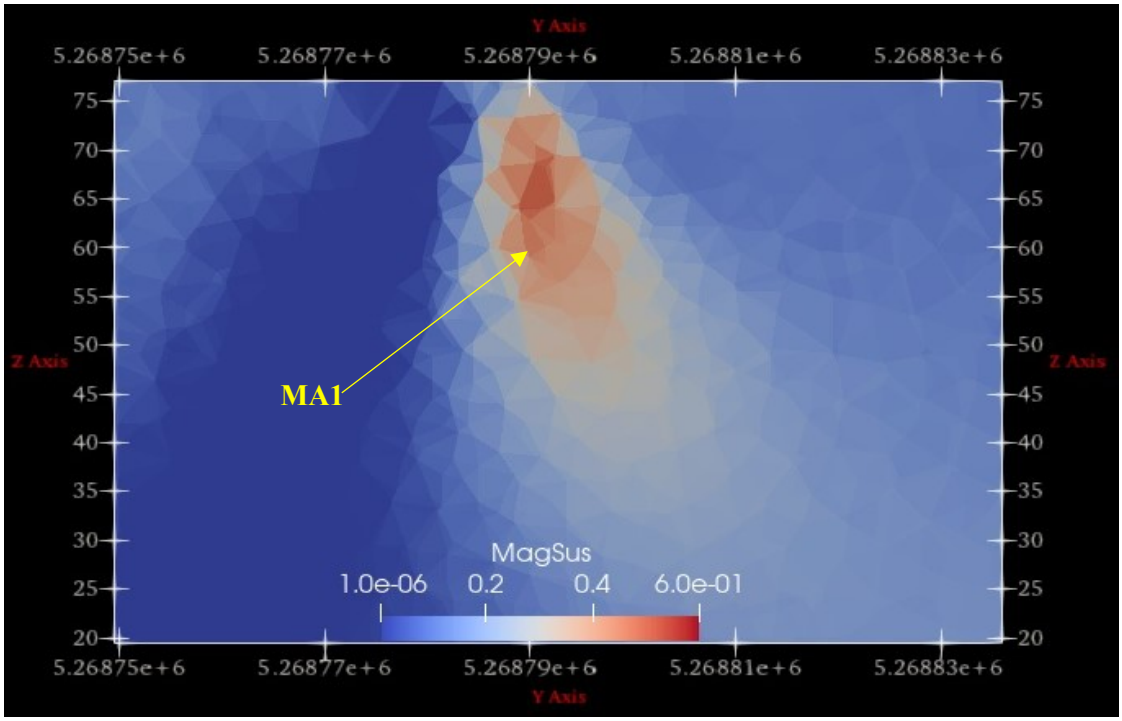

*Figure 3.19: 2D section of the anomaly, **MA1**, cut through middle of the anomaly along y-axis.*

Therefore, it can be evidently concluded that the magnetic anomalies depicted in Figure 3.9, Figure 3.10, Figure 3.13, Figure 3.18 and Figure 3.19 would be either large-sized

discarded tankers, vehicular wreckages (evidenced from the archived images) or huge lumps of remnant metallic scraps buried in anthropogenic trenches existing at the depths of about 4 to12 m in the area.

Chapter 4: DC Resistivity and Induced Polarization Surveys

4.1 Basic Principles

The direct current (DC) resistivity method, also known as the geoelectrical method, is one of the active methods in geophysics. The technique works on the basis of a physical property of a subsurface medium known as resistivity or its inverse, conductivity. It is the contrast in the physical quantity that this method is sensitive to (Dentith and Mudge, 2014). The general objective of electrical surveys is to estimate and understand the true resistivity distribution in the subsurface (Loke, 2015). In the DC resistivity technique, the time-stepped direct current is injected directly into a surface medium using a pair of current electrodes and then the potential differences (voltages) recorded using a pair of potential electrodes, at discrete points within a field of interest (Hohmann, 1988; Loke, 2015). In this method, the measured voltages using an individual or combined arrays, along with the impressed current and geometry of quadrupole, are subsequently converted into a quantity known as an 'apparent resistivity'. These resistivity data are values for an assumed half-space which can have a very complex relation to a true resistivity/conductivity distribution of the subsurface (Haber et al., 2000; Loke, 2015).

Ever since Schlumberger popularized it in 1912, the DC resistivity method typically involves the use of four metallic electrodes, a pair each of potential and current electrodes, arranged in a specific manner known as an array or configuration, for the acquisition of field measurements (Meyer DecStadelhofen, 1991; Samouëlian et al., 2005). A typical layout of a direct current resistivity survey is shown schematically in Figure 4.1. The electrodes A and B are called current electrodes as these transmit electric current into the ground while the electrodes M and N are called potential electrodes as the potential difference is measured from these. Figure 4.1 depicts the commonly used Wenner array or Schlumberger array. The Wenner array uses equal electrode spacing and has very good lateral resolution whereas the Schlumberger array deploys different

spacing between the current electrodes and usually smaller and fixed spacing between the potential electrodes and has good depth resolution/sensitivity (Loke, 2024). Any geoelectrical field operations involve adopting varieties of arrays and electrode spacing dictated specifically by the ultimate objectives of a geophysical study, the time available, budget, and available priori information (Binley & Kemna, 2005).

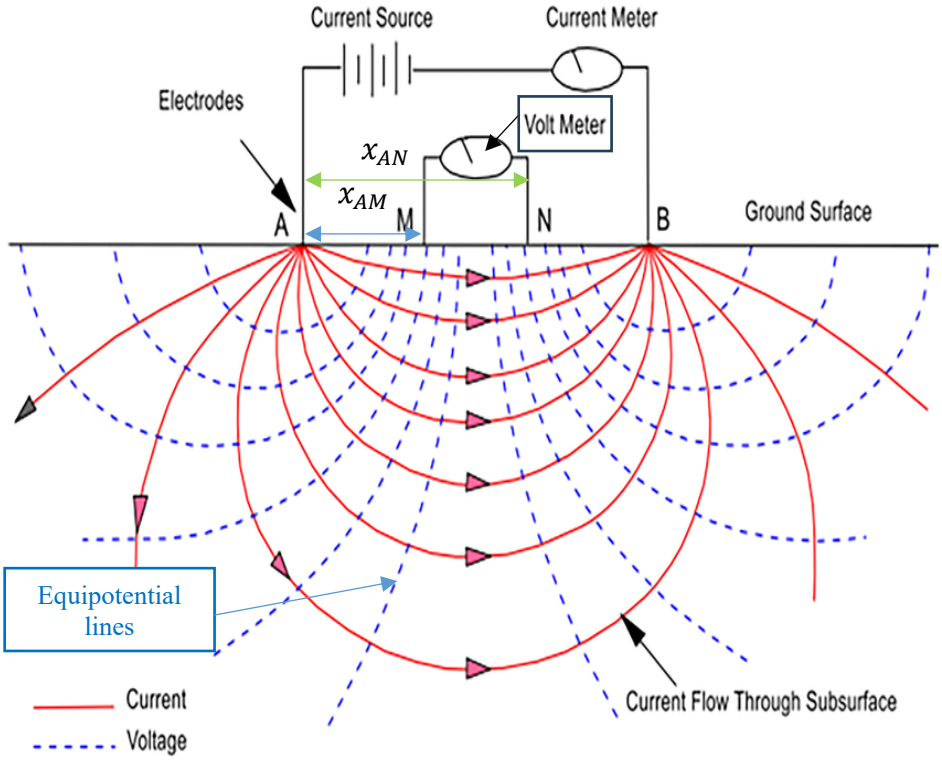

Figure 4.1: Typical working of direct current resistivity survey in homogeneous half-space.

(After Robinson & Coruh, 1988.)

Simultaneous applications of a few different arrays have been used to mitigate the weaknesses of a particular array by combining with another array which does not have that weakness in geoelectrical surveys (e.g. Hesse et al., 1986). Significant advancements have been achieved in measurement acquisition speed through the application of automatic switching systems using multi-electrode arrangements. Thereby making field data acquisition automatic, fast and economical with capability of combining several arrays in a single operation.

Another very important and intimately connected method to a geoelectrical survey is the induced polarization (IP) method (Siegel, 1959; Oldenburg and Li, 1994). According to Dentith and Mudge (2014), the IP effect is microscopically attributed to the capacitance-like nature of a medium, a capability to be polarized, when current is passed through the medium. It is primarily due to two microscopic phenomena, namely, membrane polarization and grain polarization (Dentith and Mudge, 2014). The membrane polarization is the electrical phenomenon in which charged surfaces, forming the walls, of flow paths, preferentially attract opposite charges and repel like charges. This forms a membrane of ions which impedes current flow thus leading to local concentration of charges on one side and a deficiency on the other side of the barrier. Grain polarization is a result of current flowing in a fluid due to the movement of ions, under the influence of an applied potential, that cannot continue to move at an interface with a material that conducts by a different mechanism such as conductive grains like sulphide, and this results in a charge buildup or capacitive effect (Dentith and Mudge, 2014). In practice, capacitance is measured using a time-varying current, either constant current switched on and off or alternating current (a.c.), in three different ways as discussed by Dentith and Mudge (2014). At the macroscopic level, the IP effect is most commonly measured as an apparent chargeability (m_a) by measuring the decay of the potential associated with the charge buildup, as hindered by the electrical resistance, after switching off a d.c. current (Siegel, 1959; Khesin et al 1997; Telford et al., 1990; Binley and Kemna, 2005; Dentith and Mudge, 2014; Loke, 2015).

The overall sequence of IP measurements, in the time-domain, is depicted in Figure 4.2. In Figure 4.2, it is clear that the current (I) is switched on and off for a certain duration and the time varying secondary voltage (V_s) is being measured during the switch-off state. The polarity of the input current switches consecutively and hence the voltage responses do as well. This switching is to overcome self-potentials and the potentials associated with telluric currents, which vary over slower scales.

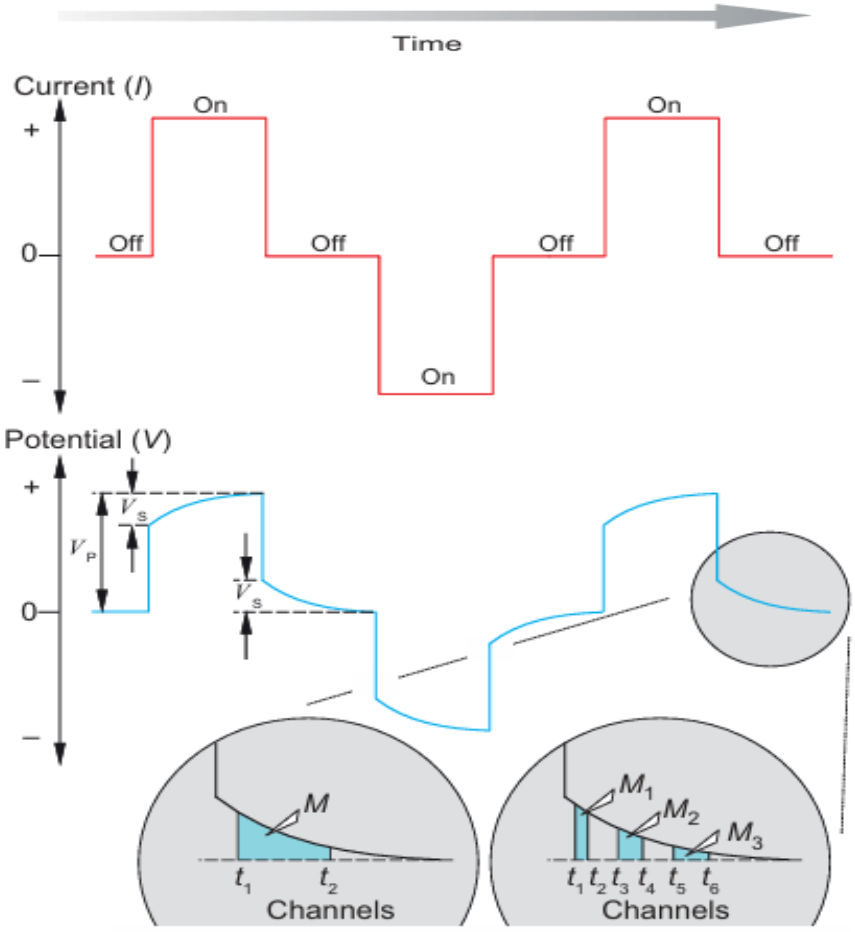

Figure 4.2: Image showing input current waveform (bipolar) and the distorted responses measured by the receiver.

(After Dentith & Mudge, 2014.)

In the IP method, the secondary voltage (the voltage associated to polarization effects) is smaller than the primary voltage (V_p), the voltage associated with the impressed current (I) into the Earth, rendering its measurements difficult to achieve. Thus, most IP measurement instrumentation adopts an integral, cumulative measure of the responses over the decay curve within a specific decay period (t).

The two aforementioned geoelectrical arrays are adopted for the IP surveys. However, it was suggested that the preferred array for the IP survey is dipole-dipole array as it is advantageous to achieve the measurements with the least electromagnetic coupling

between potential and current electrodes which is the ideal situation for an IP survey (Sumner, 1976; Loke, 2024). The dipole-dipole array is the electrode configuration in which the two poles (A-B and M-N) have a spacing between them which varies as a multiple (n) of the spacing of the two current and potential electrodes (that are the same). The n spacing is varied during the course of survey (the image of the array is shown in Appendix B).

4.2 Field Survey Methods

There are several advanced geoelectrical data acquisition systems available. In this work, a Syscal Junior system from IRIS instruments was used to collect both DC resistivity and IP data. Images of various components of the instrument used are shown in Appendix B. It is an all-in-one resistivity and IP imaging system powered using a 12V external battery. Two sets of multi-electrode cables, each with twelve take-out points, were used thereby accommodating 24 steel electrodes, which are arranged at equal spacings in a straight-line profile called a 'spread', controlled by the single control unit. This system can be programmed for numerous different arrays and different electrode spacings. For this work, a total of six resistivity and six IP profiles were laid out to transect the linear magnetic features in the area as shown in Figure 4.3. The locations of the electrodes were measured using differential GPS (DGPS, RTK). As is clear from Figure 4.3, the DCR_profile 6 is oriented slightly differently from the rest in order to cut directly across the prominent magnetic anomaly, **MA1**, to allow for specific comparison with the magnetic data over this small area.

A mixed array type known as Wenner-Schlumberger was one of the arrays chosen for this work and measured both DC resistivity and IP data. Here the roll-along technique, with a single step, was deployed for all the profiles. The roll-along was done to cover longer profile lengths when cable lengths and electrode numbers (24, here) are limited by carefully translating a single electrodes-cable arrangement along a profile with certain percentage of overlap with the previous spread (Dahlin and Bernstone, 1997). The motive behind using the mixed array is to fully exploit the individual advantages of both the arrays, thus mitigating their individual weaknesses. Hence, it can be used to achieve better overall resolution, both the lateral and vertical, of the geoelectrical image (Sumner, 1976).

The first four resistivity and IP profiles have a length of 175 m and were acquired in

June, 2023. These four survey lines covered overall measurements with the three different M-N spacings (b) of 5 m, 10 m, and 15 m, the increase in the M-N spacings increases voltage and decreases the geometric factor thus improving the signal to noise thus enabling for deeper measurements. The array has midpoint spacings (x= (A+B)/2) ranging from 7.5 m to 87.5 m for all these profiles. The last two profiles were acquired in September, 2023, with the profile lengths of 105 m each. The survey covered measurements with the three different M-N spacings (b) of 3 m, 6 m, and 9 m. The array has midpoint spacings (x= (A+B)/2) ranging from 4.5 m to 52.5 m. All these survey parameters were designed using the ElectreII program (www.iris-instruments.com) and uploaded to the control unit using the ProsysII program (www.iris-instruments.com) thus facilitating automatic data collection (a typical ElectreII program output is shown in Appendix B).

Through the one-step roll-along operation a spread overlap of about 48% of the previous spread for all the profiles was achieved. In this work, a total of 356 unique data points were acquired for each profile, with each measurement involving 3 readings, with data repetitions of about 10% for all the profiles for both the resistivity and IP data. The data reciprocity is the best choice for evaluating measurements' errors in the field, yet to measure such data is an uneconomical and time-consuming operation (LaBrecque et al., 1996). Hence, the repetitions in the measured data (double for some,10% overall) from the roll-along technique helped understand the overall quality of the measured data.

Additionally, the dipole-dipole array was also employed for the three longer profiles (DCR_profile 1 to DCR_profile 3) to collect both resistivity and IP data with the same array parameters. As a field control and monitoring strategy, the resistances between neighbouring electrodes during the survey were maintained well below 5 kΩ and cables were laid out such that loops were avoided to limit the influence of electromagnetic coupling phenomenon (Bernstone and Dahlin, 1997; Dentith and Mudge, 2014).

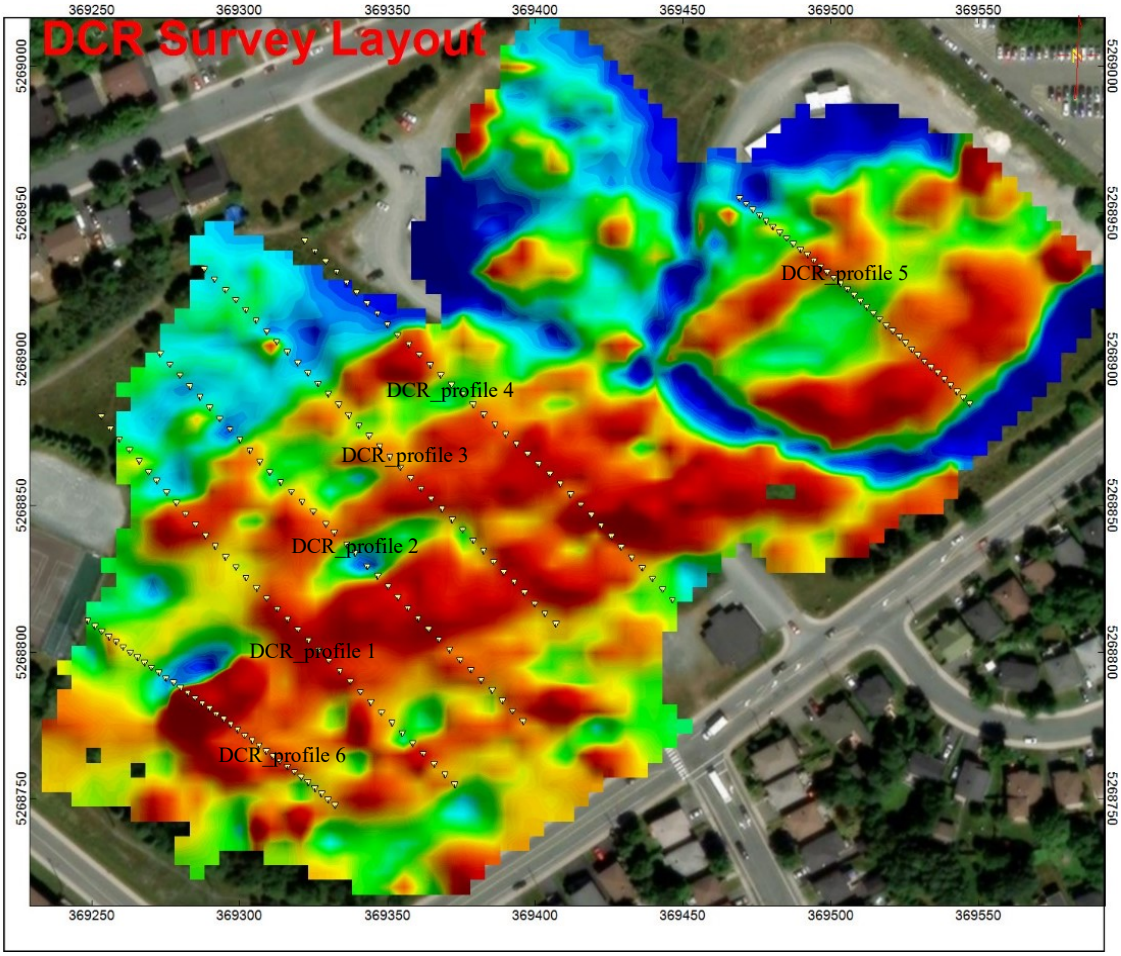

Figure 4.3: DCR survey layout and coverage superimposed on the TMI map (see Figure 3.5 for colour bar).

4.3 Data Analyses and Interpretations of DC Resistivity Survey

Following the field work, firstly, the apparent resistivity and IP data were inspected for quality control. For both the data-sets, for all six profiles, a total of 36 repeated data points were carefully sorted and compared. It was observed that an average deviation in the resistivity data is about ± 2% and in the IP data is about ± 5% for all the repeated data points. Given the minimal deviations amongst the repeated data, it is considered that the data are of good quality and hence the repeated data were averaged, thus resulting into 356 unique measurement points for each of the six profiles. Moreover, those (3-5) data points with standard deviation values, for repetitive readings at each data point taken by the Syscal system, greater than 10% and 3% for the resistivity and the IP data, respectively, were removed as they are considered to be unreliable.

The resultant apparent resistivity data were plotted for different values of ‘a’ (a=AB/2) for three different values of ‘b’ (b=MN) in the style suggested by Loke (2024). These plots were the first-pass technique to roughly comprehend the resistivity variations in the subsurface. The resulting apparent resistivity profiles for DCR_profile 1 are shown in Figure 4.4, Figure 4.5 and Figure 4.6 (zero electrode position for all the DCR profiles is at the WNW end and the other end positions in ESE).

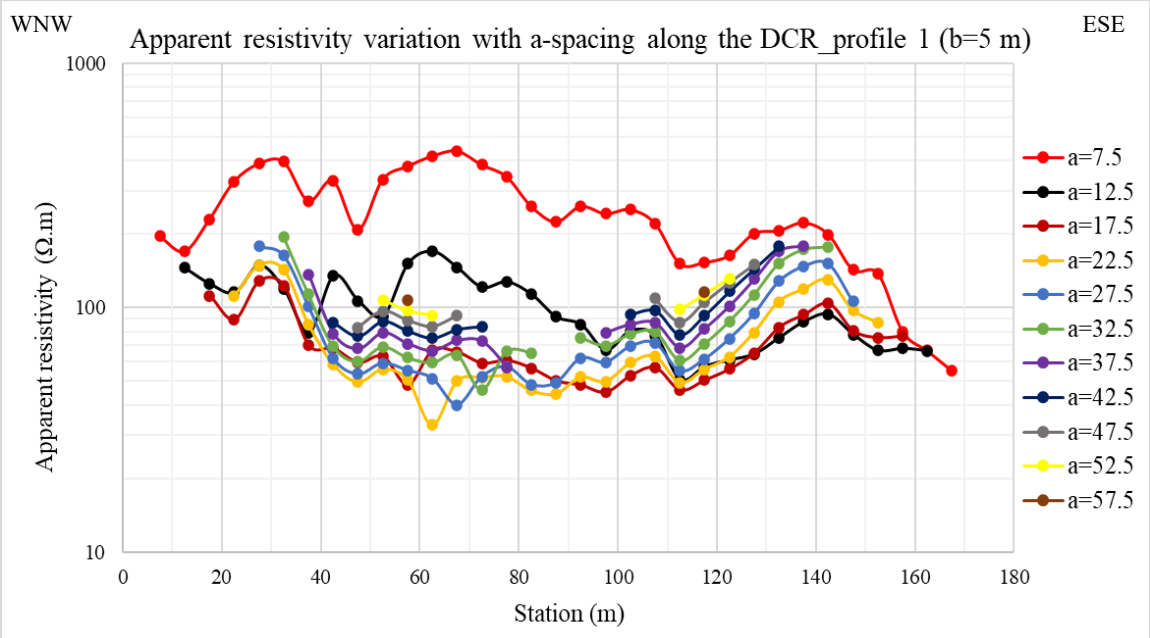

Figure 4.4: Apparent resistivity profile for DCR_profile 1 (for b=5 m).

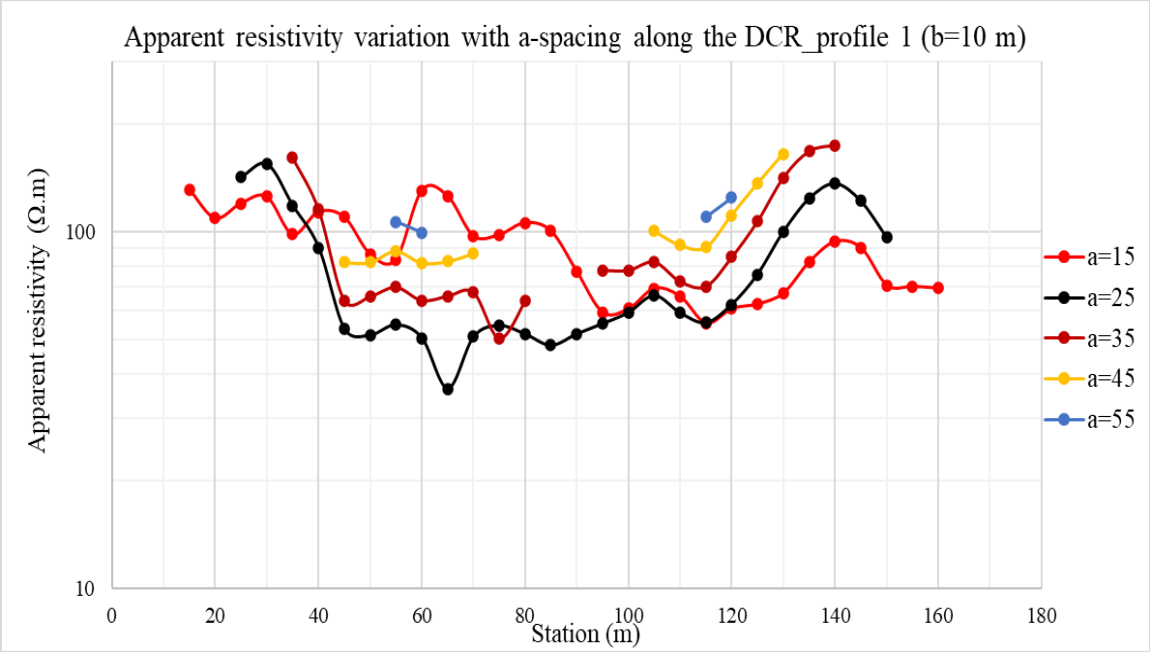

Figure 4.5: Apparent resistivity profile for DCR_profile 1 (for b=10 m).

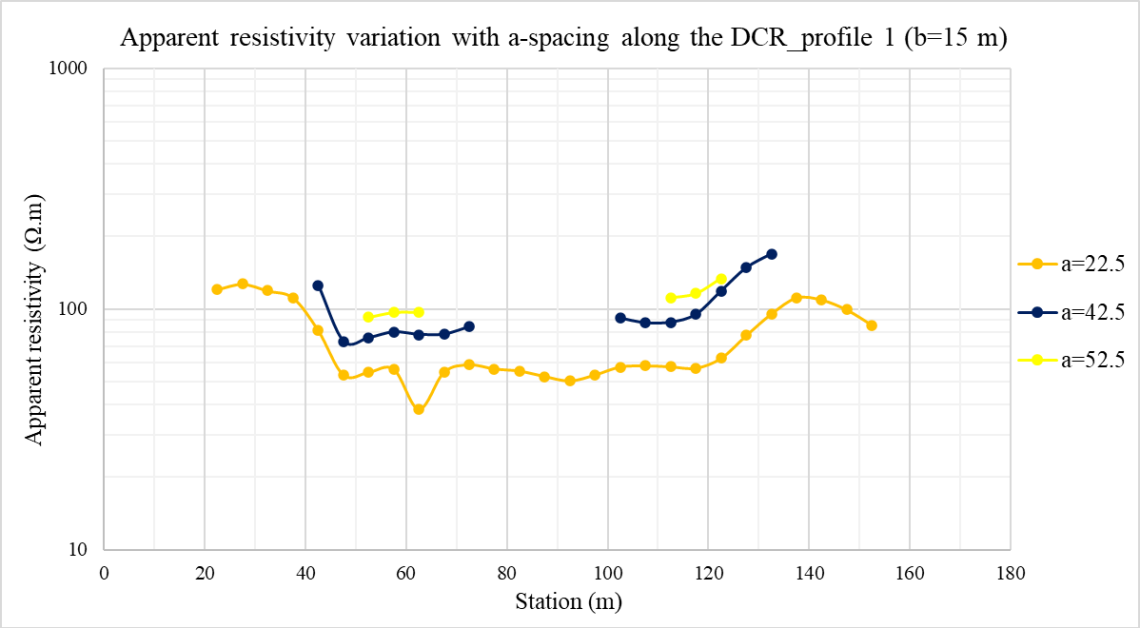

Figure 4.6: Apparent resistivity profile for DCR_profile 1 (for b=15 m).

From these three aforementioned profiles, two observations can be made. Firstly, the pattern of the resistivity distribution is such that the most resistive regions are the topmost layers (a=7.5 to 12.5 m or a=4.5 to 7.5 m) with the moderately resistive bottom layers (a=47.5 to 57.5 m or a=28.5 to 34.5 m) shown more clearly on the less cluttered graphs with larger 'b' values. Secondly, the intermediate layers (a=12.5 to 47.5 m or a=7.5 to 28.5 m) are comparatively less resistive than the top and bottom layers with the apparent resistivity values ranging between 150-40 Ωm. Thus, the common resistivity distribution patterns consist of conductive regions sandwiched between top and bottom more resistive layers.

Similar trends are observed for DCR_profile 2, DCR_profile 3, DCR_profile 4 and DCR_profile 6 (the graphs of which are given in Appendix B). However, for DCR_profile 5 acquired over the baseball field, the resistivity distribution pattern is different. Here, the relatively resistive top layers more gradually transition into deeper layers that are more conductive as shown in Figure 4.7, Figure 4.8 and Figure 4.9. A slight increase in the apparent resistivity is seen only for the deepest penetration depths.

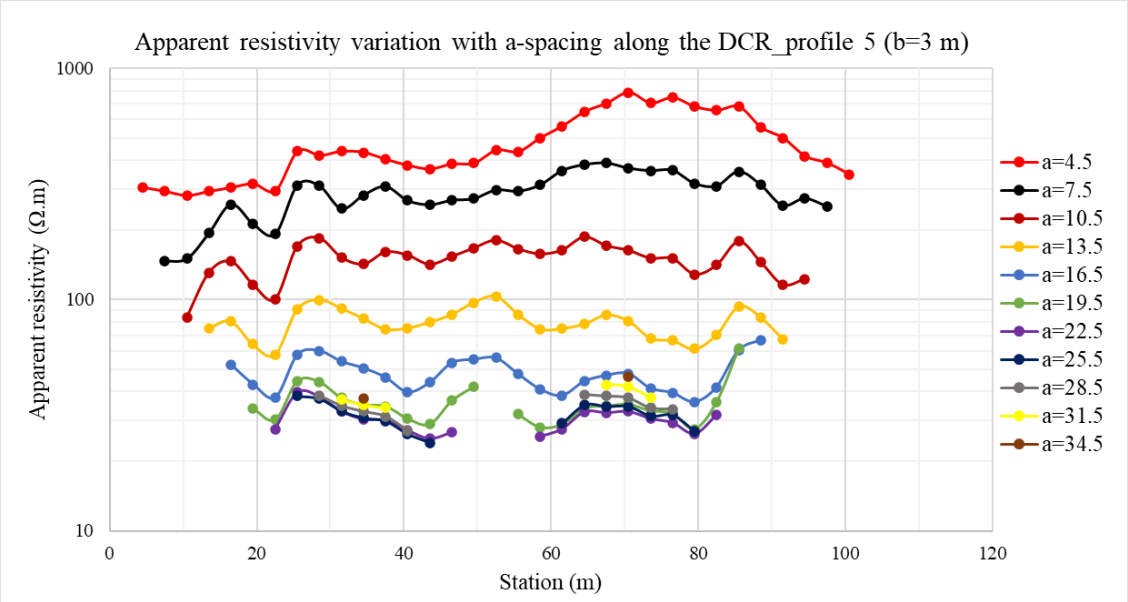

Figure 4.7: Apparent resistivity profile for DCR_profile 5 (for b=3 m).

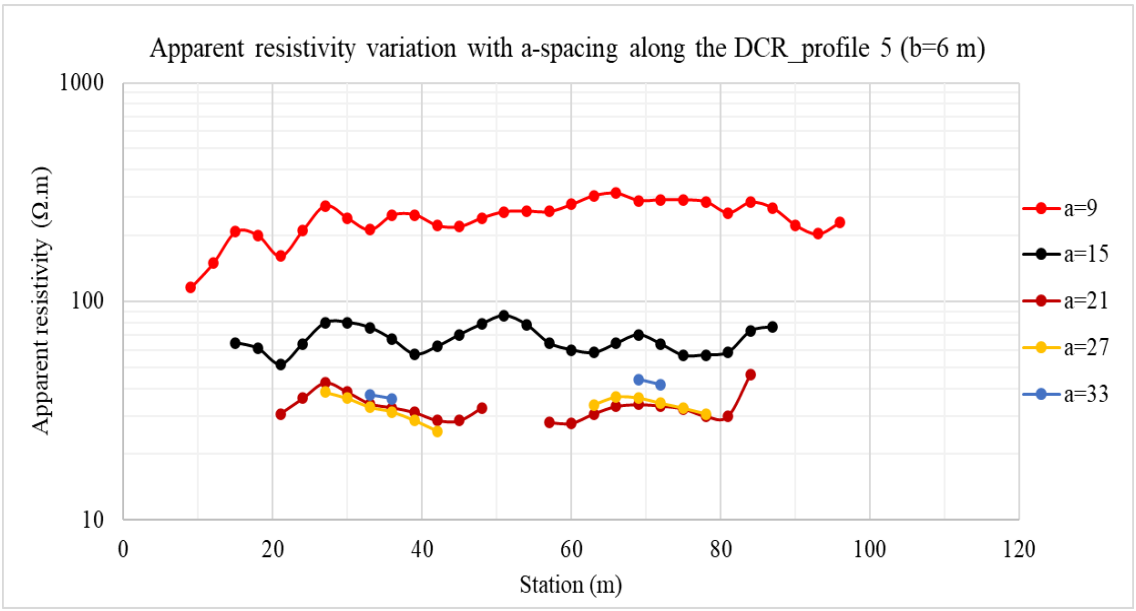

Figure 4.8: Apparent resistivity profile for DCR_profile 5 (for b=6 m).

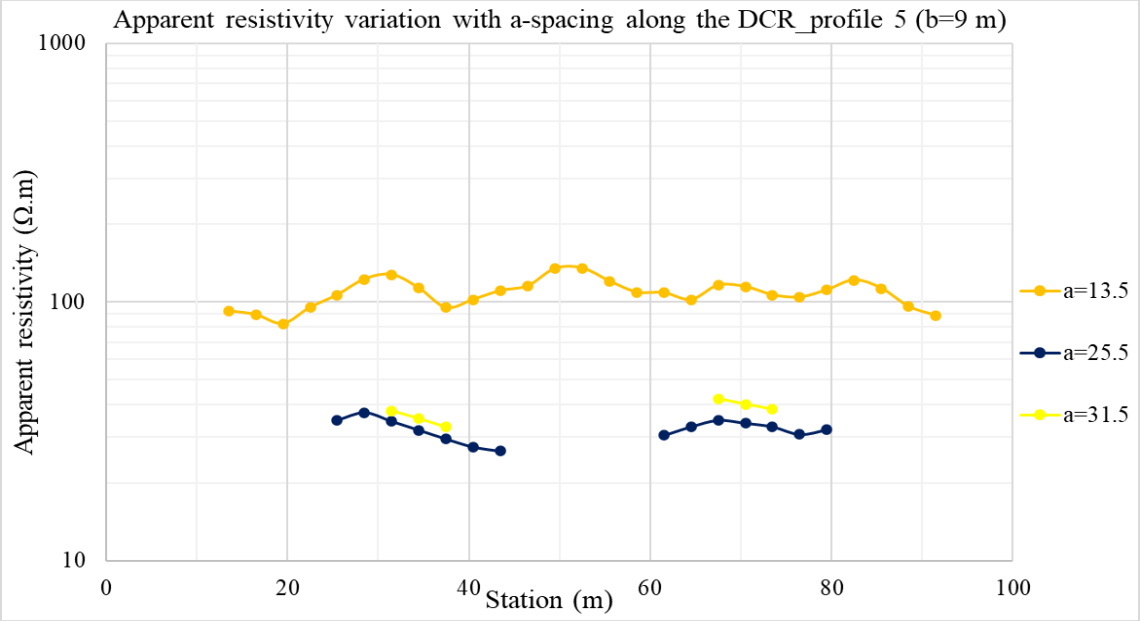

Figure 4.9: Apparent resistivity profile for DCR_profile 5 (for b=9 m).

Blanchy et al. (2020) stated that the DC resistivity and IP measurments are straightfoward processes, however, the data cannot be directly used for reliable physical interpretations. Therefore, prior to making any reliable physical interpretations, any measured resistivity and IP data must be robustly inverted thereby recovering a reliable model of the resistivity variation in the subsurface which could explain input apparent resisvitiy data within certain error limits.Various different schemes of resistivity data inversions are in use by numerous authors (Hallof, 1957; Dey and Morrison, 1979; Barker, 1992; Li and Oldenburg, 1994; Loke and Barker, 1995; LaBrecque et al., 1996; Edwards, 1997; Auken and Christiansen, 2004; Blanchy et al., 2020).

For this work, the regularized inversion algorithm after Blanchy et al. (2020) available as open-source software/python packages, *ResIPy*, was used to recover 2D conductivity and chargeability models. It is a mesh-based algorithm which is designed to solve the inverse problem. The inversion scheme uses the minimum structure technique, Occam style (Constable et al., 1987), to recover the smoothest distribution of resistivity data which can explain the meaured observations consistently. The algorithm uses a robust iterative numerical technique known as the Gauss-Newton method to solve the inversion problem

(Binley, 2023). During the inversion, the algorithm iteratively solves for the final resistivity/conductivity model by updating the intermediate model parameters using the correction vector of parameters at each iteration until the stopping criterion is met (Haber et al., 2000; Binley, 2023). The convergence criterion is prescribed in terms of the root mean square (rms) value of data misfit (deviations between the observed and the modelled data).

Here, the apparent resistivity data were formatted into RES2DINV format, one of the formats supported by ResIPy, and the elevations at every electrode location were included for all the profiles for inversion. The study area is relatively flat over the soccer and rugby fields with slight topography towards the beginning of all the profiles, except DCR_profile 6 (see Appendix E). The topographic data was included to incorporate true electrode locations to avert any discrepancies in inversion as a result of this effect. The formatted data were then converted into pseudo-sections to roughly correlate with apparent resistivity profiles presented in Figure 4.4 to Figure 4.9. A sample pseudo-section, using DCR_profile 1 (the rest are given in Appendix B), is shown in Figure 4.10. The resistivity distribution pattern, i.e., a conductive region sandwiched in between more resistive top and bottom layers (not as resistive as the top layer), can be more easily observed here as well. For this inversion work, 2D triangular finite element meshes with electrodes located at nodes were used (Geuzaine and Remacle, 2009; Binley, 2023). The sample image showing the mesh discretization for the model, DCR_profile 1, is shown in Figure 4.11.

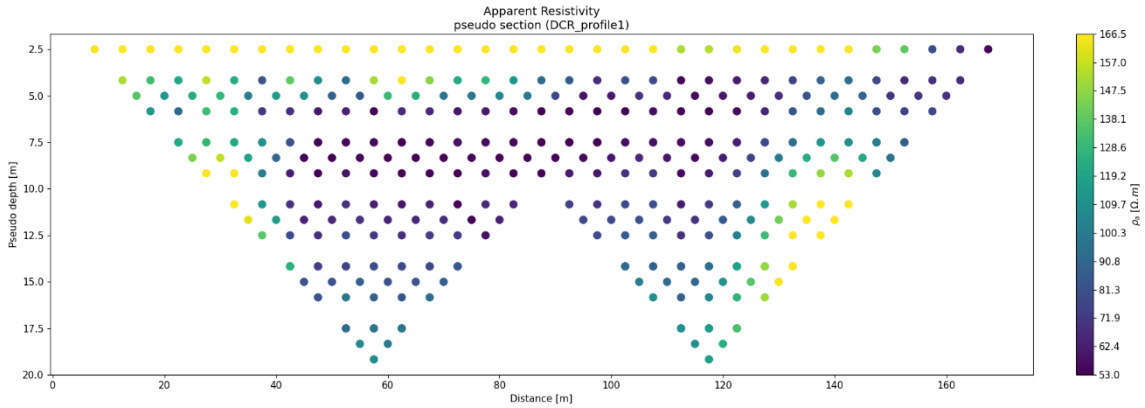

Figure 4.10: Pseudo section of DCR_profile 1 showing the apparent resistivity distribution pattern.

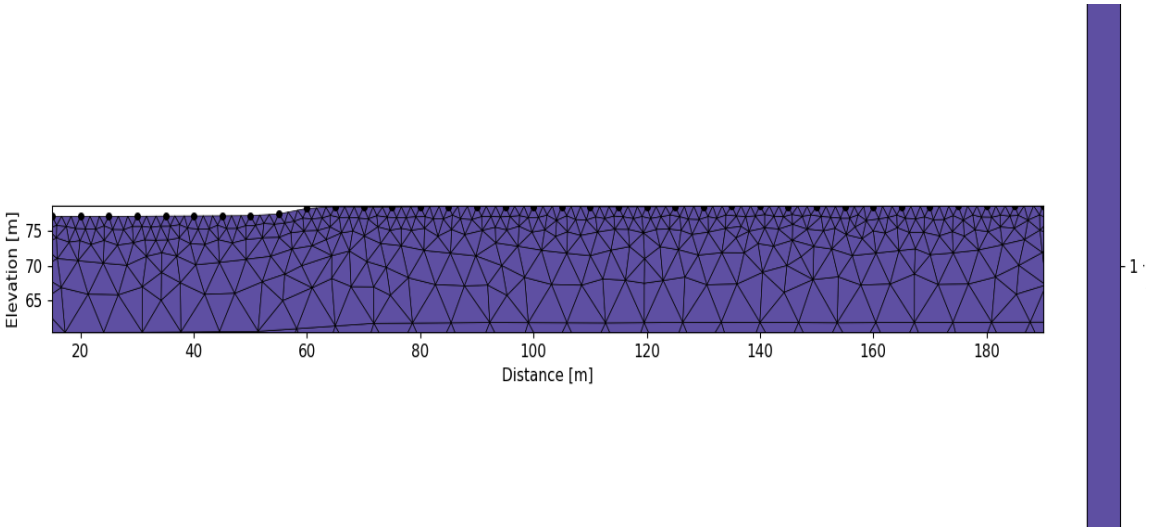

Figure 4.11: Unstructured triangular mesh for DCR_profile 1 with topography.

Along with the apparent resistivity data, additional parameters such as the target rms misfit of 1, 2% Gaussian noise and equal horizontal and vertical weights of 1 were used for the inversions. Hence, all the DCR profiles were individually inverted for conductivity models of the subsurface. Inversions for all six DCR profiles successfully converged with the rms misfit values ranging from 1 to 1.01 using a maximum of 5 iterations. The recovered 2D geoelectrical conductivity models, with normalized errors less than $\pm$3%, are shown in Figure 4.12, Figure 4.13, Figure 4.14, Figure 4.15, Figure 4.16 and Figure 4.17 (with different colour scales for each profile). All these profiles, Figure 4.12 to Figure 4.17, are arranged in order (geographically) from the west end to

the east end of the area for convenience.

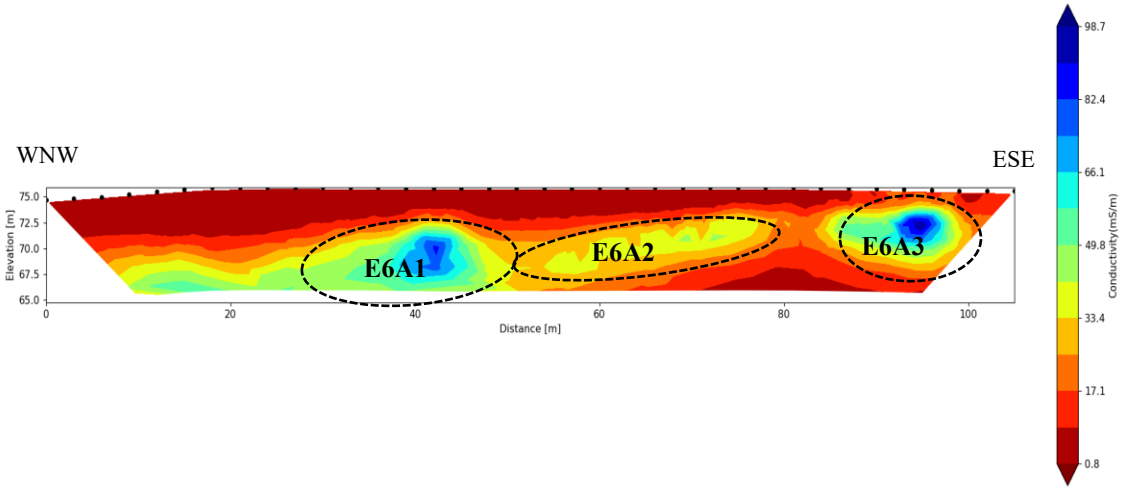

Figure 4.12: Recovered model for DCR_profile 6 showing conductivity distribution in the subsurface.

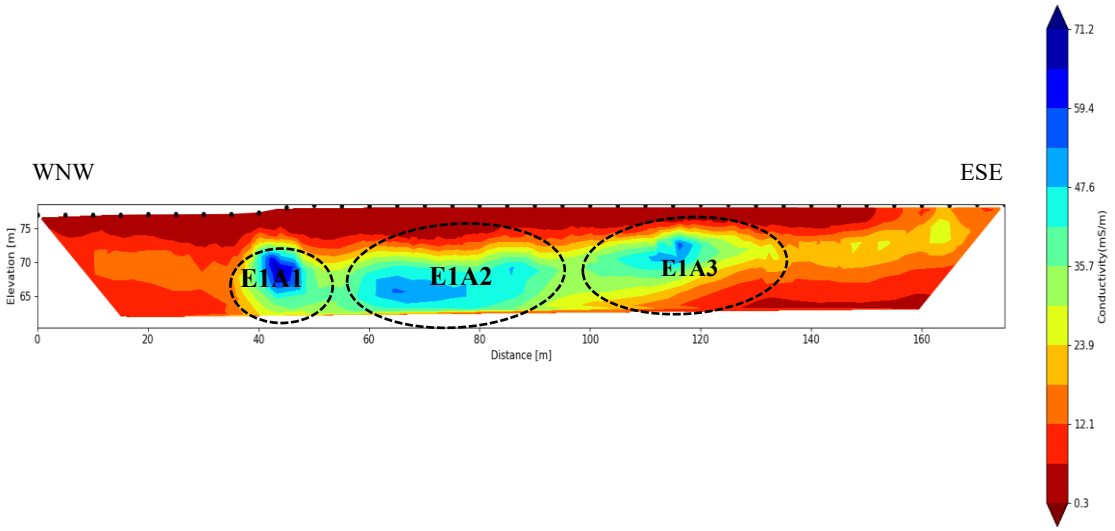

Figure 4.13: Recovered model for DCR_profile 1 showing conductivity distribution in the subsurface.

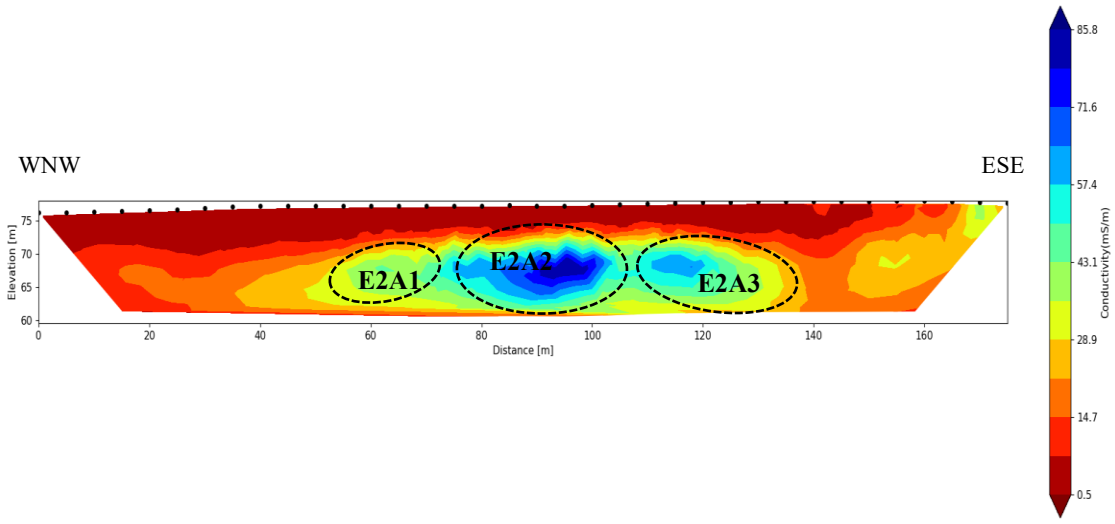

Figure 4.14: Recovered model for DCR_ profile 2 showing conductivity distribution in the subsurface.

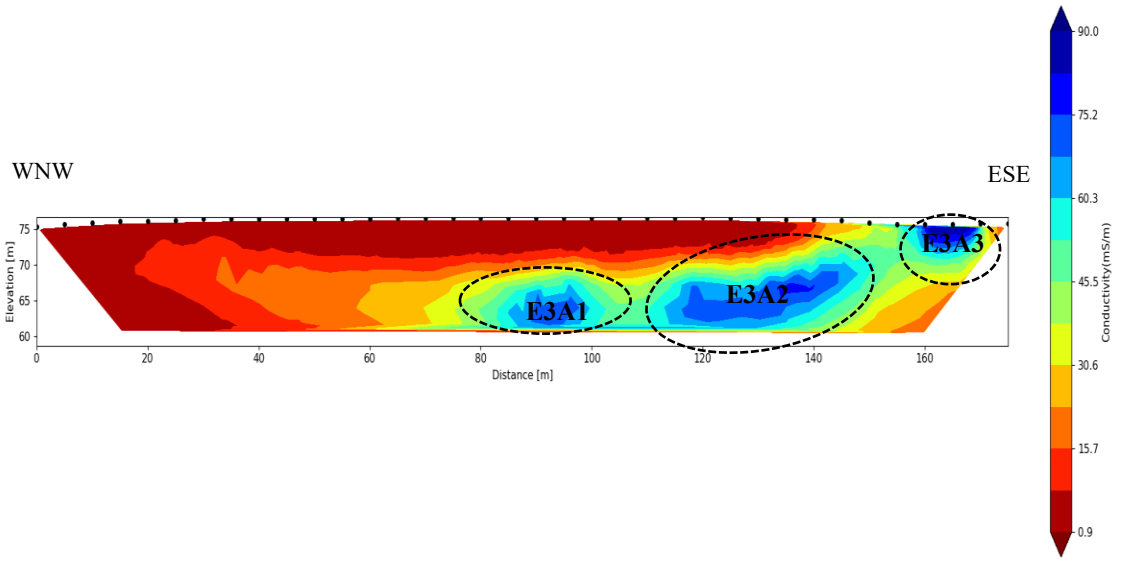

Figure 4.15: Recovered model for DCR_profile 3 showing conductivity distribution in the subsurface.

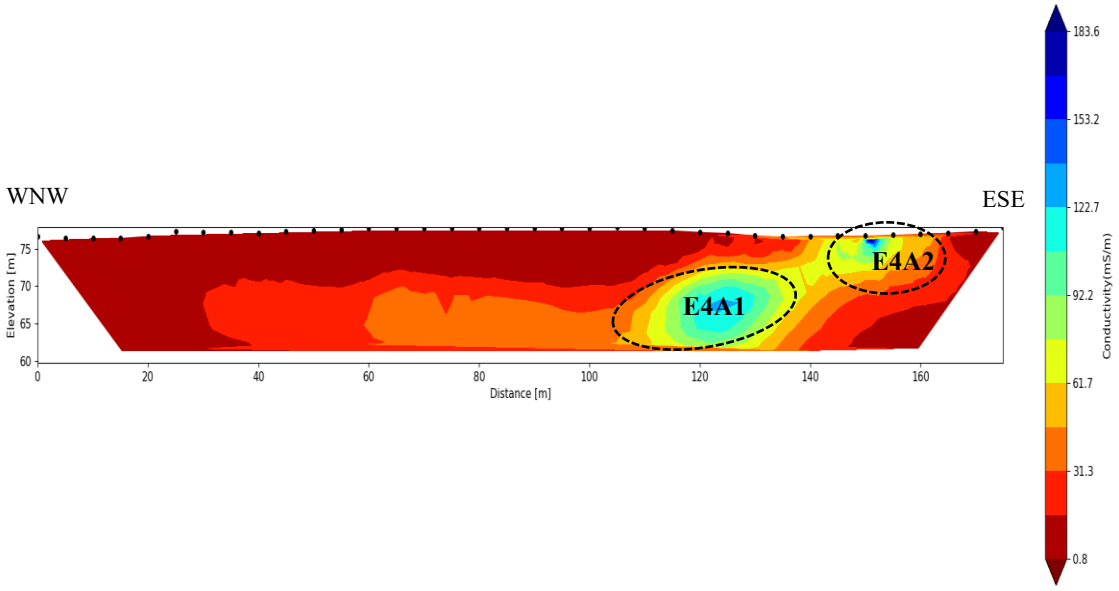

Figure 4.16: Recovered model for DCR_profile 4 showing conductivity distribution in the subsurface.

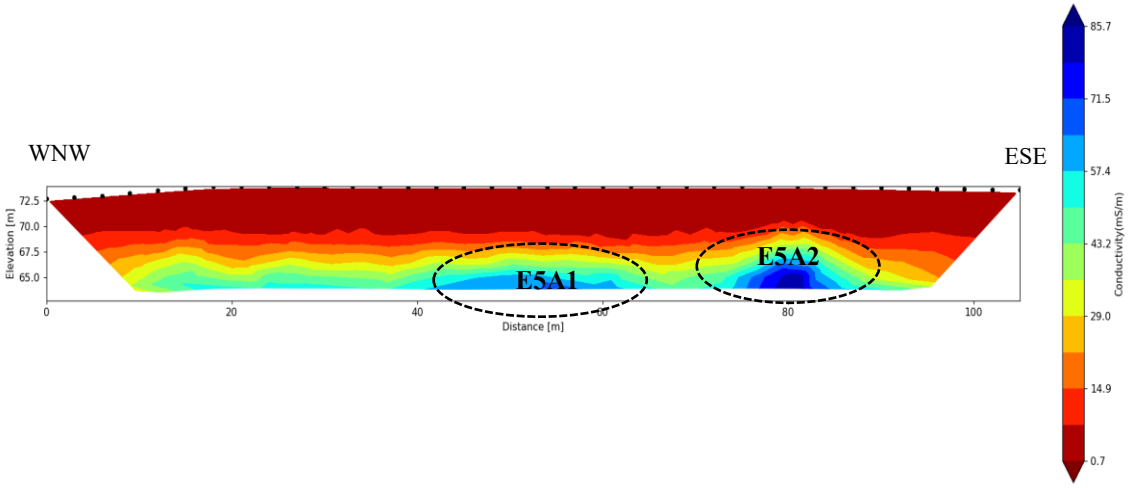

Figure 4.17: Recovered model for DCR_profile 5 showing conductivity distribution in the subsurface.

In each of the five constructed conductivity models over the rugby and soccer fields, there are several conductive anomalies at moderate depths in each model. In Figure 4.12 at least two highly conductive anomalies are recovered, **E6A1** and **E6A3**, which are indicated with ellipses. The anomaly **E6A1** is located at a depth (top) of about 5.75-6.75 metres and the anomaly **E6A3** is located at about 3-4 metres in depth (top). The third

anomaly, marked **E6A2**, is moderately conductive and located at a depth of about 4-6.5 metres. In Figure 4.13, there are three isolated conductive anomalies, marked **E1A1**, **E1A2** and **E1A3**. The conductive anomalies **E1A2** and **E1A2**, which are more diffuse, occur at depths of approximately 4-8 metres. The third conductive anomaly, **E1A1**, is markedly localized and is located roughly at a depth of about 7 metres from the surface.

Similarly, Figure 4.14 has three markedly distinct conductive anomalies namely **E2A1**, **E2A2** and **E2A3**. The anomalies **E2A1** and **E2A3** are moderately conductive (< 60 mS/m) and the anomaly **E2A2** is highly conductive (>85mS/m) and contributes to a zig-zag pattern on the apparent resistivity section (see Appendix B). All of them are located at a depth of about 6.5-7 metres from the surface. Similarly, Figure 4.15 depicts at least three conductive anomalies indicated as **E3A1**, **E3A2**, and **E3A3**. The anomalies **E3A1** and **E3A2** are highly conductive and located at about a depth of 7–8 metres from the surface while **E3A3** is located at the ground surface. Figure 4.16 displays two highly conductive anomalies **E4A1** and **E4A2**. The anomaly **E4A1** is located at the depth of about 6 metres while the anomaly **E4A1** is at the surface. All the conductivity profiles, except DCR_profile 2, suggest likely flow paths of runoff infiltrating into the ground in the area.

The resistivity line, DCR_profile 5, taken over the baseball field, was inverted and the constructed model is shown in Figure 4.17. This model, in contrast to the others, shows a relatively uniform thickness resistive top layers and the deeper conductivity anomalies, clearly **E5A1** and **E5A2**. This can be likely due to much thicker layers of fill used during the construction of the baseball field to level the old ground which could have been at a comparatively lower elevation compared with the soccer and rugby fields.

One very important aspect of any geophysical survey, at any scale, is the depth of investigation (DOI). It is an abstract depth down to which a survey can image a subsurface with reasonable resolution (Oldenburg and Li, 1999). The initial choice of

array and spacing was made based on the rule-of-thumb proposed by Edwards (1997) to image down to a depth of about 15-25 metres. However, this was just a crude estimate used during the design phase. Here, a more realistic depth of investigation was computed applying the technique proposed by Oldenburg and Li (1999) of running two inversions with different reference models with resistivities of 100 Ωm and 1000 Ωm and assessing the depth at which the models constructed by the two inversions start to deviate from one another. All the anomalies in Figure 4.12, Figure 4.13, Figure 4.14, Figure 4.15 and Figure 4.16 occur well within the depth of investigations and, hence, are physically realistic. The conductivity sections with DOI lines superimposed are given in Appendix B.

As the DC resistivity lines are designed roughly perpendicular to the magnetic trends, see Figure 4.3, it is paramount to understand the spatial distributions of these conductive anomalies in the area. To this end, the pseudo-3D inversion was carried out using the four roughly parallel DCR profiles, DCR_profile1 through DCR_profile 4, with an average profile separation of 30 m in *ResIPy*. This scheme carries out the inversion of the individual geoelectrical lines and spatially arrange them in 3D space. The recovered pseudo-3D solution, rotated about 45 degrees from their original orientations, is shown in Figure 4.18.

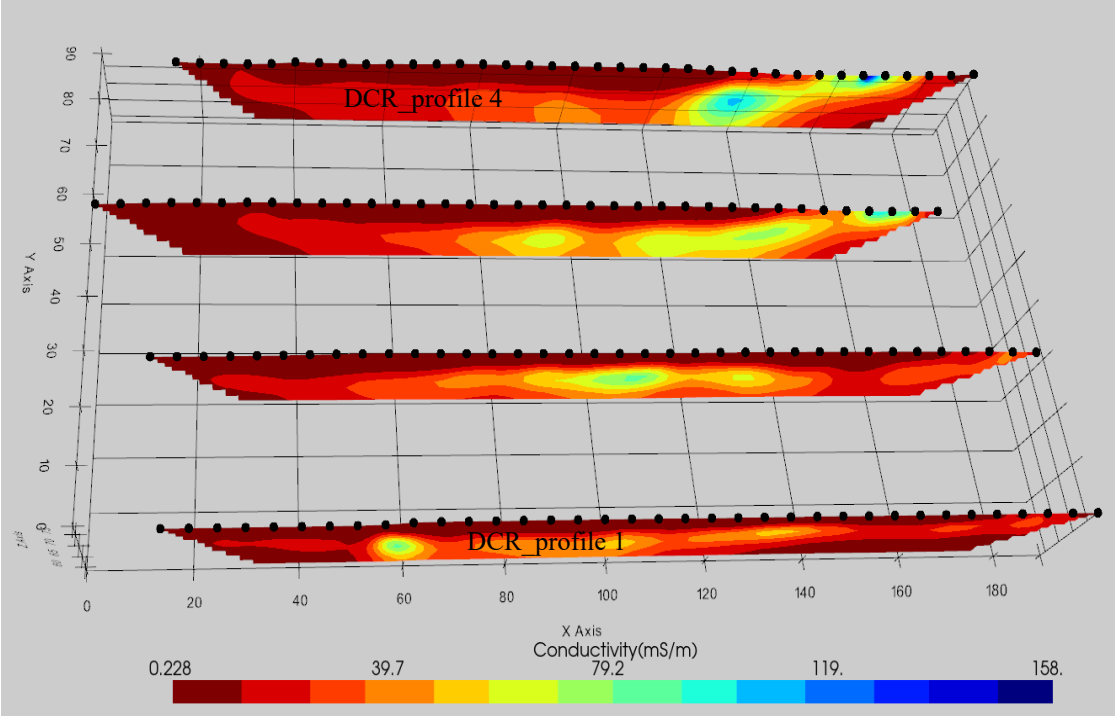

Figure 4.18: Pseudo-3D image showing spatial distribution of conductive anomalies in the area (rotated 45 degrees anticlockwise, using the same color scale for all four models).

From Figure 4.18, the conductive anomalies observed in the area predominantly exhibit a pattern of linearly interconnected channels/trenches. This network of linear conductive anomalies is consistent with the linear magnetic anomalies observed in Section 3.3. (Detailed comparisons are given in Chapter 7). The overall colour intensity looks slightly different from what is shown in Figure 4.13 to Figure 4.16, due to the presence of few very conductive anomalies, especially in DCR_profile 4, which dominate the common color scale.

For all the conductivity profiles discussed above, the inversion errors were monitored in terms of normalized inversion errors. According to Binley et al. (1995), in the absence of actual noise measurements (which is the case here), the constructed inversion models must have the normalized inversion errors within ± 3 for them to be physically plausible. Sample error plots, (a) error pseudo-section and (b) error of each datum, for DCR_profile 1 are given in Figure 4.19 (error plots for the rest of the DCR lines are given in Appendix B). As shown in Figure 4.19, all the 2D conductivity profiles were constructed with

normalized error lesser than ± 2.8.

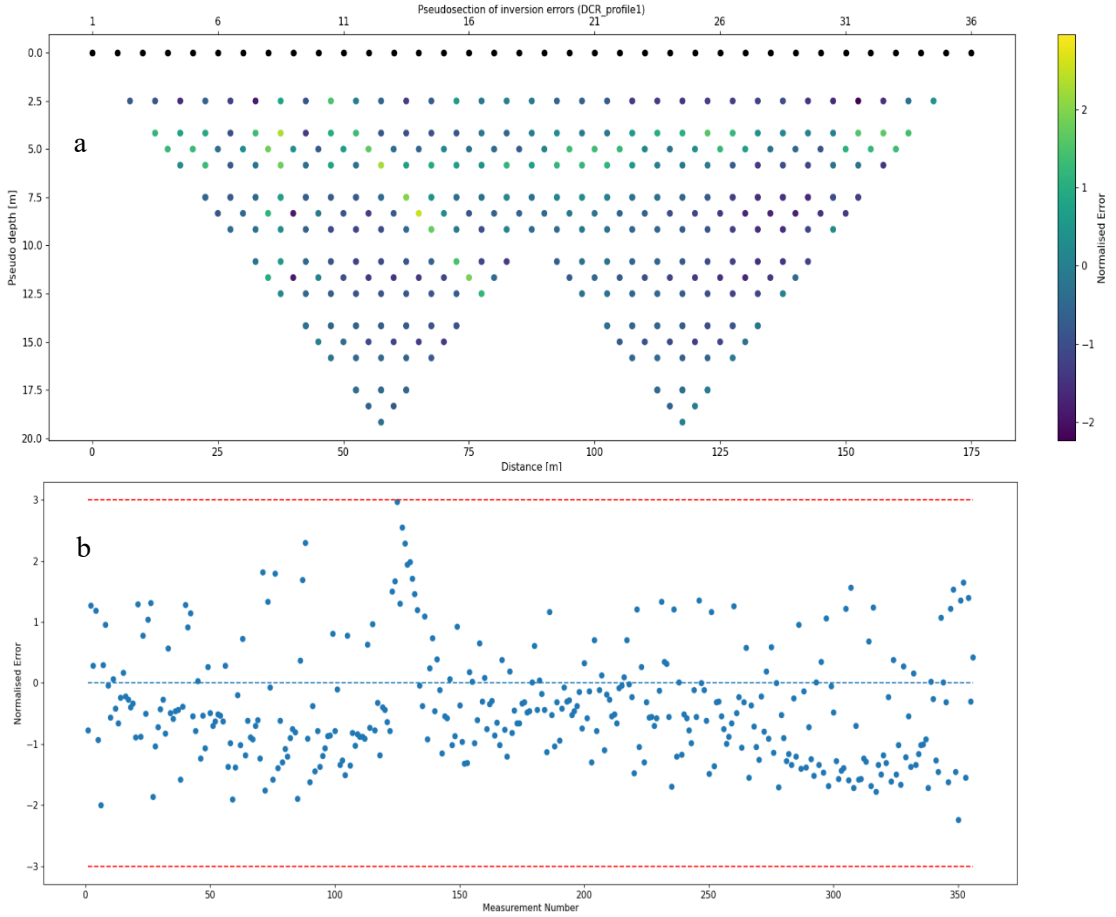

Figure 4.19: Inversion error plots, pseudo-section of errors (a) and normalized errors (b), for DCR_profile 1.

4.4 Data Analyses and Interpretations of Induced Polarization Survey

The apparent chargeability data were plotted for different values of 'a' (a=AB/2) for three different values of 'b' as the first-pass technique to roughly comprehend the apparent chargeability variations in the subsurface. The sample plots, for DCR_profile 1, are shown in Figure 4.20, Figure 4.21 and Figure 4.22, with the rest of the plots given in Appendix B.

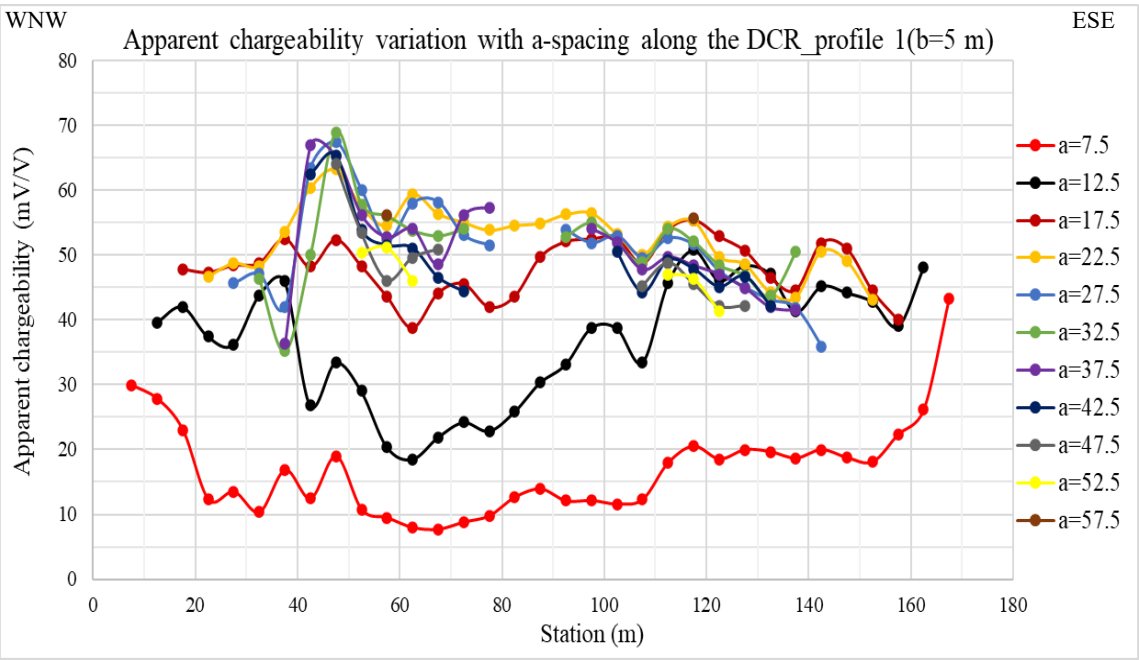

Figure 4.20: Apparent chargeability profile for DCR_profile 1 (for b=5 m).

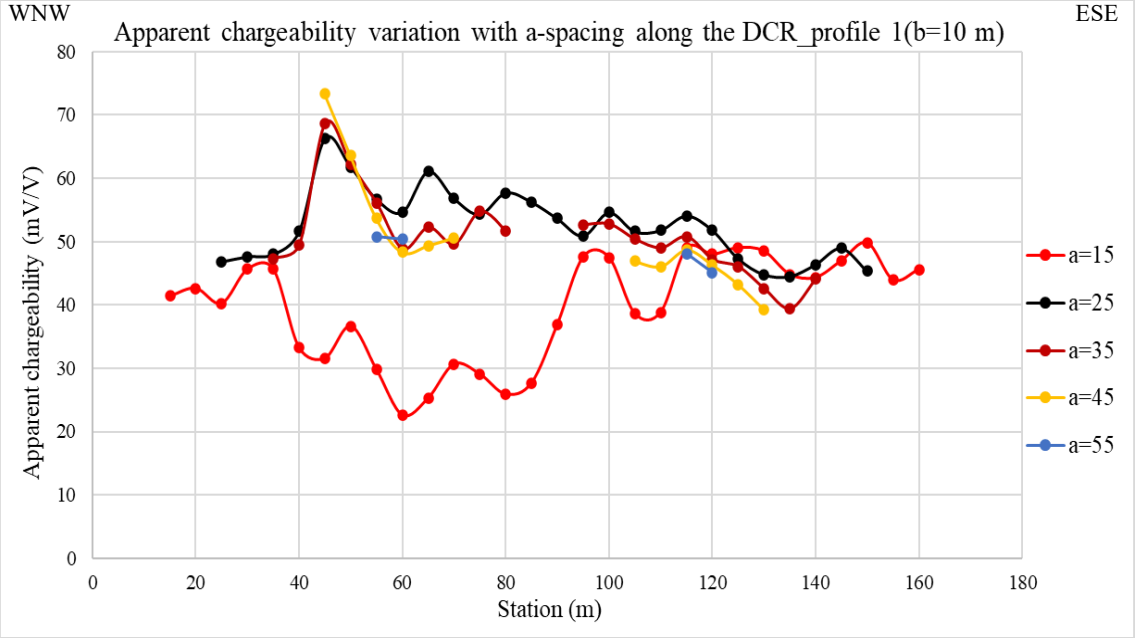

Figure 4.21: Apparent chargeability profile for DCR_profile 1 (for b=10 m).

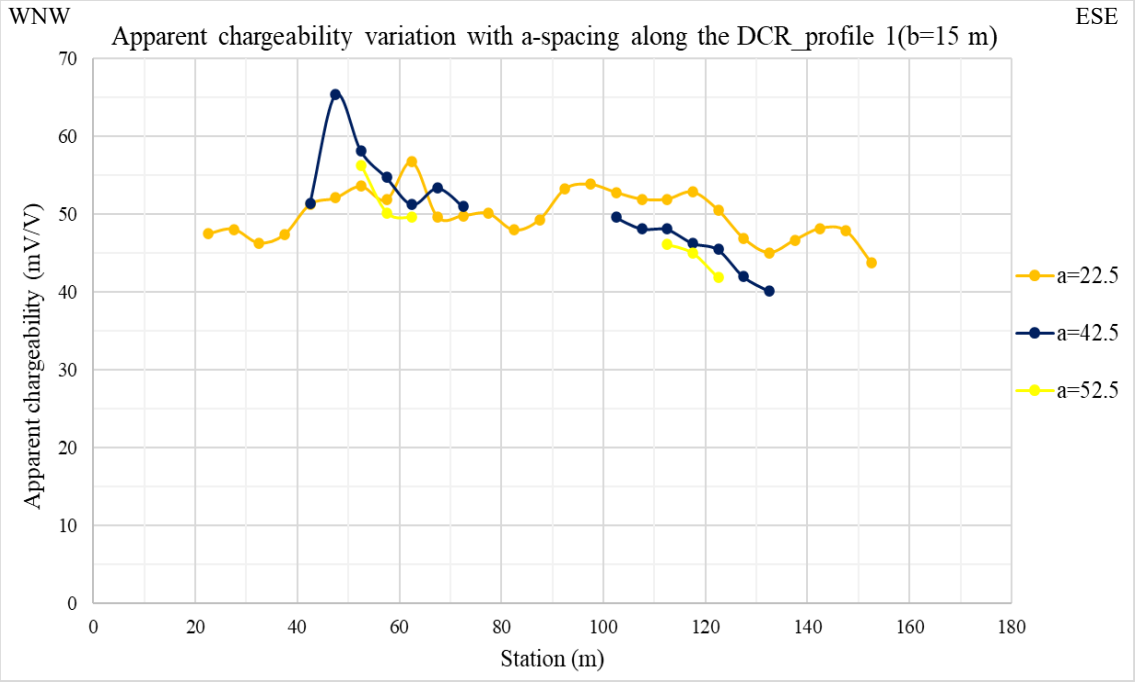

Figure 4.22: Apparent chargeability profile for DCR_profile 1 (for b=15 m).

From Figure 4.20, Figure 4.21 and Figure 4.22, it is clear that there is a common pattern of the apparent chargeability variations, i.e., the chargeability is relatively low for top and

bottom layers and comparatively higher values for the intermediate layers. For DCR_profile 5, the apparent chargeability is relatively lower for the top layers with the values relatively higher for deeper layers similar to that of the apparent resistivity.

IP inversions were performed to construct the IP models. In this work, the IP inversion approach popularized by Binley and Kemna (2005) and Kemna et al. (2012), is used to invert the apparent chargeability data using the complex resistivity package *cR2* of *ResIPy*. Here, the apparent chargeability data were converted into the required format, complex format, using a conversion constant equal to 1.2, which is suitable for landfill applications using the Syscal system (Ntarlagiannis et al., 2016). Also, the program uses the model obtained from the resistivity inversion as the reference model. As discussed in DC resistivity, all the models were constructed with data misfit (rms) of 1 to 1.01 using a maximum of 5 iterations with one iteration of final phase improvement with the phase misfit (rms) of 0.735 to 0.972. The inversion errors limit is the same as it is discussed in Section 4.3.

The constructed 2D models of magnitude (resistivity in Ωm) and phase (negative in resistivity space expressed in milliradian, mrad) of the complex resistivity inversion is given in Figure 4.23 and Figure 4.24 for DCR_profile 1. The magnitude model indicates resistivity distribution while the phase model depicts chargeability variations in the subsurface. From these figures, it is clear that those regions with low resistivity, top depth of about 6 m and the bottom depth of about 12 m, correspond very well with the phase lows. These zones indicate high polarization effects in the subsurface.

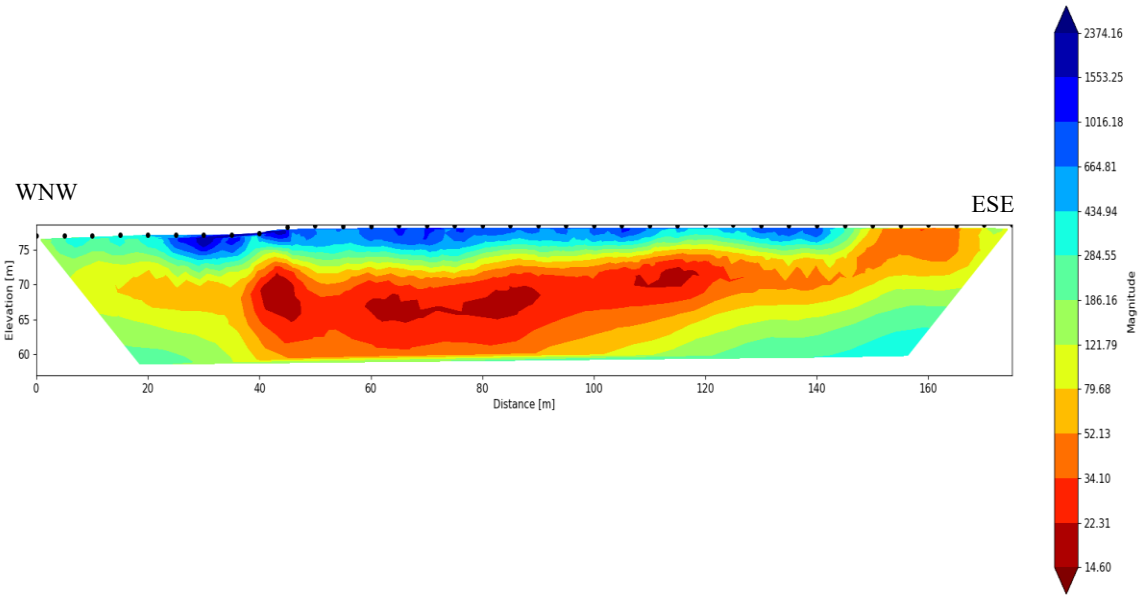

Figure 4.23: Recovered magnitude model of the complex resistivity inversion for DCR_profile 1(red zones are more conductive).

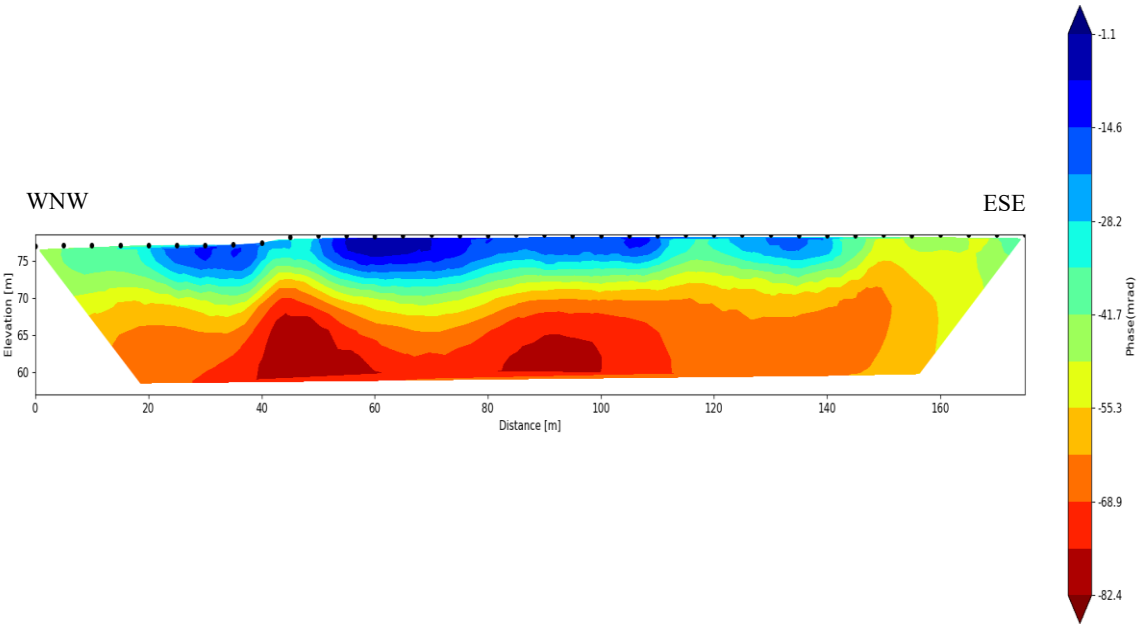

Figure 4.24: Recovered phase model of the complex resistivity inversion for DCR_profile 1.

Alternately, results of the complex resistivity can be analyzed in terms of real and imaginary conductivity/resistivity (Binley and Kemna, 2005; Mwakanyamale et al., 2012; Ntarlagiannis et al., 2016). The real conductivity model represents conduction primarily

due to electro-migration, which measures flow of charges/ions via fluid under applied potential, while the imaginary model represents conductivity contributed only by surface conduction, which is the measure of conduction occurring along mineral-fluid interfaces (Binley & Kemna, 2005; Mwakanyamale et al., 2012). The sample real and imaginary conductivity models (both in log scale) for DCR_profile 1 are given in Figure 4.25 and Figure 4.26. Both of these figures depict high conductivity regions corresponding to the phase lows or resistivity lows within the depth of about 6-12 m. Here, both the real, at least an order higher in magnitude, and imaginary models show similar structures. According to Mwakanyamale et al. (2012), this similarity can be attributed to the surface conduction being the dominant case.

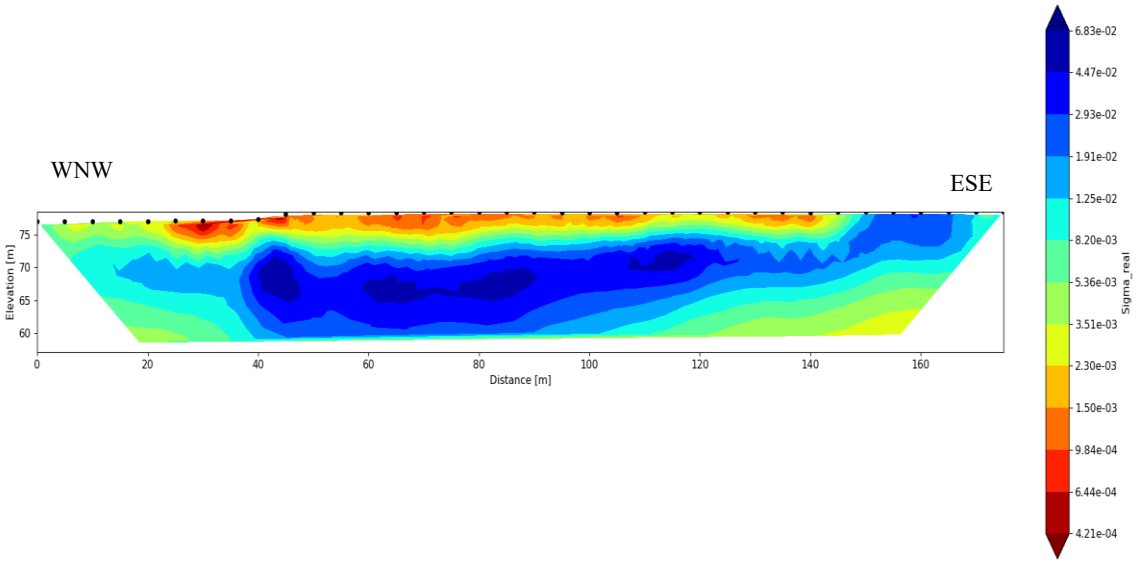

Figure 4.25: Recovered real conductivity model of the complex resistivity inversion for DCR_profile 1.

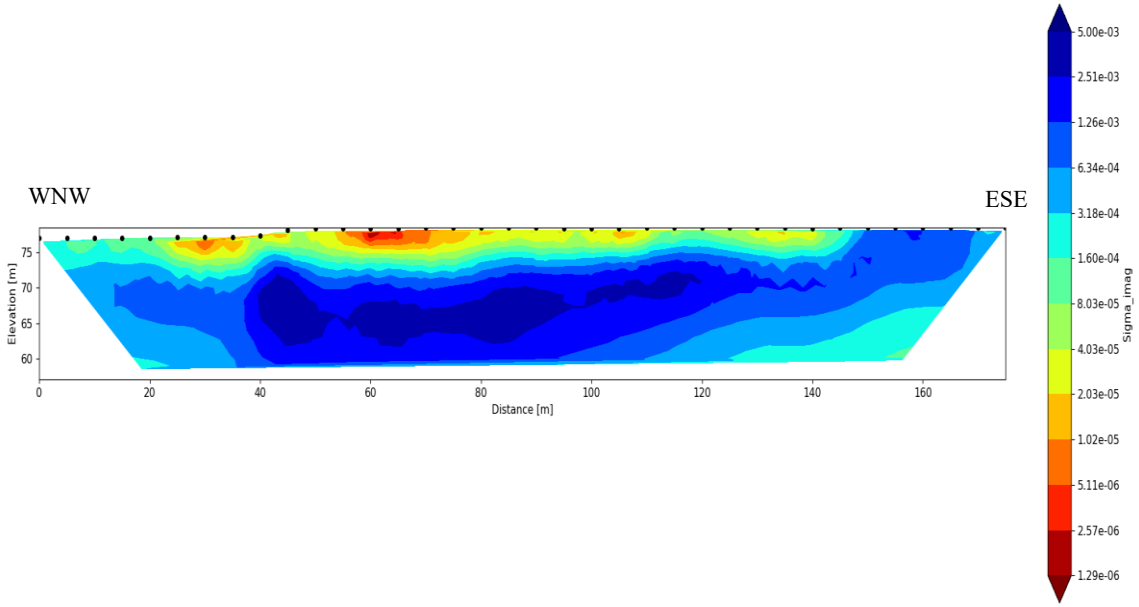

Figure 4.26: Recovered imaginary conductivity model of the complex resistivity inversion for DCR_profile 1.

To further ascertain accuracy of the results obtained from the complex resistivity inversion, a smoothness-constrained inversion scheme, known as RES2DINV (Loke and Barker, 1995) was used for an inversion, for both the resistivity and chargeability data, for all the geoelectrical profiles. The sample constructed 2D resistivity and chargeability models, converged with rms of 2 and 3.5 respectively using maximum iteration of 5 for DCR_profile 1, are given in Figure 4.27 and Figure 4.28.

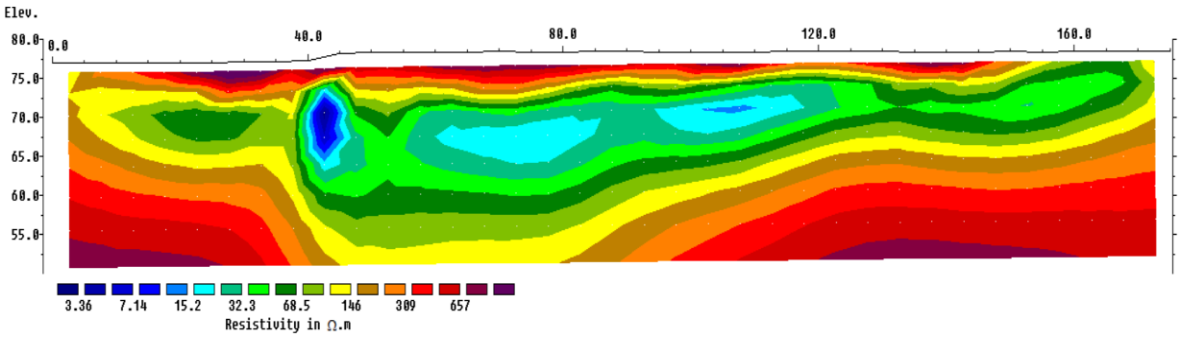

Figure 4.27: Resistivity model, of RES2DINV routine, for DCR_profile 1.

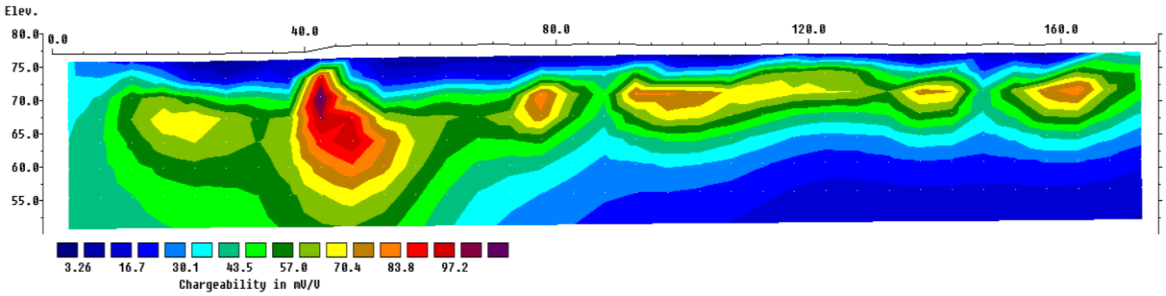

Figure 4.28: Chargeability model, of RES2DINV routine, for DCR_profile 1.

Clearly, Figure 4.27 shows very good agreement in the resistivity distribution with the resistivity lows within about 6-12 m in the subsurface as in Figure 4.23. Figure 4.28 depicts chargeability highs at about the same depth extent as the resistivity models. Moreover, the real and imaginary conductivity models in Figure 4.25 and Figure 4.26 exhibit very close resemblance to the chargeability distribution pattern in the subsurface (see Figure 4.28). Thus, only the real and imaginary conductivity models are used for the remaining discussions on IP.

The constructed 2D induced polarization models, real parts in log scale which represents the contribution from electro-migration, the movement of charged particles through porous media on account of an applied electric potential (Mwakanyamale et al., 2012), for the rest of the five DCR lines are shown in Figure 4.29, Figure 4.30, Figure 4.31, Figure 4.32 and Figure 4.33. All these profiles are arranged in order (geographically) from the west end to the east end of the area for convenience. Clearly, the recovered real conductivty models depict dominant effects from electro-migration phenomenon possibly due to leachate plumes and also predominantly indicate possible flow-paths of infiltrating runoff recharging existing plumes and ground water in the subsurface (indicated by dashed red lines). Similar observation was reported by Ntarlagiannis et al. (2016) in their landfill study. On the contrary, the constructed IP model for the DCR_profile 5 depicts rather low electro-migration effects within the DOI and much greater influence at the deeper depths as shown in Figure 4.33.

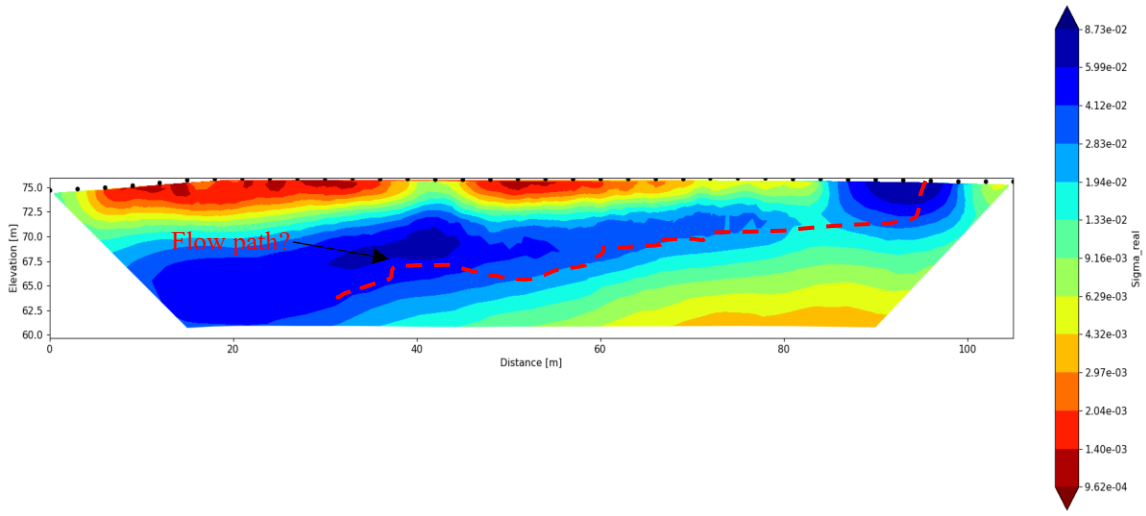

Figure 4.29: Recovered real conductivity model of the complex resistivity inversion for DCR_profile 6.

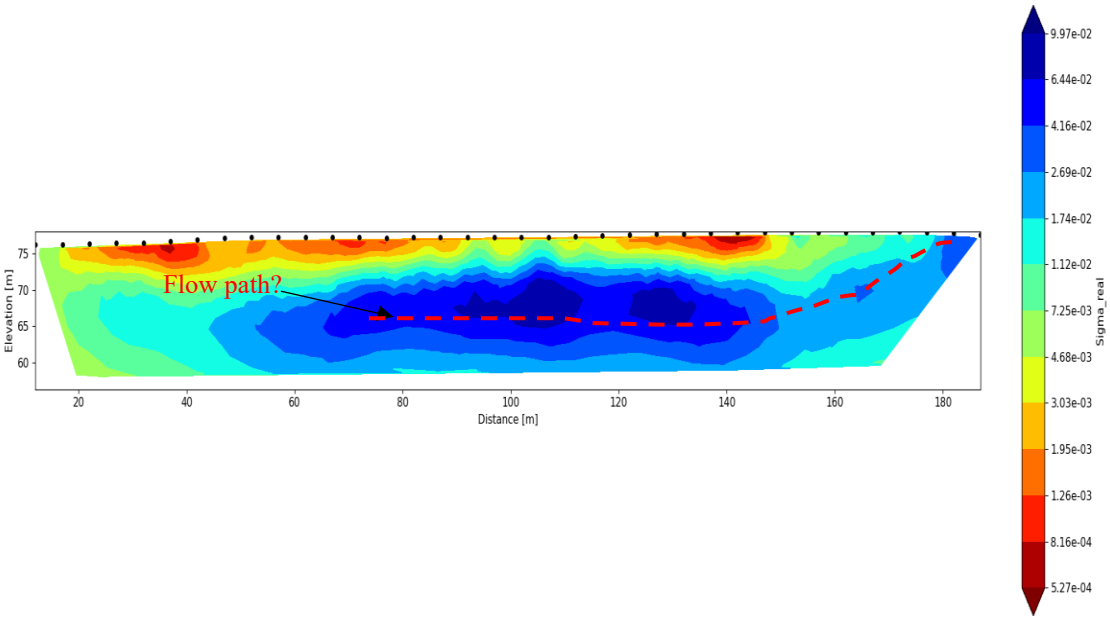

Figure 4.30: Recovered real conductivity model of the complex resistivity inversion for DCR_profile 2.

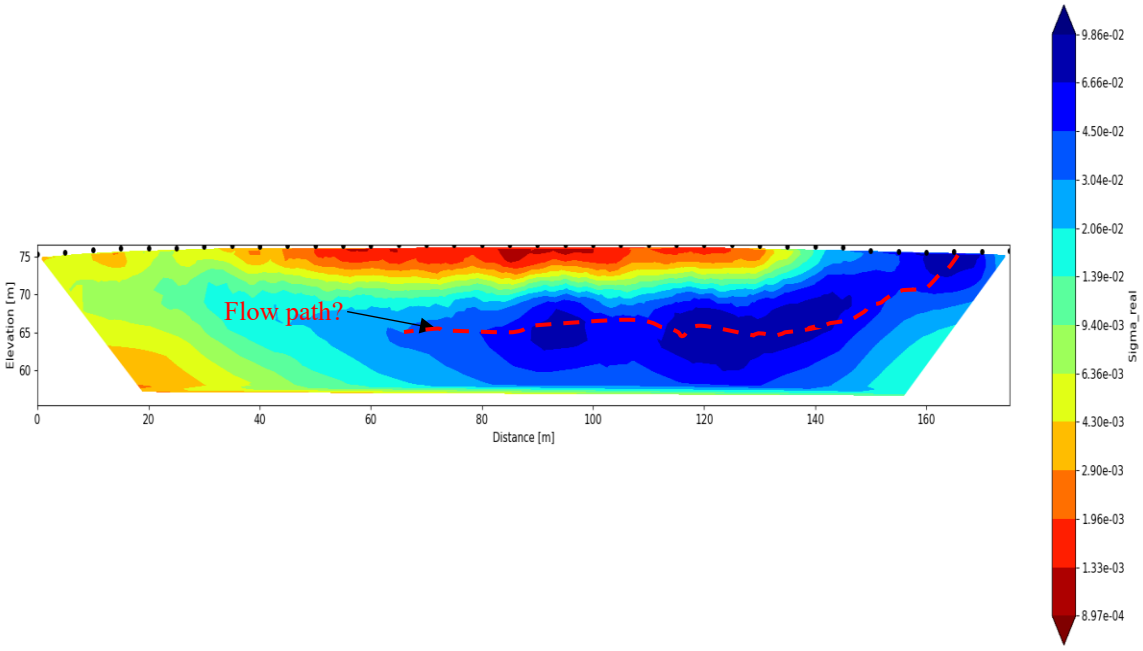

Figure 4.31: Recovered real conductivity model of the complex resistivity inversion for DCR_profile 3.

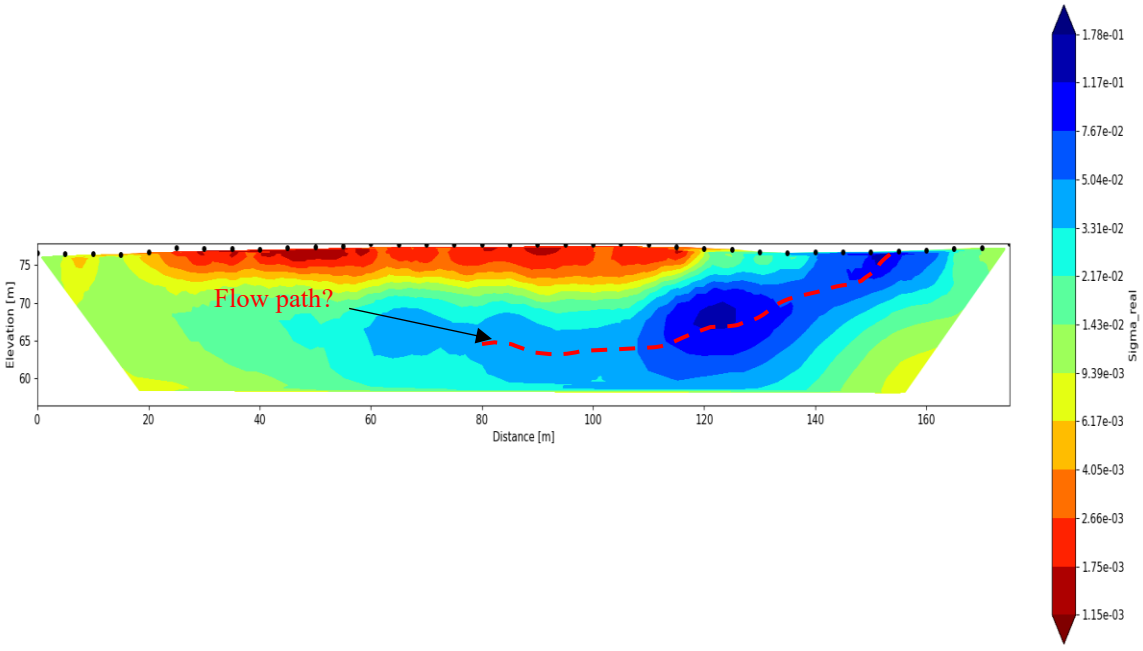

Figure 4.32: Recovered real conductivity model of the complex resistivity inversion for DCR_profile 4.

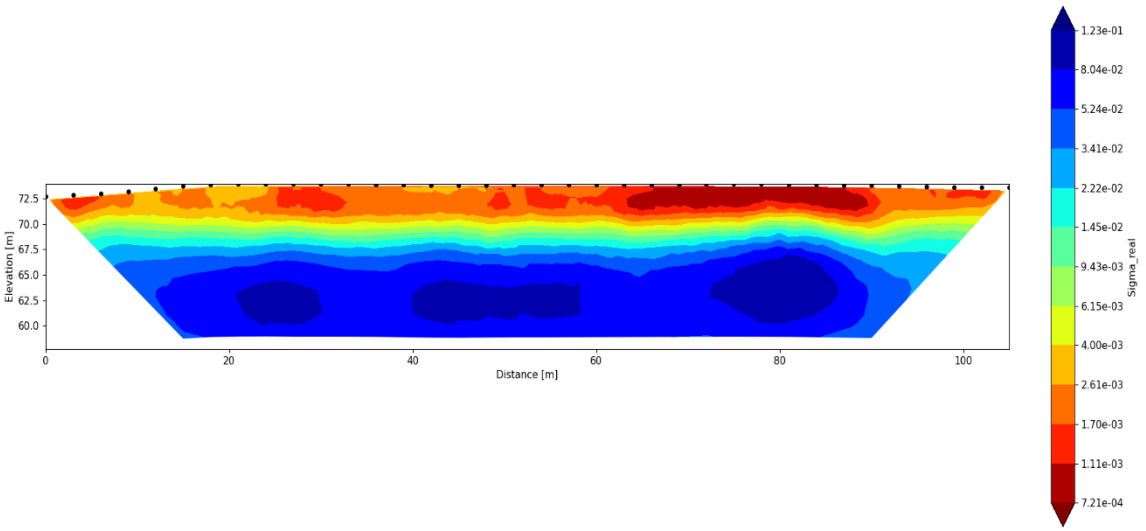

Figure 4.33: Recovered real conductivity model of the complex resistivity inversion for DCR_profile 5 (over the baseball field).

The real conductivity highs have an average depth of about 6 metres for the top resistive layers which possibly suggest compacted top fill which gradually transition up to actual ground surface in the ESE corner. Leroux et al. (2007) and Carlson et al. (2015) showed the increased chargeability in landfills compared with their surroundings, similar to the observations in this study. From Figure 4.4 and Figure 4.22 through Figure 4.33, it can be seen that conductive anomalies agree well with magnetic responses in most cases (see Section 7.2), indicating the existence of buried remnant metallic waste (vehicular wreckages/ lumps of metallic scraps etc.).

Further, the imaginary conductivity model, see Figure 4.26, exhibit similar trends of conductivity distribution to that of the real conductivity for DCR_profile 1. Here, the imaginary conductivity models for the rest of the geoelectrical profiles are given in Figure 4.34, Figure 4.35, Figure 4.36, Figure 4.37 and Figure 4.38.

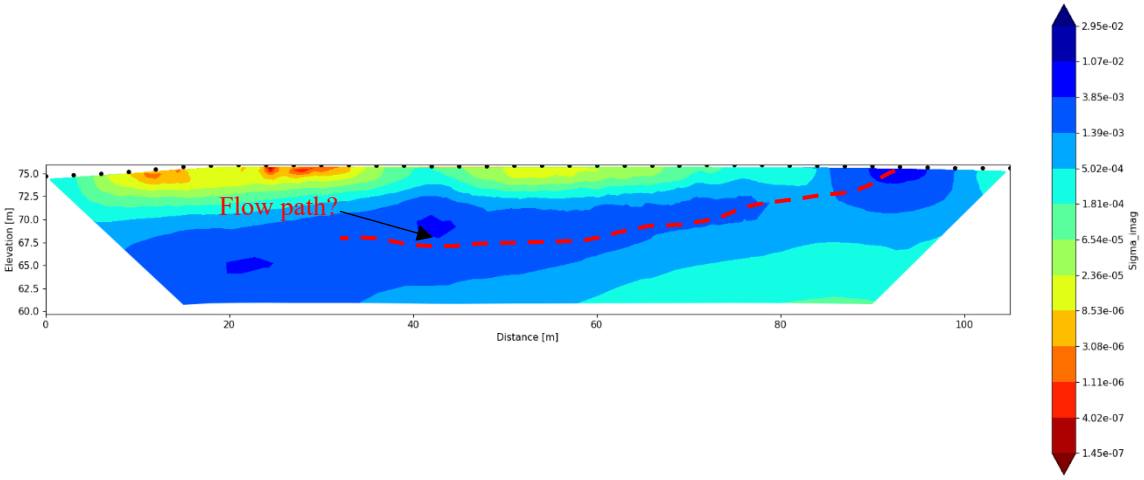

Figure 4.34: Recovered imaginary conductivity model of the complex resistivity inversion for DCR_profile 6.

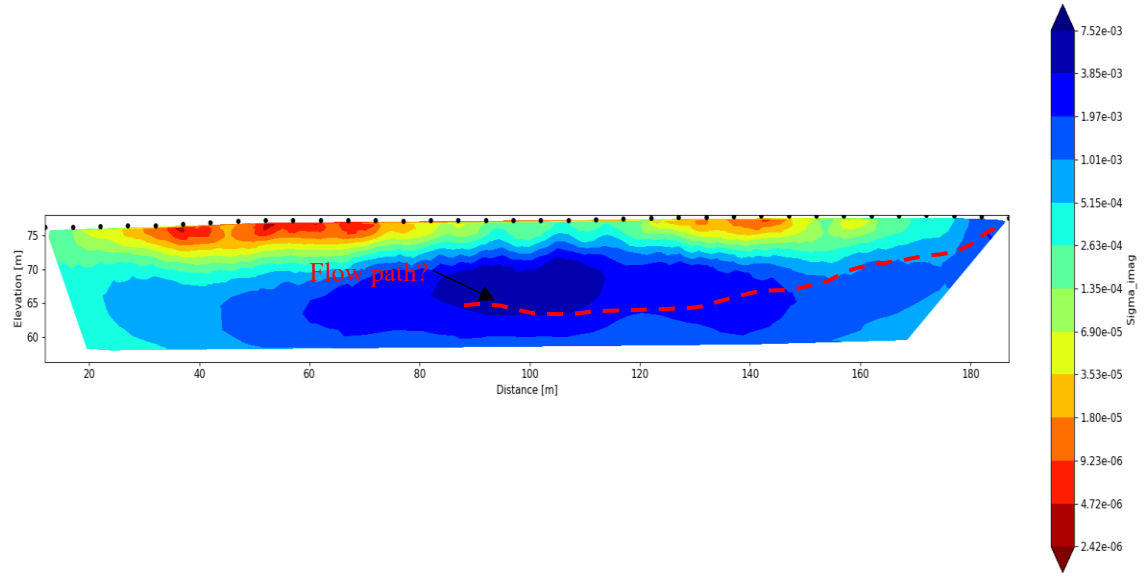

Figure 4.35: Recovered imaginary conductivity model of the complex resistivity inversion for DCR_profile 2.

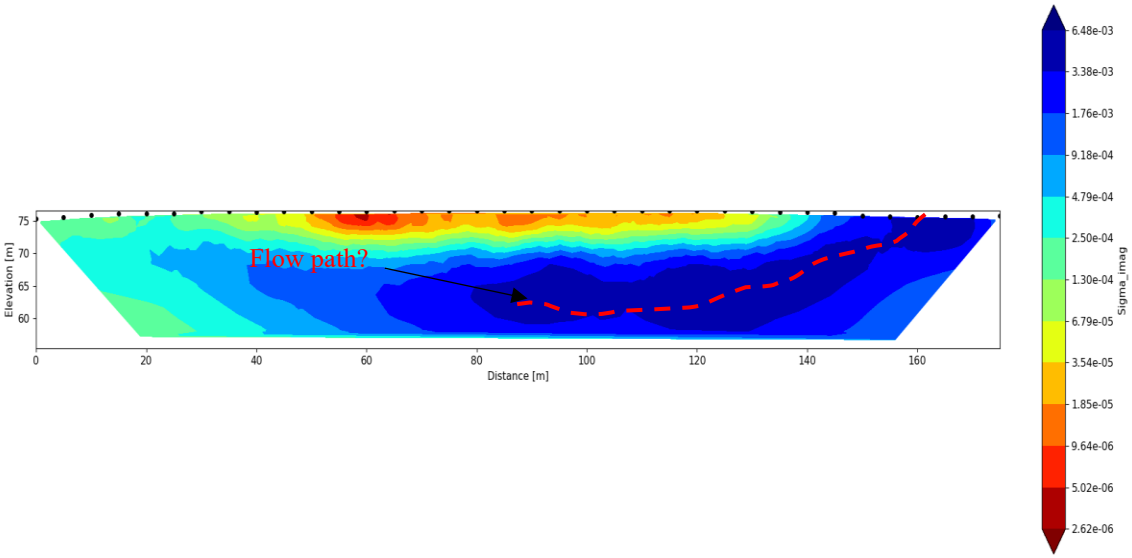

Figure 4.36: Recovered imaginary conductivity model of the complex resistivity inversion for DCR_profile 3.

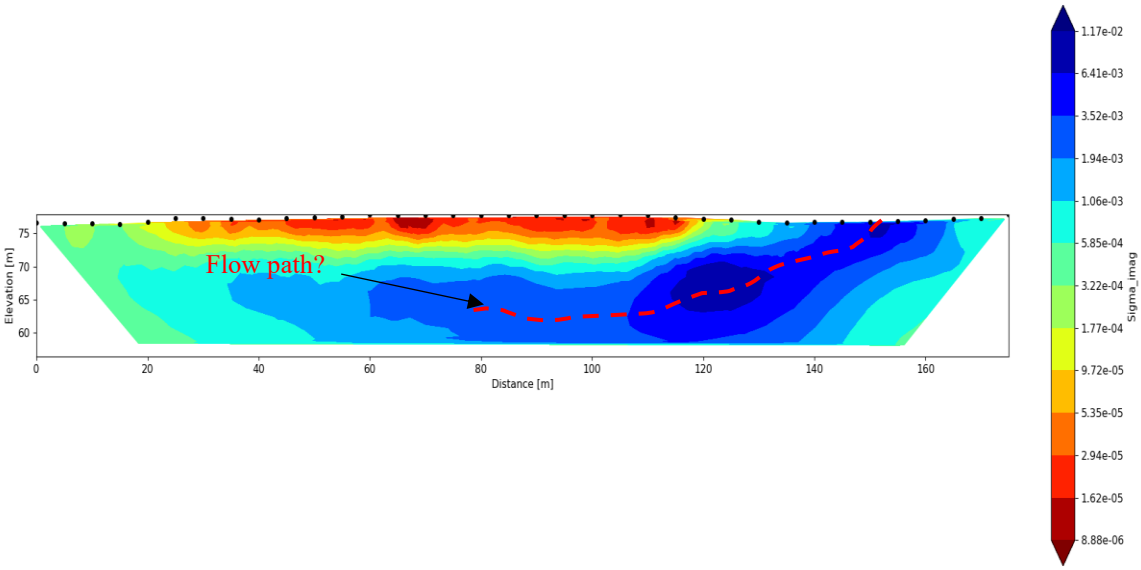

Figure 4.37: Recovered imaginary conductivity model of the complex resistivity inversion for DCR_profile 4.

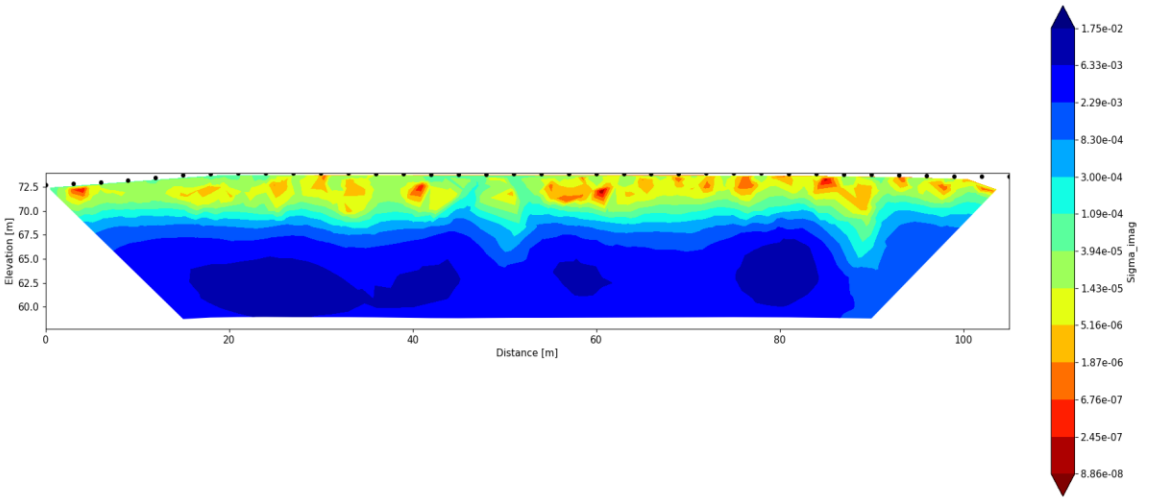

Figure 4.38: Recovered imaginary conductivity model of the complex resistivity inversion for DCR_profile 5 (over the baseball field).

The magnitude of imaginary conductivity, due to polarization, is an order of magnitude lower than the real values. Nevertheless, the imaginary conductivity exhibits very similar distribution trends as the real conductivity. Ntarlagiannis et al. (2016) reported slightly higher range of imaginary conductivity values in their landfill study than what is observed here. They concluded that both the real and the imaginary conductivity highs correspond to leachate plumes existing in the landfill. Also, the zones of high conductivity, possibly corresponding to leachate plumes, may be a complex mixture of organic and inorganic components (Ntarlagiannis et al., 2016; Leroux et al., 2007). The imaginary conductivity shows interconnection in subsurface zones through likely flow-paths of infiltrating runoff in the area, similar to the real conductivity models, from the gravel carpark. Such a connection with the near surface was not observed in the baseball field (see Figure 4.38) which is not adjacent to an area of open gravel for both the real and imaginary models. Detailed integrated interpretations are given in Chapter 7.

Chapter 5: Electromagnetic Survey

5.1 Basic Principles

An electromagnetic (EM) survey is a type of non-invasive geophysical method. It works based on the electromagnetic phenomenon called induction. Electromagnetic induction is the phenomenon in which a time-varying magnetic field, produced by a time-varying electric current in the transmitter, induces an electro-motive force (emf) in nearby media. The magnitude of the induced emf, or voltage, depends on the rate of change of the magnetic field through any current path in the medium.

The induced emf can drive ‘eddy’ currents in a suitably conductive medium, and the magnetic field from these secondary currents in turn induces a secondary emf on the receiver. Geophysical application of the EM method involves the use of transmitters (Tx) consisting of wire coils with a.c. currents as the source of the time-varying magnetic field, geophysical targets as the intermediate medium in which currents are induced, and receiver coils (Rx) to measure the secondary magnetic field arising from the currents induced in the subsurface target(s). All these interactions and components are schematically represented in Figure 5.1.

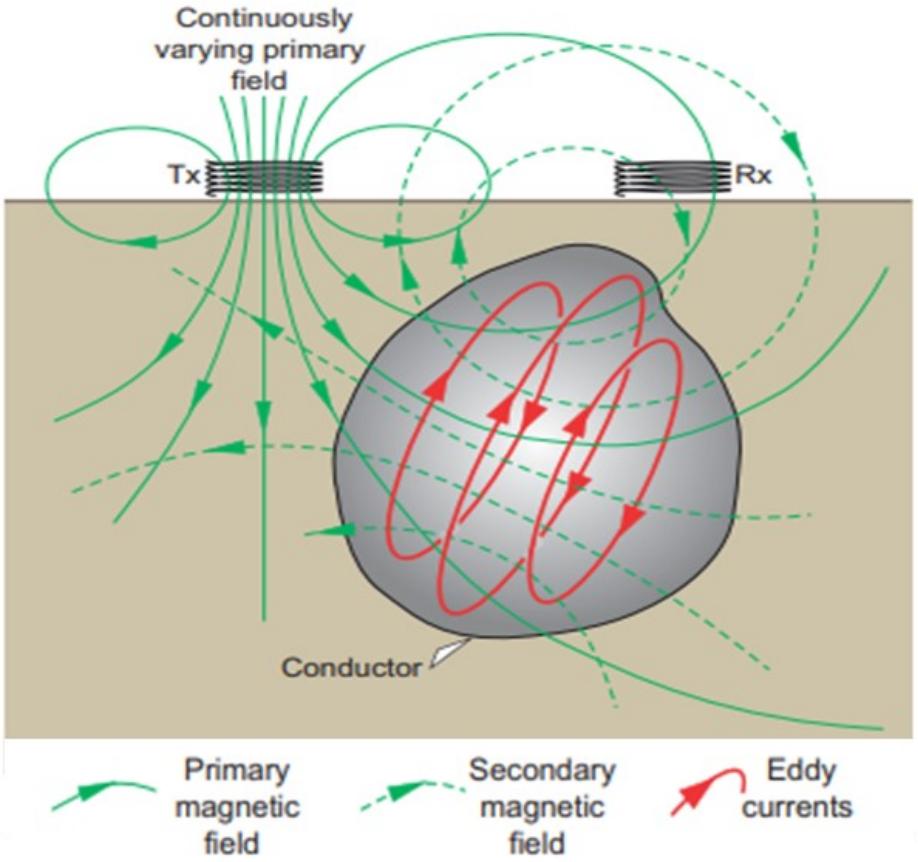

Figure 5.1: Diagram showing the working mechanism of an electromagnetic survey using a half-space with a localized conductive body. (After Dentith and Mudge, 2014.)

The induced eddy current distribution in a geophysical target (conductor) measured by the receiver coil (Rx) is dependent on the electrical conductivity of the target and surrounding host medium (Dentith and Mudge, 2014), coupling of the receiver and the transmitter with the target and the size and orientation of the target. This technique can be either active (e.g. Slingram) or passive (e.g. magneto-telluric) and time-domain or frequency-domain (Dentith and Mudge, 2014; Telford et al., 1990).

Of numerous variants of the method, small loop-loop, modified Slingram and low-induction number, frequency-domain systems have gained popularity for geotechnical and environmental (near-surface) studies due to their ease of operations, portability and the sensitivity to the conductivity of the ground (Frischknecht et al., 1991). The low-

induction number systems, in which the ratio between the coils' separation and skin depth is much lesser than unity, assumes the fact that within the typical ranges of conductivities of the ground, an apparent conductivity can be directly obtained from the quadrature component of the secondary magnetic field (McNeill, 1980) (e.g. EM31).

The frequency (parametric) sounding systems commonly operate within a range of frequencies, using a source-receiver pair at a fixed separation, and thus exciting responses from different depths as it is moved along a survey line. This particular variant of a frequency-domain survey is generally the preferred option although a geometrical sounding using variable source-receiver separations with a single frequency are in use (Spies and Frischknecht, 1991; Won et al., 1996). According to Huang (2005), skin depth is the widely used estimate of depth of investigation for the EM systems. It is defined as the distance in a homogeneous medium over which the amplitude of an incident plane wave reduces by 37%.

A frequency sounding involves a series of measurements using multiple frequencies (Spies and Frischknecht, 1991). Hence, using the advantage of the frequency-domain system, for which making measurements at different frequencies is equivalent to probing different depths, the conductivity variations at various different depths can be simultaneously studied. Generally, electromagnetic responses are measured using mutual coupling ratio, the ratio of mutual impedance between a source and a receiver in the presence of the earth/targets to the mutual impedance between the same source and receiver in free space, which is equivalent to the secondary magnetic field normalized by primary field in free space (Grant and West, 1965; Ward and Hohmann, 1988; Spies and Frischknecht, 1991; Won et al., 1996). This method uses various combinations of loop configurations while making physical measurements in the field (Frischknecht et al., 1991; Won et al., 1996).

According to Telford et al. (1990), for a frequency-domain survey, the primary and

secondary fields would be out of phase by an angle $\lambda = 90 + \varphi$ degrees. The 90-degree phase lag originates from inductive coupling while the additional angle φ originates from electrical properties of the medium. The additional phase lag φ ranges from 0 to 90 degrees. In the EM parlance, the secondary field is broken up into components which are either 180 or 90 degrees out of phase with respect to the applied primary field. The former component is referred to as inphase (real) and the latter being termed as quadrature (imaginary) (Grant and West, 1965; Ward and Hohmann, 1988). The inphase and quadrature responses depend on many parameters such as the frequency of the primary EM signal, the conductivity of media/ targets, the survey configurations, the coil separation and the height at which a survey is operated (Frischknecht et al., 1991, see Fig 7a and 7b of the text).

5.2 Field Survey Methods

In this research, a frequency-domain electromagnetic instrumentation known as GEM-2 from Geophex was used for data collection. It is a portable, digital and multi-frequency broadband electromagnetic sensor (Won et al., 1996). Up to five frequencies can be used. The designed frequencies for the GEM-2 used in this research are 990 Hz, 6210 Hz and 39030 Hz. Here, taking EM measurements at three different frequencies provides some indication of how the subsurface conductivity is varying with depth, with the lowest frequency being most sensitive to the largest depth and the highest frequency to the shallowest depth. The instrument operates on the principle of frequency sounding with a very high data-logging capability of 3 readings per second (Won et al., 1996). Due to its fixed bistatic configuration, a transmitter and a receiver coil separated by 1.67 m, only two loop configurations—horizontal coplanar (HCP) and vertical coplanar (VCP)—are possible (Won et al., 1996). Images of various components of the GEM-2 instrument are shown in Appendix C.

The field survey was conducted by traversing lines with the GEM-2 ski hung at waist-height ($h \approx 1$ m) in horizontal coplanar mode (HCP). Two types of EM data, inphase and quadrature, were collected along sets of parallel lines, roughly 5 m apart, running along the soccer and rugby fields, in two different phases of field work as shown in Figure 5.2. For the ease of operation and speed, the data were acquired continuously in back-and-forth manner. The GEM-2 system used here does not have a global positioning system to automatically record the geographic locations of the data points. Hence, the positions of the start and end points of all profiles were measured using DGPS. The intermediary measurement points were obtained through constant interval interpolation, based on constant walking pace maintained during the survey. The choice of the HCP configuration was based on its capability to image layered media, to maintain a high signal to noise ratio and the visually simpler nature of anomalies on EM profiles (Frischknecht et al., 1991; Won et al., 1996).

Importantly, the GEM-2 system deployed in this work has not been calibrated. Hence the absolute values of the readings taken are not reliable and thus it is not possible to generate correct Earth models through inversion. However, the maps showing spatial variations is suggested to provide good overall qualitative information (Won et al., 1996). Accordingly, the EM data in this work was analyzed using simple gridding of inphase and quadrature responses at different frequencies to understand regions with anomalous responses (Won et al., 1996; Huang and Fraser, 2000), and also profiling for a few prominent EM anomalies (Frischknecht et al., 1991).

Figure 5.2: Combined layout of GEM2 survey at Wishingwell Park (white=phase I and black=phase II).

5.3 Data Analyses and Interpretations of Electromagnetic Survey

As mentioned in Chapter 3, the study area hosts a lot of anthropogenic features such as metallic soccer goals, rugby posts, aluminum bleachers (gallery for rugby and baseball spectators), copper electric cables (sport lighting), metallic chain-link fences and a few buildings (see Figure 3.6). These are inevitable sources of cultural noise which could affect electromagnetic responses from subsurface target(s) (Dentith and Mudge, 2014). EM data were accordingly checked for possible signals from those anthropogenic features. The metallic soccer goals and one of the aluminum bleachers in the area have evidently affected the electromagnetic measurements significantly. The inphase responses from these existing features are shown as profiles in Figure 5.3. From this figure, it is clear that these above-ground anthropogenic metal features give large and localized signals, by at least a factor of 3 (for 39030 Hz) and about 4.5 (for 6210 and 990 Hz) compared to the surrounding amplitude in the area, with all of the three frequencies responding in the same manner. The building in the south-eastern corner of the survey area has moderately affected the measured data.

The sample grids of the raw EM data, without removing the influence of soccer goals, bleacher and building, using both the inphase and quadrature responses for 990 Hz, is shown in Figure 5.4 (maps for the other two frequencies are given in Appendix C). The signals from these features are clearly shown. These localized responses vary from the general background inphase responses and responses likely from anomalies (buried waste) in the area. Thus, these localized responses were removed from the data-set before further mapping.

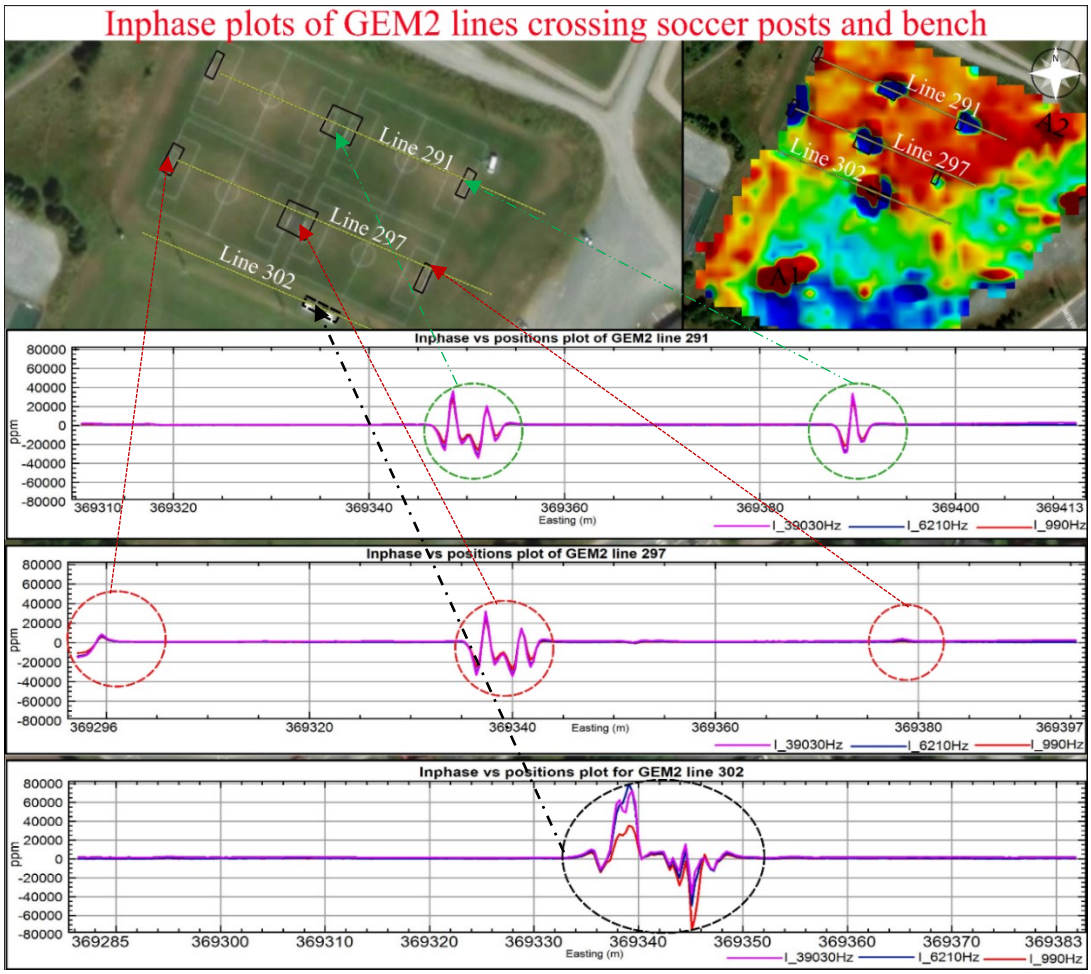

Figure 5.3: Effects of anthropogenic features on the inphase responses in the study area (Lines 291, 297 and 302 are the GEM2 survey lines).

Similarly, the maps for both the inphase and quadrature responses for the corrected electromagnetic data, for all three frequencies, were prepared using a grid size of 5 m and are shown in Figure 5.5, Figure 5.6 and Figure 5.7. As depicted in the quadrature grids, quadrature responses are dominant in the southern, south-eastern and south-western parts of the area. These regions predominantly include the car parking and the access road in between the soccer and rugby fields. Interestingly, ground surfaces in these regions are made up of medium-to-coarse granitic gravels compacted with soils, forming comparatively drier surface with significant portion of the access road, with gravels on top, being partially covered with thin patches of grasses. The quadrature is probably

indicating the difference in conductivity and hence composition of the immediate near-surface layer across the survey area as shown in Figure 5.5b, Figure 5.6b and Figure 5.7b.

For the GEM-2 system, the lowest frequency, 990 Hz, can approximately probe the Earth down to about 6-8 metres while 6210 Hz and 39030 Hz can approximately probe down to about 4-6 metres and 0.5-3 m respectively (Huang, 2005; Won et al., 1996). Figure 5.5a shows the inphase variation pattern from the deeper part of the area. For the lowest frequency data, the map probably starts exhibiting a few trench-like linear features which are seen in the magnetic data at about 6-7 metres down in the subsurface (see Section 3.3). Similarly, Figure 5.6a shows almost the same pattern of inphase variations as in Figure 5.5a. These two data-sets are probably indicating the presence of linear trenches hosting waste. In both of these data-sets, the trench-like features are more pronounced over the soccer field with few localized anomalies over the rugby field, similar to the vertical gradient observations in the magnetic survey.

From the maps mentioned above, there are a few regions with strong signal in both the inphase and quadrature at all three frequencies in the same locations as the strong magnetic anomalies. The EM anomalies here are indicated by **A1** and **A2** which correspond to the magnetic anomalies identified as **MA1** and **MA7** respectively in Chapter 3. The anomaly **A1** was further isolated and examined by plotting profiles of the inphase data as shown in Figure 5.8.

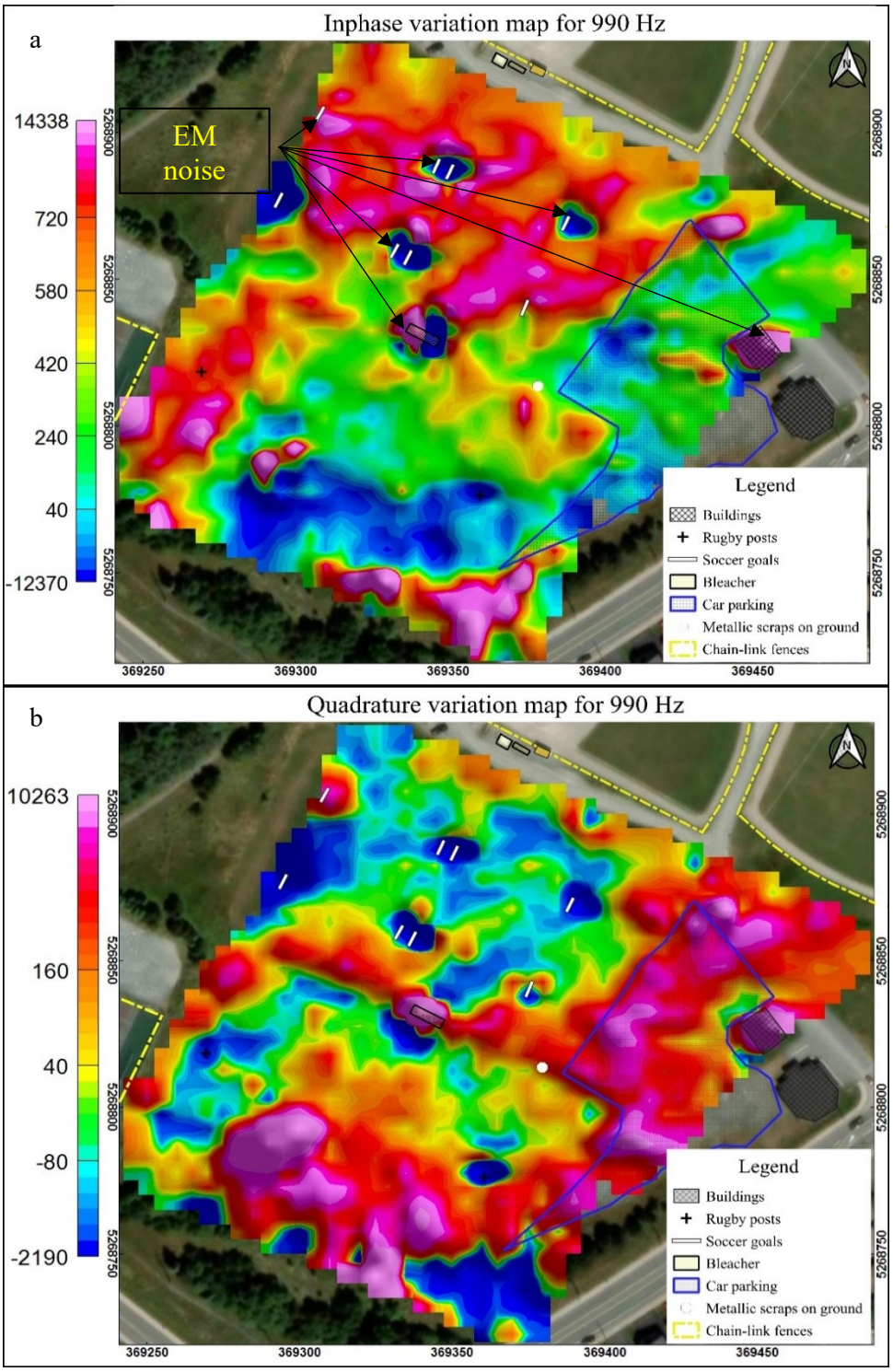

Figure 5.4: Raw-gridded electromagnetic responses for frequency of 990 Hz. Inphase (a) and quadrature (b) (minimum curvature method was applied with a grid size of 5 m in Oasis Montaj).

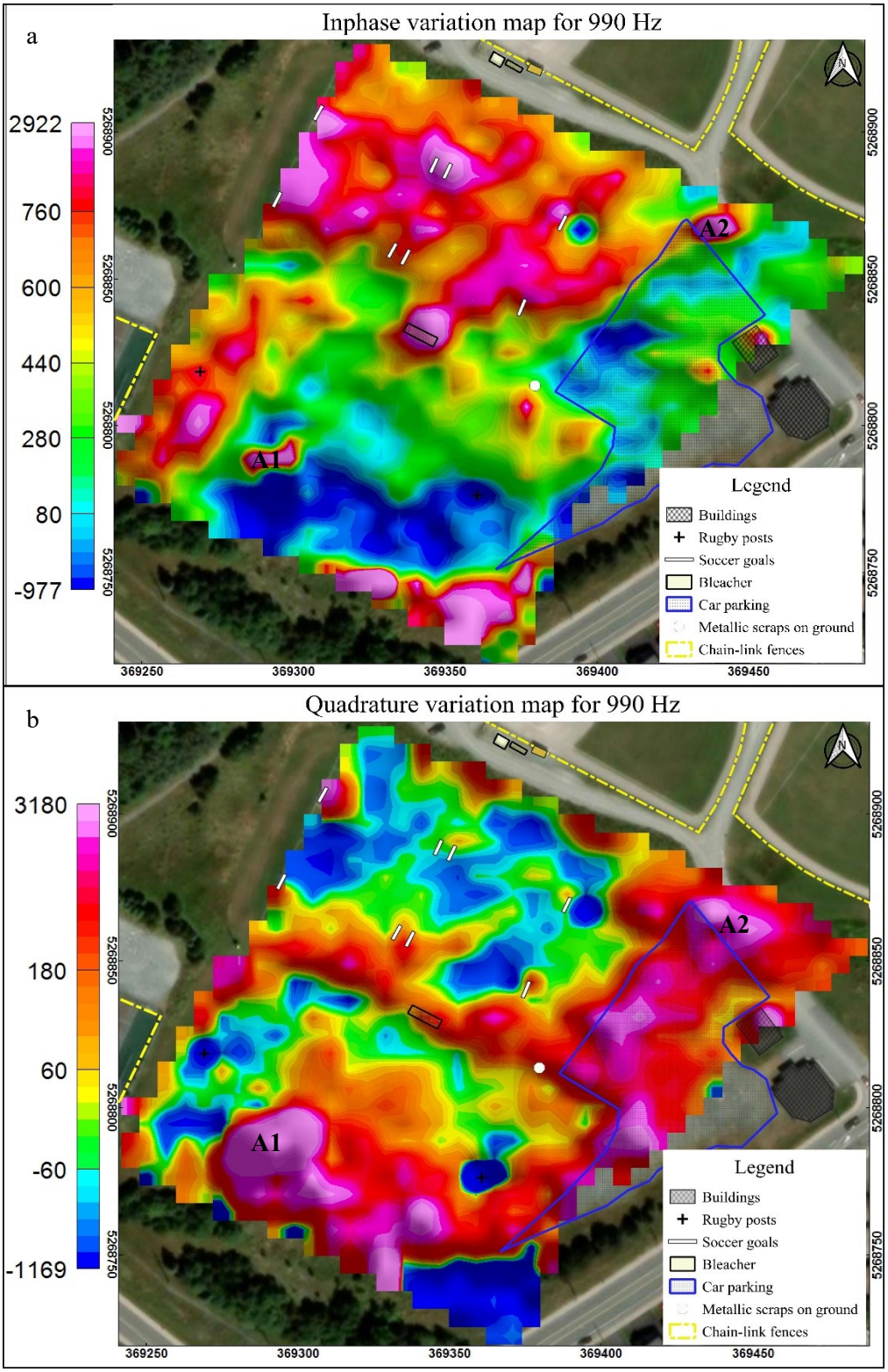

Figure 5.5: Gridded electromagnetic responses for transmitter frequency of 990 Hz. Inphase (a) and quadrature (b).

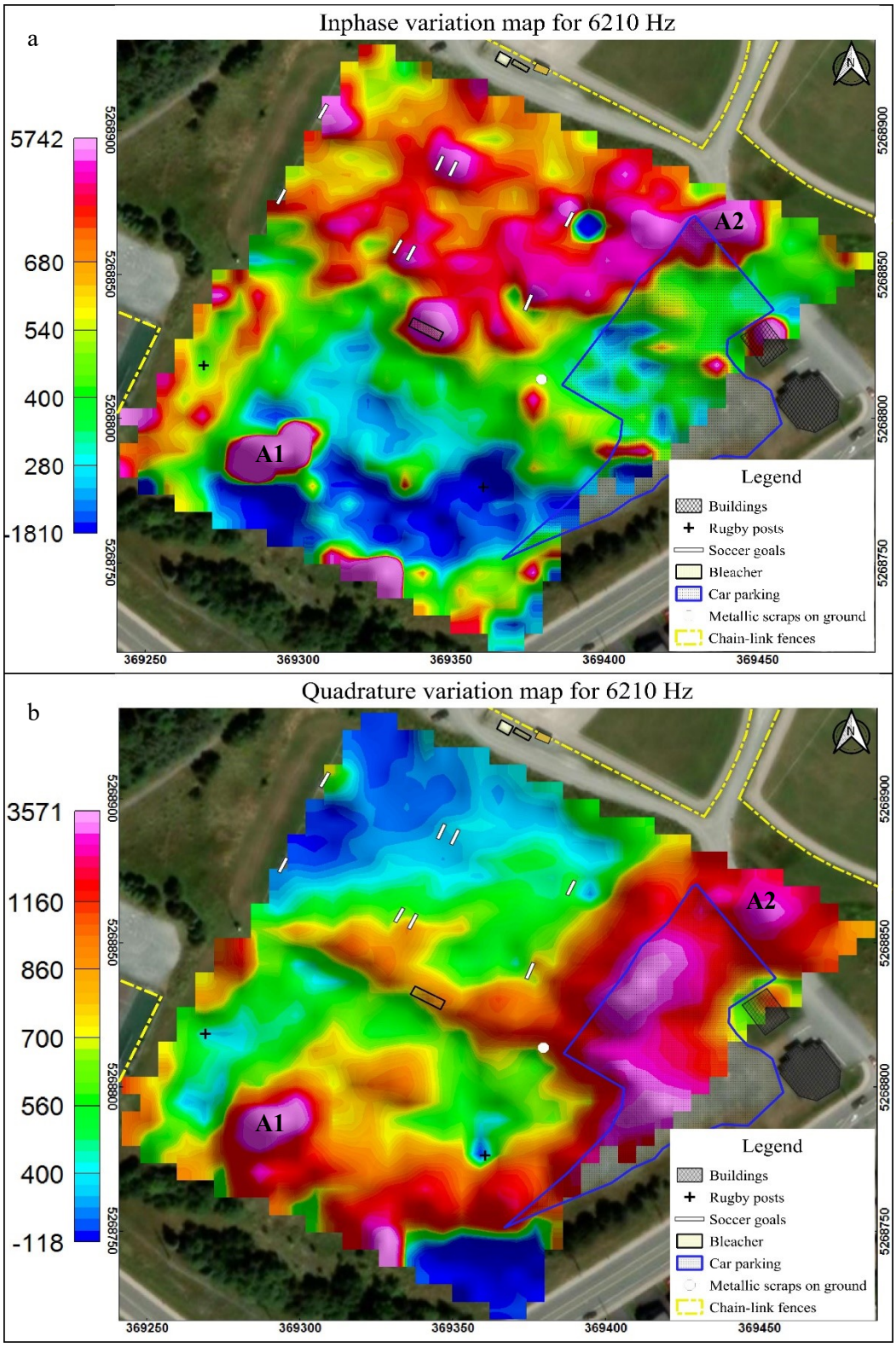

Figure 5.6: Gridded electromagnetic responses for transmitter frequency of 6210 Hz. Inphase (a) and quadrature (b).

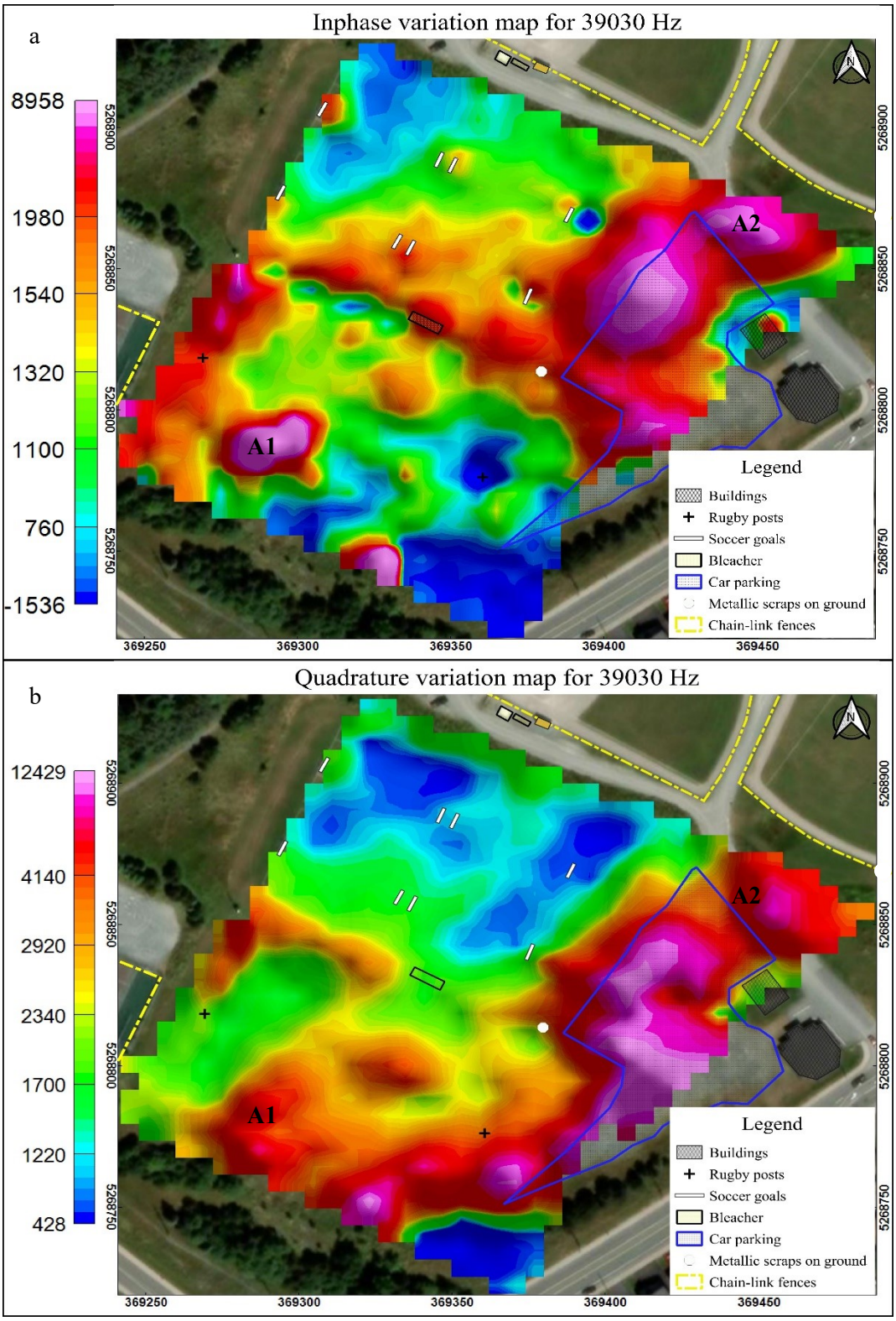

Figure 5.7: Gridded electromagnetic responses for transmitter frequency of 39030 Hz. Inphase (a) and quadrature (b).

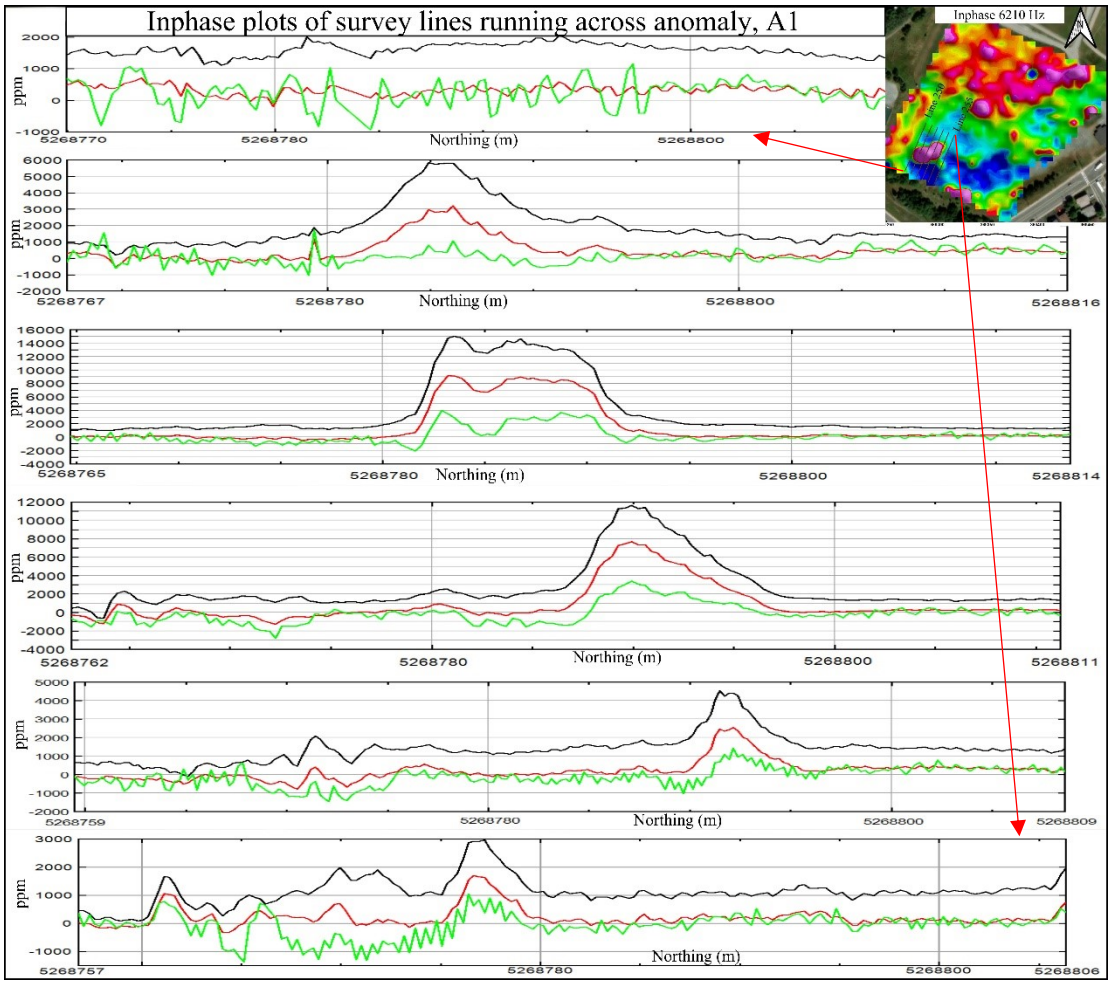

*Figure 5.8: Spatially aligned inphase profile running across the anomaly, **A1**.*

(990 Hz=green line, 6210 Hz=red line and 39030 Hz= black line).

Figure 5.8 clearly depicts a strong (inphase) response over anomaly **A1**. This likely suggests that there is a very good conductor here, most likely some things that are metal, that are more conductive than the natural ground. The anomaly **A1** trends WSW-ENE with the spatial spread of about 20-30 metres, as evidenced in the magnetic data as well (see Chapter 7).

Similarly, another prominent EM anomaly **A2** was singled out and examined here. The profile plots running directly across the anomaly **A2** are shown in Figure 5.9. The inphase profile across the anomaly **A2** is typical of a buried 3D prismatic body with the

intermediate-to-high conductivity contrast with the surroundings (Frischknecht et al., 1991, Fig.53a). However, the peak inphase responses over this anomaly are only about half the peak responses from anomaly **A1**. There is another anomaly close to the anomaly **A2** (red dashed-line) which is likely dipping in nature. The anomaly trends roughly WSW-ENE with a spatial spread of about 4-6 metres and lies exactly over the paved access road.

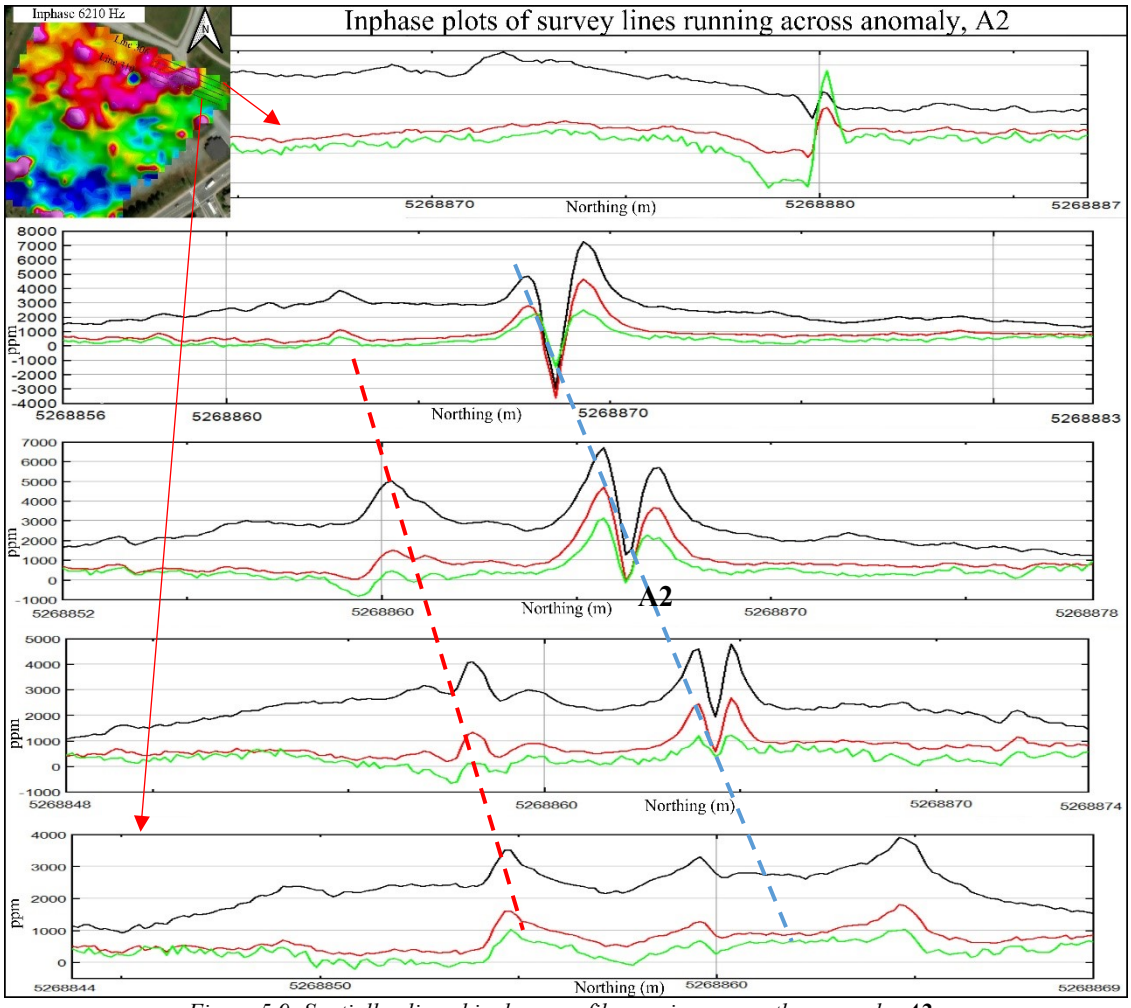

*Figure 5.9: Spatially aligned inphase profile running across the anomaly, **A2**.*

(990 Hz=green line, 6210 Hz=red line and 39030 Hz= black line).

Most of the linear trends that do exist in the inphase data, particularly for 990 Hz, coincide with the linear trends in the magnetics and the geoelectrical observations. This helps corroborate the probable presence of remnant metallic waste distributed across the

entirety of the area within a network of trenches, as opposed to only the one trench conjectured by Garland (2006). Detailed and integrated interpretations are given in Chapter 7.

Chapter 6: Ground Penetrating Radar Survey

6.1 Basic Principles

Ground Penetrating Radar (GPR), also known as georadar, is a type of electromagnetic (EM) method. It works on the principle of higher-frequency propagating electromagnetic waves, unlike induction (diffusion) and geoelectrical methods (Barker et al., 2007). It mostly operates on the basis of contrasts in a particular physical property of a medium or a target called the dielectric constant, in particular the relative dielectric permittivity (Ulaby, 2001; Barker et al., 2007). The relative permittivity is an ability of a material to store and then transmit the imposed electromagnetic energy (Barker et al., 2007). Good media for an ideal GPR survey range from the lossless to low-loss dielectric media with the target/s having very good contrast with the media.

Not only is the GPR response dependent on the relative permittivity but also electrical conductivity, which affects GPR responses by dampening a GPR signal. According to Maxwell's equations, the total electric current constitutes (i) conduction current and (ii) displacement current. The displacement current is the time rate of change of electric displacement field while the conduction current is the flow of moving charges. Either current can be dominant depending on the values of relative permittivity, conductivity and frequency. Importantly, for GPR waves, it is the displacement current which should dominate the conduction current.

In order to have the displacement current dominate over the conduction current, we need the conductivity to be small, the dielectric permittivity to be large and the frequency to be large (Ulaby, 2001). The frequency must exceed a transition frequency limit, a threshold frequency of a medium below which the EM waves undergo induction and energy diffusion, of media/targets (Barker et al., 2007). As we keep increasing the frequency, the signal dampening increases. Moreover, the amplitude and attenuation characteristics of

the radio waves depend on the electrical conductivity (leads to ohmic dissipation loss) (Ward and Hohmann, 1988; Ulaby, 2001; Baker et al., 2007; Cassidy, 2009). Hence, GPR survey usually is a trade-off. As the conductivity of the Earth remains largely unchanged, the trade-off in GPR is primarily between depth of penetration and the overall resolution (an ability to distinguish the reflection from the top of a layer from the reflection from the bottom of the layer) which is the function of the operating frequency.

According to Barker et al. (2007), the propagation velocity of the GPR wave essentially depends on the dielectric permittivity of media/targets. The propagating velocity affects the wavelength of the propagating EM wave. The propagation velocity and dielectric permittivity of common materials is tabulated in Table 6.1.

Table 6.1: Relative permittivity values and EM wave velocity for some common geological materials (Barker et al., 2007; Sensors and Software Inc., 2022).

Serial Number	Material type	Relative Permittivity (ε_r)	Velocity (m/ns)
1	Air	1	0.3
2	Fresh water	80-81	0.03
3	Sea water	80-81	0.03
4	Sand, dry	3-6	0.12-0.17
5	Sand, wet	10-30	0.05-0.09
6	Clay, dry	2-6	0.12-0.21
7	Clay, wet	15-40	0.05-0.08
8	Silts	3-30	0.05-0.13
9	Soil, sandy dry	4-6	0.12-0.15
10	Soil, sandy wet	15-30	0.05-0.08
11	Soil, clayey dry	4-6	0.12-0.15
12	Soil, clayey wet	10-15	0.08-0.09
13	Soil, loamy dry	4-6	0.05-0.08
14	Soil, loamy wet	15-30	0.07-0.09

The primary thing of concern in GPR survey is the reflection of the EM wave off an interface between materials of different wave speeds. The resolvability, i.e., whether or not one can make out the reflection from the top of a layer from the reflection from the bottom of the layer, depends on the wavelength of the EM wave. Hence, the shorter the wavelength the thinner a layer (or smaller a feature) we can distinguish the reflection from the top and bottom from. Figure 6.1 shows a schematic diagram demonstrating the working mechanism of a GPR survey, in the commonly used bistatic configuration, using a transmitter antenna (Tx) and a receiver antenna (Rx) in reflection mode. As depicted in Figure 6.1, a GPR survey concerns only the reflection of radio waves off any geophysical targets (point reflectors or layers) and their signatures (hyperbola or linear continuous band) in the GPR profile.

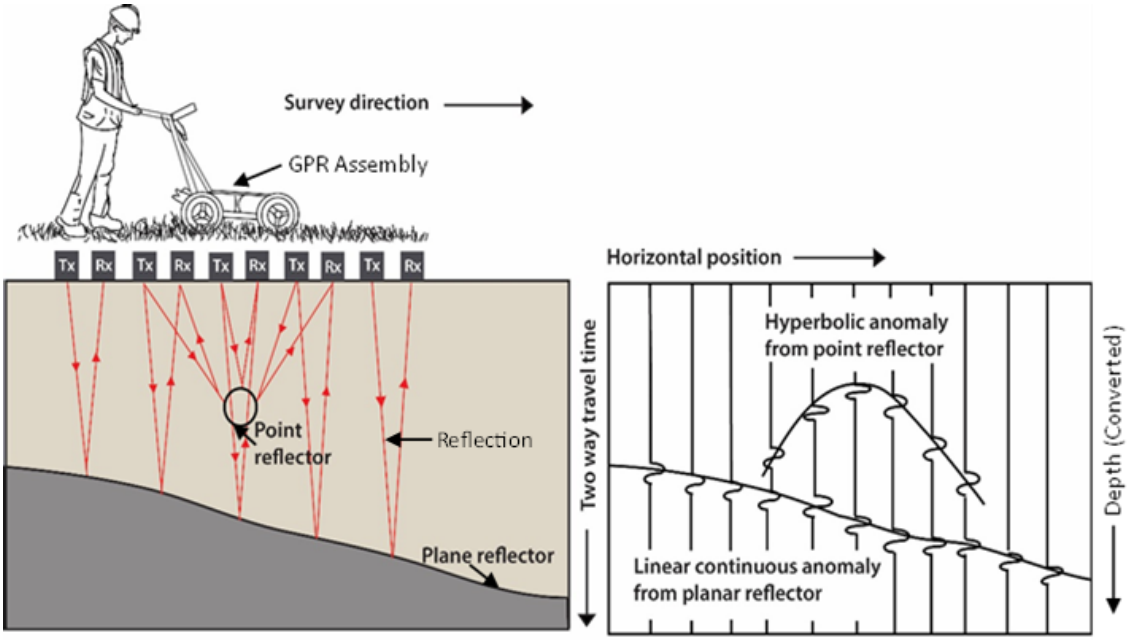

Figure 6.1: Diagram showing typical reflections in a GPR survey and how they appear in the data that are recorded. (After Scantech Geoscience, 2018.)

One of the crucial aspects of a GPR survey, like any other geophysical method, is knowing how deep it can probe the Earth with good resolution. The depth of investigation in GPR is most commonly expressed in terms of 'skin depth'. Thus, for non-ferromagnetic materials, the depth of investigation is inversely proportional to square

root of product of the conductivity and the operating frequency. Given the very high frequency generally used in GPR surveys, such that the displacement current dominates the conduction current, it usually leads to shallow depth of exploration (Ulaby, 2001), although GPR can be used to explore several kilometers depth especially in ice. For a given conductivity, its skin depth can be increased by using lower frequency system but at the expense of resolution. The skin depth estimates for some common geologic materials are given in Table 6.2.

Table 6.2: Typical conductivity values for common geologic materials and approximate skin depths (Sensors and Software Inc., 2022).

Serial Number	Material type	Conductivity(mS/m)	Skin depth(m) (best cases)
1	Air	0	∝
2	Silt	20	2
3	Clay	50	1
4	Gravel	2	20
5	Sand, wet	2	20
6	Sand, dry	1	40
7	Ice/snow	0.1	>400
2	Fresh water	low TDS-high TDS	40-0.5
3	Sea water	400-4000	0.01

Moreover, the efficacy of a GPR survey to resolve targets of interest is dependent on the type of antennae (transmitter and receiver) used and their polarization orientation (directivity) (Daniels, 2000; Annan, 2009; Barker et al., 2007). Annan (2009) concluded that the directivity of GPR antennae is largely a function of subsurface conditions and ground roughness (undulations) of a survey area. Hence, the final decision to choose the right GPR system suitable for resolving geophysical target(s), though not a straight-forward task (Utsi, 2017), is the primary responsibility of a geophysicist/surveyor.

6.2 Field Survey Methods

For this research, a robust and shielded PulseEkko Pro system from Sensors and Software Inc. was used for data collection. This instrument is designed as a center-fed, broadside perpendicular antennae system using the bistatic configuration. This antennae configuration corresponds to the highest signal to noise ratio and is the most commonly used (Daniels et al., 2003). The transmitter and the receiver are arranged with an antennae separation of 38 cm with the transmitter capable of transmitting a broadband signal with the central frequency of 250 MHz. The whole assembly was mounted on a Smartcart with 4 wheels. An odometer wheel was used to determine distances along traverses. The other parameters that were used were: a time window of 90 nanoseconds (ns), a step size of 0.05 m, a sampling rate of 0.67 ns and the system set to the reflection survey mode. Stacking was set to 'DynaQ', whereby the instrument calculates the maximum number of stacks based on the speed of the traverse. Images of various components of the PulseEkko Pro system are shown in Appendix D.

A total of 35 GPR profiles, running roughly north-west to south-east in the study area, were acquired along parallel lines with a separation of about 5 m between lines covering the soccer and the rugby fields. The length of the GPR lines vary across the area. For ease and speed of operations, data acquisition was achieved by pushing the Smartcart back and forth in continuous manner. The orientation of the GPR lines were later corrected to make them consistent. The geographic locations of the start and end points of each GPR profile were acquired using DGPS and intermediate points were interpolated and plotted as shown in Figure 6.2. The GPR profiles are named XLINE 0 to XLINE 34, in east-west direction, as shown in Figure 6.2.

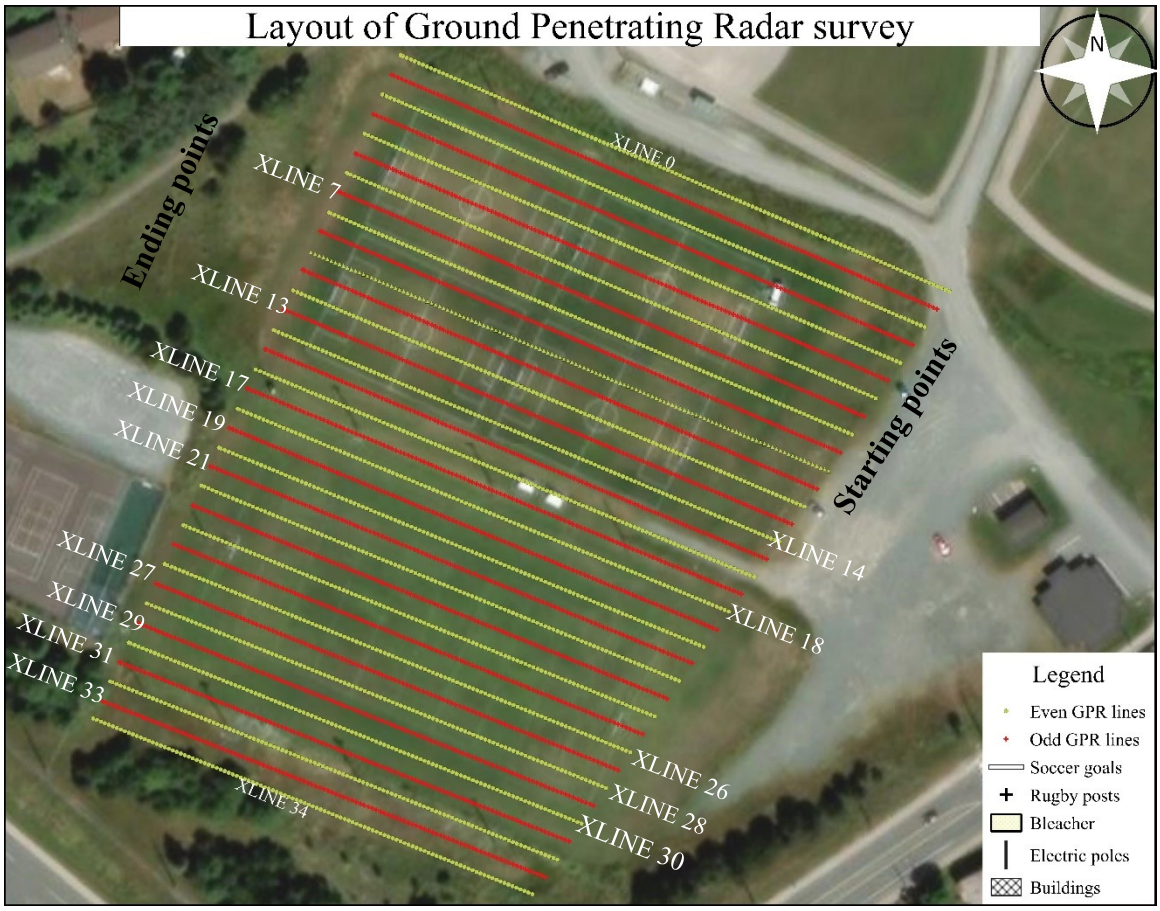

Figure 6.2: Layout of GPR survey at Wishingwell Park. Traverses discussed in this chapter are labelled.

As discussed in Chapter 3, the study area has numerous anthropogenic features of metallic nature such as soccer and rugby posts, bleacher and chain-link fences and overhanging electric lines. These features will likely influence GPR images and thus the broadside antennae orientation with high signal to noise ratio and the use of a shielded system were deemed necessary. However, the PulseEkko Pro system with the transmitter's central frequency of 250 MHz was the only system available, while the other transmitters of lower frequency are not operational. So, all the GPR data for this research are collected using the available system.

6.3 Data Analyses and Interpretations of GPR Survey

In this research, the ground penetrating radar survey was particularly used to produce very high-resolution subsurface images. This was driven by two ultimate goals—understanding the near-surface stratigraphy and mapping the spatial distribution of potential scatterers—as is generally the case in landfill investigations. Given the site conditions and the aforementioned objectives, each GPR profile was measured and represented as a 2D section, profile length and the two-way-travel time (TWT) as abscissa and ordinate respectively, with a finite number of stacked traces. This is equivalent to having a zero-offset seismic reflection section. Various basic GPR processing methods were applied to enhance the GPR sections for visualization as discussed below. The processing steps applied in this work are SEC2 gaining, dewow filtering, background subtraction, time-zero correction and topography correction (Cassidy, 2009; Dawrea, 2021). All these processing steps were done using EkkoProject (V5R3) from Sensors and Software Inc.

SEC2 gaining

A GPR signal attenuates linearly and exponentially (Cassidy, 2009; Sensors and Software Inc., 2021). This phenomenon is mainly attributed to geometrical spreading and ohmic dissipation losses associated with GPR signals (Cassidy, 2009). Hence, GPR signals need to be properly gained to compensate for all the losses. Hence, a gain scheme called 'Spreading and Exponential Calibrated Compensation' (SEC2 gain) is adopted in this work with the final parameters used being an attenuation rate of 5 dB/m, an initial again of 1.17 and a maximum gain of 145. The raw (ungained) and the gained GPR sections, using two sample GPR lines namely XLINE 29 and XLINE 30 running over the rugby field, are compared as shown in Figure 6.3 and Figure 6.4. In the raw signals, ground and direct air waves dominate the near-surface responses and the reflections from beyond about 30 ns are strongly attenuated as depicted in Figure 6.3a and Figure 6.4a. In Figure 6.3b and Figure 6.4b, interesting features from deeper depths were revealed through the

application of SEC2 gain.

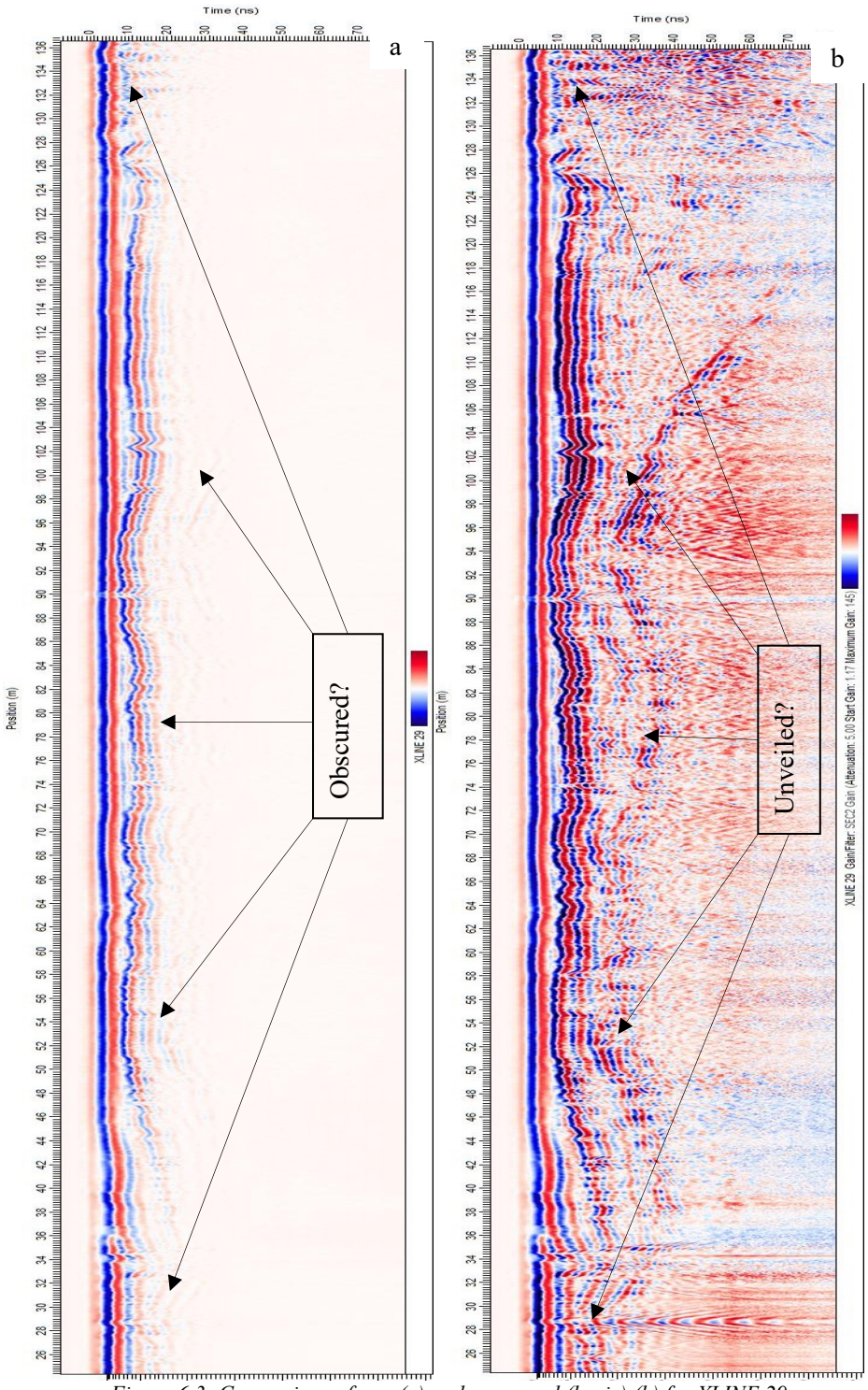

Figure 6.3: Comparison of raw (a) and processed (basic) (b) for XLINE 29.

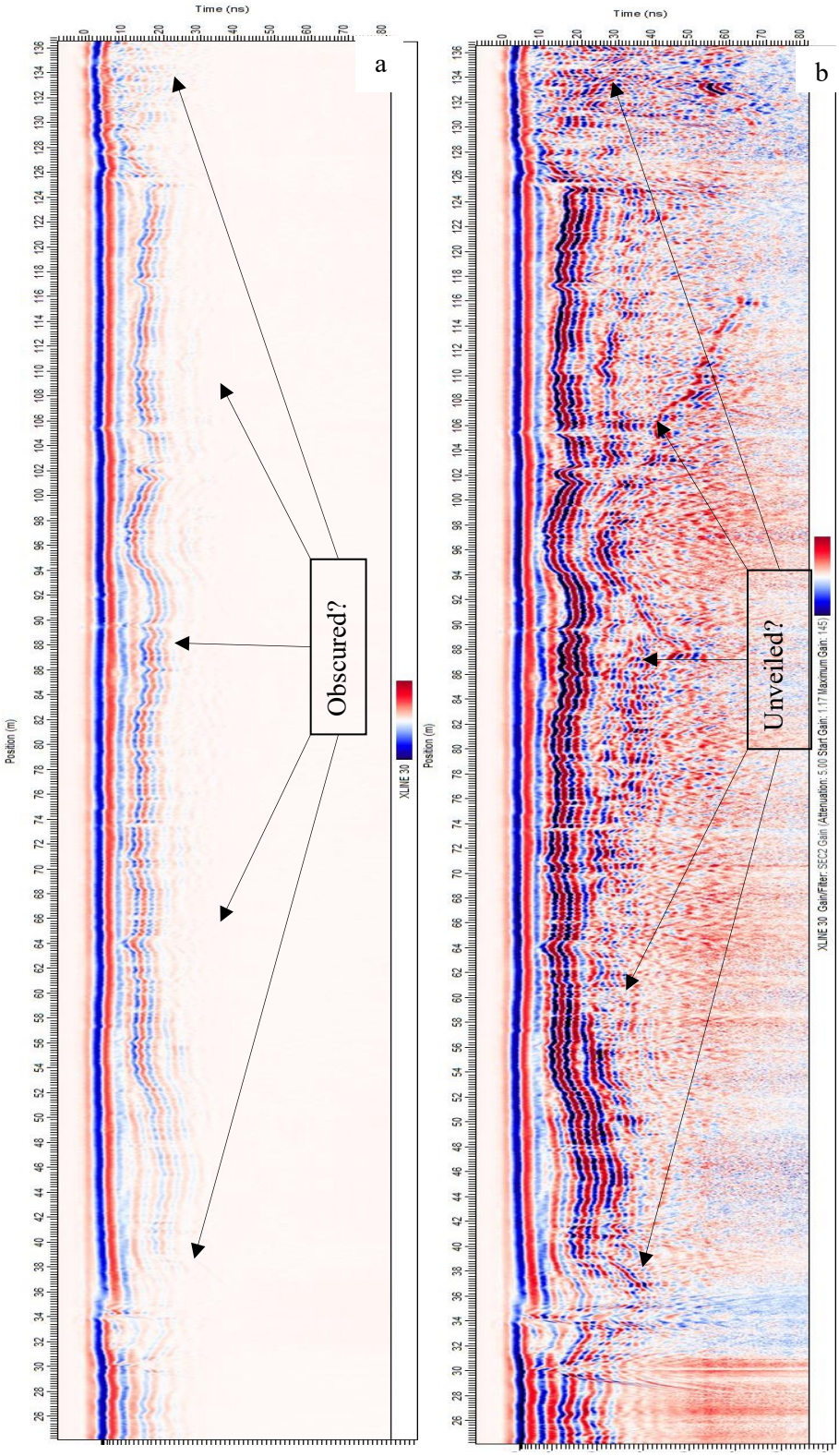

Figure 6.4: Comparison of raw (a) and processed (basic) (b) for XLINE 30.

Dewow filtering

Dewow filtering removes low-frequency 'wow', characteristically decaying slowly, from the high frequency reflections. The 'wow' occurs due to the early arrivals saturating the recorded GPR signal (Annan, 1993) and /or the inductive coupling effects which depend on ground conditions and the transmitter-receiver separation (Cassidy, 2009). In this work, all the GPR profiles contain 'wow' and a sample average frequency spectrum (AFS) plot is shown in Figure 6.5.

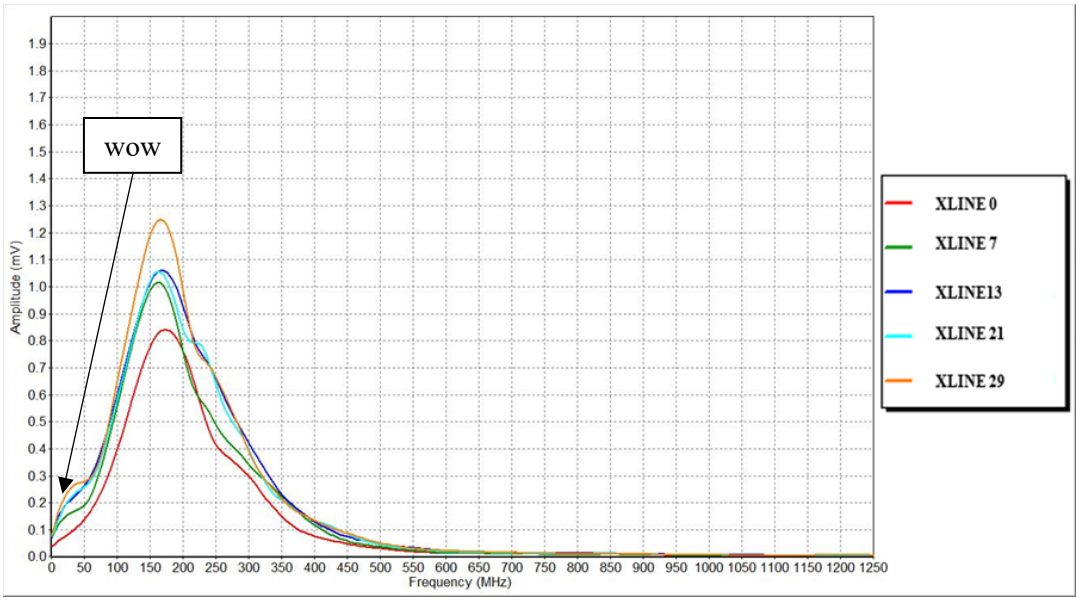

Figure 6.5: Average frequency spectrum plots, without dewow, of 5 GPR lines.

In Figure 6.5, there are clear 'wow' of significant amplitudes. Hence, the Dewow filter was applied to all the GPR profiles and the 'wow' was removed by first implementing a running average filter with a one-pulse width window, which is 1.5 cycles at the transmitter central frequency (Sensors and Software Inc., 2021). Then, the resulting average in a window was subtracted from the corresponding central point and the operation was carried out repetitively by successively moving by a point each time along each GPR trace until all the traces were completely corrected for 'wow'. The AFS plot after removing 'wow' is shown in Figure 6.6. Clearly, Figure 6.6 shows that the 'wow' has been removed from the data.

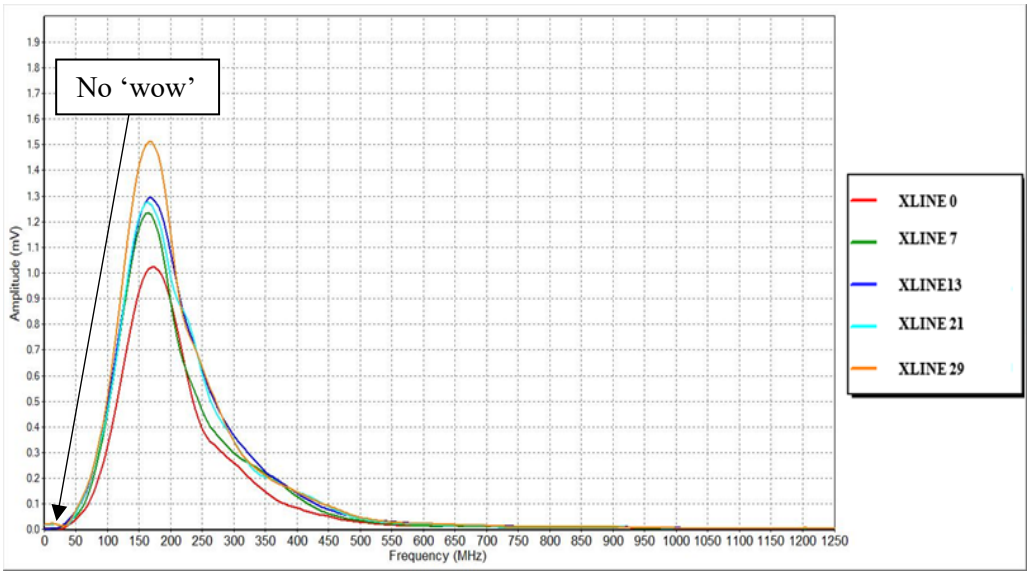

Figure 6.6: Average frequency spectrum plots, after dewow, for 5 GPR lines.

Background Subtraction filtering

Following the dewow filtering, a background subtraction filter was applied to the data. This filter applies a running-average background subtraction to the data using different filter widths. It helps remove strong direct air and ground waves from the GPR data. GPR profiles, in this work, show significant influence of the direct air waves. A sample comparison of a GPR section, XLINE 29, with and without the filter is as shown in Figure 6.7 using XLINE 29. Figure 6.7a shows the section with the air/ground wave (enclosed in dashed-black rectangular box).

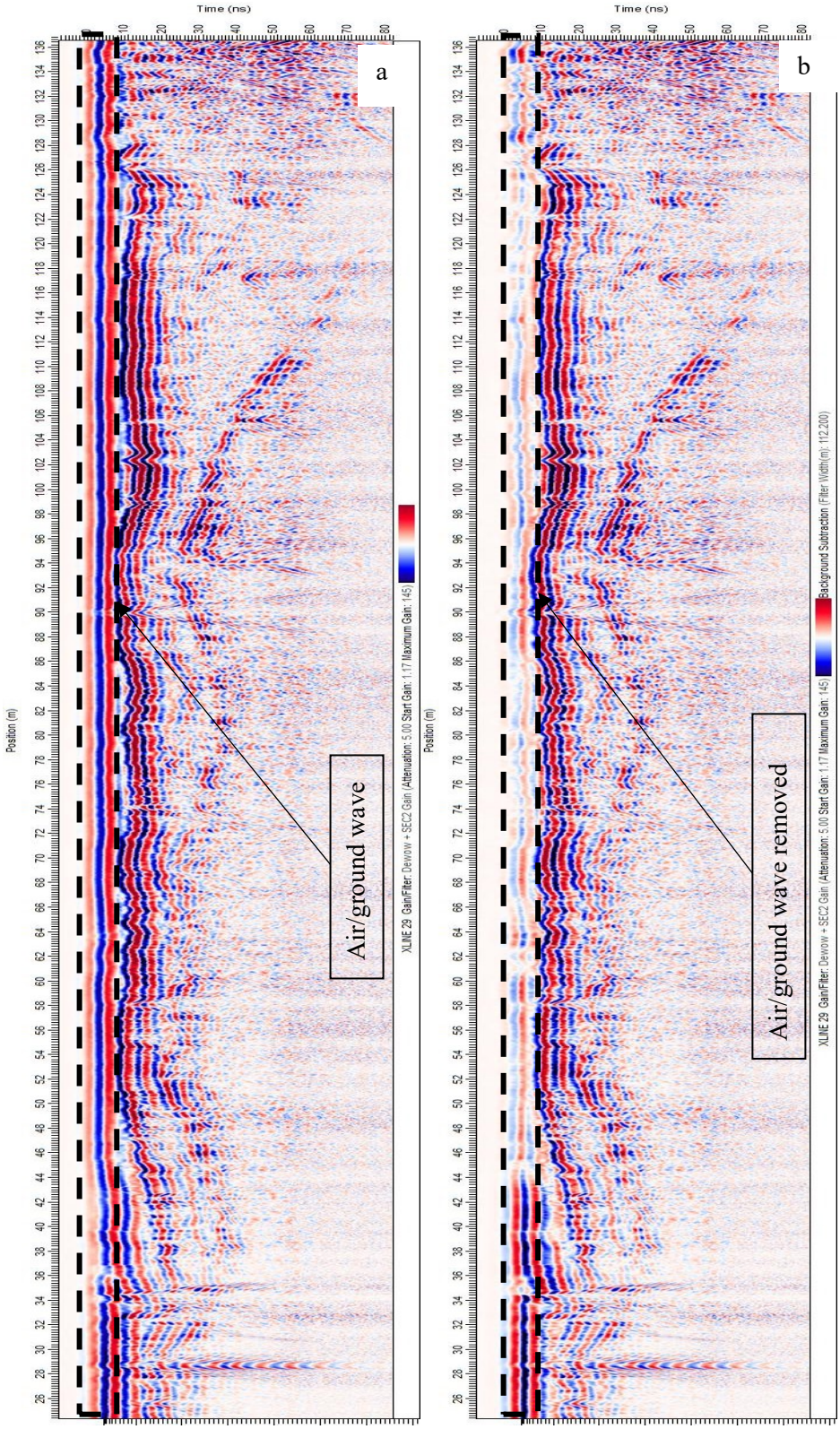

Figure 6.7: Comparison of XLINE 29 without (a) and with (b) the background subtraction filter.

Here, the background subtraction filter was applied to all GPR data using a running-average of the 'full-length' window, i.e., along the entire length of each GPR profile. Figure 6.7b shows the same GPR section after background subtraction filtering (with dewow and gain applied). Clearly, the filter effectively removed the air/ground waves from the section.

Time-zero correction

Time-zero errors occur in GPR signals mainly due to antennae air-gap, electronic instability and thermal drift (Cassidy, 2009). Hence, a recorded GPR section depicts 'jumps' in the first arrival of the air/ground wavelet leading to deviations in the time sequences of later reflections and signal polarity with respect to the surrounding traces. Hence, GPR traces need to be corrected for the time-zero effect to synchronize each trace in time, i.e., having a common time-zero position. Here, all the recorded GPR profiles clearly exhibit some time-zero effects.

A sample comparison of a GPR section, XLINE 29, with and without the time-zero correction (dewow, background subtraction and gain applied) is depicted in Figure 6.8. Figure 6.8a shows the section with the time-zero effect. Clearly, a significant amount of time-zero variability is exhibited by the GPR data-set and the correction is applied to all the sections. Here, the time-zero correction was carried out by setting time limit to zero using EkkoProject (V5R3). The time-zero corrected section is shown in Figure 6.8b.

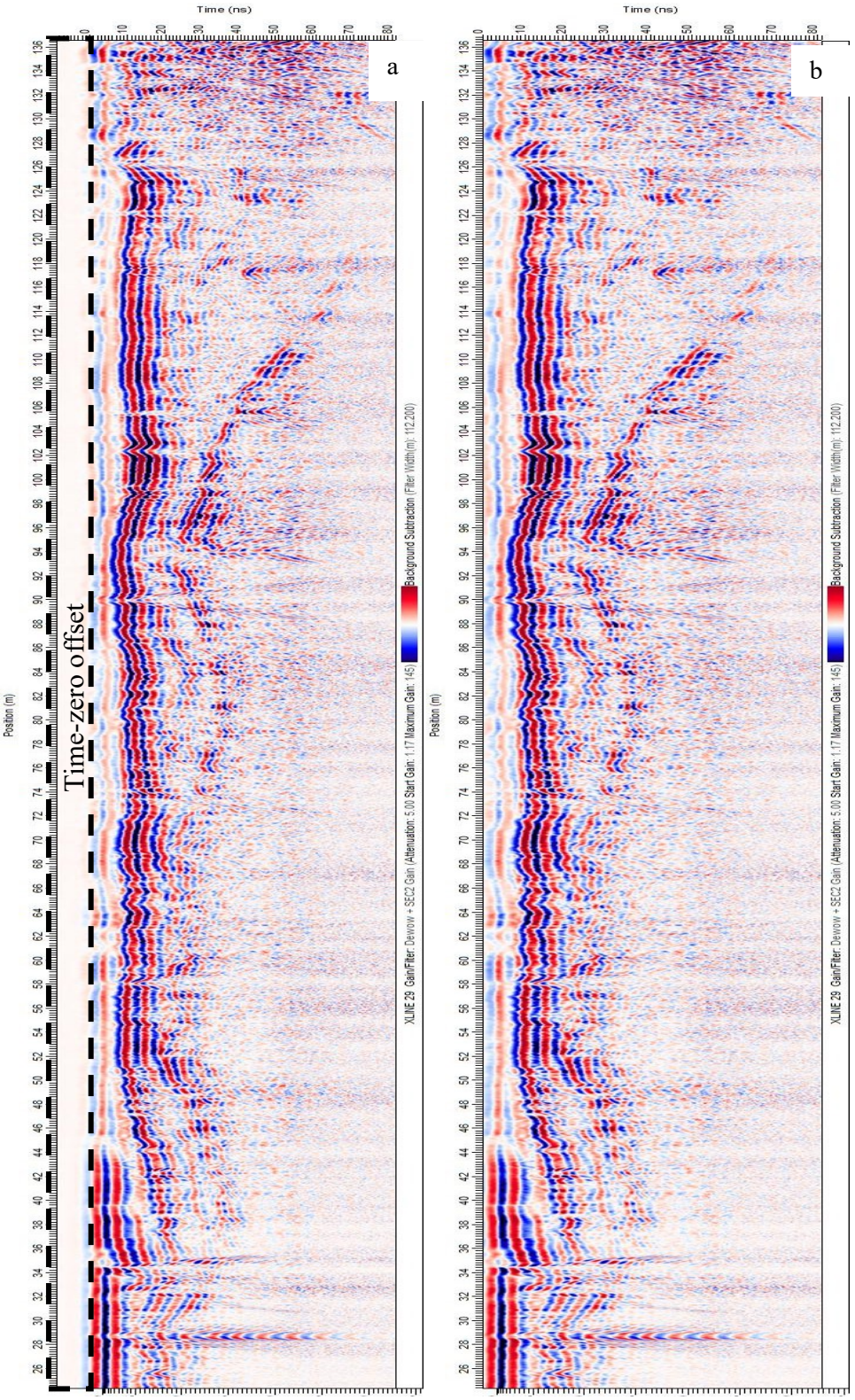

Figure 6.8: Comparison of XLINE 29 without (a) and with (b) the time-zero correction.

Topographic correction

Following the time-zero corrections, numerous authors (e.g. Cassidy, 2009; Utsi, 2017) suggest the necessity of doing topographic corrections to rule-out possibilities of GPR artefacts due to the presence of significant topography. Accordingly, although no significant topographic variations exist in the area (see Appendix E), the topographic corrections were carried out for all the profiles. A sample comparison of a GPR section, XLINE 29, with and without the topographic corrections (dewow, background subtraction, time-zero correction and gain applied) is depicted in Figure 6.9. Figure 6.9a depicts the section without the topography correction and Figure 6.9b after the topography correction. The effect of topography can be clearly observed in the GPR section as indicated.

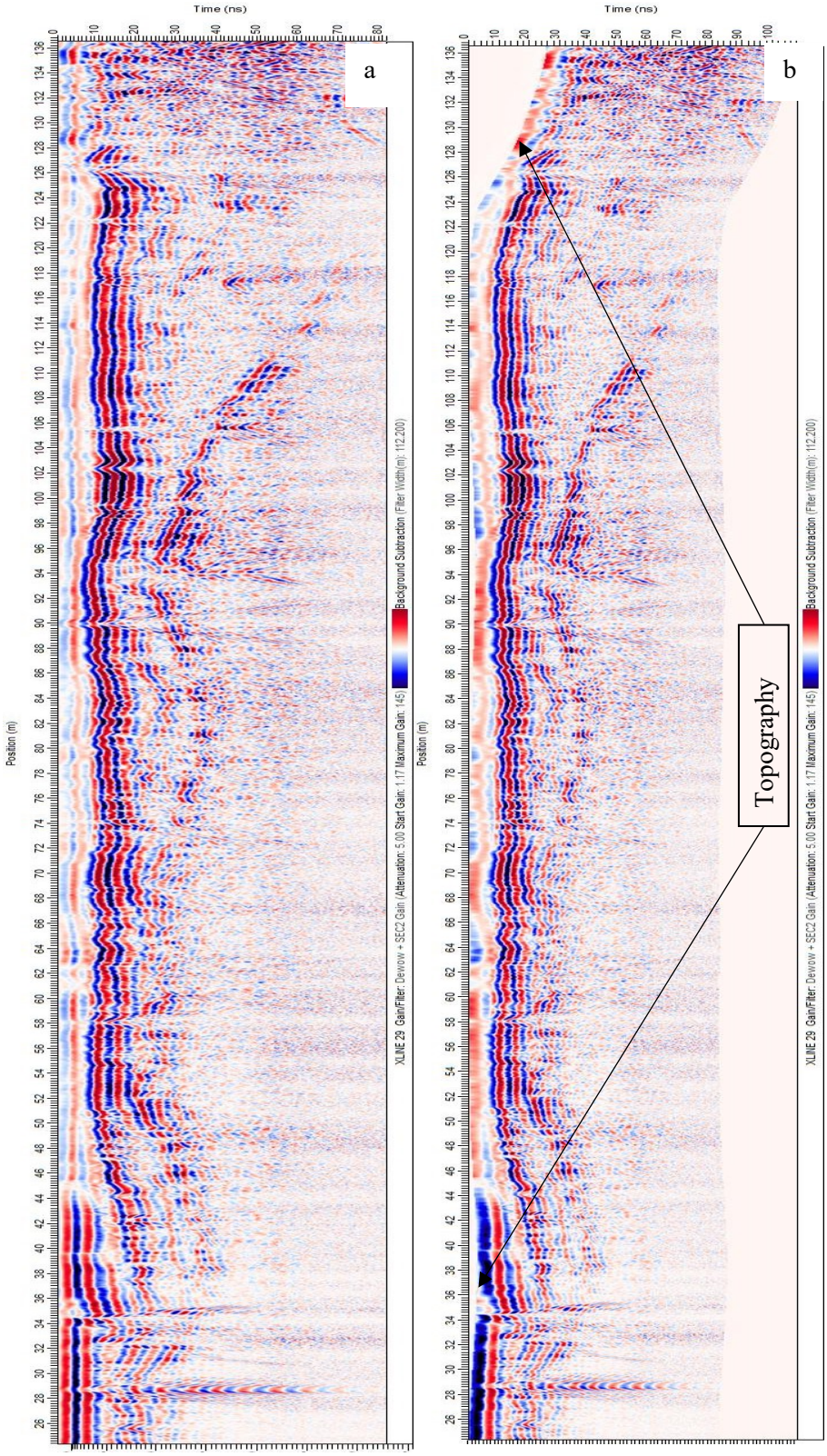

Figure 6.9: Comparison of XLINE 29 without (a) and with (b) the topography correction.

Velocity calibration

For any type of GPR investigation, knowing the correct propagation velocity is important yet not straightforward (Utsi, 2017). This is because the propagation velocity depends on the dielectric properties of the medium, which in turn affects the resolvability of GPR targets and the conversion from a time section to a depth section for physical interpretations (Barker et al., 2007). Hence, velocity calibration constitutes a crucial step in GPR image processing (Cui et al., 2018; Utsi, 2018). There are two popular approaches to this end – field-based and empirical calibrations (Utsi, 2017). Field-based techniques to calibrate velocity include common mid-point (CMP) and wide-angle reflection and refraction (WARR) methods (Cui et al., 2018; Sensors and Software Inc., 2021). These are considered comparatively better methods as these involve actual field observations. However, these field-based methods demand more measurements using separate transmitter and receiver with varying antennae separations or sometimes it involves periodically recurring GPR surveys to ensure good velocity estimations. Hence, these methods are uneconomical and time consuming. The empirical calibration methods such as hyperbolic velocity calibration and cross-correlation are in common use. Of the two, the hyperbolic velocity calibration method has been proven to be the better scheme (Cui et al., 2018). For this work, given the time constraint and resource limitations (no separate Tx and Rx), the hyperbolic velocity calibration was chosen which is suitable for a single Tx-Rx separation (38 cm, here).

The hyperbolic fitting was carried out for all the profiles using EkkoProject (V5R3). Figure 6.10 shows a sample of hyperbola fitting done for two GPR sections, XLINE 29 and XLINE 30. For each profile, two prominent hyperbolas were fitted. The resulting propagation velocities for all the GPR profiles were averaged, obtaining the mean velocity of 0.08 m/ns, as the propagation velocity in the area with the standard deviation of 0.006 m/ns. Hence, all the GPR sections in time were converted to corresponding depth sections. Hence, the approximate vertical and horizontal resolution of GPR sections here is about 0.08 m and 0.490 m respectively using the formulae from Sensors and

software Inc. (2016) where vertical resolution is taken as quarter of wavelength and the horizontal resolution is the root of half of the product of depth and wavelength.

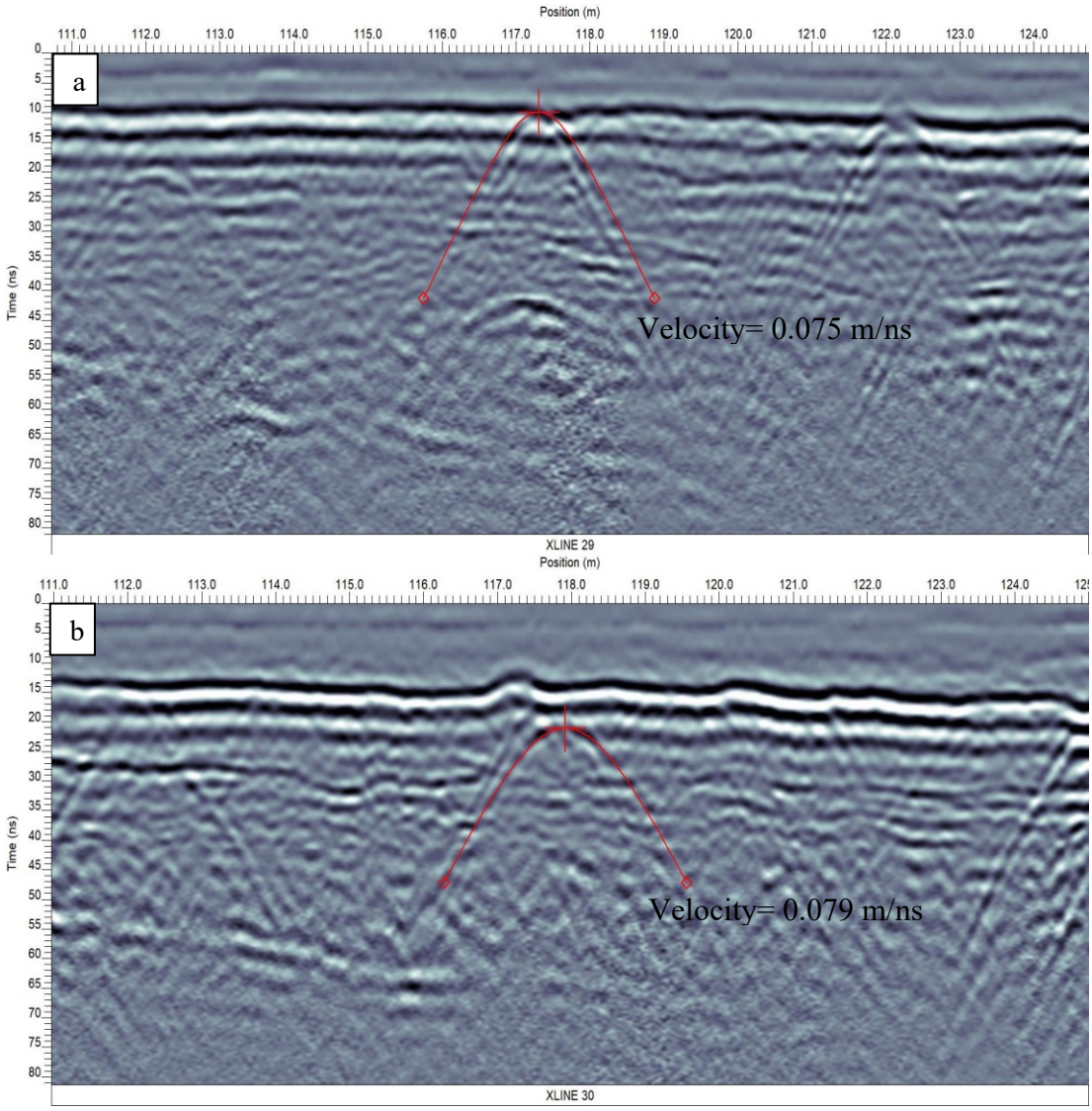

Figure 6.10: Hyperbola fitting to calibrate propagation velocity using all the above processing steps for XLINE 29(a) and XLINE 30(b).

All the processing steps discussed above were applied to all the GPR sections. Figure 6.11 shows the processed GPR sections, XLINE 7 and XLINE 29, depicting the reflection events over the soccer and rugby fields and Figure 6.12 depicts GPR responses in the periphery of these two playing fields.

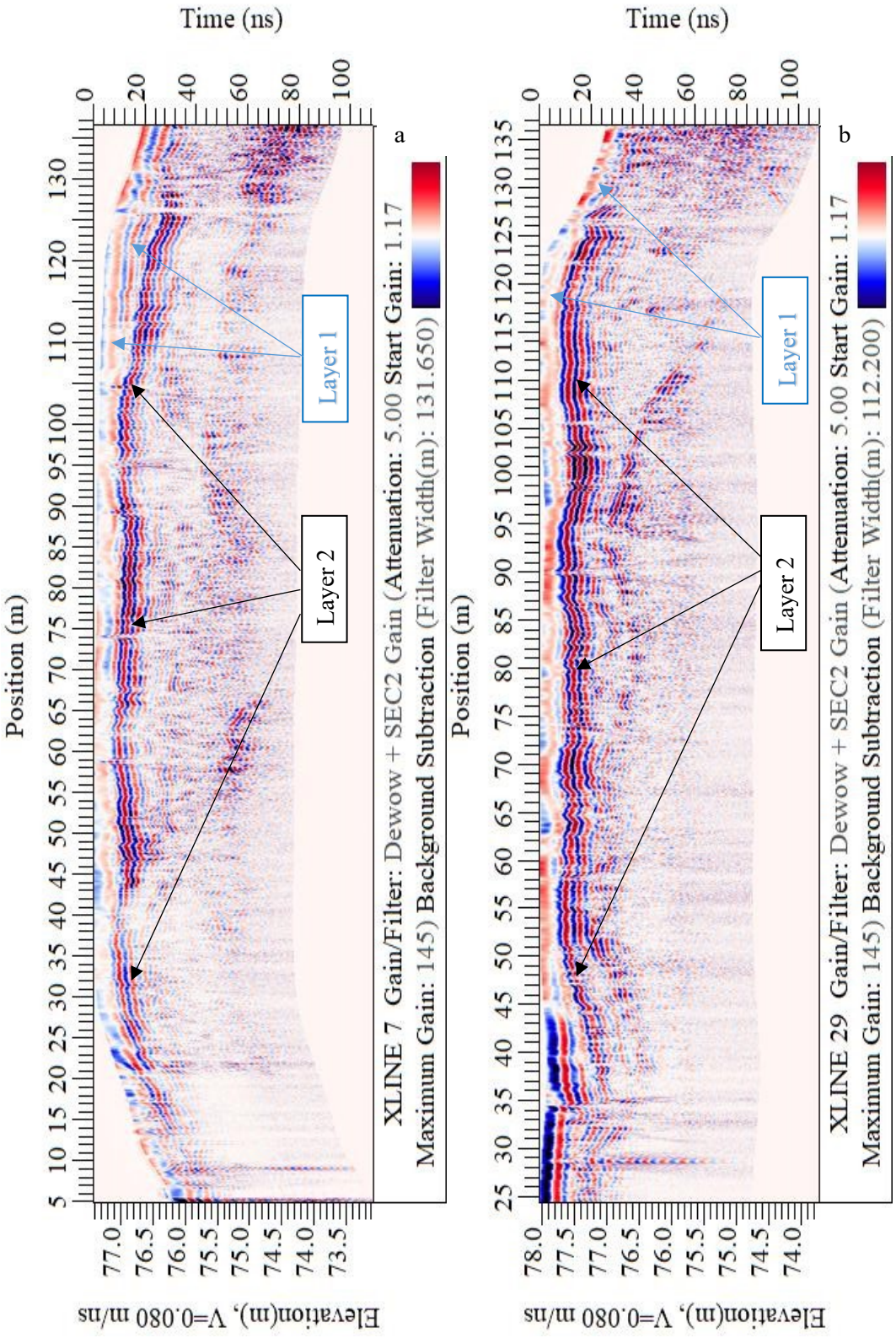

Figure 6.11: GPR responses over the soccer and rugby fields using XLINE 7 (a) and XLINE 29 (b).

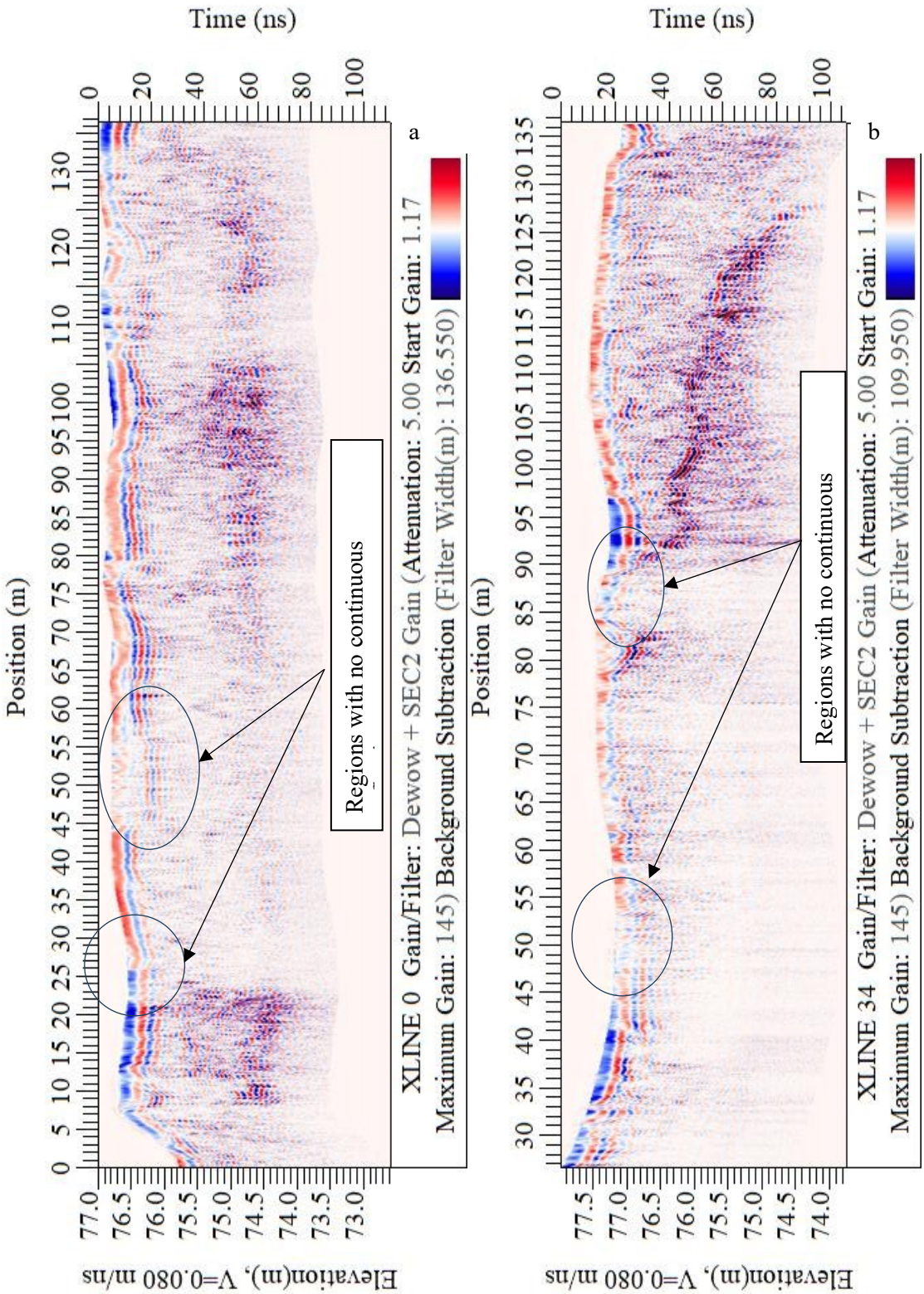

Figure 6.12: GPR responses in the periphery of the soccer and rugby fields using XLINE 0(a) and XLINE 34(b).

From Figure 6.11, it can be observed that the area is predominantly layered with several distinct layers. The layering was observed in all the GPR profiles though the ones in the periphery of the soccer and rugby fields, see Figure 6.12, exhibit a few regions with gaps. It can be observed that the top layer, about 25 cm-40 cm, in all the sections is probably indicating the topmost loosely compacted layer (indicated as 'Layer 1') of the playing fields. Immediately below this layer, there is a layer with very strong and continuous GPR reflections, indicated as 'Layer 2' in Figure 6.11 and Figure 6.12a. The layer is about half a metre thick over both the soccer and the rugby field. However, this layer is not as distinctly imaged in the periphery as it is over the two playing fields.

These two layers can probably be interpreted as embanked layers put in place to level and elevate the playing fields with respect to the surrounding area as the elevations were relatively higher in the western corner than in the eastern corner (roughly about 3-4 metres, see Figure 1.5) before the area was transformed into the park. This can be observed through the topographic mapping of the area which shows that the rugby field is at a relatively higher elevation than the soccer field (see current topographic map, Figure E2, in Appendix E). There is likely another layer beneath the 'Layer 2' discussed above. This layer is called 'Layer 3' over the soccer field and is relatively flatter, shown in Figure 6.13, while the third layer indicated as 'dipping layer' over the rugby field is flatter near the soccer field but it gets steeper towards the western corner of the field as shown in Figure 6.14. These layers are about 40-50 cm thick and are probably indicating the original ground surface before artificial layers are laid out in the area. Here, the dipping layers, under the rugby field, are observed at about a metre above the 'Layer 3', observed under the soccer field, and it is more dominant towards the western corner of the area as seen in XLINE 34 in Figure 6.12b. The rest of the processed GPR profiles are given in Appendix D.

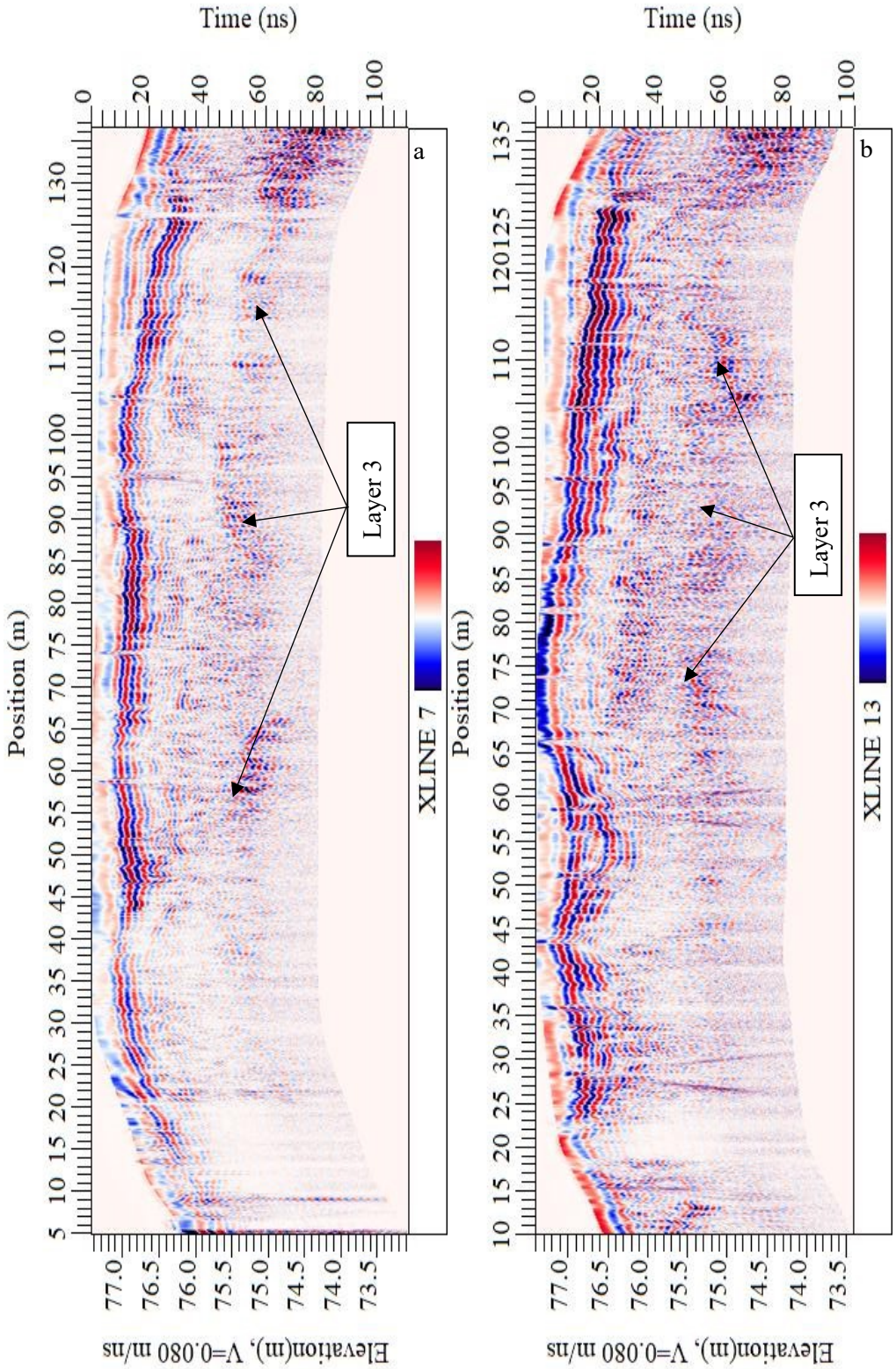

Figure 6.13: Nature of the subsurface stratigraphy over the soccer field using XLINE 7 (a) and XLINE 13 (b).

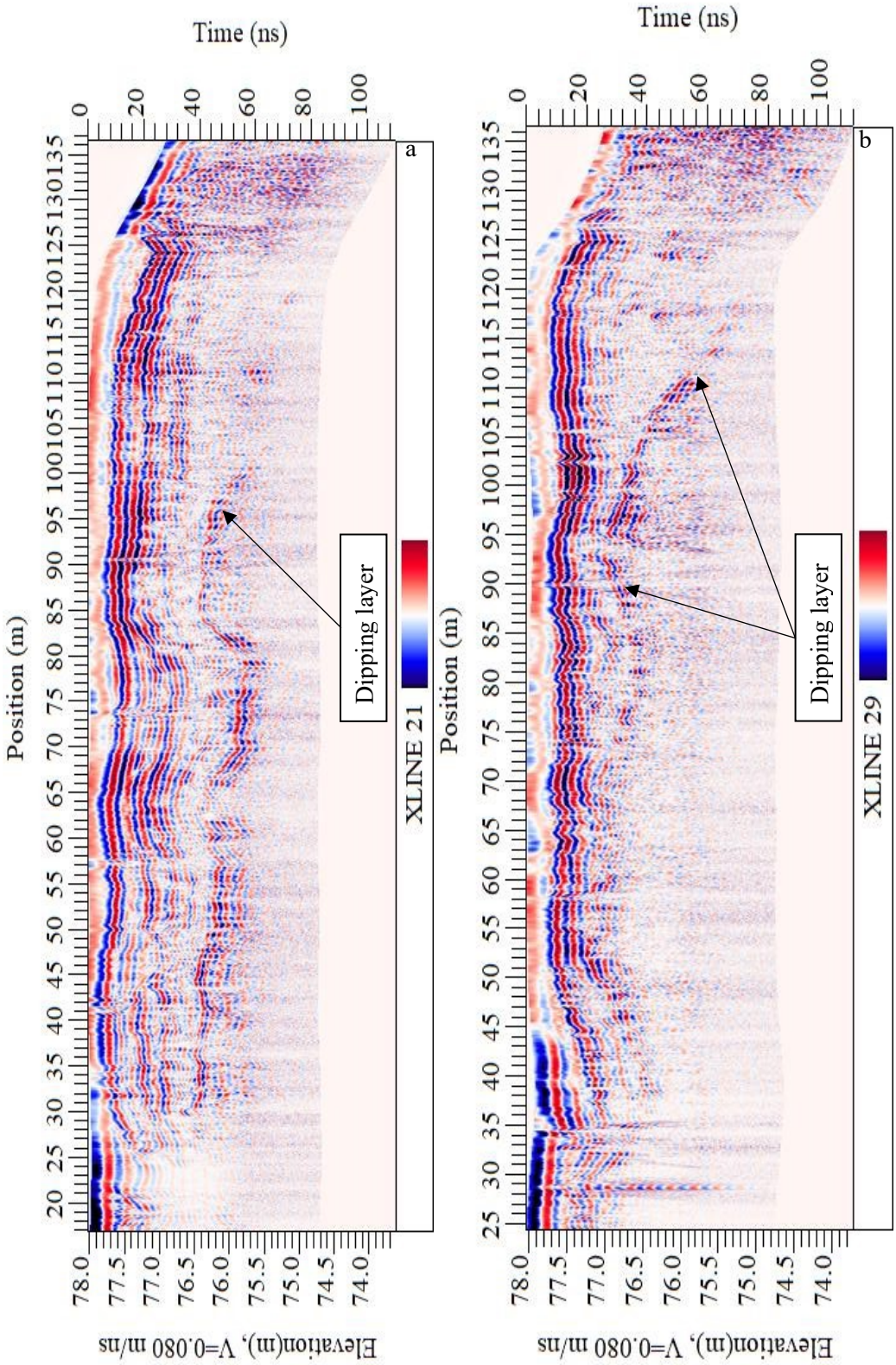

Figure 6.14: Nature of the subsurface stratigraphy over the rugby field using XLINE 21 (a) and XLINE 29 (b).

It is obvious that the GPR images can see only the shallow part of the subsurface. It is mainly due to very rapid attenuation of the high operating frequency available for this work. Figure 6.15 shows GPR signal attenuations, in terms of amplitude, with travel time for a few GPR lines. Clearly, the amplitude decays beyond about 10-18 ns and it corresponds to depths of about 0.4 m to 0.8 m respectively, corresponding to 10 ns and 18 ns.

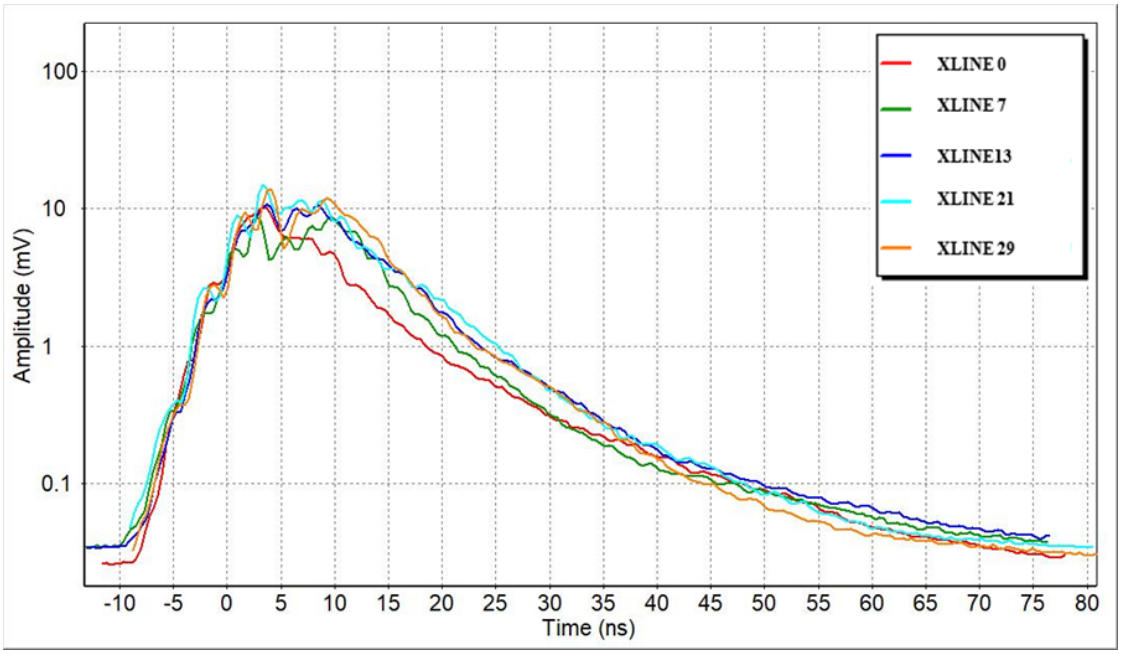

Figure 6.15: Average trace amplitude plot for 5 GPR lines.

Also, Figure 6.16 shows depth slices of the GPR responses in the area. Clearly, the data-set shows stronger amplitudes down to about 1 m beyond which GPR signals are completely attenuated. One clear observation in Figure 6.16 is that the stronger amplitudes GPR responses occur exactly under the soccer and rugby fields. This can be likely due to the existence of embanked layers as discussed.

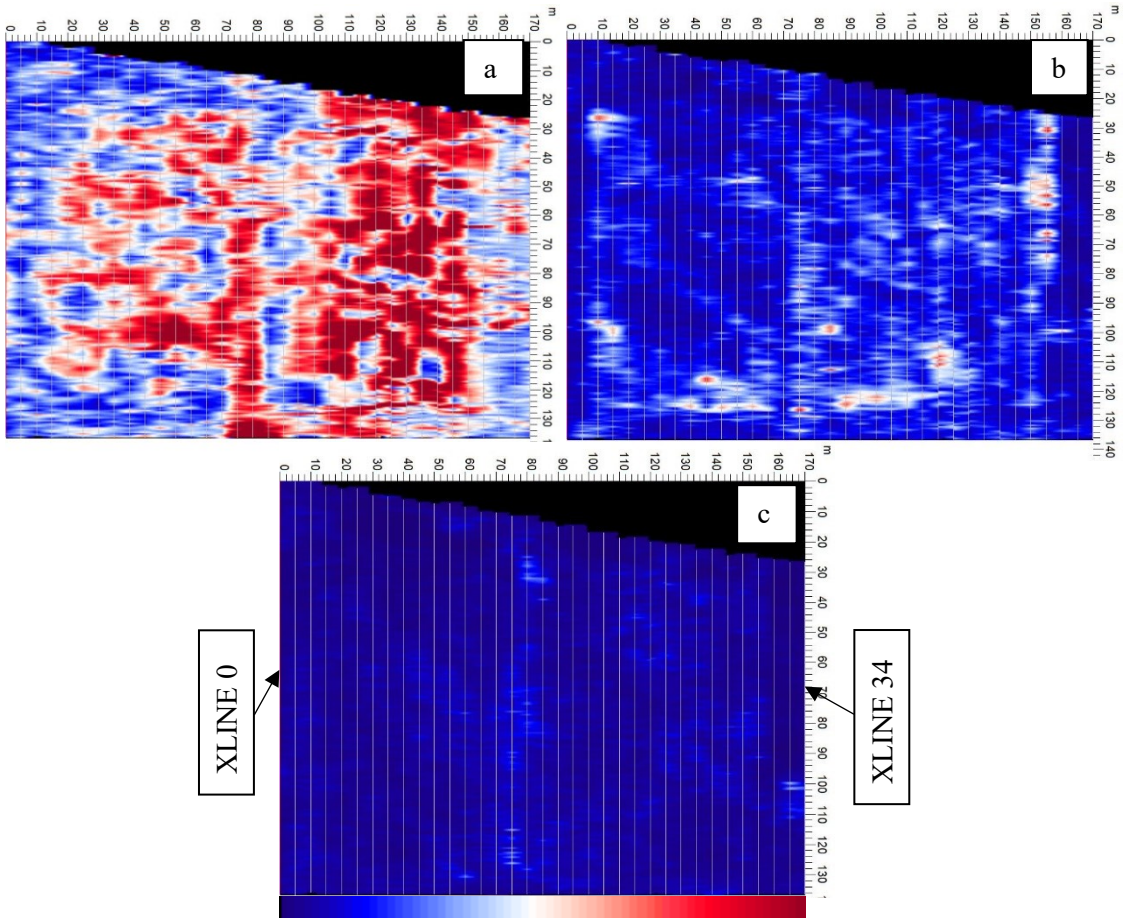

Figure 6.16: Depth slice at 0.5 metre (a), 1 metre (b) and 1.4 metres(c).

Following the aforementioned discussions, it can be concluded that the GPR method can only image the near-surface features/ layers existing down to the maximum depth of about a metre and half only. This means that any information on the existing trenches and constituent waste cannot be obtained from the GPR data-set.

Chapter 7: Summary, Integration and Conclusions

Following the discussions of the individual geophysical methods in Chapters 3, 4, 5 and 6, integrated interpretations of the geophysical data-sets are dealt with here.

7.1 Magnetic Survey

As discussed under Section 3.3, magnetic data unveiled several linear anomalous features prominently trending WSW-ENE across the whole survey area. Moreover, the data also shows numerous isolated magnetic anomalies in the area. The anomalous magnetic intensity map with the four linear features and the isolated magnetic anomalies indicated is shown in Figure 7.1.

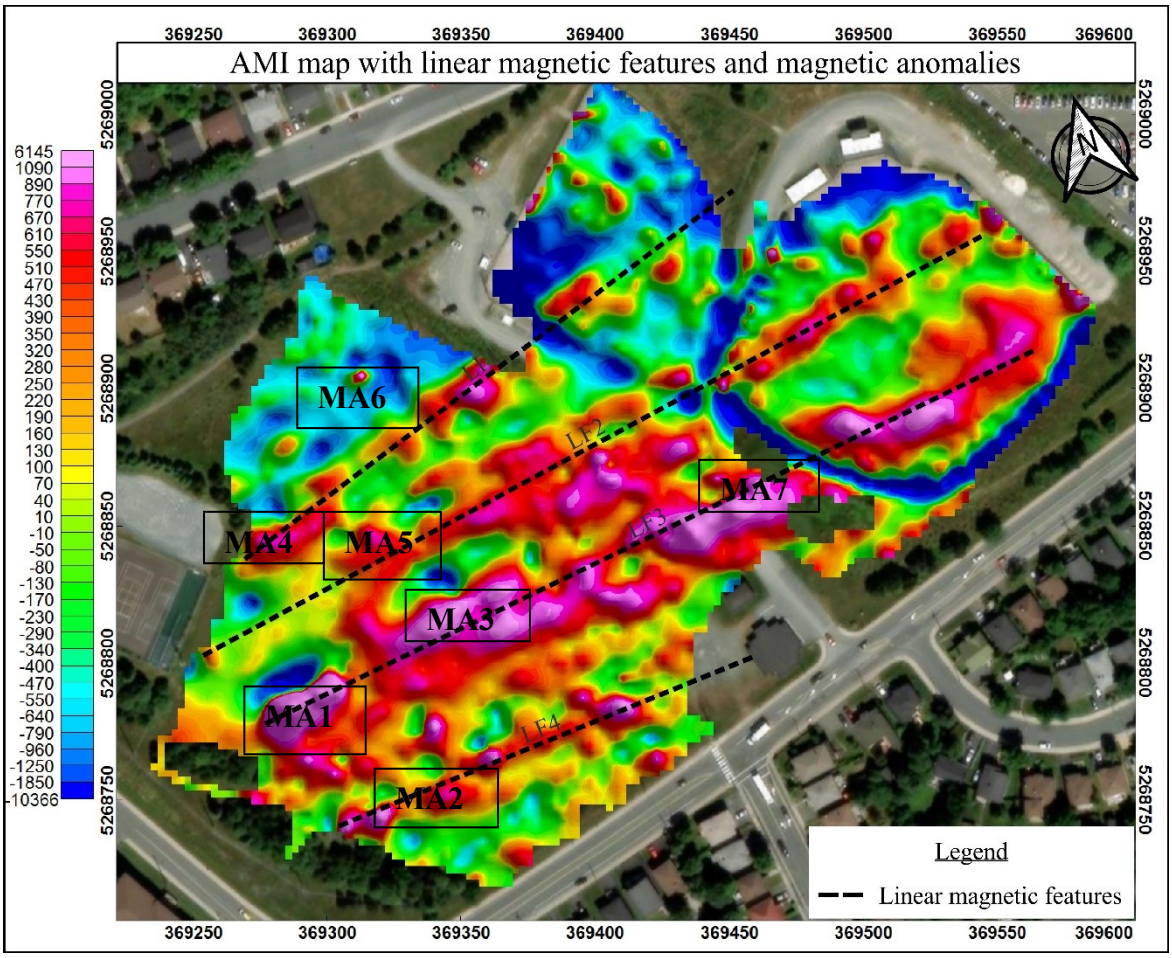

Figure 7.1: Anomalous intensity map showing linear magnetic features and main anomalies.

The approximate depths, ranging from about 3.75 m down to 10.5 m, to the magnetic sources in the area were obtained using Euler deconvolution as shown in Figure 3.14. The largest, most obvious magnetic anomaly, **MA1** (see Figure 7.1), was inverted for a 3D susceptibility distribution. The recovered 3D model is as shown in Figure 3.17 with its 2D sections shown in Figure 3.18 and Figure 3.19. The susceptibility model recovered very high susceptibility values for the anomaly **MA1**, with its top at about 4-5 m and bottom at about 12 m from the surface. The depth estimate from the inversion agrees well with depth estimates from the Euler deconvolution for the anomaly.

The recorded intensity range of the magnetic anomalies (-10366 to +6145 nT) is very high (at least 4x) compared to the typical values reported in the literature concerning municipal landfills investigations (e.g., Khalil and Hassan, 2016 and Whiteley, 2010) but it agrees well with the ranges reported in Barrows and Rocchio (1999) who studied a landfill with buried steel drums. The vertical gradient data in the area is also very high compared to values reported in similar landfill studies (e.g. Ibraheem et al., 2021) even those including the magnetic responses of buried steel drums (Marchetti et al., 2011). These results indicate that there is metallic waste throughout the area distributed in a roughly linear pattern. The most magnetically susceptible waste might include metallic waste (likely iron/steel) such as vehicular wreckages or lumps of discarded metallic scraps as can be evidenced from Figure 1.6. Additionally, the TMI profiles across anomaly **MA1** suggest the absence of significant remnance effects with different magnetization directions. The profiles show a high to the magnetic south and a smaller low to the magnetic north, which is the expected shape for a source magnetized by the Earth's field only or the Earth's field and a parallel remnance (see Figure 3.16).

7.2 DC Resistivity and Induced Polarization Survey

A geoelectrical survey is regarded as the best method to be integrated with a magnetic survey to resolve ambiguities in landfill characterization studies (e.g., Bernstone and Dahlin, 1997; Khalil and Hassan, 2016; Yannah et al., 2017). Accordingly, six DC resistivity and IP profiles were acquired. Four profiles transected the interpreted linear magnetic features covering a length of 175 m, one profile of 105 m ran across magnetic anomaly **MA1**, and one profile of 105 metres length across the baseball field.

All the resistivity data were inverted to construct a 2D conductivity section for each profile. Each constructed 2D conductivity section shows several high-conductivity anomalies (conductivity ranges from 75 mS/m to 185 mS/m). The range of conductivity of anomalies obtained in this work shows very good agreement with the range of conductivity reported in several landfill investigations over buried metallic objects (e.g., Bernstone and Dahlin, 1997). Hence, these conductive anomalies are likely due to buried metallic waste, enhanced by high porosity and permeability within the buried waste in trenches and probable infiltrations of surface runoff (Meju, 2000). Figure 7.2 shows all the constructed 2D conductivity profiles and the spatial distribution of these anomalies in the area.

From Figure 7.2, most high-conductivity anomalies are approximately coincident in location with the interpreted magnetic linear features. Also, the depth to the top of conductive anomalies is about 4-6 m and the depth to the bottom is about 12 m. In particular, in the 2D conductivity section for DCR_profile 6 (farthest to the SW) the high-conductive anomaly, **E6A1**, is at the exactly same location as magnetic anomaly **MA1**. The approximate depth to the top of the anomaly is approximately about 5.75 m. Similarly, conductive anomaly **E6A3** is coincident with magnetic anomaly **MA2**, geoelectrical anomaly **E1A1** is located exactly at the same location as magnetic anomaly **MA4** and the anomaly **E1A3** is coincident to one end of magnetic anomaly **MA3**. The

conductive anomalies **E2A2** and **E2A3** of DCR_profile 3 overlap with magnetic anomaly **MA5** and **MA3** respectively. Similarly, geoelectrical anomaly **E4A1** coincides with one end of magnetic anomaly **MA7** and conductive anomaly of DCR_profile 5 is coincident with the magnetic anomaly in the baseball field (see Figure 7.1 and Figure 7.2). Additionally, anomaly **E2A2** also exhibits the zig-zag pattern of apparent resistivity across magnetic anomaly **MA5** likely suggesting the presence of localized lump of conductive waste within 6.5-7 metres.

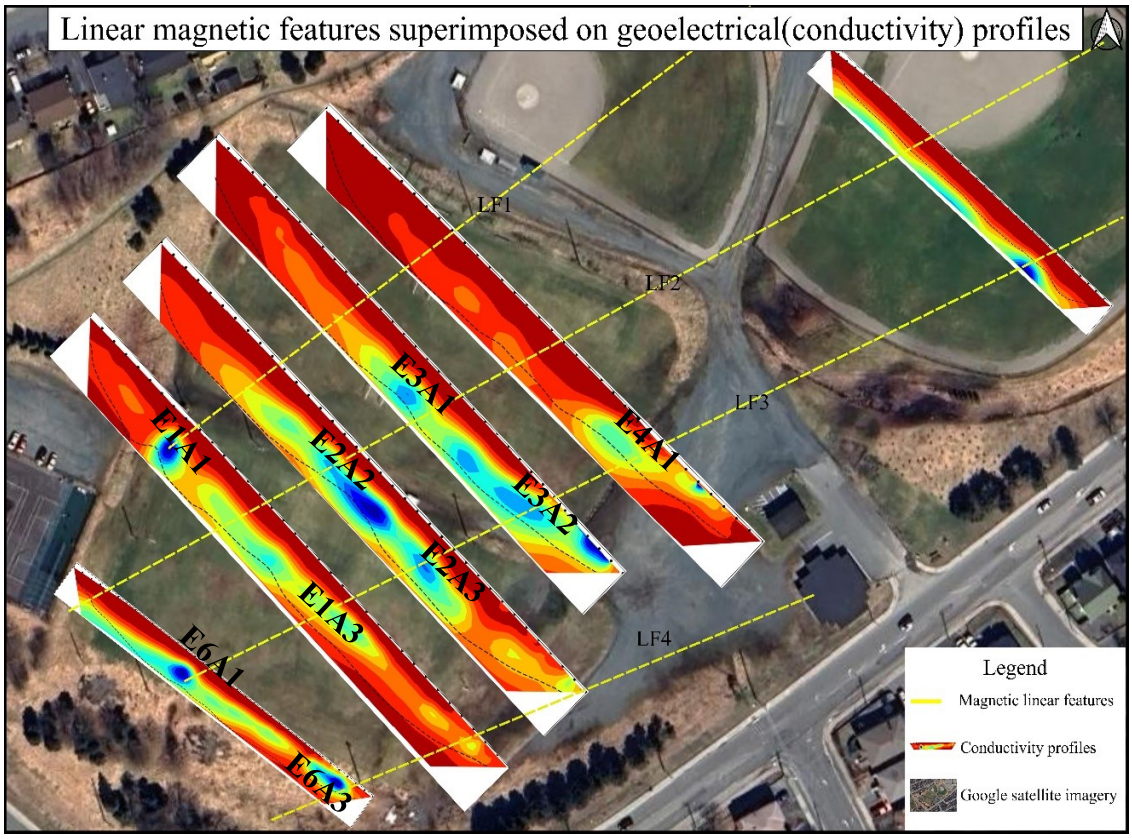

Figure 7.2: Interpreted linear magnetic features superimposed over the conductivity profiles (North arrow= geographic north).

A figure showing a direct comparison of the conductivity profiles and anomalous magnetic intensity in the area is given in Figure 7.3. From Figure 7.2 and Figure 7.3, it is clear that the conductive anomalies in the area align well with the linear magnetic features. This agreement supports the existence of linear trenches hosting waste

underneath the surface of the entirety of Wishingwell Park.

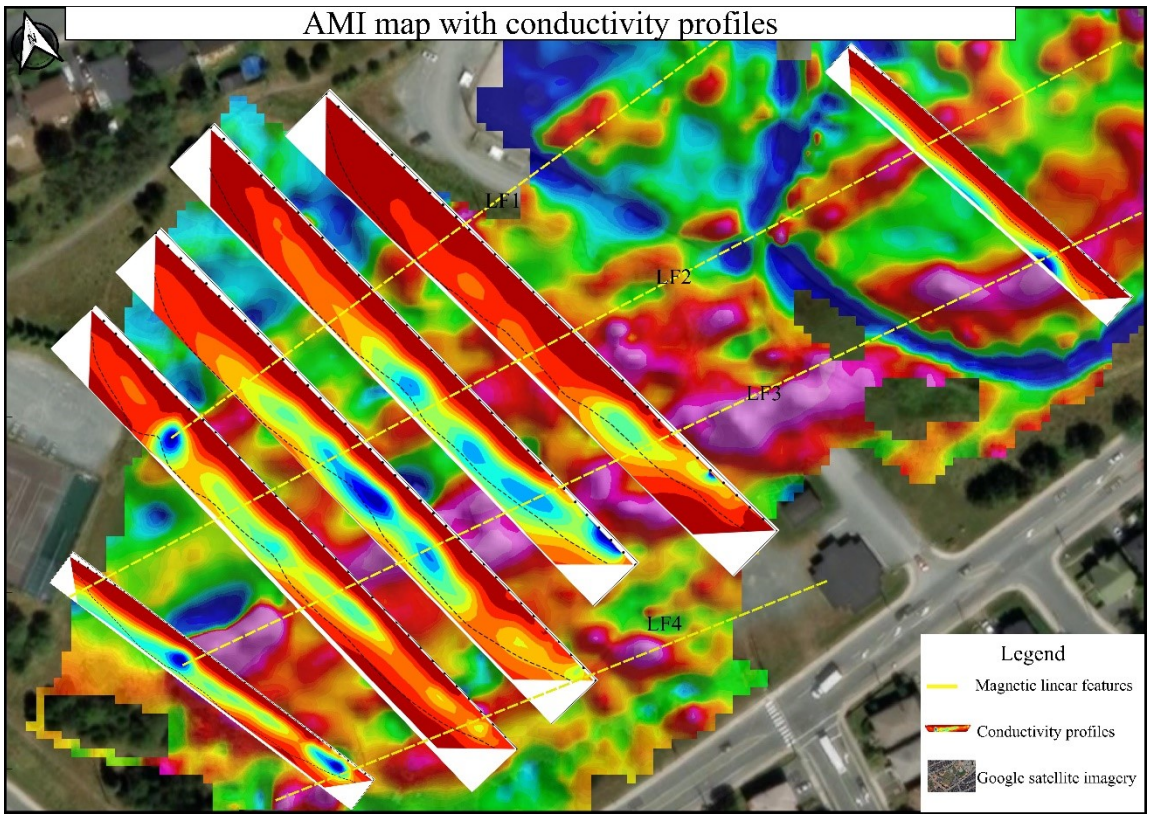

Figure 7.3: Conductivity profiles on AMI map (North arrow=magnetic north).

Also, all the IP data were inverted for 2D complex conductivity models, two models each, for every profile. The 'real' 2D constructed conductivity models for all the geoelectrical profiles depict regions with high real conductivity values (0.095 mS/m to 0.165 mS/m) roughly about the same depth in the area. Ntarlagiannis et al. (2016) reported slightly higher range of values of real conductivity, compared to values obtained in this work, understood to be due to leachate plumes. The imaginary conductivity values of each model section show several anomalies, and exhibit a slightly greater range (0.1-1 mS/m) of values than it is reported by Ntarlagiannis et al. (2016). This may be due to mixed waste resulting into complex leachate (mixture of organic and inorganic components) in certain parts of trenches. Hence, the complex 2D conductivity models help ascertain that both the conduction, which is likely due to runoff infiltration, and the polarization, likely due to leachate accumulation, can be observed in the subsurface.

7.3 Electromagnetic Survey

As proposed by Huang and Won (2000), the frequency-domain EM profiling technique is a useful addition to magnetic and geoelectrical surveys. Three different frequencies, 990Hz, 6210 Hz and 39030 Hz, were used to probe different depths of the subsurface. Huang (2005) demonstrated that the depth of investigation using a multi-frequency system is highly variable based on numerous factors such as conductivity contrast within layers, conductivity of top layer and EM noise. For the GEM-2 system, the lowest frequency, 990 Hz, can approximately probe the Earth down to about 6-8 metres while 6210 Hz and 39030 Hz can approximately probe down to about 4-6 metres and 0.5-3 metres respectively (Huang, 2005; Won et al., 1996).

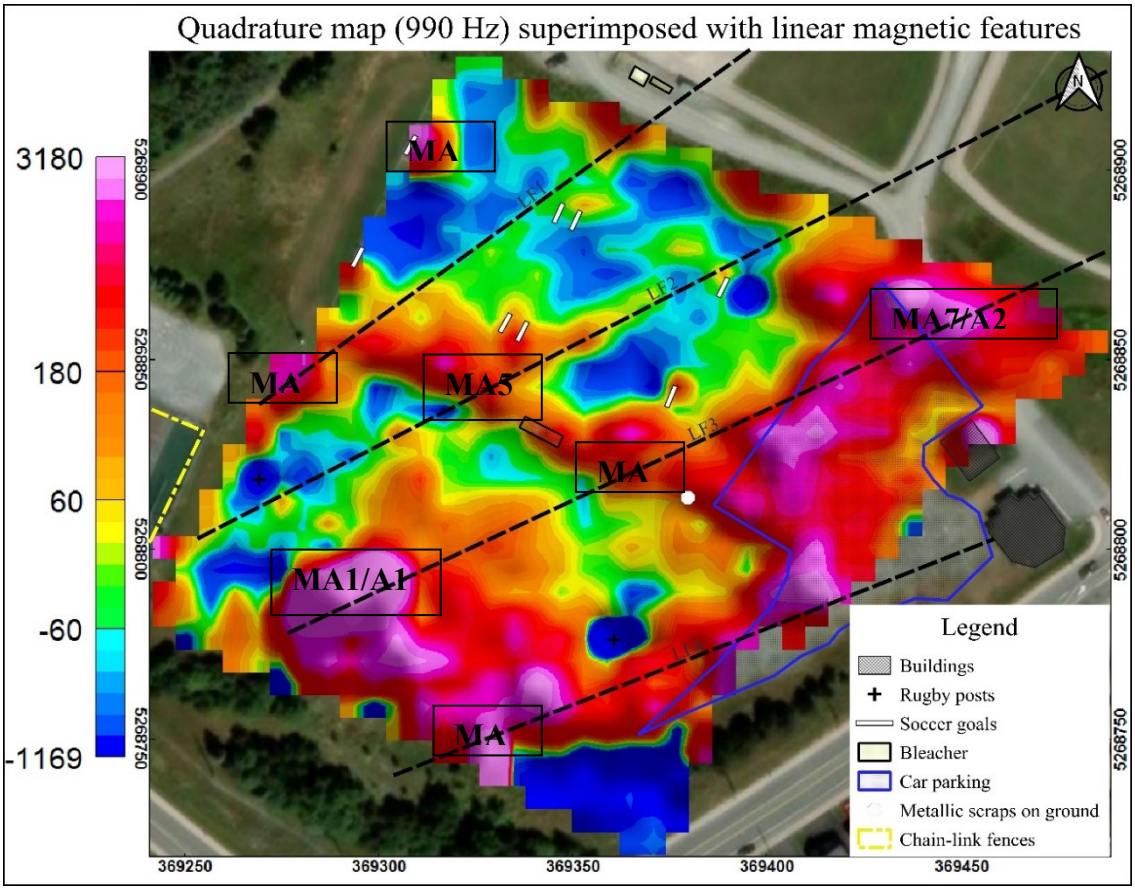

Figure 7.4: Quadrature responses for 990 Hz with the linear magnetic features (North arrow= geographic north).

Figure 7.4 shows the quadrature map for frequency 990 Hz. It can be observed that, apart from responses coinciding with major magnetic anomalies, the quadrature responses are largely dominated by immediate near-surface composition of the ground. The playing fields have disturbed till forming its immediate near-surface (Garland, 2006) while the car park has a gravelly near-surface and there are rough fills in between and surrounding the playing fields (used as access road). Quadrature responses recorded for the other two frequencies exhibit similar features (see Section 5.3).

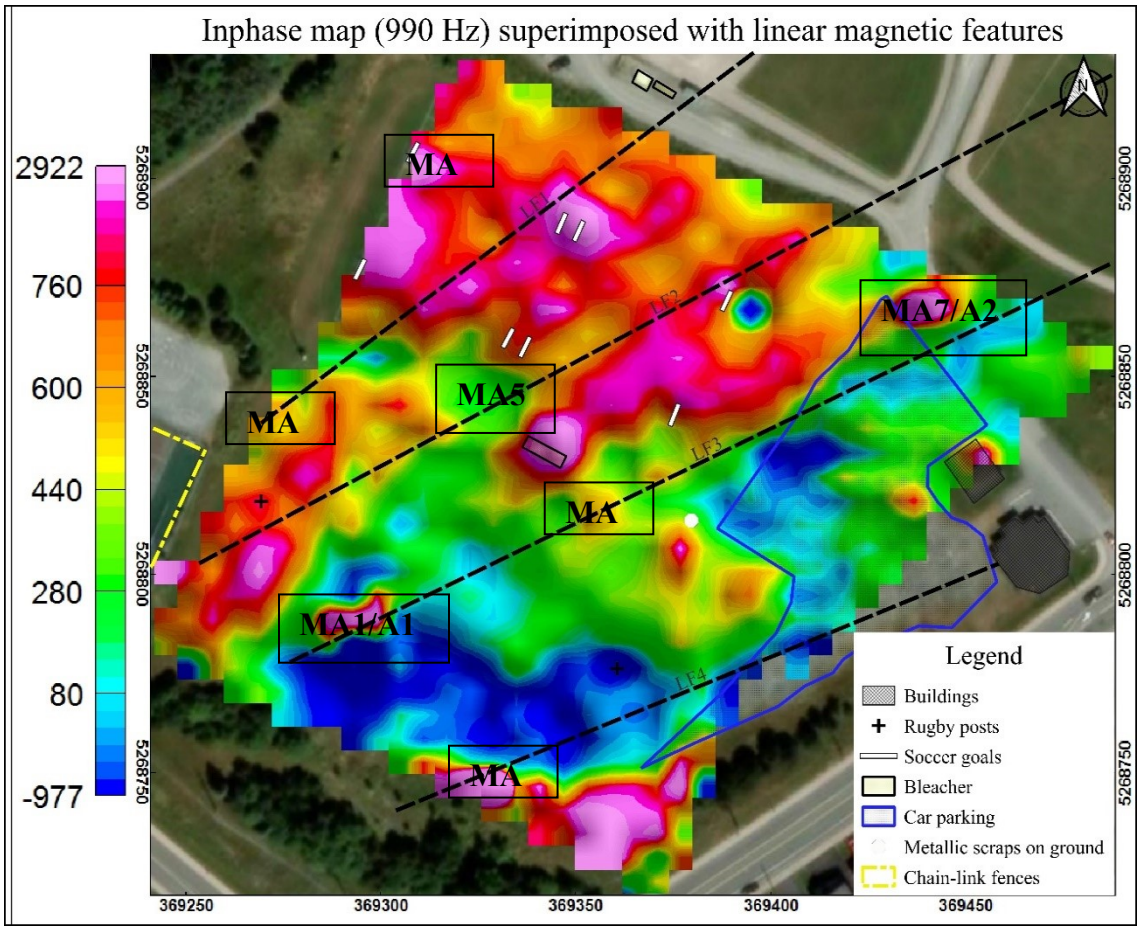

Figure 7.5: Inphase responses for 990 Hz with the linear magnetic features.

Figure 7.5 shows the inphase map for frequency 990 Hz. The lowest frequency inphase data exhibits some trench-like linear features. Similar observation can be made for inphase map of frequency 6210 Hz (see Figure 5.6).

From Figure 7.5, it is seen that the trench-like linear features show similar orientation (roughly WSW-ENE) although not completely overlapping the magnetic responses. Further, Figure 7.4 and Figure 7.5 show that EM anomalies **A1** and **A2** occur in the same locations as magnetic anomalies **MA1** and **MA7**. Several other magnetic anomalies, **MA2**, **MA3**, **MA4**, **MA5** and **MA6** are all coincident with the EM anomalies with an exception of anomaly **MA5** in the inphase map.

EM data are compared with geoelectrical results in Figure 7.6. Here, EM anomaly **A1** and high-conductivity anomaly **E6A1** are coincident in their positions. Moreover, high-conductivity anomalies **E6A3**, **E1A1**, **E2A2**, **E3A1**, **E3A2** and **E4A1** agree very well with EM anomalies with exception of **E1A3** which corresponds with a region of low inphase.

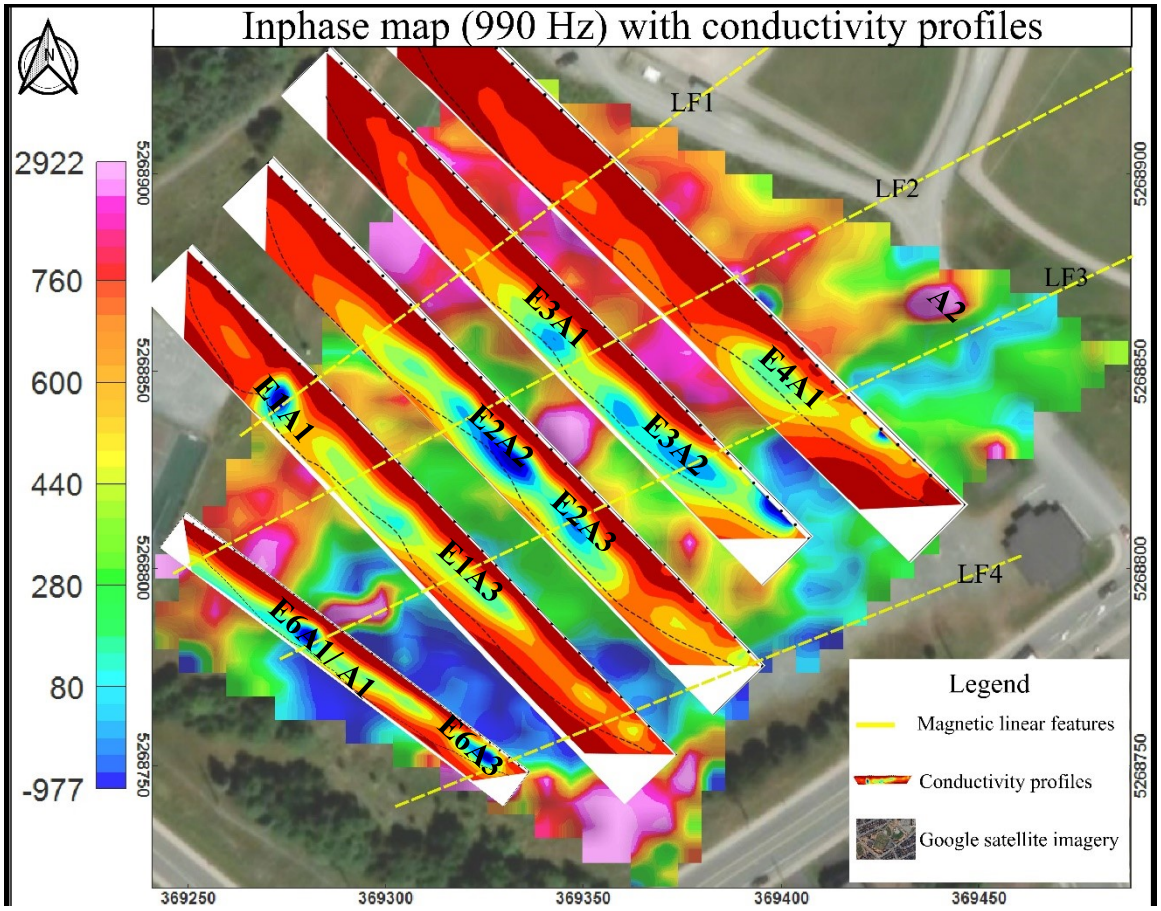

Figure 7.6: Quadrature (990Hz) map with five geoelectrical conductivity profiles (North arrow= geographic north).

Very good agreements amongst EM, magnetics and geoelectrical results ascertain the existence of multiple trenches, as opposed to the single one conjectured by Garland (2006), hosting waste, including significant metallic objects, in the area.

7.4 Ground Penetrating Radar Survey

To further augment the aforementioned three methods, with the objective to image the extent and outlines of the trenches with very high resolution, ground penetrating radar surveys were carried out. The surveys were done using the only system available which is one with an operating frequency of 250 MHz. Owing to the high operating frequency used and the high conductivity of the subsurface, the GPR data could only probe to a limited maximum depth of about 1.4 metres as discussed in Section 6.3. Thus, the GPR data here can only resolve with good resolution the artificial layers of embanked soil, underneath the soccer and the rugby field, put in place to level and elevate the ground surfaces for the playing fields.

The GPR sections here see at least three distinct layers. The topmost layer is soft soil, about 0.4 m thick, on the fields within which grasses are grown. Immediately below this layer is the 'Layer 2' associated with very high energy reflections which probably represent very well compacted layer, of roughly a metre thick, forming the main stratum underneath the playing fields. The third layer is flat and discontinuous over the soccer field. This layer appears continuous and flat towards the southern end (starting point) and it gradually dips at the other end (end point) over the rugby field. All of the layers occur at higher elevation in the rugby field than the soccer field.

Given very limited depth of investigation, the GPR survey here cannot probe down to the depths, approximately 6 m to 12 m, at which trenches are located as observed in the magnetic data, DC resistivity inversion results and 990 Hz EM data. Nevertheless, the GPR data did provide useful information about the immediate near-surface in the area. Figure 7.7 shows GPR lines used here along with the geoelectrical lines superimposed on the AMI map. Particularly, the strongest magnetic anomaly **MA1**, which corresponds to the geoelectrical anomaly **E6A1** and the EM anomaly **A1**, is observed to occur approximately over the region where the third layer dips as shown in Figure 7.8 and

Figure 7.9.

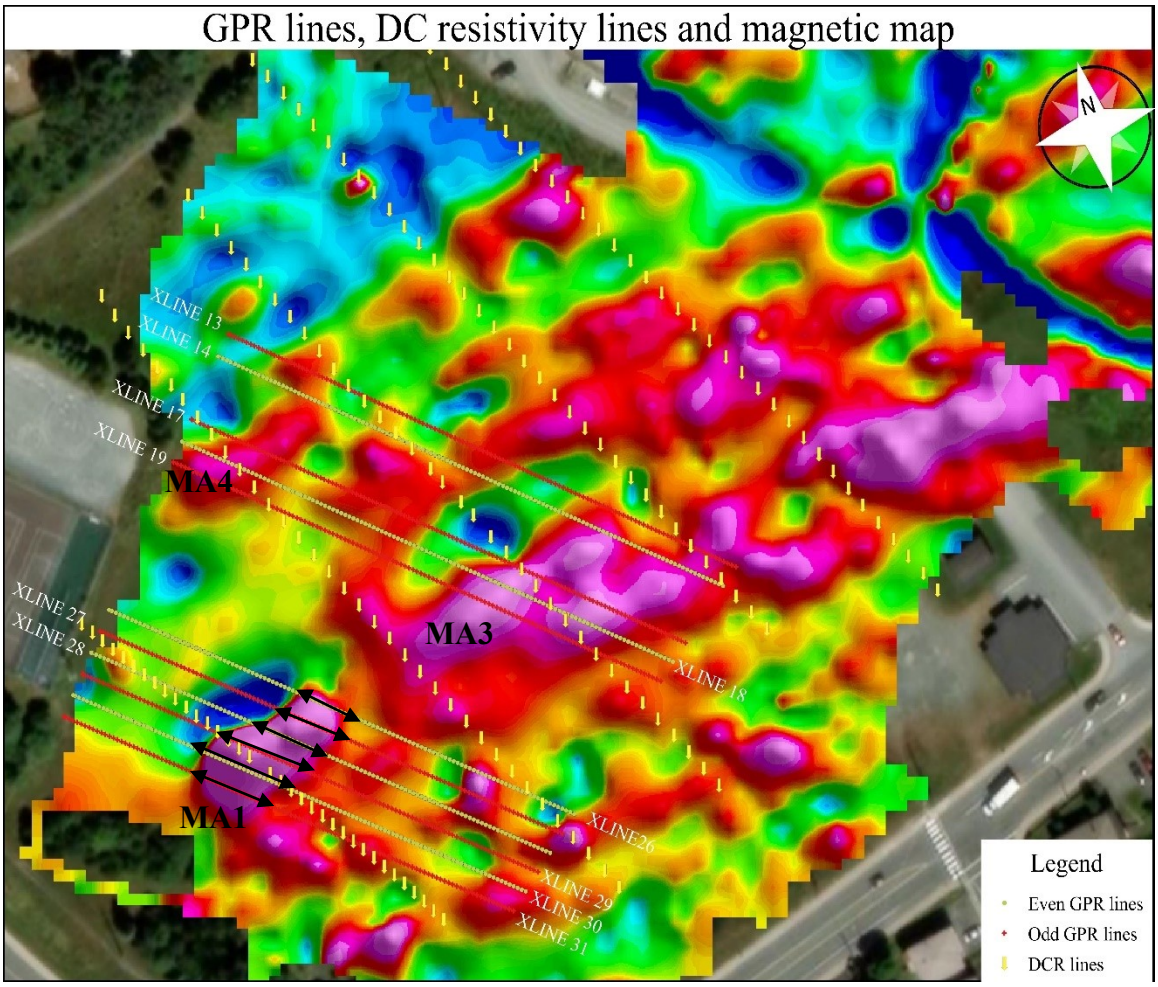

*Figure 7.7: Map showing GPR lines and DCR lines superimposed on the magnetic anomaly map (Black lines with arrow show the extent of GPR lines crossing magnetic anomaly **MA1** indicated with yellow diamonds in Figure 7.8 and Figure 7.9, north arrow=magnetic north).*

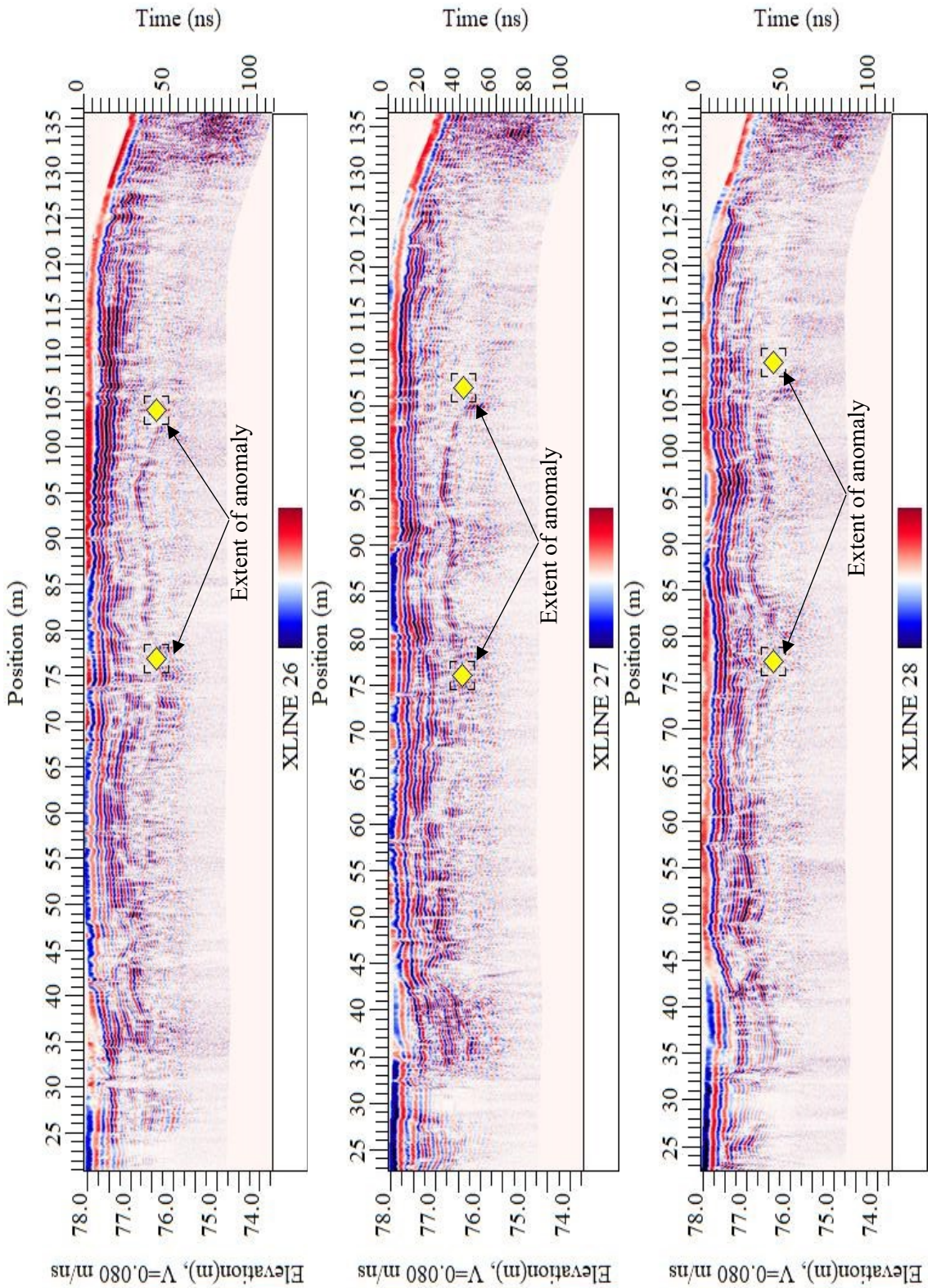

*Figure 7.8: Dipping layers compared against the anomaly **(MA1/E6A1/A1)** using XLINE 26, XLINE27 and XLINE28.*

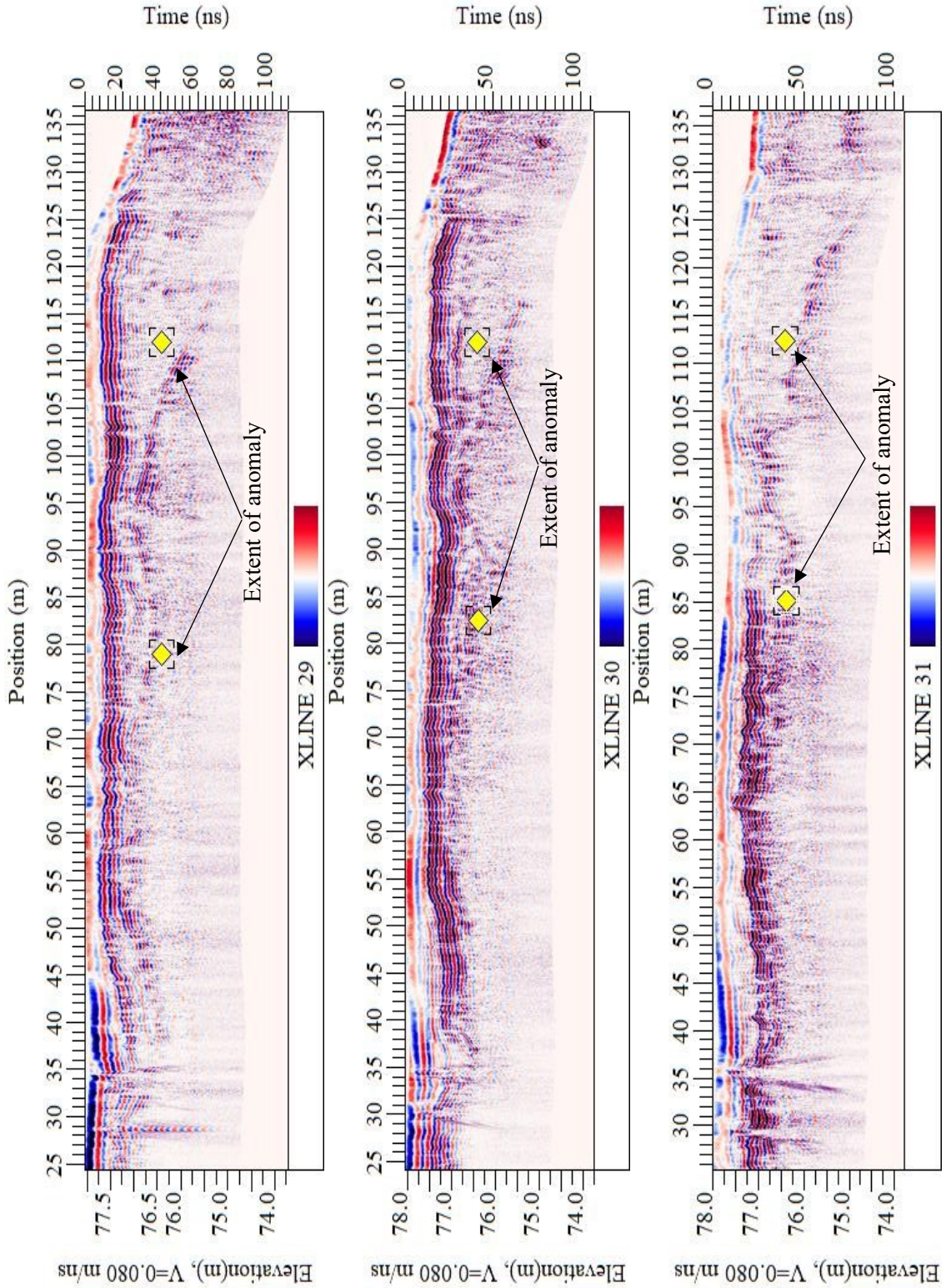

*Figure 7.9: Dipping layers compared against the anomaly (**MA1/E6A1/A1**) using XLINE 29, XLINE 30 and XLINE 31.*

The dipping interface at the top of Layer 3 underneath the anomaly **MA1**/**E6A1**/**A1**, exhibits a slight increase in elevation in all the GPR sections in Figure 7.9. Further, the GPR profiles which run across anomalies **MA4**/**E1A1** and **MA3**/**E2A2** are shown in Figure 7.10. From Figure 7.10, it is observed that the extent of GPR sections within the spread of anomaly **MA3**/**E2A2** (enclosed in red rectangles) depicts strong reflections off the 'Layer 3' similar to the sections underneath anomaly **MA1**. However, the GPR sections in the vicinity of anomaly **MA4**/**E1A1** do not depict any prominent scatterers or clear layering.

Similarly, correspondence between the GPR data and the three previous methods is further examined over the soccer field. Figure 7.11 shows GPR lines XLINE13 and XLINE 14 running across some magnetic linear features and geoelectrical anomaly **E3A2**. GPR responses in the vicinity of anomaly **E3A2** appear noisier. The extent of GPR sections in Figure 7.11, over linear magnetic features LF2 and LF1, show strong reflections similar to the case discussed above. Thus, GPR data consistently show only shallow near-surface features with good resolution, with only some hints of deeper structure, whereas the magnetic, DC resistivity and EM (lowest frequency) data can observe several trenches hosting metallic waste deeper into the subsurface. Further, the average depth (bottom) of the inferred trenches observed in the DC resistivity data is approximately similar (despite a few regions with 0.5-2 metres difference) to the depths of the fill-till interfaces reported in Garland (2006), shown in Figure 7.12. Thus, good agreements among all these data ascertain the existence of trenches hosting waste within this depth in the area.

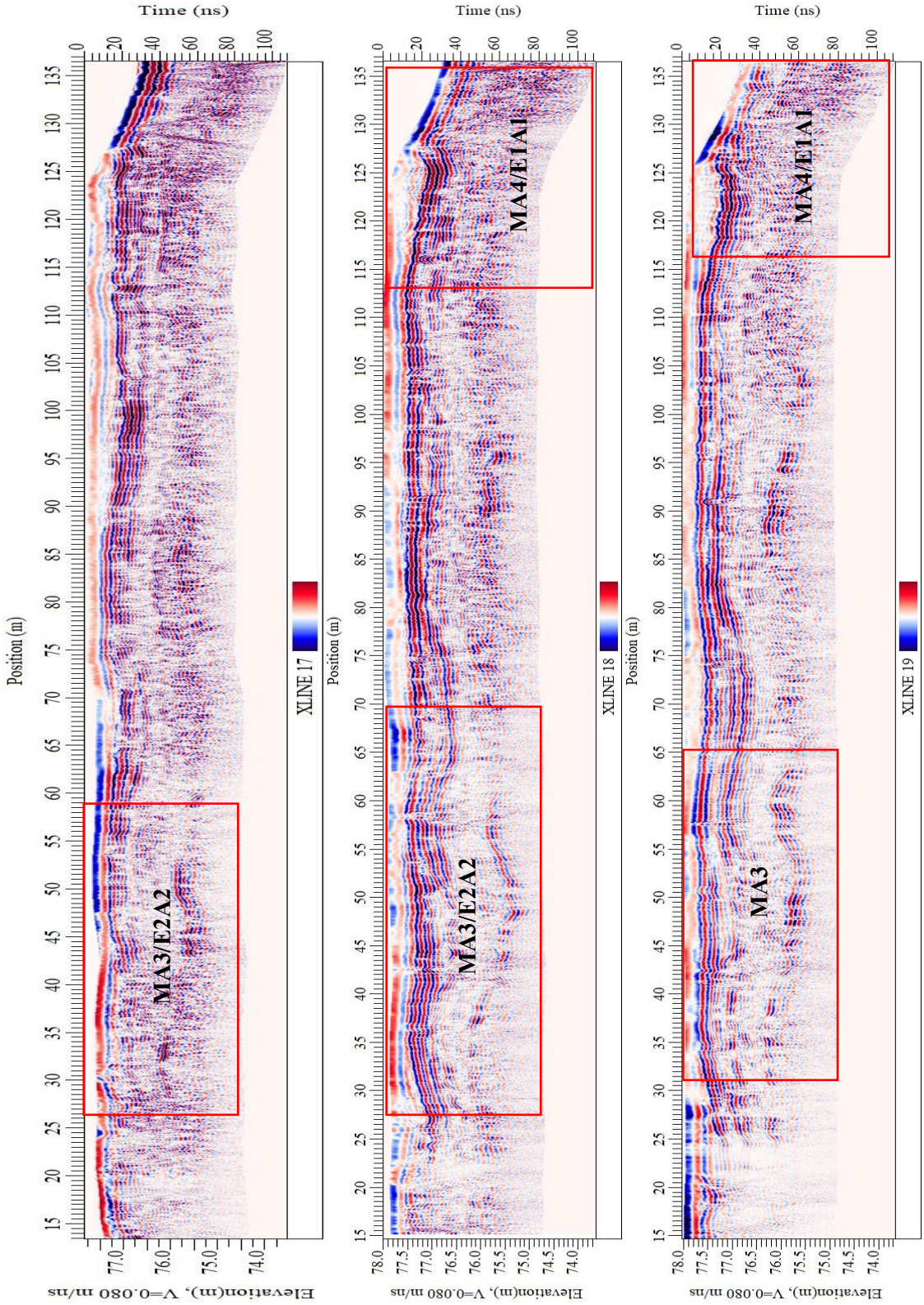

Figure 7.10: Comparison of XLINE 17, XLINE18 and XLINE 19 with anomalies in other 3 data sets.

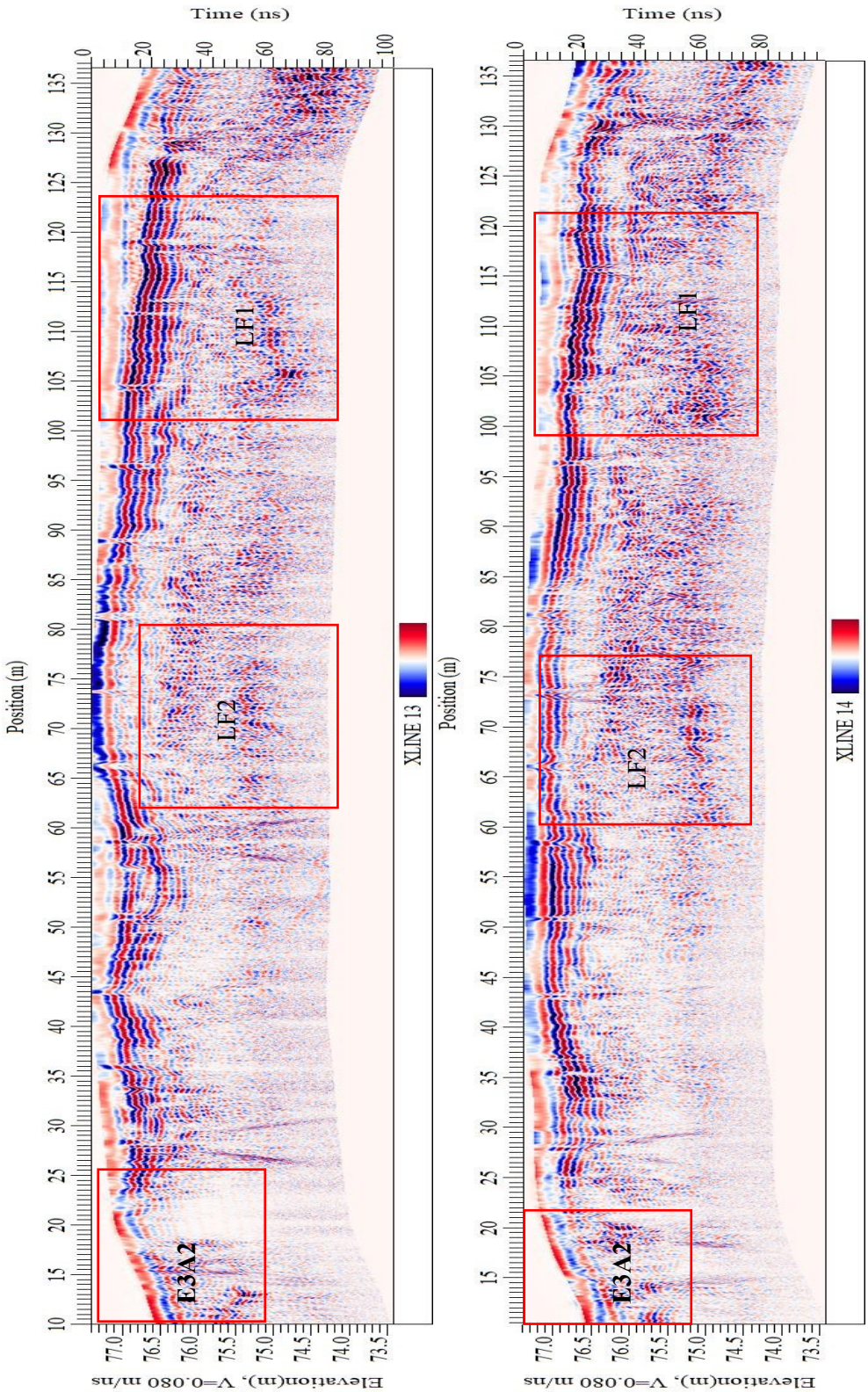

Figure 7.11: Comparison of GPR and three other methods over soccer field.

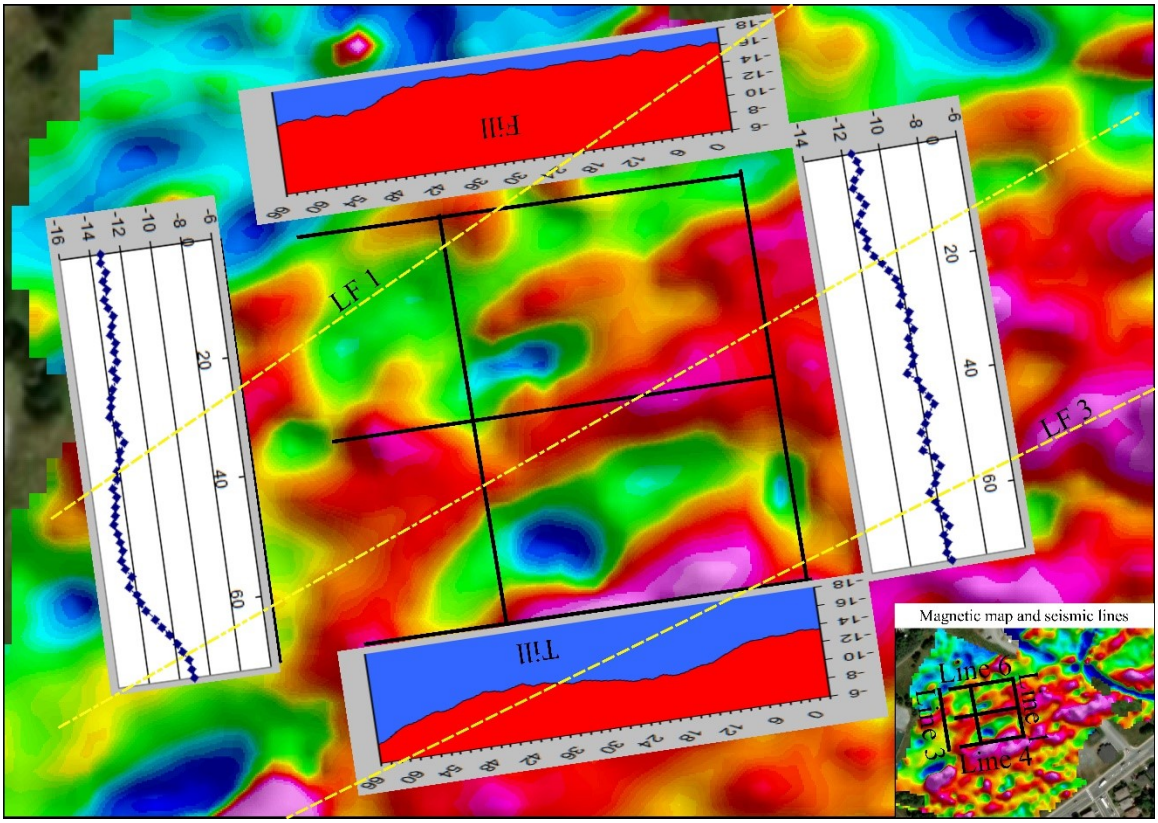

Figure 7.12: Garland (2006) results from seismic tomography with the magnetic features.

7.5 Conclusions

A comprehensive study of the historical landfill at Wishingwell Park was conducted as an integrated geophysical investigation using four different methods. Through the results of this work, a much better understanding of this site was achieved. The principal findings/conclusions of this investigation are as follows:

1. The landfill was operated using a trenching technique. Geophysical signatures of at least four artificial trenches can be clearly observed in the magnetics and DC resistivity with hints in the EM data-set. These filled trenches are at depths of about 4-5 metres (top) and about 10-12 metres (bottom). This bottom depth is consistent with fill-till depth reported by Garland (2006).
2. Buried waste in these trenches and other localized areas are strongly magnetic in nature. Many of these magnetic anomalies are revealed as highly conductive anomalies in the DC resistivity results and EM anomalies (lowest frequency) as well. This helps suggest that a significant fraction of the waste concealed in the area consists of discarded metallic (iron) objects (lumps or vehicular wreckages).
3. There are possible indications of leachate plumes depicted in terms of elevated chargeability, real conductivity and complex conductivity below top layers a few metres thick (although the results can be due to existence of metals, loose fill and waste with high water content). Also, there exist clear flow-paths of likely run-off infiltration from the higher ground level and the gravel car park into the subsurface.
4. GPR survey effectively imaged the nature of shallow covering layers up to the maximum depth of 1.2 m.

References

Abdel-Shafy, H.I., Ibrahim, A.M., Al-Sulaiman, A.M., & Okasha, R.A. (2024). Landfill leachate: Sources, nature, organic composition, and treatment: An environmental overview. Ain Shams Engineering Journal, *15*(1), 1-11. https://doi.org/10.1016/j.asej.2023.102293

Adewuyi, O.I., & Oladapo, A.G. (2011). Use of geophysical methods in landfill site investigation: A case study of Ibadan, Southwest Nigeria. *New York Science Journal*, *4*(10),1-10.

Annan, A. P. (1993). Practical processing of GPR data. In Proceedings of the second government workshop on ground penetrating radar, October 1993, Columbus Ohio. Sensors and software Inc.

Annan, A.P. (2002). History, trends, and future developments. *Subsurface Sensing Technologies and Applications, 3*,253-270. *https://doi.org/10.1023/A:1020657129590*

Annan, A. P. (2009). Electromagnetic principles of ground penetrating radar. In Jol, H.M (Ed.), *Ground Penetrating Radar: Theory and Applications* (pp. 1-40). Elsevier. https://doi.org/10.1016/B978-0-444-53348-7.00001-6

Appiah, I., Wemegah, D. D., Asare, V.D. S., Danuor, S. K., & Forson, E. D. (2018). Integrated geophysical characterisation of Sunyani municipal solid waste disposal site using magnetic gradiometry, magnetic susceptibility survey and electrical resistivity tomography. *Journal of Applied Geophysics*, *153*,143-153. https://doi.org/10.1016/j.jappgeo.2018.02.007

Auken, E., & Christiansen, A.V. (2004). Layered and laterally constrained 2D inversion of resistivity data. *Geophysics,69*(3), 752–761.

Baedecker, M.J., & Apgar, M.A. (1984). Hydrogeochemical studies at a landfill in Delaware. *Studies in geophysics groundwater contamination* (Report No. DOE/ER/12018—T8, pp. 127-138). National Academy Press.

Baranov, V., & Naudy, H. (1964). Numerical calculation of the formula of reduction to the magnetic pole. *Geophysics, 29*, 67-79. http://dx.doi.org/10.1190/1.1439334

Barker, G. S., Jordan, T. E., & Pardy, J. (2007). An introduction to ground penetrating radar (GPR). In Baker, G. S and Jol, H.M (Eds.), *Stratigraphic Analyses using GPR* (Geological Society of America Special Paper No. 432, pp. 1-18). The Geological Society of America. https://doi.org/10.1130/2007.2432(01)

Barker, R.D. (1992). Recent applications of electrical imaging surveys in the United Kingdom. In *proceedings of 9th EEGS Symposium on the Application of Geophysics to Engineering and Environmental Problems* (pp. 134). European Association of Geoscientists & Engineers. https://doi.org/10.3997/2214-4609-pdb.205.1996_134

Barrows, L., & Rocchio, J.E. (1999). Magnetic Surveying for Buried Metallic Objects. *Groundwater monitoring and remediation,* 10(3), 204-211. https://doi.org/10.1111/j.1745-6592.1990.tb00016.x

Belmonte-Jiménez, S.I., Jiménez-Castañeda, M.E., Pérez-Flores, M.A., Campos-Enríquez, J.O., Reyes-López, J.A., &Salazar-Peña, L. (2012). Characterization of a leachate contaminated site integrating geophysical and hydrogeological information. *Geofísica internacional, 51*(4), 309-321.

Benson, R., Glaccum, R., & Noel, M. (1984). *Geophysical techniques for sensing buried wastes and waste migration* (PB84-198449). U.S. Environmental protection Agency.

Bernstone, C., & Dahlin, T. (1997). DC resistivity mapping of old landfills: Two case studies. *European Journal of Environmental and Engineering Geophysics*, *27*(2), 21-136.

Bièvre, G., & Garambois, S. (2023). Characterization of a small abandoned municipal solid waste scattered landfill combining Remote Sensing and near-Surface geophysical

investigations. *Journal of Environmental and Engineering Geophysics, 28* (4),155-168.

Binley, A. (2023). R2 user guides (version 4.11)[User manual]. Lancaster University. http://www.es.lancs.ac.uk/people/amb/Freeware/R2/R2.htm

Binley, A., & Kemna, A. (2005). DC resistivity and induced polarization methods. In Y. Rubin & S. S. Hubbard (Eds.), *Hydrogeophysics* (Vol. 50, pp. 129–156). Springer.

Binley, A., Ramirez, A., & Daily, W. (1995). Regularized image reconstruction of noisy electrical resistance tomography data. In M. S. Beck, B. S. Hoyle, M. A. Morris R. C. Waterfall, R. A. Williams (Eds.), *Process Tomography 1995: Proceedings of the 4th Workshop of the European Concerted Action on Process Tomography, Bergen, April 6–8, 1995* (pp. 401–410).

Blakely, R. J. (1996). *Potential theory in gravity and magnetic applications*. Cambridge university press.

Blanchy, G., Saneiyan, S., Boyd, J., McLachlan, P., & Binley, A. (2020). ResIPy, an intuitive open source software for complex geoelectrical invesion/modeling. *Computers and Geosciences*,*137*, 1-12.

Bland, J. (1946). *Report on the City of St. John's Newfoundland made for the commission on town planning*. St. John's town planning commission.

Briggs, I.C. (1974). Machine contouring using minimum curvature. *Geophysics,39*(1), 39-48. https://doi.org/10.1190/1.1440410

Callahan, B. (1991). Kelly's Brook Babbling Once Again. *Evening Telegram*. https://dai.mun.ca/digital/telegram18/

Carlson, N., Bouzid, N., &Byrd, R. (2015). Environmental applications of the IP method: Surveys of subsurface waste. *The Leading Edge, 34*(2), 214-220. https://doi.org/10.1190/tle34020214.1

Carpenter, P.J., Kaufmann, R.S., & Price, B. (1990). Use of resistivity soundings to determine landfill structure. *Groundwater, 28*(4), 569-575. https://doi.org/10.1111/j.1745-6584.1990.tb01713.x

Cassidy, N. J. (2009). Ground penetrating radar data processing, modelling and analysis. In Jol, H.M (Ed*.), Ground penetrating radar: theory and applications* (pp. 141-172). Elsevier.

Cochran, J. R., & Dalton, K. E. (1995, April). Using high-density magnetic and electromagnetic data for waste site characterization: A case study. In *Proceedings of the Symposium on the Application of Geophysics to Engineering and Environmental Problems (SAGEEP)* (pp. 117–127). EEGS.

Collier, K. (2011). *Six decades of expansion: St. John's suburbs and surrounding communities*. Newfoundland and Labrador Heritage. https://www.heritage.nf.ca/articles/society/st-johns-suburbs.php

Constable, S.C., Parker, R.L., & Constable, C.G. (1987). Occam's inversion: A practical algorithm for generating smooth models from electromagnetic sounding data. *Geophysics, 52*(3), 289-300. http://dx.doi.org/10.1190/1.1442303

Crook, N., Levitt, M., & McNeill, M. (2016). *Geophysical survey of the Los Angeles landfill, Albuquerque NM* (Report No. RPT-2016-031, pp. 1-36). HGI HydroGeophysics.

Cui, F., Li, S., & Wang, L. (2018). The accurate estimation of GPR migration velocity and comparison of imaging methods. *Journal of Applied Geophysics*, *159*, 573-585.

Dahlin, T., & Loke, M. H. (1997). Quasi-3d resistivity imaging: Mapping of three dimensional structures using two dimensional dc resistivity techniques. In *Proceedings of the 3rd Meeting Environmental and Engineering Geophysics* (pp. 143-146). Denmark.

Dahlin, T., Bernstone, C., & Loke, M. H. (2002). A 3-D resistivity investigation of a contaminated site at Lernacken, Sweden. *Geophysics*, *67*(6), 1692–1700. https://doi.org/10.1190/1.1527070

Dahlin, T., & Zhou, B. (2004). A numerical comparison of 2-D resistivity imaging with ten electrode arrays. *Geophysical Prospecting*,*52*(5), 379-398. https://doi.org/10.1111/j.1365-2478.2004.00423.x

Daily News (1959a, April 16). Dump not filled in. *The Daily News*. https://dai.mun.ca/digital/dailynews/

Daily News (1959b, December 4). Briefs in the "News". *The Daily News*. https://dai.mun.ca/digital/dailynews/

Daily News (1961a, June 8). Dump odor drives people from homes. *The Daily News.* https://dai.mun.ca/digital/dailynews/

Daily News (1961b, June 13). The problem of the city dump. *The Daily News*. https://dai.mun.ca/digital/dailynews/

Daily News (1962, December 4). In the news: notes and comments. *The Daily News*. https://dai.mun.ca/digital/dailynews/

Daily News (1963, October 1). New city dump. *The Daily News*. https://dai.mun.ca/digital/dailynews/

Daniels, D.J. (2006). A review of GPR for landmine detection. *Sensing and Imaging: An International Journal, 7*(3), 90-123. https://doi.org/ 10.1007/s11220-006-0024-5

Daniels, J. J. (2000). *Ground penetrating radar fundamentals* (U.S.EPA, Region V). U.S.EPA.https://www.researchgate.net/publication/237508286_Ground_Penetrating_Radar_Fundamentals

Daniels, J. J., Wielopolski, L., Radzevicius, S., & Bookshar, J. (2003). 3D gpr polarization analysis for imaging complex objects. In *proceeding of the 16th symposium on the Application of Geophysics to Engineering and Environmental Problems* (SADEEP, 2003).

Daniels, J. J., Lee, R., Yi, Y., Ortega, R., & Shalek, K. (2009). Broadband finite difference time domain modeling. In proceeding of s*ymposium on the Application of Geophysics to Engineering and Environmental Problems (SADEEP, 2009)(pp. 47-56)*.

Darijani, M. (2019). *Investigating modelling and inversion techniques for overburden*

stripping for uranium exploration in the Athabasca Basin, Canada [Doctoral thesis, Memorial University of Newfoundland and Labrador]. MUN Research repository. https://research.library.mun.ca/

Dawrea, A., Zytner, R.G., & Donald, J. (2021). Enhanced GPR data interpretation to estimate in situ water saturation in a landfill. *Waste Management, 120*(1), 175-182. https://doi.org/10.1016/j.wasman.2020.11.033

Dawson, C.B., Lane, J.W., White, E.A., & Belaval, M. (2002). Integrated geophysical characterization of the Winthrop landfill southern flow path, Winthrop. *In proceeding of symposium of the Application of Geophysics to Engineering and Environmental Problems (SADEEP, 2002)*.

Deng, E. A., Doro, K. O., & Bank, C. G. (2020). Suitability of magnetometry to detect clandestine buried firearms from a controlled field site and numerical modeling. *Forensic Science International*, *314*, 1-9. https://doi.org/10.1016/j.forsciint.2020.110396

Dentith, M., & Mudge, S.T. (2014). *Geophysics for the mineral exploration geoscientists*. Cambridge University Press. United Kingdom.

Dey, A., & Morrison, H. F. (1979). Resistivity modelling for arbitrary shaped two-dimensional structures. *Geophysical Prospecting, 27,* 1020-1036. https://doi.org/10.1111/j.1365-2478.1979.tb00961.x

Dumont, G., Robert, T., Marck, N., & Nguyen, F. (2017). Assessment of multiple geophysical techniques for the characterization of municipal waste deposit sites. *Journal of Applied Geophysics*, *145*, 74-83. https://doi.org/10.1016/j.jappgeo.2017.07.013

Edwards, L. S. (1997). A modified pseudosection for resistivity and IP.*Geophysics, 42(5),* 1020-1036.

Fenning, P. J., & Williams, B. S. (1997). Multicomponent geophysical surveys over completed landfill sites . In *Modern geophysics in engineering geology* (Engineering geology special publication no. 12, pp. 125-138). Geological society of London.

Ferrier, G., Frostick, L.E., & Splajt, T. (2009). Application of geophysical monitoring techniques as aids to probabilistic risk-based management of landfill sites. *The Geographical Journal, 175*(4), 304-314. https://doi.org/10.1111/j.1475-4959.2009.00340.x

Fraser, D.C. (1969). Contouring of VLF-EM Data. *Geophysics, 34*, 958-967. https://doi.org/10.1190/1.1440065

Fraser, D. C. (1972). A new multicoil aerial electromagnetic prospectingsystem. *Geophysics*, *37*(3), 518–537.

Frischknecht, F. C., Labson, V. F., Spies, B. R., & Anderson, W. L. (1991). Profiling methods using small sources. In M.N. Nabighian (Ed.), *Electromagnetic methods in applied geophysics* (pp. 105-270). Society of Exploration Geophysicists.

Garland, C. (2006). *Site characterization of the former wishing well dump site: Seismic refraction investigations* [Honours thesis, Memorial University of Newfoundland].

Genelle, F., Sirieix, C., Riss, J., & Naudet, V. (2012). Monitoring landfill cover by electrical resistivity tomography on an experimental site. *Engineering Geology*, *145*, 18-29. 10.1016/j.enggeo.2012.06.002

Geotexera Inc. (2023). *MAGNUM and PODIUM manual (Educational Version)*. St. John's, Newfoundland and Labrador, Canada. https://www.geotexera.com/

Geuzaine, C., & Remacle, J.-F. (2009). Gmsh: A 3-D finite element mesh generator with built-in pre and post-processing facilities. *International Journal for Numerical Methods in Engineering*, *79* (11), 1309-1331.

Grant, F. S., & West, G. F. (1965). *Interpretation Theory in Applied Geophysics.* McGraw-Hill Book Co. New York.

Green, A., Lanz, E., Maurer, H., & Boerner, D. (1999). A template for geophysical investigations of small landfills. *THE LEADING EDGE*,*18*(2), 248-254.

Griffiths, D. H., & Barker, R. D. (1993). Two-dimensional resistivity imaging and modelling in areas of complex geology. *Journal of Applied Geophysics*, *29*, 211-226. http://dx.doi.org/10.1016/0926-9851(93)90005-J

Haber, E., Ascher, U. M., & Oldenburg, D. (2000). On optimization techniques for solving

nonlinear inverse. *Inverse Problems*, *16*(5),1263-1280.

Hajar, B., Piga, C., Loddo, F., Ranieri, G., & Touhami, A.O. (2013). Geophysical surveys for the characterization of landfills. *International Journal of Innovation and Applied Studies, 4*(2), 254-263.

Hallof, P.G. (1957). *On the interpretation of resistivity and induced polarization field measurements* [Doctoral thesis, Massachusetts Institute of Technology]. http://hdl.handle.net/1721.1/54400

Hart, J. (2013). Geophysical Investigation of the Clay Cap at a Closed Landfill in Southwestern Ontario, Canada [Master thesis, University of Windsor]. https://scholar.uwindsor.ca/etdhub/

Hesse, A., Jolivet, A., & Tabbagh, A. (1986). New prospects in shallow depth electrical surveying for archeological and pedological applications. *Geophysics, 51*(3), 585-594. https://doi.org/10.1190/1.1442113

Hohmann, G. W. (1988). Numerical modeling for electromagnetic methods of geophysics. In M. N. Nabighian (Ed.), *Electromagnetic Methods in Applied Geophysics: Volume 1, Theory* (pp. 313-363). Society of Exploration Geophysicists.

Hrvoic, I. (1989). *Overhauser Magnetometers for measurement of the Earth's magnetic field* (User manual). GEM Systems Inc. https://www.geophysik.uni-bremen.de/statisch/downloads/254/Overhauser-Magnetometers.pdf

Huang, H. (2005). Depth of investigation for small broadband electromagnetic sensors. *Geophysics, 7*(6), 135-142. https://doi.org/ 10.1190/1.2122412

Huang, H., & Fraser, D. C. (2000). Airborne resistivity and susceptibility mapping in magnetically polarizable areas. *Geophysics*, *65*(2), 502–511. https://doi.org/10.1190/1.1444744

Huang, H., & Won, I. J. (2000). Conductivity and susceptibility mapping using broadband electromagnetic sensors. *Journal of Engvironmental and Engineering Geophysics*, *5*(4), 31-41.

Hutchinson, P. J. (1994). The geology of landfills. *Environmental Geosciences, 2*(1), 2-14.

Ibraheem, I. M., Tezkan, B., & Bergers, R. (2021). Integrated interpretation of magnetic and ert data to characterize a landfill in the north-west of Cologne, Germany. *Pure and Applied Geophysics*, *178*, 2127–2148. https://doi.org/10.1007/s00024-021-02750-x

Idris, A., Inanc, B., & Hassan, M.N. (2004). Overview of waste disposal and landfills/dumps in Asian countries. *Material cycles and waste management in Asia, 6,* 104–110.

Jackson, A., Jonkers, A.R.T., & Walker, M.R. (2000). Four centuries of geomagnetic secular variation from historical records. *Phil. Trans. R. Soc. A.,358*(1768), 957-990. https://doi.org/10.1098/rsta.2000.0569

Johnson, T.C., Slater, L.D., Ntarlagiannis, D., Day-Lewis, F.D.,& Elwaseif, M.(2012). Monitoring groundwater-surface water interaction using time-series and time-frequency analysis of transient three-dimensional electrical resistivity changes. *Water Resources Research, 48*(7), 1-13. https://doi.org/10.1029/2012WR011893

Junior, J.T.A., Pires, P.J.M., Domingues, D.L.P., & Campos, T.M.P. (2016). The use of ground penetrating radar in municipal solid waste landfill geotechnical investigation. *Journal of Engineering and Architecture, 10*(7), 822-827. doi: 10.17265/1934-7359/2016.07.011

Kearey, P., Brooks, M., & Hill, I. (2002). *An introduction to geophysical exploration* (3rd Ed.). Cambridge University Press.

Kearey, P., & Brooks, M. (1991). *An Introduction to geophysical exploration* (2nd ed.). Blackwell Scientific Publications Limited.

Kemna, A., Binley, A., Cassiani, G., Niederleithinger, E., Revil, A., Slater, L., Zimmermann, E. (2012). An overview of the spectral induced polarization method for near-surface applications. *Near Surface Geophysics*, *10*(6), 453-468. https://doi.org/10.3997/1873-0604.2012027

Khalil, M. H. (2012). Magnetic, geo-electric, and groundwater and soil quality analysis over a landfill from a lead smelter, Cairo, Egypt. *Journal of Applied Geophysics*,

86, 146-159. https://doi.org/10.1016/j.jappgeo.2012.08.004

Khalil, M. H., & Hassan, N. A. (2016). Ground Magnetic, GPR, and Dipole-Dipole Resistivity for Landfill Investigation. *International Journal of Geosciences*,*7*(6), 828-848.

Khesin, B., Alexeyev, V., & Eppelbaum, L. (1997). Rapid methods for interpretation of induced polarization anomalies. *Journal of Applied Geophysics*, *37*(2), 117-130. https://doi.org/10.1016/S0926-9851(97)00006-2

LaBrecque, D., Miletto, M., Daily, W., Ramirez, A., & Owen, E. (1996). The effects of noise on Occam's inversion of resistivity tomography data. *Geophysics*, *61*(2), 538-548. https://doi.org/10.1190/1.1443980

Lelièvre, P. G. (2023). *Tutorials and documentation for various programs written at Mount Allison University and Memorial University.* Geotexera Inc.

Lelièvre, P.G., Farquharson, C.G., & Hurich, C.A. (2012). Joint inversion of seismic travel times and gravity data on unstructured grids with application to mineral exploration. *Geophysics, 77*(1), k1-k15. https://doi.org/10.1190/GEO2011-0154.1

Leroux, V., Dahlin, T., & Svensson, M. (2007). Dense resistivity and induced polarization profiling for a landfill restoration project at Harlov. *SAGE*, *25*(1), 49-60. https://doi.org/10.1177/0734242X07073668

Li, Y., & Oldenburg, D. W. (1996). 3-D inversion of magnetic data. *Geophysics*, *61*(2), 394-408. http://dx.doi.org/10.1190/1.1443968

Loke, M. H. (2001). *Electrical imaging surveys for environmental and engineering studies. A practical guide to 2-D and 3-D surveys.* IRIS Instruments. https://pages.mtu.edu/~ctyoung/LOKENOTE.PDF

Loke, M.H. (2015). *2-D and 3-D electrical imaging surveys* (User manual). Geotomo software. https://web.gps.caltech.edu/classes/ge111/Docs/ResNotes_Loke.pdf

Loke, M.H., & Barker, R.D. (1995). Least-squares deconvolution of apparent resistivity pseudosections. *Geophysics, 60*, 1682-1690.

Loke, M.H. (2024). *Tutorial: 2-D and 3-D electrical imaging surveys* (User manual). Geotomo Software. https://www.geotomosoft.com/

Loke, M. H., Chambers, J.E., Rucker, D.F., Kuras, O., & Wilkinson, P.B. (2013). Recent developments in the Direct-Current geoelectrical imaging Method. *Journal of Applied Geophysics, 95*, 135-156. https://doi.org/10.1016/j.jappgeo.2013.02.017

Loperte, A., Bavusi, M., Lapenna, V., Moscatelli, U., & Mingizzi, S. (2010). Magnetic and ground penetrating radar for the research of medieval buried structures in Marche region. *Advance Geoscience, 24*, 89–95. https://doi.org/10.5194/adgeo-24-89-2010

Mack, T.J. (1993). Detection of contaminant plumes by borehole geophysical logging. *Ground water monitoring and remediation review, 13*(1),107-144.

Marchetti, M., Mauro, D. D., Cafarella, L., & Zirizzotti, A. (2002). Ground magnetometric surveys and integrated geophysical methods for solid. *Annals of Geophysics*, *45*(3), 563-573. https://doi.org/10.4401/ag-3519

Marchetti, M., Sapia, V., & Settimi, A. (2011). Magnetic anomalies of steel drums: a review of the literature and research results of the INGV. *Annals of geophysics, 56* (1), 1-12.

Massarelli, C., Campanale, C., & Uricchio, V.F. (2021). Ground penetrating radar as a functional tool to outline the presence of buried waste: A case study in South Italy. *Sustainability 2021, 13*(7)*,* 1-18. https://doi.org/10.3390/su13073805

McConnell, T.J., Lo, B., Ryder-Turner, A., & Musser, J.A. (1999, August). Enhanced 3D seismic surveys using a new airborne pipeline mapping system. In *6th International Congress of the Brazilian Geophysical Society* (pp. 516–519). European Association of Geoscientists & Engineers.

McNeill, J. D. (1980). *Electromagnetic Terrian Conductivity Measurement at Low Induction Numbers.* Geonics Limited. https://www.geonics.com/pdfs/technicalnotes/tn6.pdf

Meju, M.A. (2000). Geoelectrical investigation of old/abandoned, covered landfill sites in urban areas: Model development with a genetic diagnosis approach. *Journal of*

Applied Geophysics, *44*(2), 115-150. https://doi.org/10.1016/S0926-9851(00)00011-2

Meyer De Stadelhofen, C. (1991). Application de la géophysique aux recherches d'eau**.** In Singhal, B. B. S., & Gupta, R. P. (Eds.), *Applied hydrogeology of fractured rocks* (pp. 133-155). Springer. http://dx.doi.org/10.1007/9789048187997

Missiaen, T., & Feller, P. (2008). Very-high-resolution seismic and magnetic investigations of a chemical munition dumpsite in the Baltic Sea. *Journal of Applied Geophysics*, *65*(3), 142–154. https://doi.org/10.1016/j.jappgeo.2008.07.001

Mwakanyamale, K., Slater, L., Binley, A., & Ntarlagiannis, D. (2012). Lithologic imaging using complex conductivity: Lessons learned from the Hanford 300 Area. *Geophysics*, *77*(6), 397-409. https://doi.org/10.1190/geo2011-0407.1

Nabighian, M. N., Grauch, V. J., Hansen, R. O., LaFehr, T. R., Li, Y., Peirce, J. W., Ruder, M. E. (2005). The historical development of the magnetic method in exploration. *Geophysics, 70(6),* 33-61. https://doi.org/10.1190/1.2133784

Ntarlagiannis, D., Robinson, J., Soupios, P., & Slater, L. (2016). Field-scale electrical geophysics over an olive oil mill waste deposition site: Evaluating the information content of resistivity versus induced polarization (IP) images for delineating the spatial extent of organic contamination. *Journal of Applied Geophysics*, *135*, 418-426. https://doi.org/10.1016/j.jappgeo.2016.01.017

Oldenburg, D. W., & Li, Y. (1994). Inversion of induced polarization data. *Geophysical Prospecting, 59*(9), 1327-1341. https://doi.org/10.1190/1.1443692

Oldenburg, D.W., & Li, Y. (1999). Estimating Depth of Investigation in DC resistivity and IP surveys. *Geophysics, 64*(2)*,*403-416. https://doi.org/10.1190/1.1444545

O'Neill, P. (2008). *The Oldest City: The Story of St. John's Newfoundland.* Boulder Publications Ltd.

Osmond, S. (2021). *Out of sight, out of mind: The story of Kelly's Brook, the Empire Avenue Landfill, and the Future of Urban Streams in St. John's, NL*.

https://storymaps.arcgis.com/stories/c948a716ac874ae08af8b74eaac27ef0

Overhauser, A.W. (1953). Paramagnetic Relaxation in Metals. *Phys. Rev., 89*(4), 689-700.

Park, S., Yi, M.J., Kim, J.H., & Shin, S.W. (2016). Electrical resistivity imaging (ERI) monitoring for ground water contamination in an uncontrolled landfill. *Journal of Applied Geophysics, 135,* 1-7. 10.1016/j.jappgeo.2016.07.004

Pellerin, L. (2002). Applications of electrical and electromagnetic methods for environmental and geotechnical investigations. *Surveys in Geophysics, 23*(2), 101–132.

Porsani , J. L., Filho , W. M., Elis , V. R., Shimeles , F., Dourado , J. C., & Moura , H. P. (2004). The use of GPR and VES in delineating a contamination plume in a landfill site: A case study in SE Brazil. *Journal of Applied Geophysics* , *55*(3), 99-209. https://doi.org/10.1016/j.jappgeo.2003.11.001

Prezzi, C., Orgeira, M.J., Ostera, H., & Vasquez, C.A. (2005). Ground magnetic survey of a municipal solid waste landfill: Pilot study in Argentina. *International Journal of Geosciences, 47,*889–897.

Pujari, P.R., Pardhi, P., Muduli, P., Harkare, P., & Nanoti, M.V. (2007). Assessment of pollution near landfill site in Nagpur, India by resistivity imaging and GPR. *Environmental Monitoring and Assessment, 131*,489–500. https://doi.org/10.1007/s10661-006-9494-0

Rajagopalan, S. (2003). Analytic signal vs. reduction to pole: Solutions for low magnetic latitudes. *Exploration Geophysics*, *34*(4), 257-262. https://doi.org/10.1071/EG03257

Reyes-Lopez, J.A., Ramírez-Hernández, J., Lázaro-Mancilla, O., Carreón-Diazconti, C., & Martín-Loeches Garrido, M. (2008). Assessment of groundwater contamination by landfill leachate: A case in México. *Waste Management, 28*(1), 33-39. https://doi.org/10.1016/j.wasman.2008.03.024

Ripka, P., & Arafat, M.M. (2019). Magnetic Sensors: Principles and Applications. *Encyclopedia of materials: Electronics,3,*14-27. https://doi.org/10.1016/B978-0-12-819728-8.00137-6

Robinson, S. & Coruh, C. (1988). *Basic Exploration Geophysics.* John Wiley and Sons.

Samouëlian, A., Cousin, I., Tabbagh, A., Bruand, A., & Richard, G. (2005). Electrical resistivity survey in soil science: A review. *Soil &Tillage Research, 83,* 173-193. http://dx.doi.org/10.1016/j.still.2004.10.004

Schultz, J.J. (2012). *Detecting buried remains using ground penetrating radar* (Report No. 238275). U.S department of Justice. https://www.ojp.gov/pdffiles1/nij/grants/238275

Scott, J., Beydoun, D., Amal, R., Low, G., & Cattle, J. (2007). Landfill Management, Leachate Generation, and Leach Testing of Solid Wastes in Australia and Overseas. *Critical Reviews in Environmental Science and Technology, 35*(3), 239-332.

Seaton, W. J., & Burbey, T. J. (2002). Evaluation of two-dimensional resistivity methods in a fractured crystalline-rock terrane. *Journal of Applied Geophysics*, *51*(1),21-41. https://doi.org/10.1016/S0926-9851(02)00212-4

Seequent Inc. (2022). Gridding Data Methods - Overview and Comparison. *Bentley system*. https://help.seequent.com/Oasismontaj

Sensors and Software Inc. (2016). Understanding GPR resolution and target detection. https://www.sensoft.ca/blog/understanding-gpr-resolution-and-target-detetction/

Sensors and Software Inc. (2021), EKKO_Project processing module (User guide). Sensor and software Inc. https://www.sensoft.ca/wp-content/uploads/2021/07/2016-00064-03.pdf

Sensors and Software Inc. (2022). GPR velocity table and Analysis. Geophysical equipment rental LLC and K.D. Jones instrument corp. https://gprrental.com/gpr-velocity-table-analysis/

Seymour, E.A. (1963, March 20). The passing scene: New city hall. *The Daily News*. https://dai.mun.ca/digital/dailynews/

Siegel, H.O. (1959). Mathematical formulation and type curves for Induced Polarization. *Geophysics, 24*, 547-563. https://doi.org/10.1190/1.1438625

Smith, B.D., McCafferty, A.E., & McDougal, R.R. (2000). Utilization of airborne magnetic, electromagnetic, and radiometric data in abandoned mine land investigations. In Church, S.E (Ed.), *Preliminary release of scientific reports on the acidic drainage in the Animas River watershed, San Juan County, Colorado* (pp. 86-91). U.S. Geological Survey.

Soupios, P., Papadopoulos, N., Papadopoulos, I., Kouli, M., Vallianatos, F., Sarris, A., & Manios, T. (2007). Application of integrated methods in mapping waste disposal areas. *Springer, 3*(53), 661-675.

Spector, A., & Grant, F.S. (1970). Statistical Models for interpreting aeromagnetic data. *Geophysics, 35*, 293-302. https://doi.org/10.1190/1.1440092

Spies, B. R., & Frischknecht, F. C. (1991). Electromagnetic sounding. In M. N Nabighian (Eds.), *Electromagnetic Methods in Applied Geophysics.*Society of Exploration Geophysicists.

Splajt, T., Ferrier, G., & Frostick, L.E. (2003). Application of ground penetrating radar in mapping and monitoring landfill sites. *Springer, 4,*963–967.

Stenson, R. W. (1988). Electromagnetic Data acquisition techniques for landfill investigations. *Symposium on the Application of Geophysics to Engineering and Environmental Problems*, 833.

Sumner, J. S. (1976). *Principles of induced polarization for geophysical exploration.* Elsevier Scientific Publishing company. U. S.A.

Telford, W. M., Geldart, L. P., & Sheriff, R. E. (1990). *Applied geophysics*. Cambridge

university press. New York.

Ulaby, F. T. (2001). *Fundamentals of applied electromagnetics.* Prentice Hall. U.S.A.

Utsi, E.C. (2017). *Ground Penetrating Radar: Theory and Practice*. Joe Hayton. United Kingdom.

Vollprecht, D., Bobe, C., Stiegler, R., Vijver, E. V., Wolfsberger, T., Küppers, B., & Scholger, R. (2019). Relating magnetic properties of municipal solid waste constituents to iron content – implications for enhanced landfill mining. *Detritus*, *8*, 31-46. https://doi.org/10.31025/2611-4135/2019.13876

Voukkali, I., Papamichael, I., Loizia, P., & Zorpas, A. (2023). Urbanization and solid waste production: prospects and challenges. *Environmental Science and Pollution Research, 31*, 1-12.

Ward, S. H., & Hohmann, G. W. (1988). Electromagnetic theory for geophysical applications. In M.N Nabighian (Ed.), *Electromagnetic Methods in Applied Geophysics.* Society of Exploration Geophysicists.

Wicks, A. J. (n.d.). *Down in the dumps: Garbage Disposal in St. John's (1892-1930).* St. John's archive center.

Whiteley, R. J. (2010). Geophysics at Australian Landfills: Case Studies. *ASEG Extended Abstract*s, *2010*(1), 1-4. https://doi.org/10.1081/22020586.2010.12041880

Won, I. J., Keiswetter, D. A., Fields, G. R., & Sutton, L. C. (1996). GEM-2: A new multifrequency electromagnetic sensor. *Journal of Environmental and Engineering Geophysics,1*(2), 129-137. https://doi.org/10.4133/JEEG1.2.129

Wu, T.N., Huang, Y.C. (2006). Detection of illegal dump deposit with GPR: case study. *Practice periodical of hazardous, toxic, and radioactive Waste Manag., 10*(3), 144–149. https://doi.org/10.1061/(ASCE)1090-025X(2006)10:3(144)

Yannah, M., Martens, K., Camp, M.V., & Walraevens, K. (2017). Geophysical exploration of an old dumpsite in the perspective of enhanced landfill mining in Kermt area, Belgium. *Bull Eng Geol Environ., 2*,1-13. https://doi.org/10.1007/s10064-017-1169-2.

Yochim, A., Zytner, R.G., McBean, E.A., & Endres, A.L. (2013). Estimating water content in an active landfill with the aid of GPR. *Waste Management*, *33,* 2015-2028. http://dx.doi.org/10.1016/j.wasman.2013.05.020

Zhang, C., Mushayandebvu, M.F., Reid, A.B., J. Derek Fairhead, J.D., & Mark E. Odegard, M.E. (2000). Euler deconvolution of gravity tensor gradient data. *Geophysics, 65*(2), 512–520.

Zhang, T., Zhang, D., Zheng, D., Guo, X., & Zhao, W. (2022). Construction waste landfill volume estimation using ground penetrating radar. *Waste Management & Research, 40*(8),1167-1175.

Appendix A: Magnetic Survey

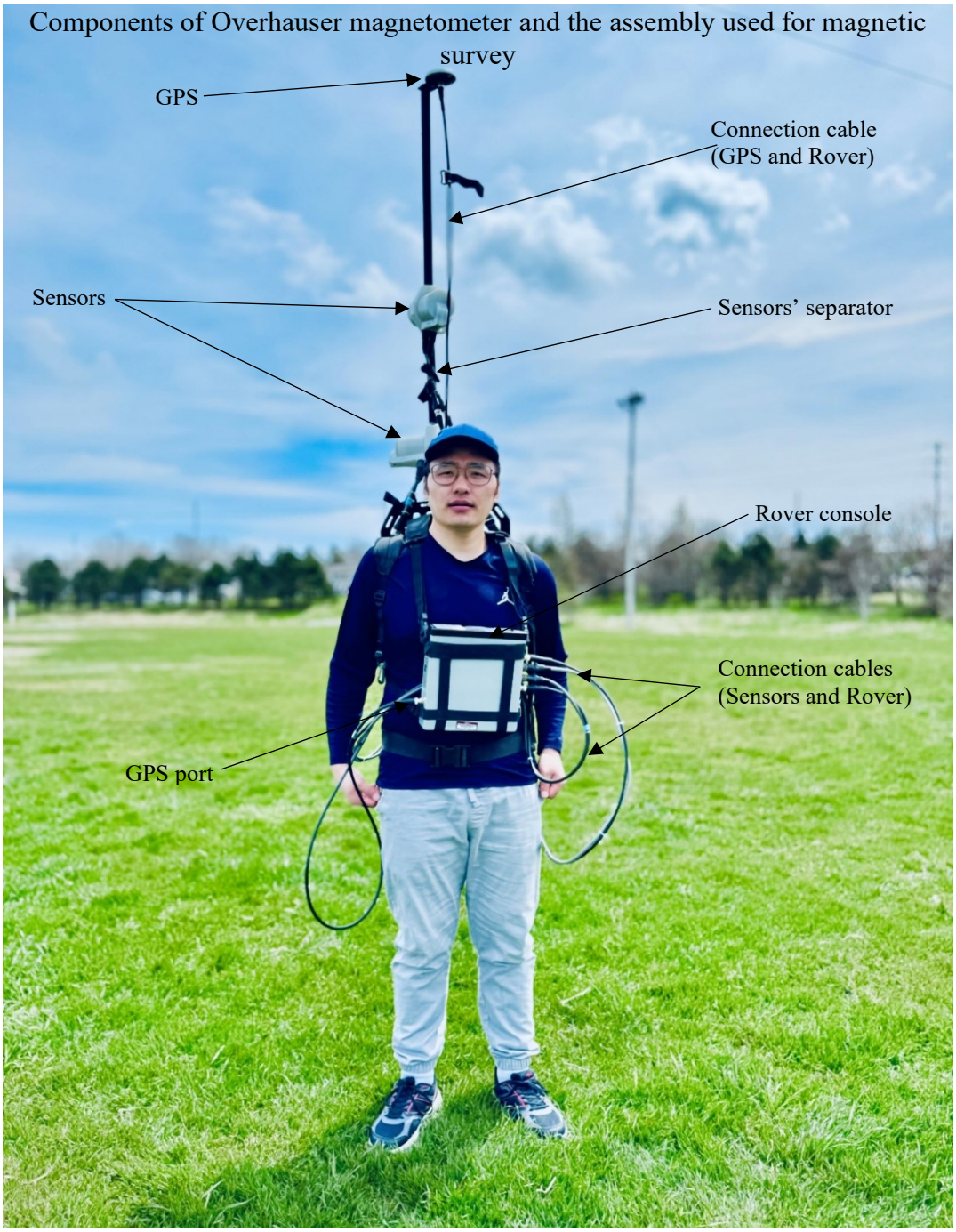

Figure A.1: Details of Overhauser magnetometer and its components.

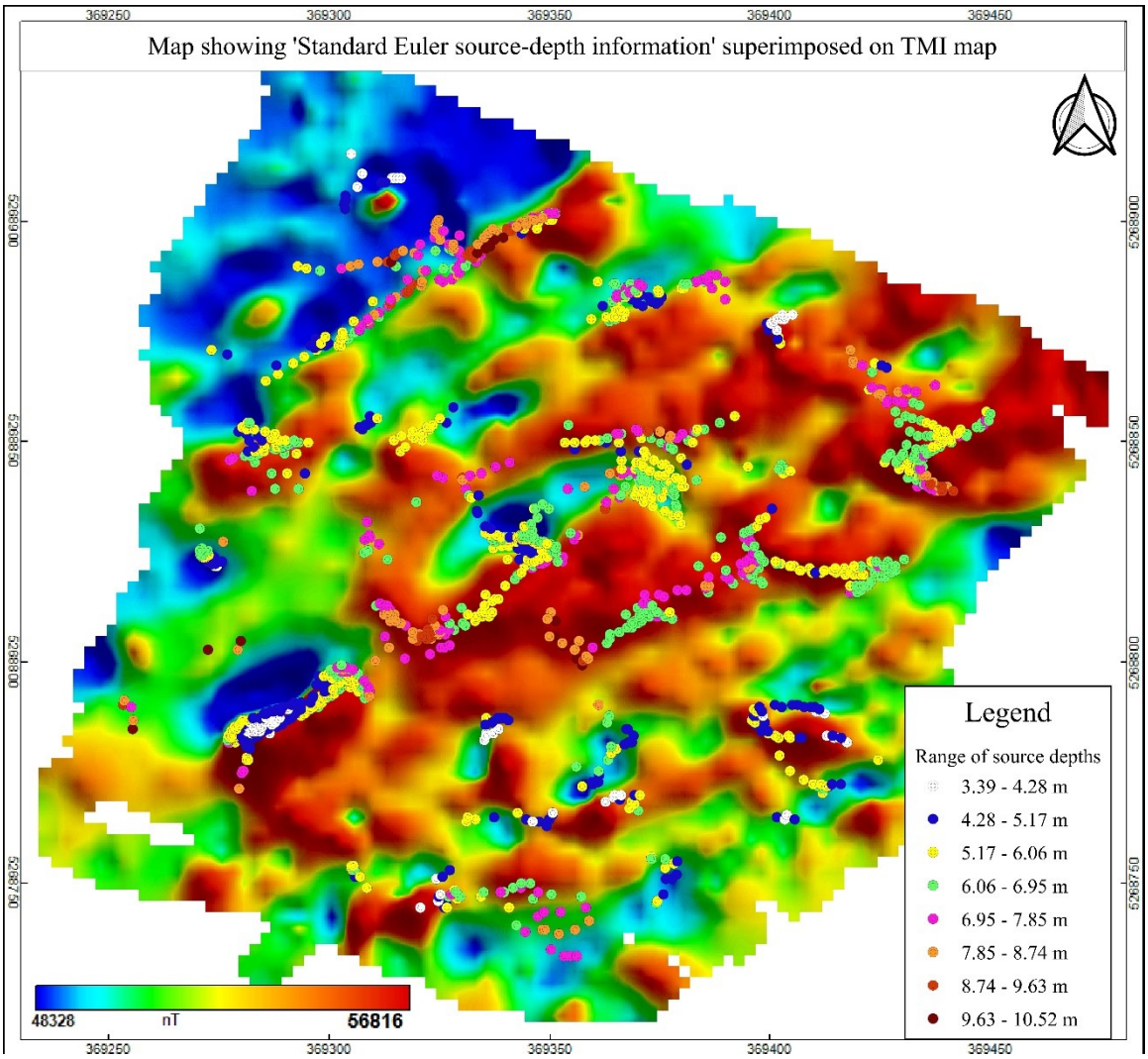

Figure A.2: Depth-to-sources estimates from the standard Euler algorithm.

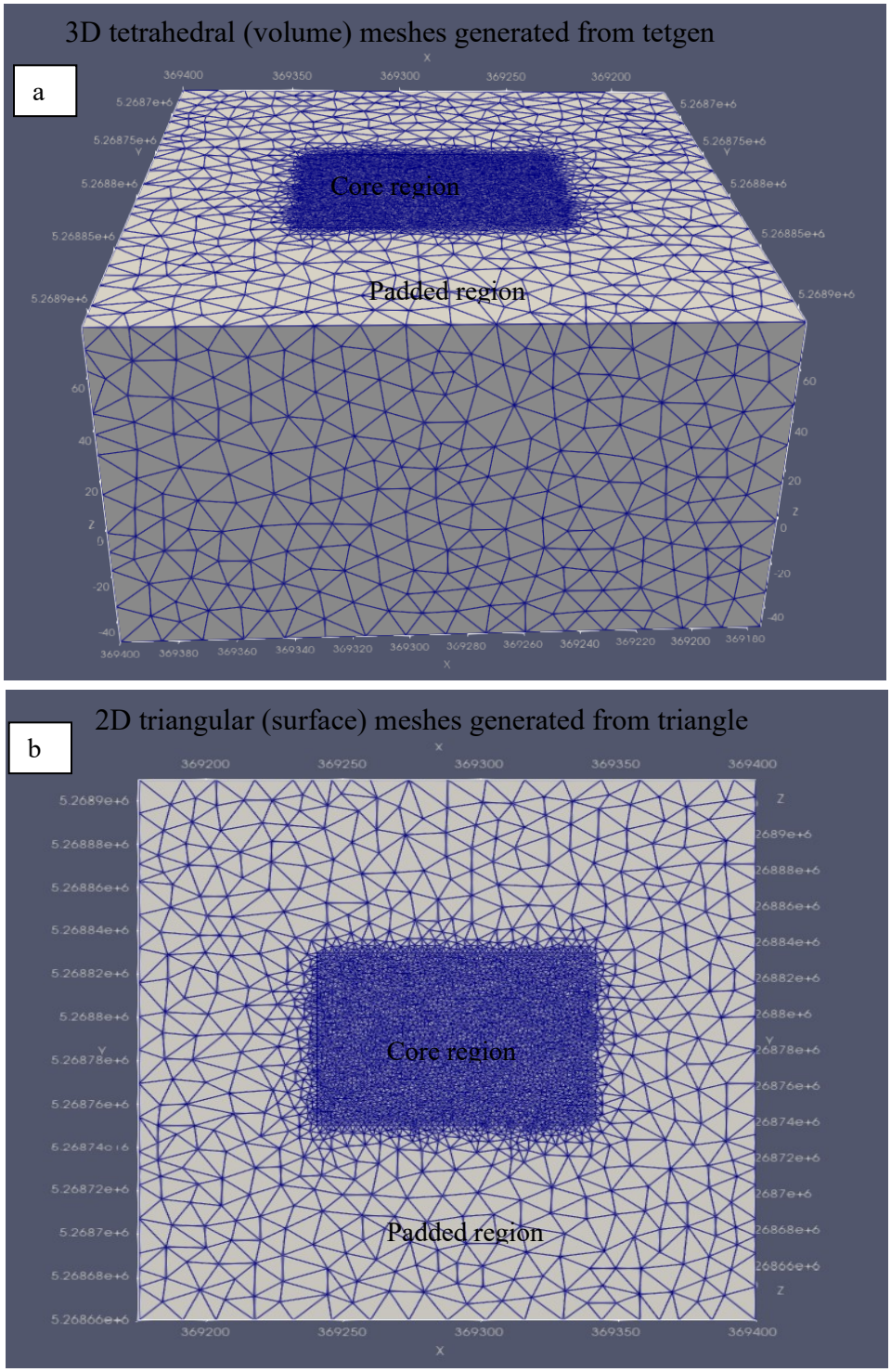

Figure A.3: Details of model regions and mesh used for 3D susceptibility inversion.

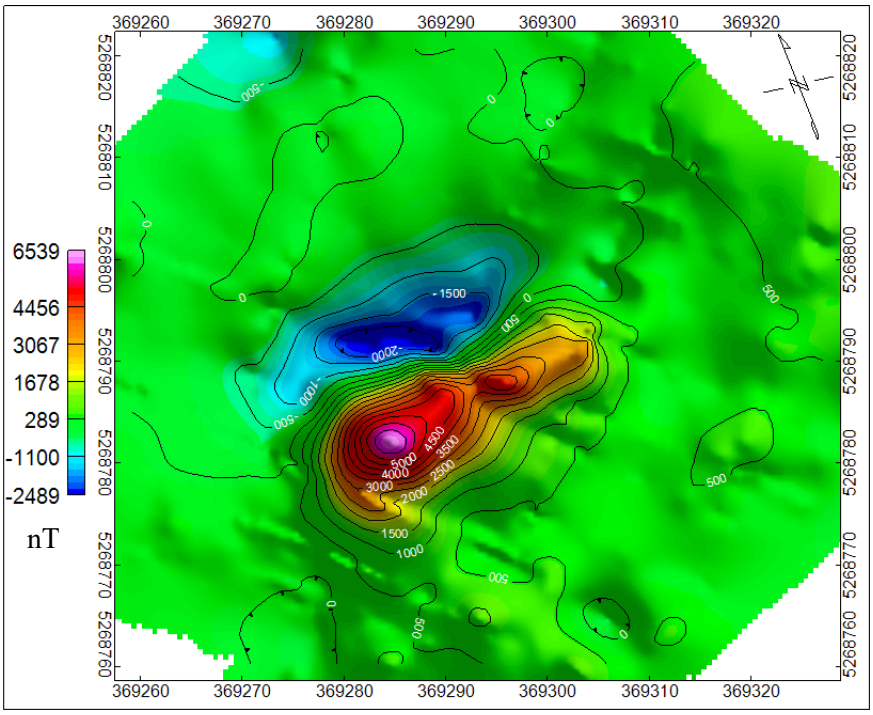

Figure A.4: Residual magnetic data used for 3D susceptibility inversion (Color scale=linear).

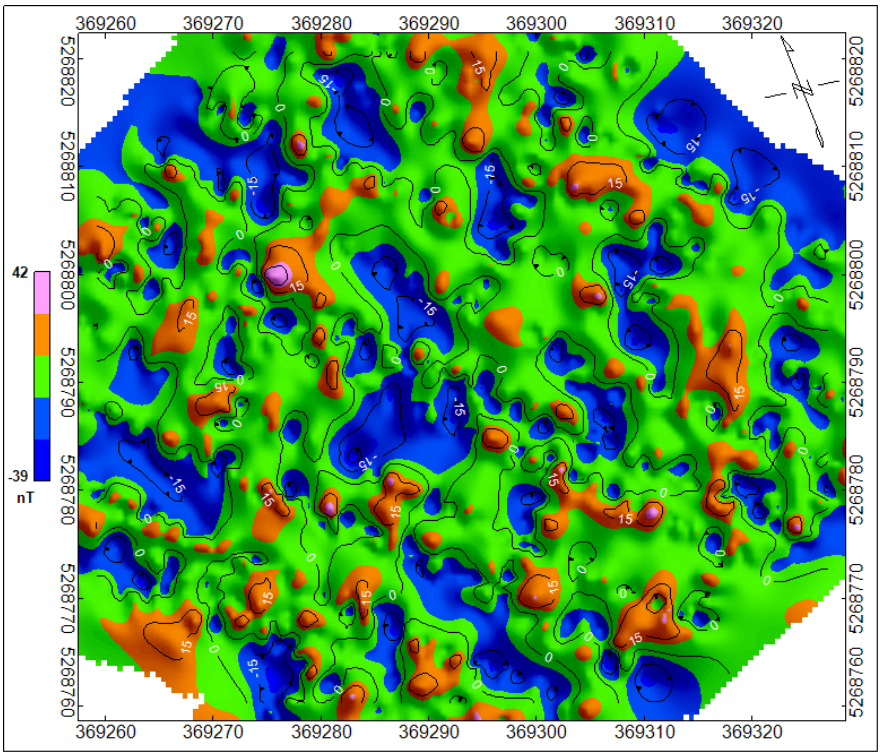

Figure A.5: Differences of input data and inversion data (Color scale=linear).

Appendix B: DC Resistivity and IP Surveys

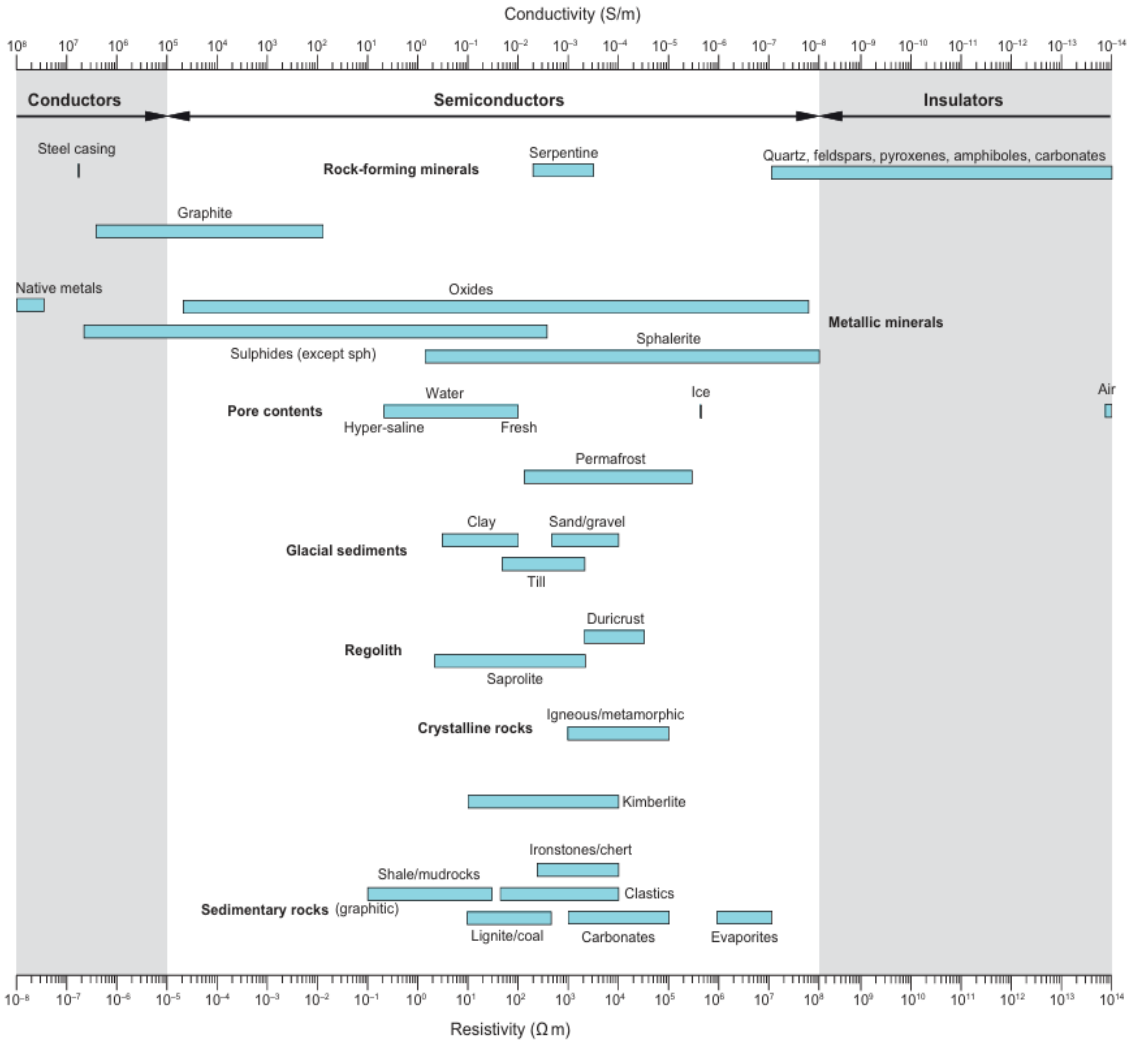

Figure B.1: Typical ranges of resistivity values for rock types and common Earth materials. (Courtesy: Dentith and Mudge, 2014).

Dipole-Dipole

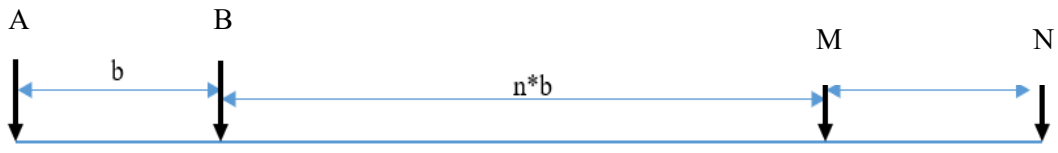

Figure B.2: Typical Dipole-Dipole array.

Figure B.3: The automatic sequence designed in ElectreII.

Figure B.3 depicts illustrations of sequence of measurements taken for the Wenner-Schlumberger array surveys. The sequence was created with a minimum electrode

spacing of 3 m, and used for all the six profiles. However, the actual minimum electrode spacing deployed for the first four profiles (DCR_profile 1 to DCR_profile 4) was 5 m. Hence, the electrode spacings and apparent resistivity values in the data files were adjusted appropriately before the models were computed. The designed sequence has the three different M-N spacings, each with 9 levels (green marker), 6 levels (yellow marker), 2 levels (blue marker) and 1 level (red marker).

Figure B.4: Components of the Syscal Junior system from Iris instruments used in this work.

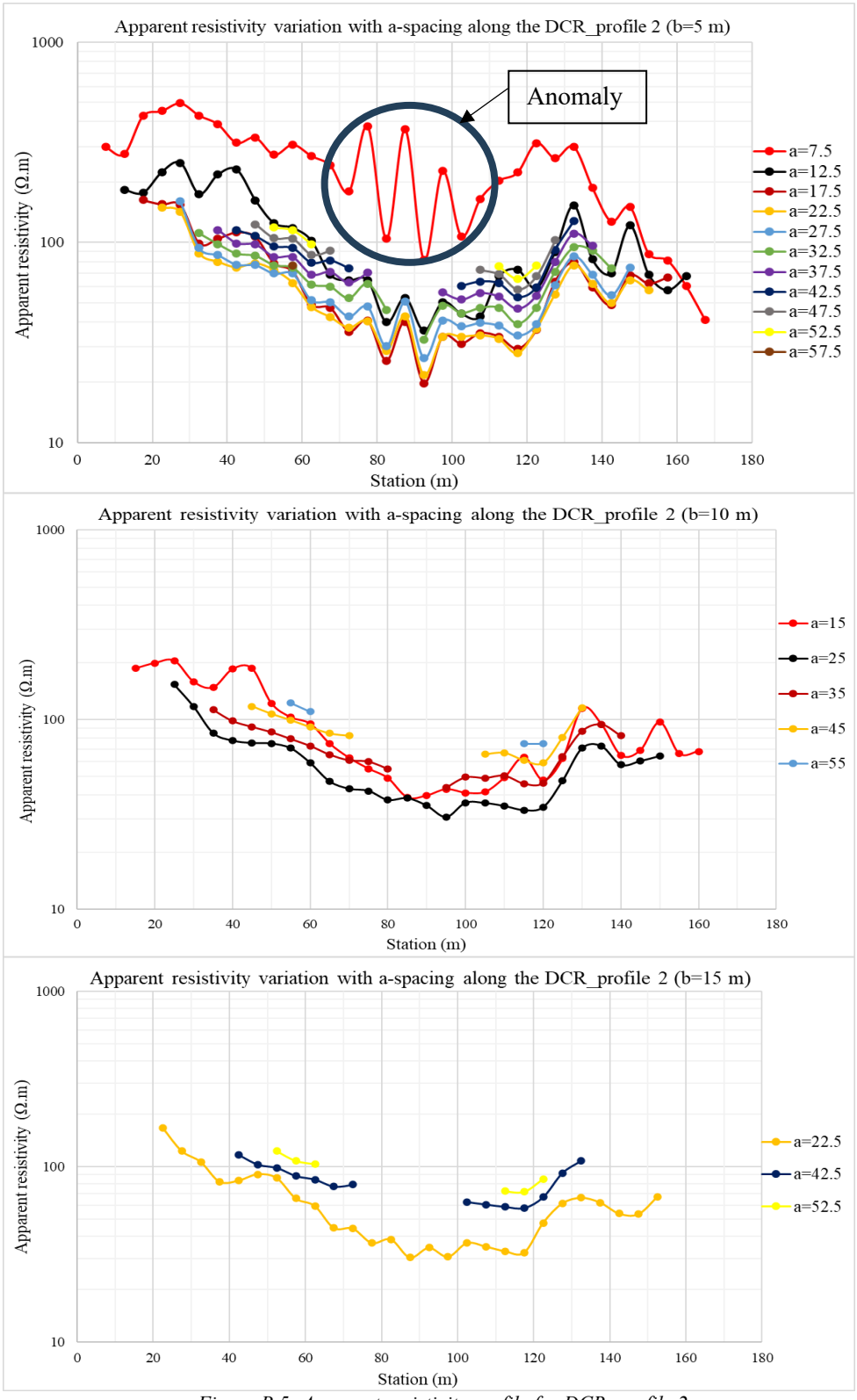

Figure B.5: Apparent resistivity profile for DCR_profile 2.

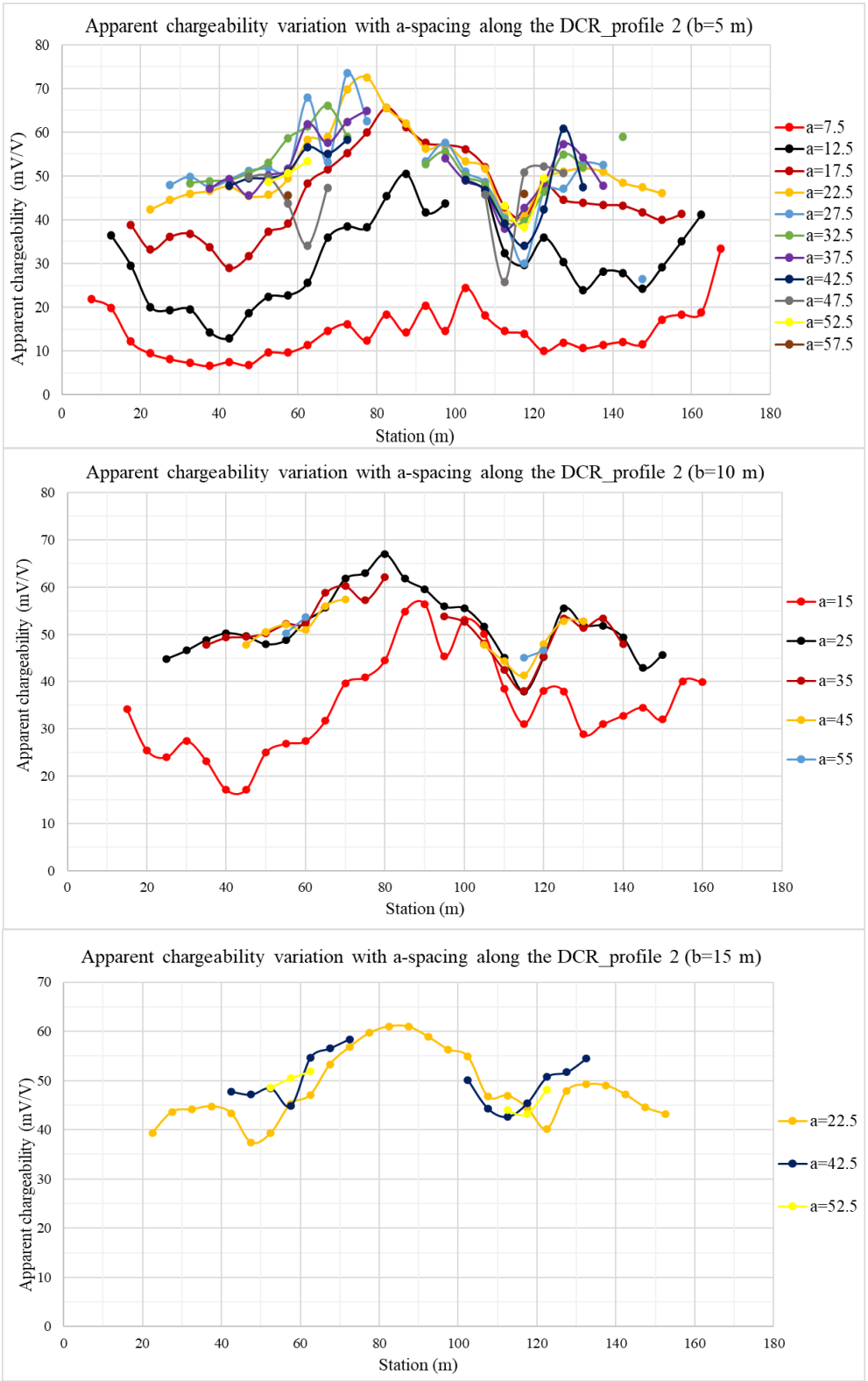

Figure B.6: Apparent chargeability profile for DCR_profile 2.

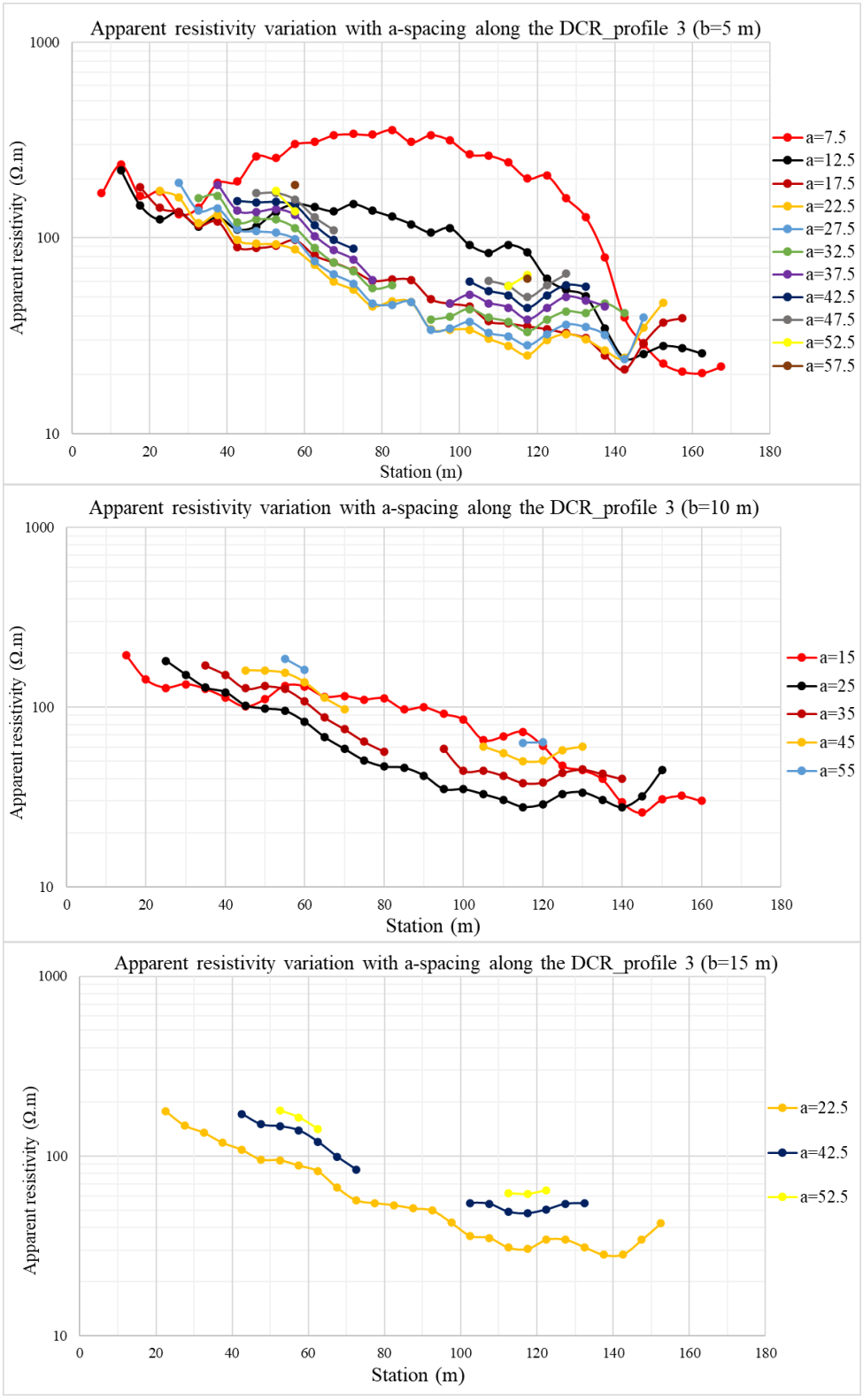

Figure B.7: Apparent resistivity profile for DCR_profile 3.

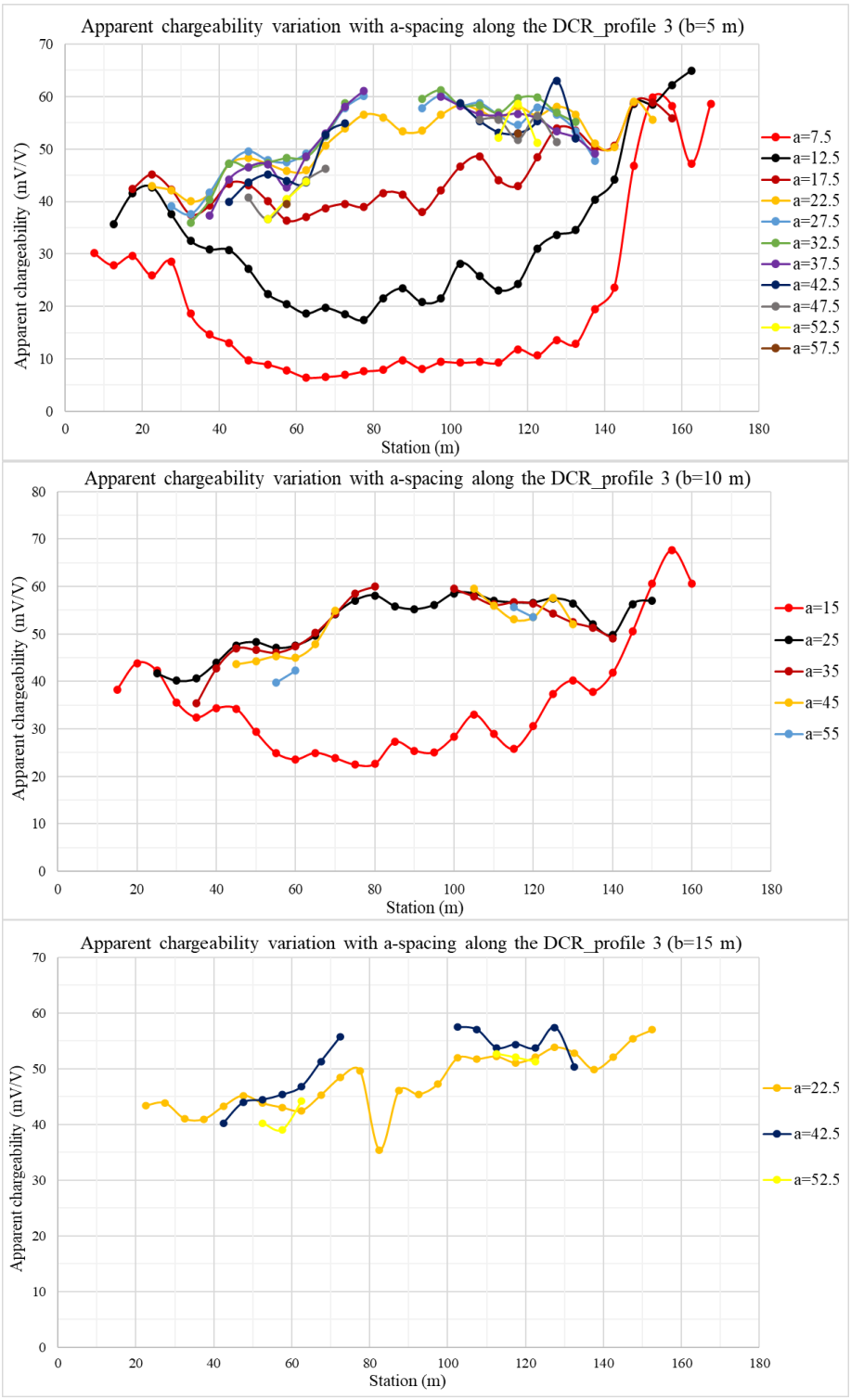

Figure B.8: Apparent chargeability profile for DCR_profile 3.

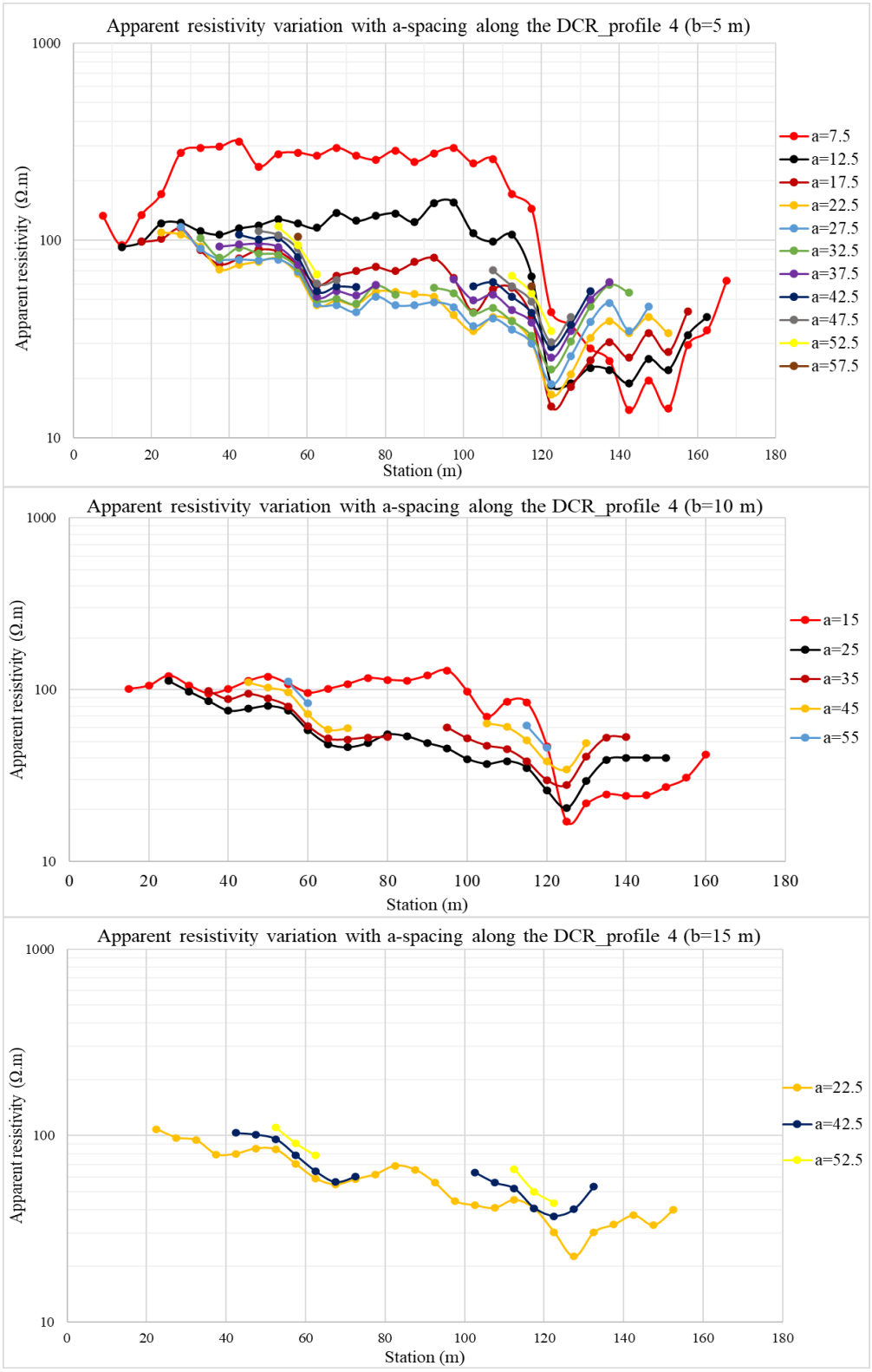

Figure B.9: Apparent resistivity profile for DCR_profile 4.

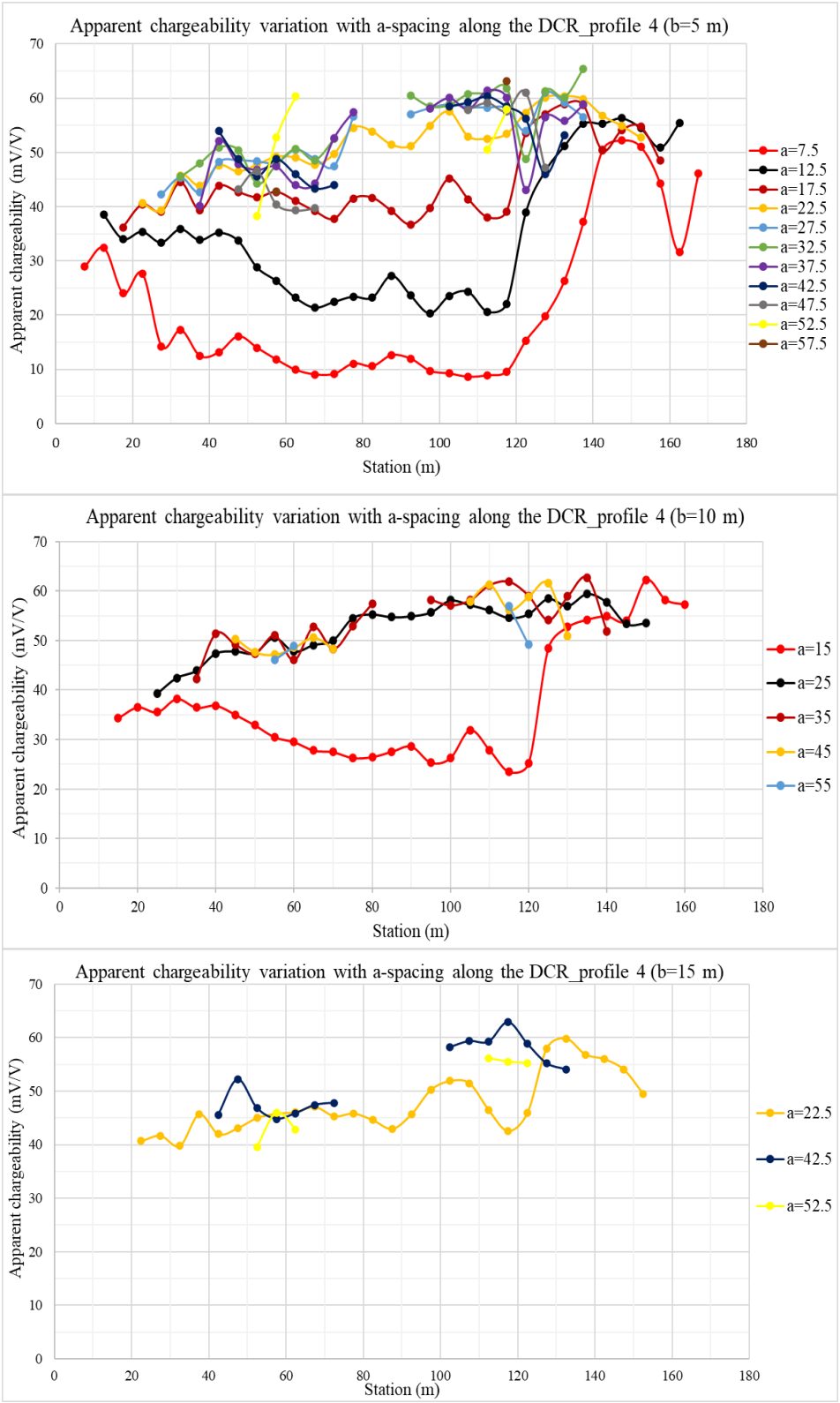

Figure B.10: Apparent chargeability for DCR_profile 4.

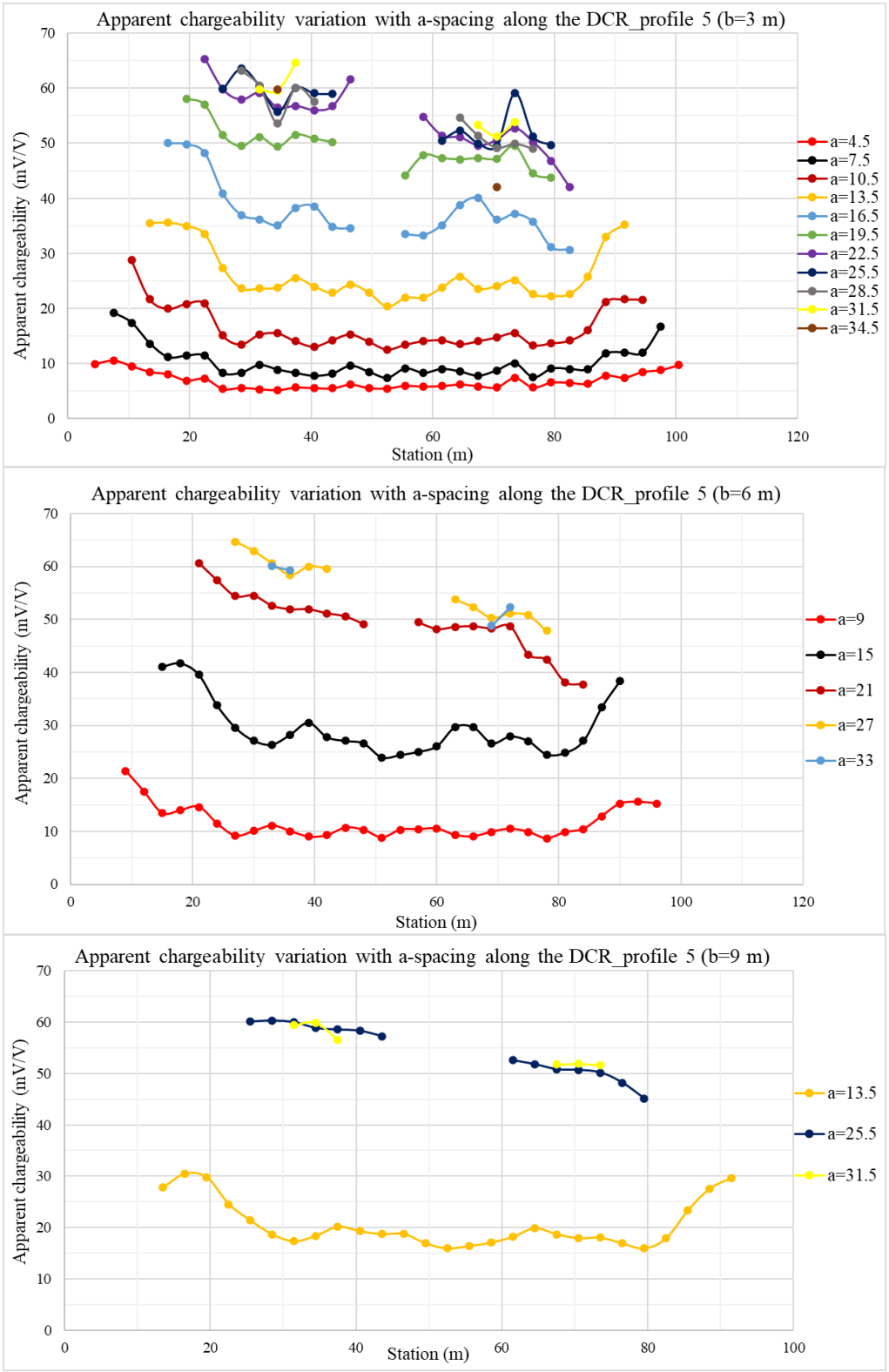

Figure B.11: Apparent chargeability for DCR_profile 5.

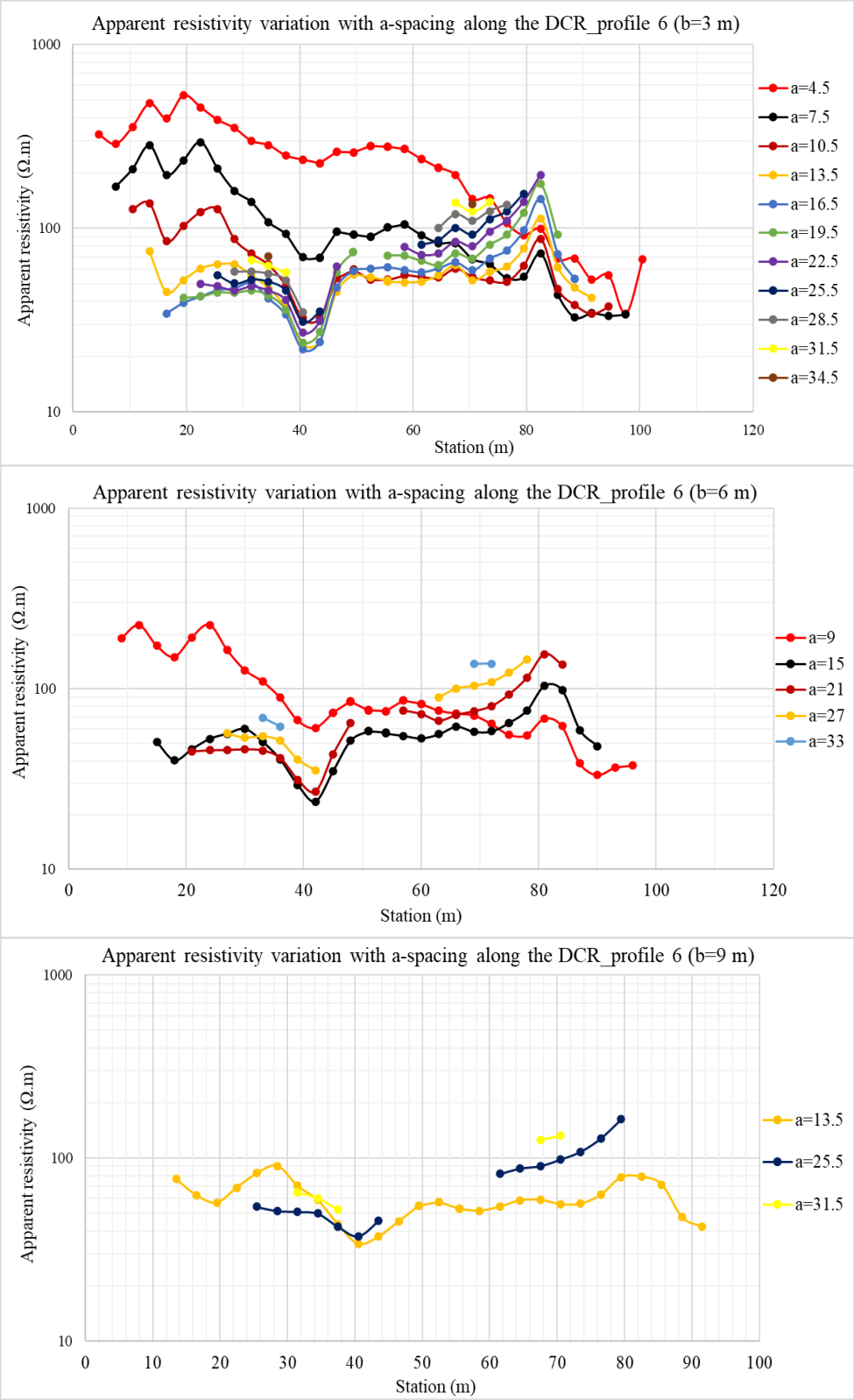

Figure B.12: Apparent resistivity for DCR_profile 6.

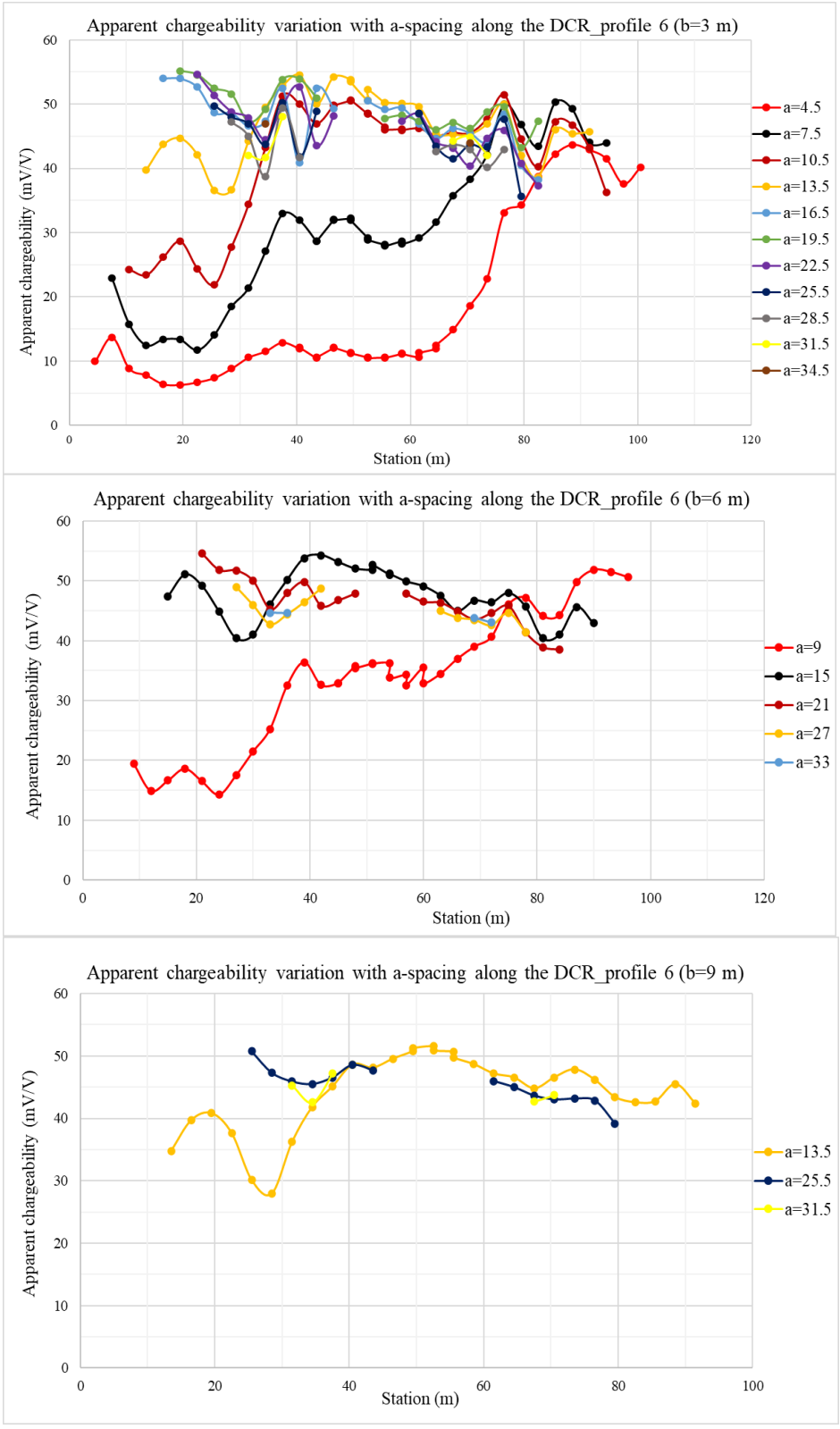

Figure B.13: Apparent chargeability for DCR_profile 6.

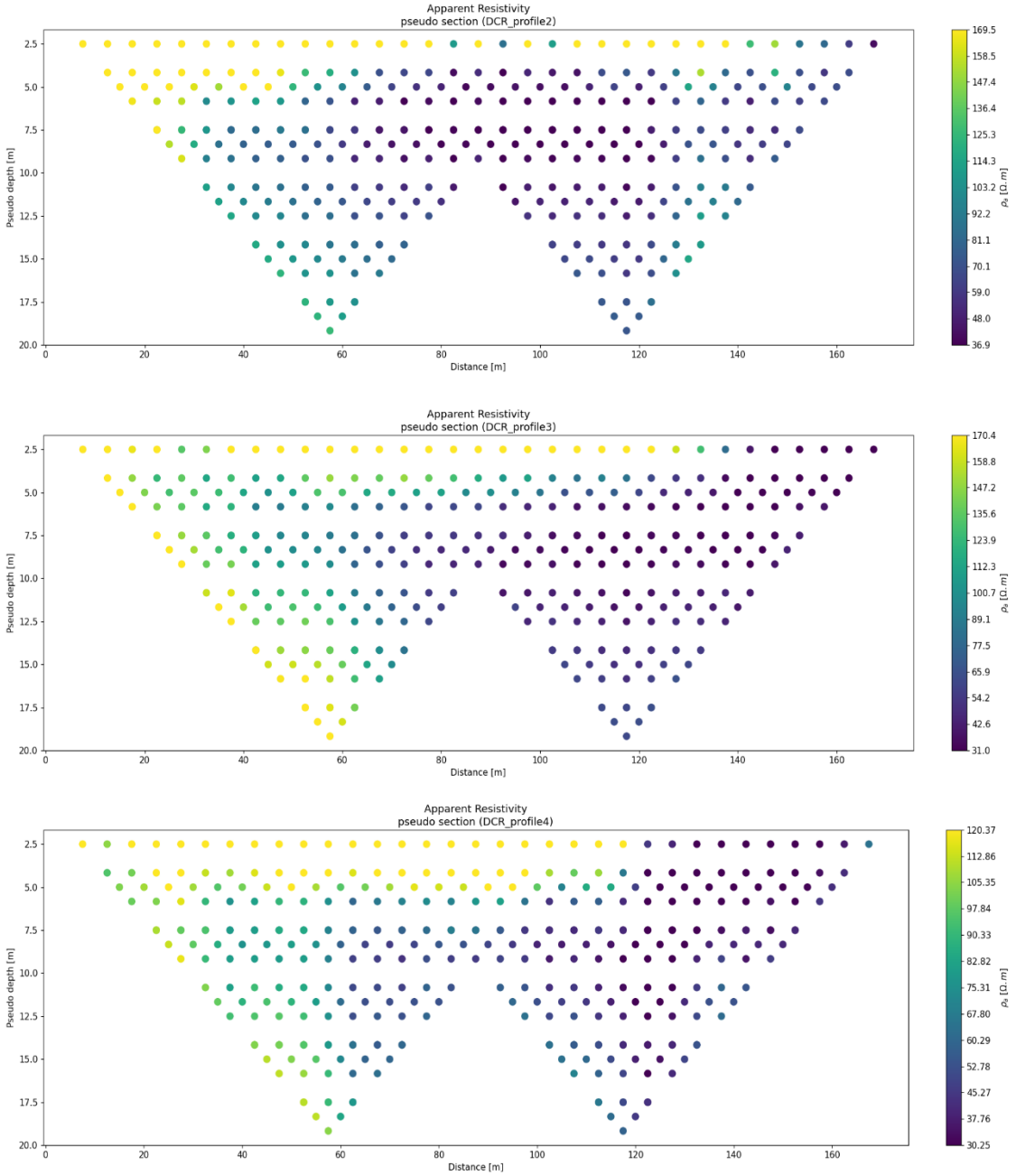

Figure B.14: Apparent resistivity for DCR_profile 2 to DCR_profile 4.

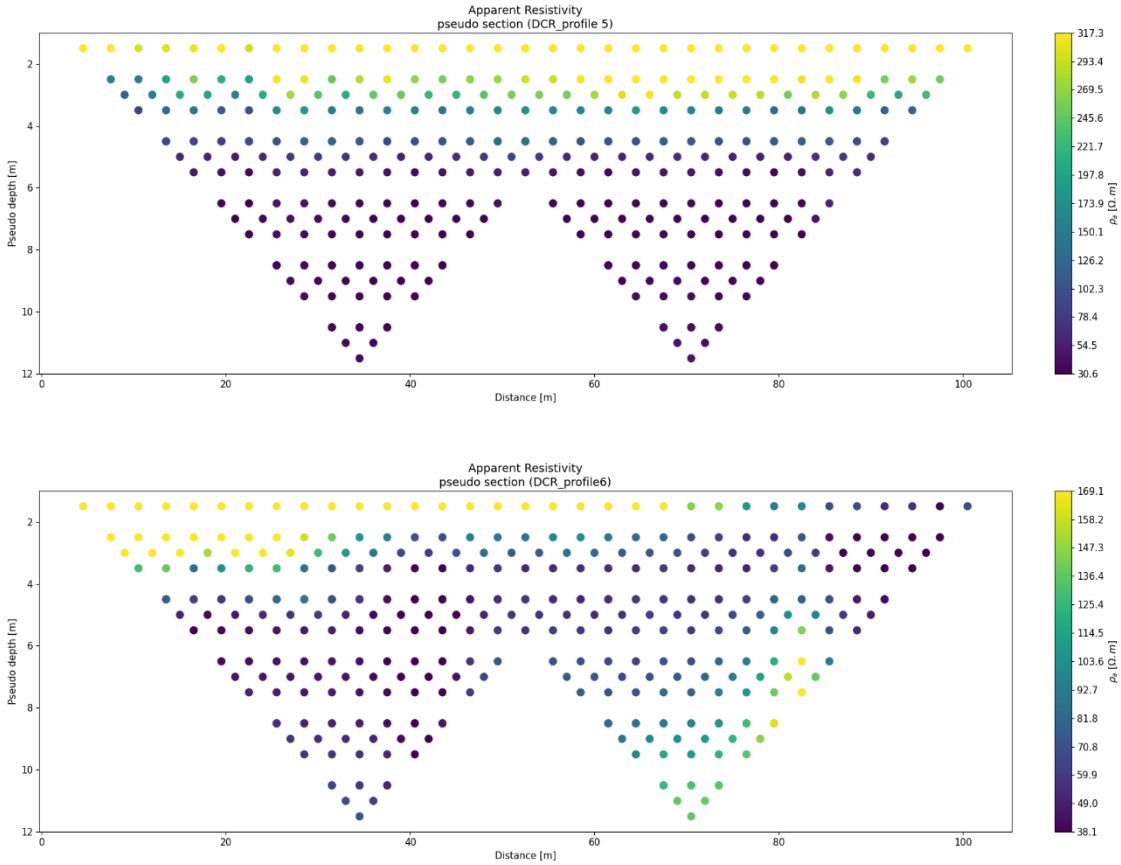

Figure B.15: Apparent resistivity for DCR_profile 5 to DCR_profile 6.

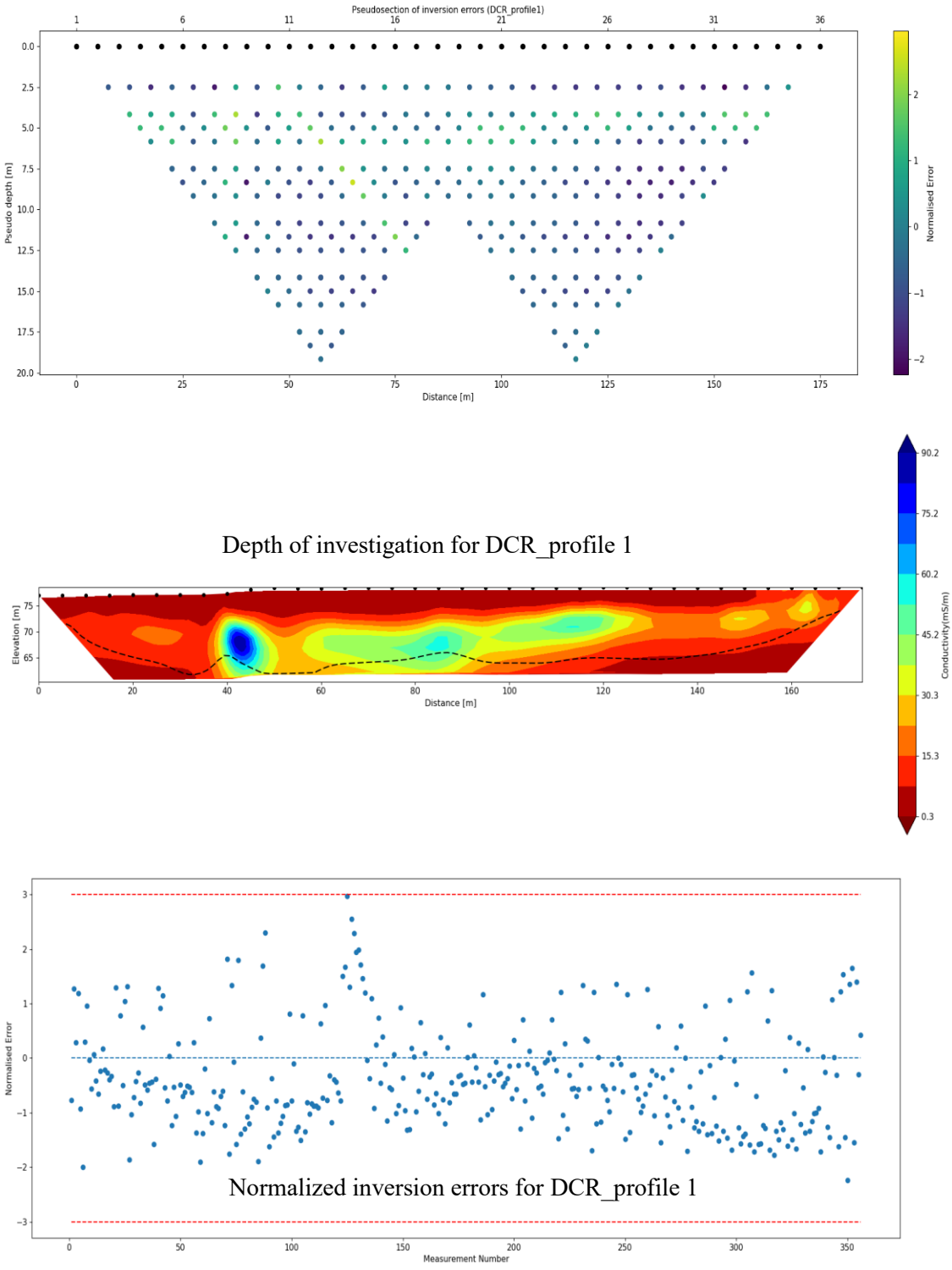

Figure B.16: Pseudo-section of inversion errors, DOI and normalized errors for DCR_profile 1.

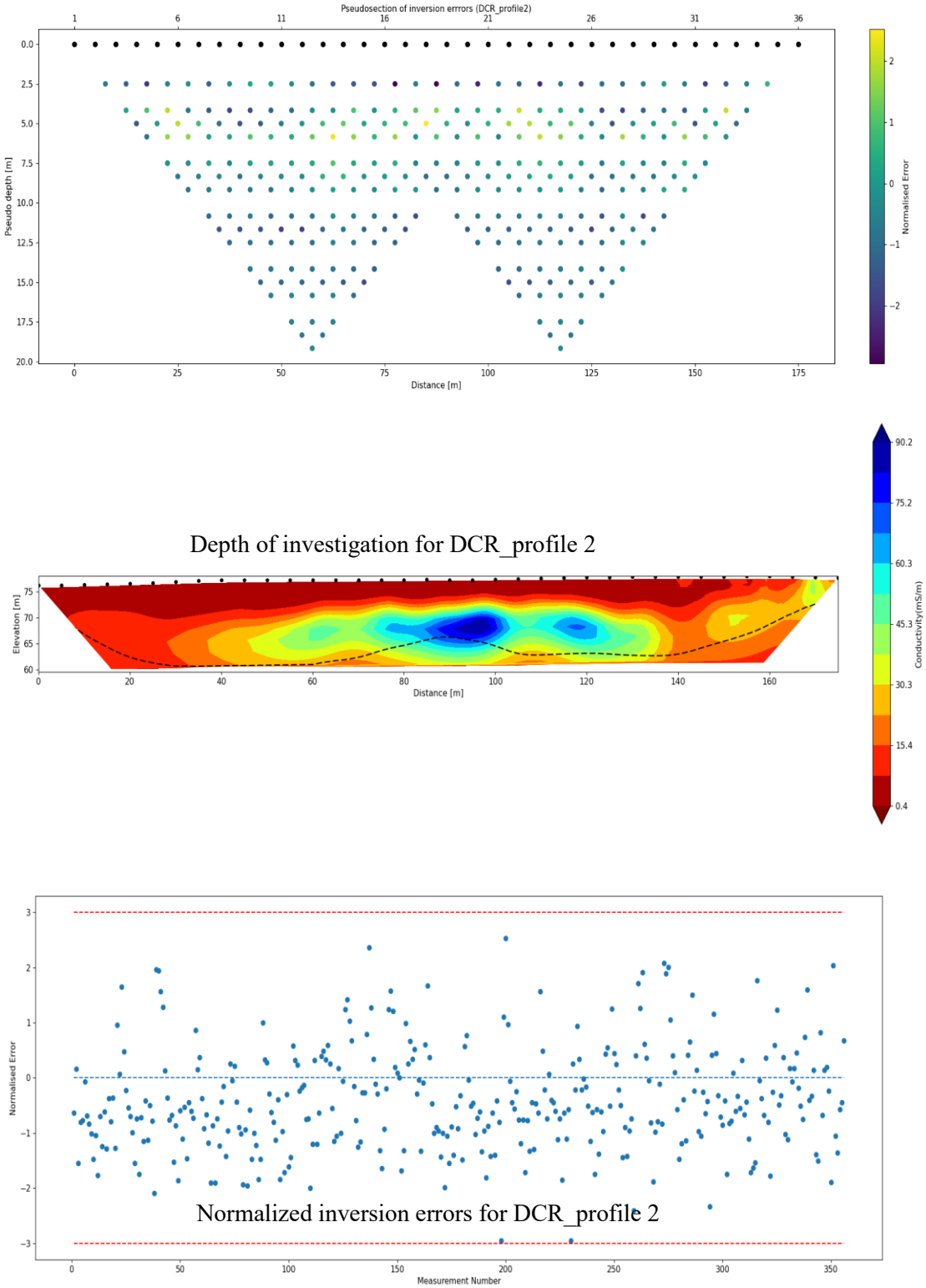

Figure B.17: Pseudo-section of inversion errors, DOI and normalized errors for DCR_profile 2.

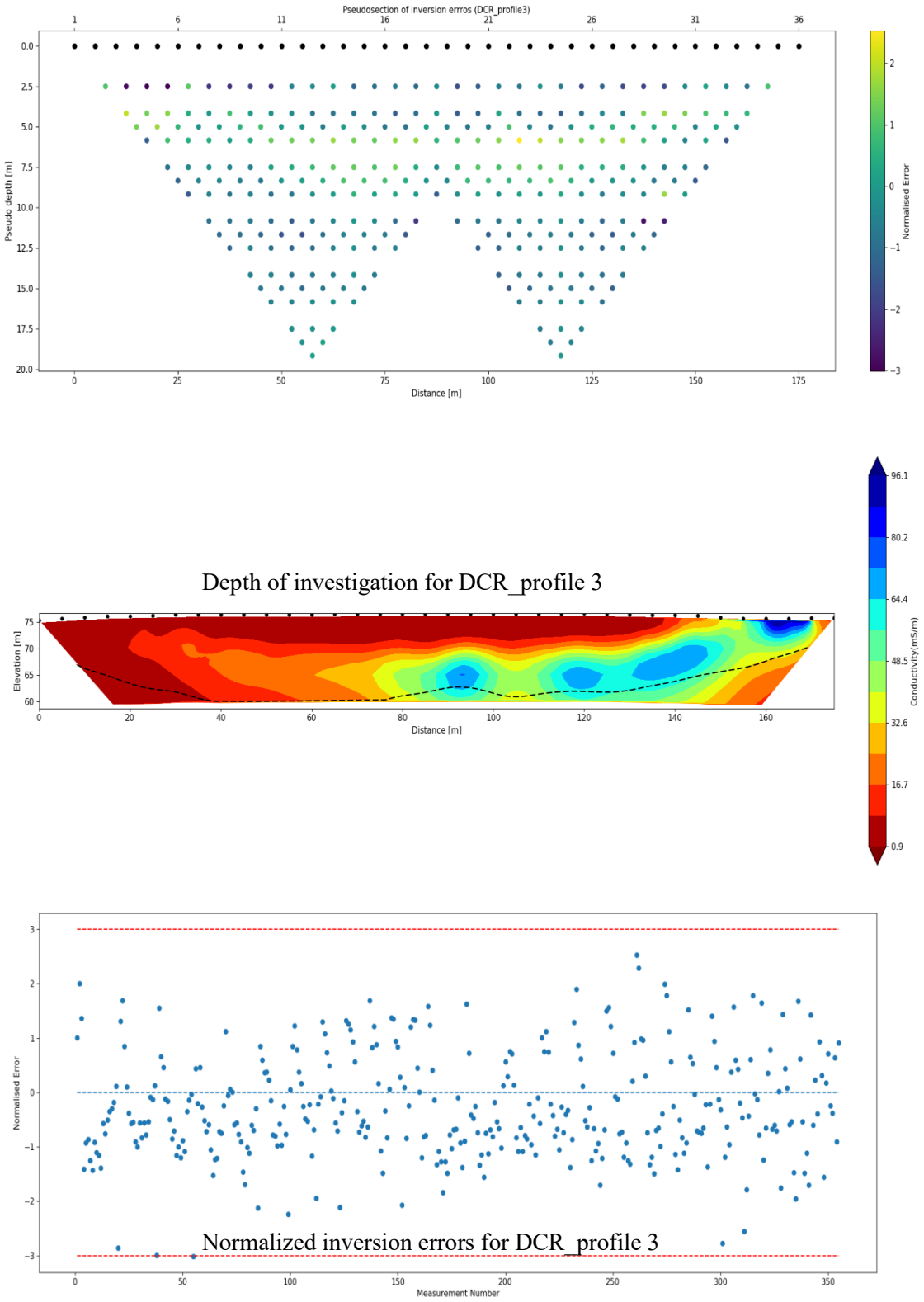

Figure B.18: Pseudo-section of inversion errors, DOI and normalized errors for DCR_profile 3.

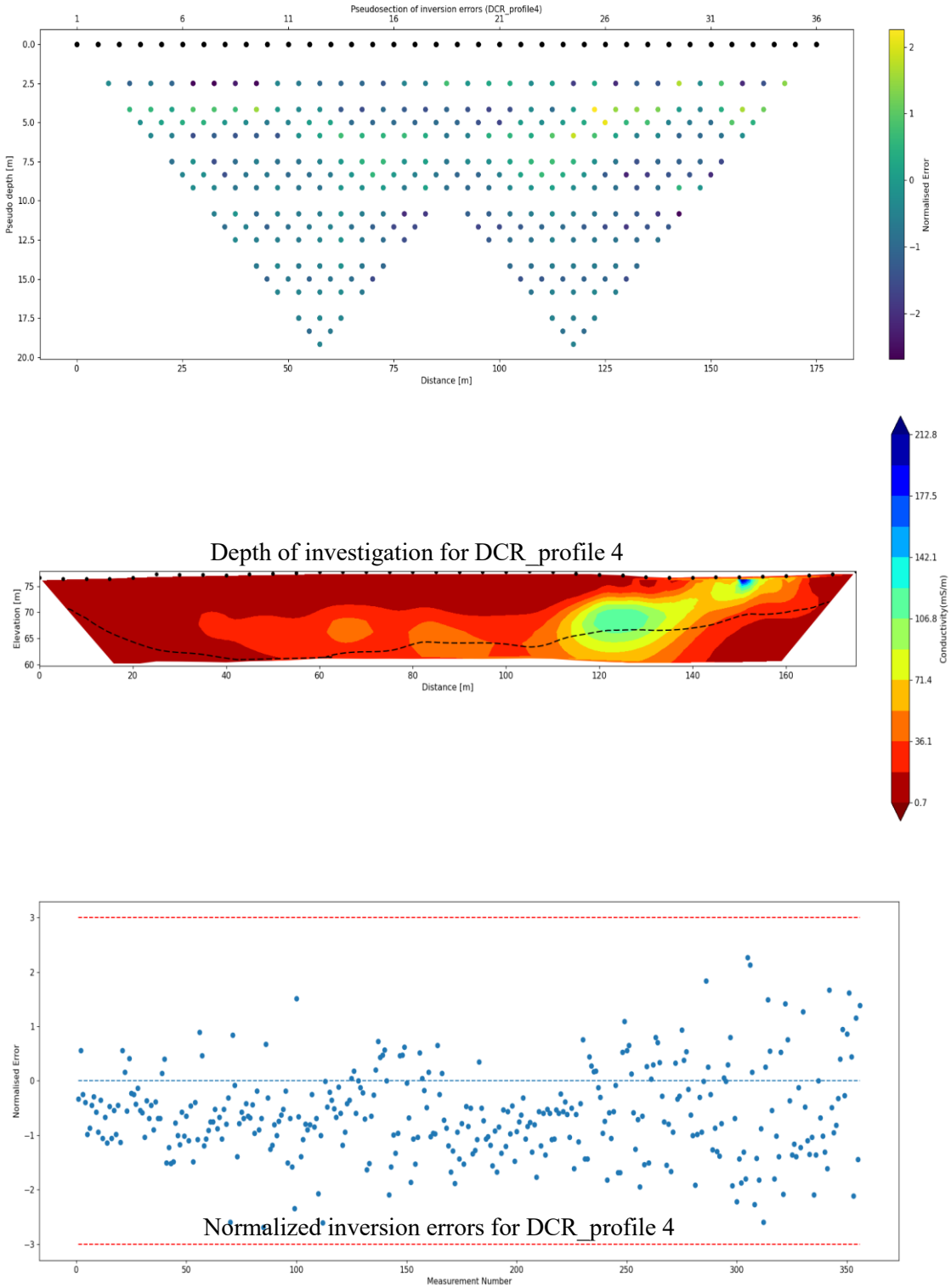

Figure B.19: Pseudo-section of inversion errors, DOI and normalized errors for DCR_profile 4.

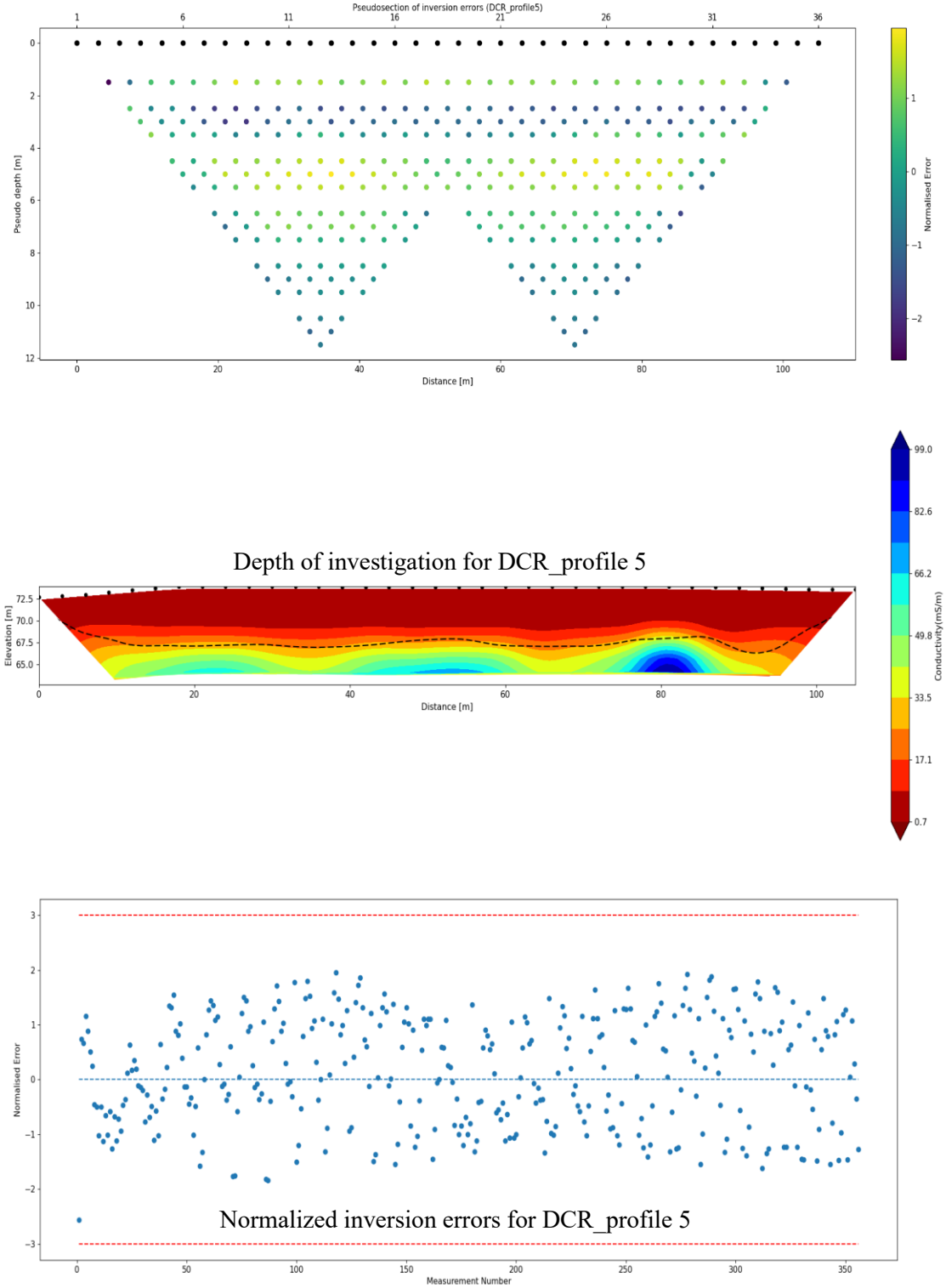

Figure B.20: Pseudo-section of inversion errors, DOI and normalized errors for DCR_profile 5.

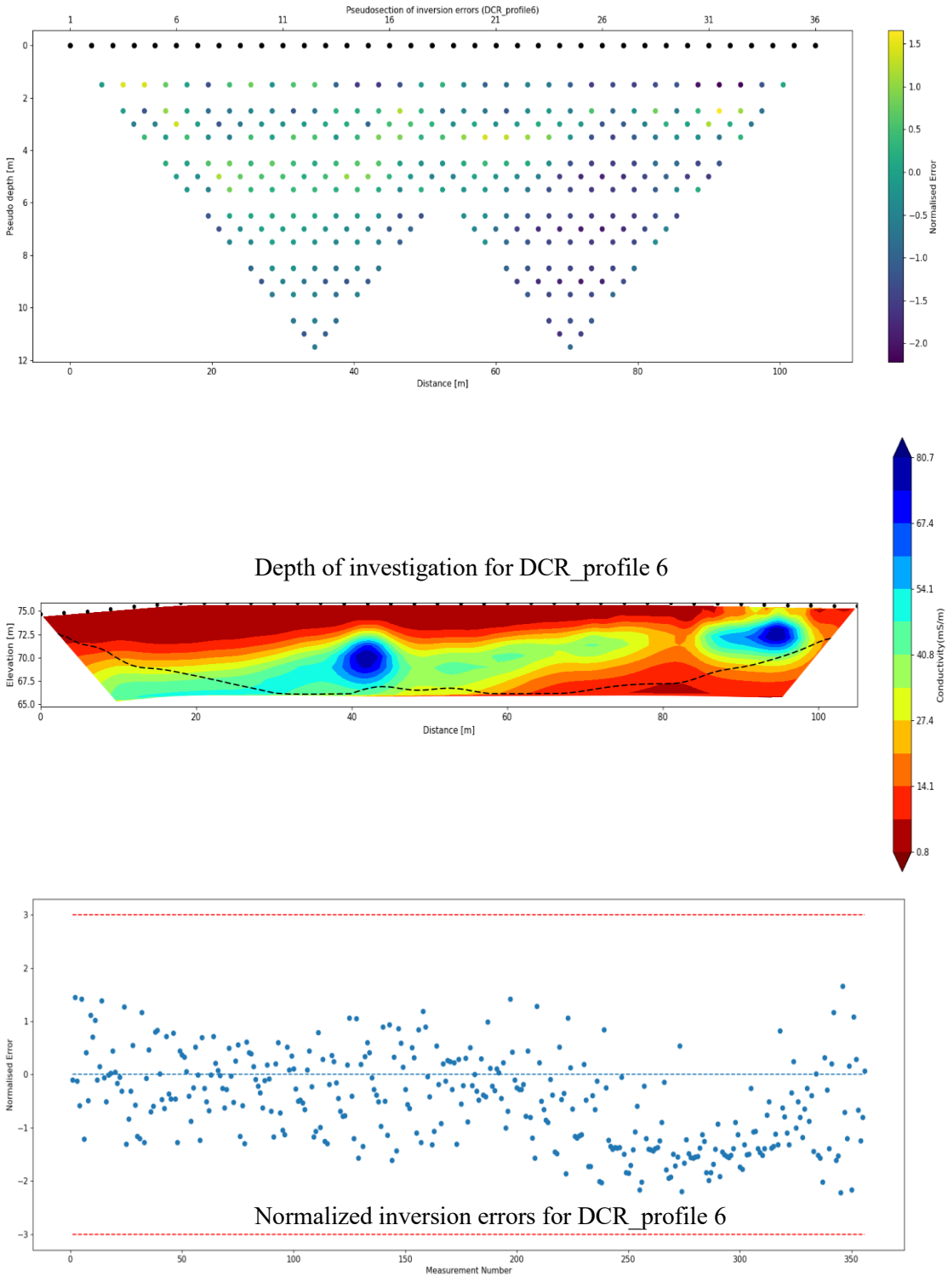

Figure B.21: Pseudo-section of inversion errors, DOI and normalized errors for DCR_profile 6.

Dipole-Dipole Conductivity Sections

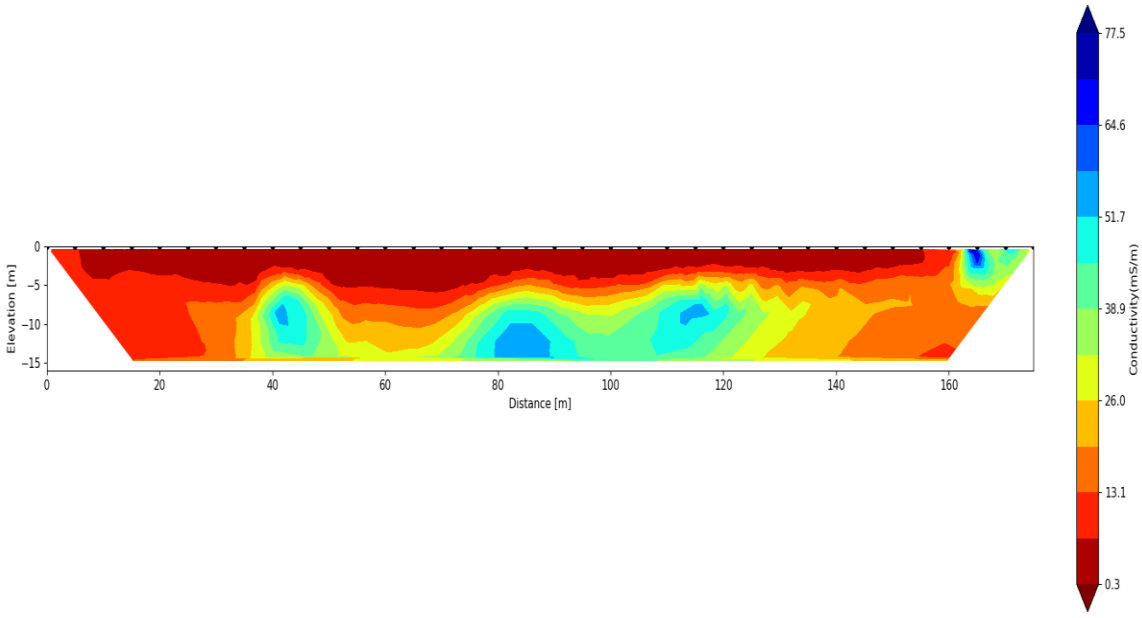

Figure B.22: Dipole-Dipole 2D conductivity model for DCR_profile 1.

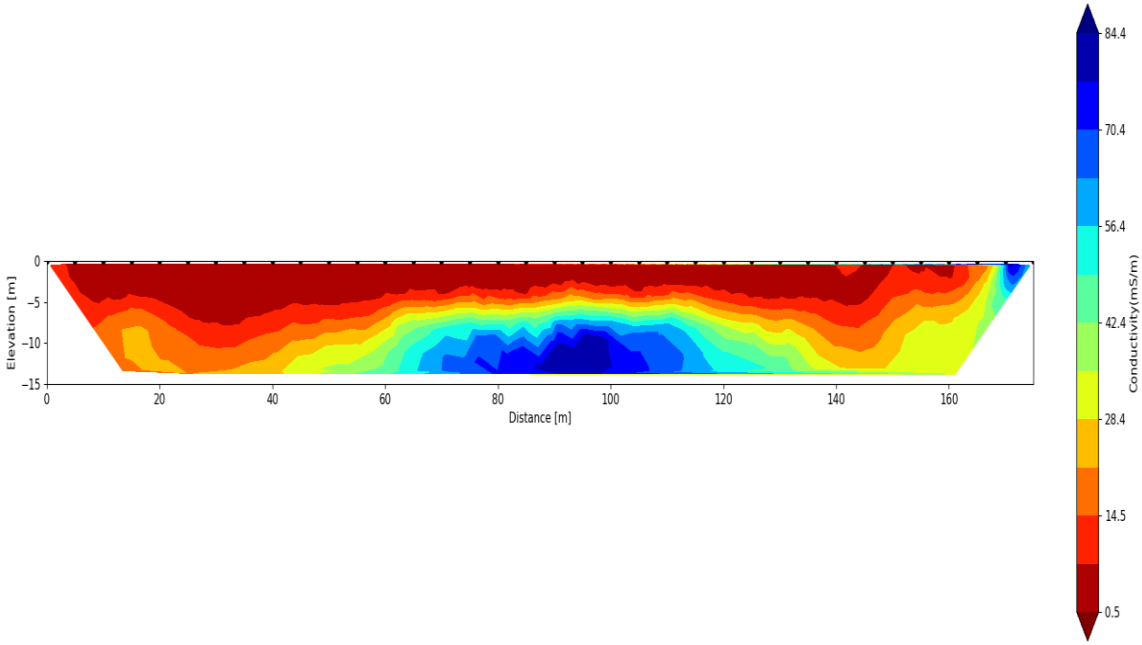

Figure B.23: Dipole-Dipole 2D conductivity model for DCR_profile 2.

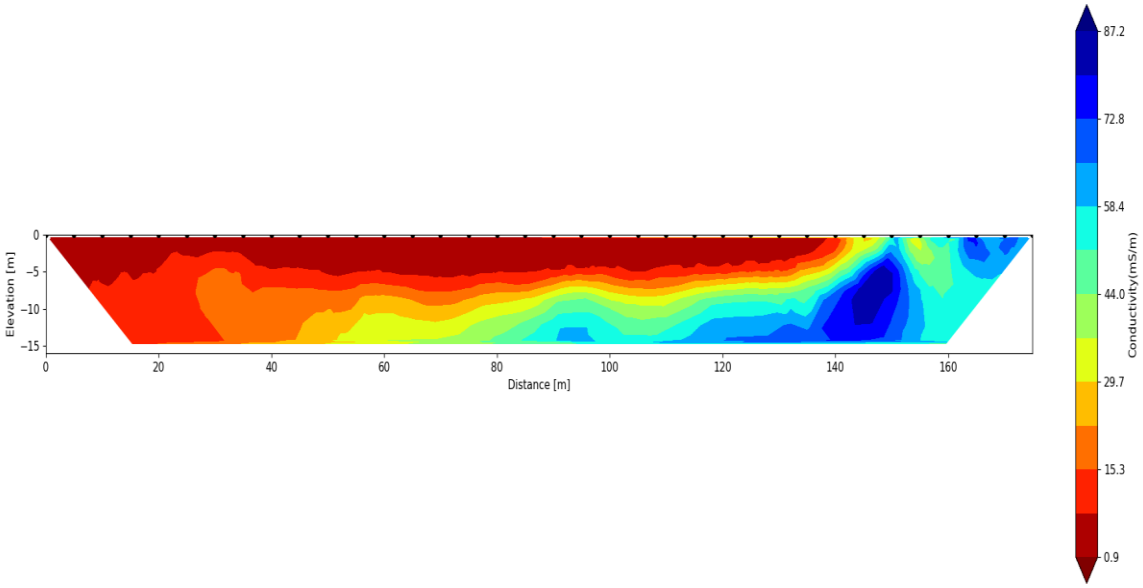

Figure B.24: Dipole-Dipole 2D conductivity model for DCR_profile 3.

Appendix C: Electromagnetic Survey

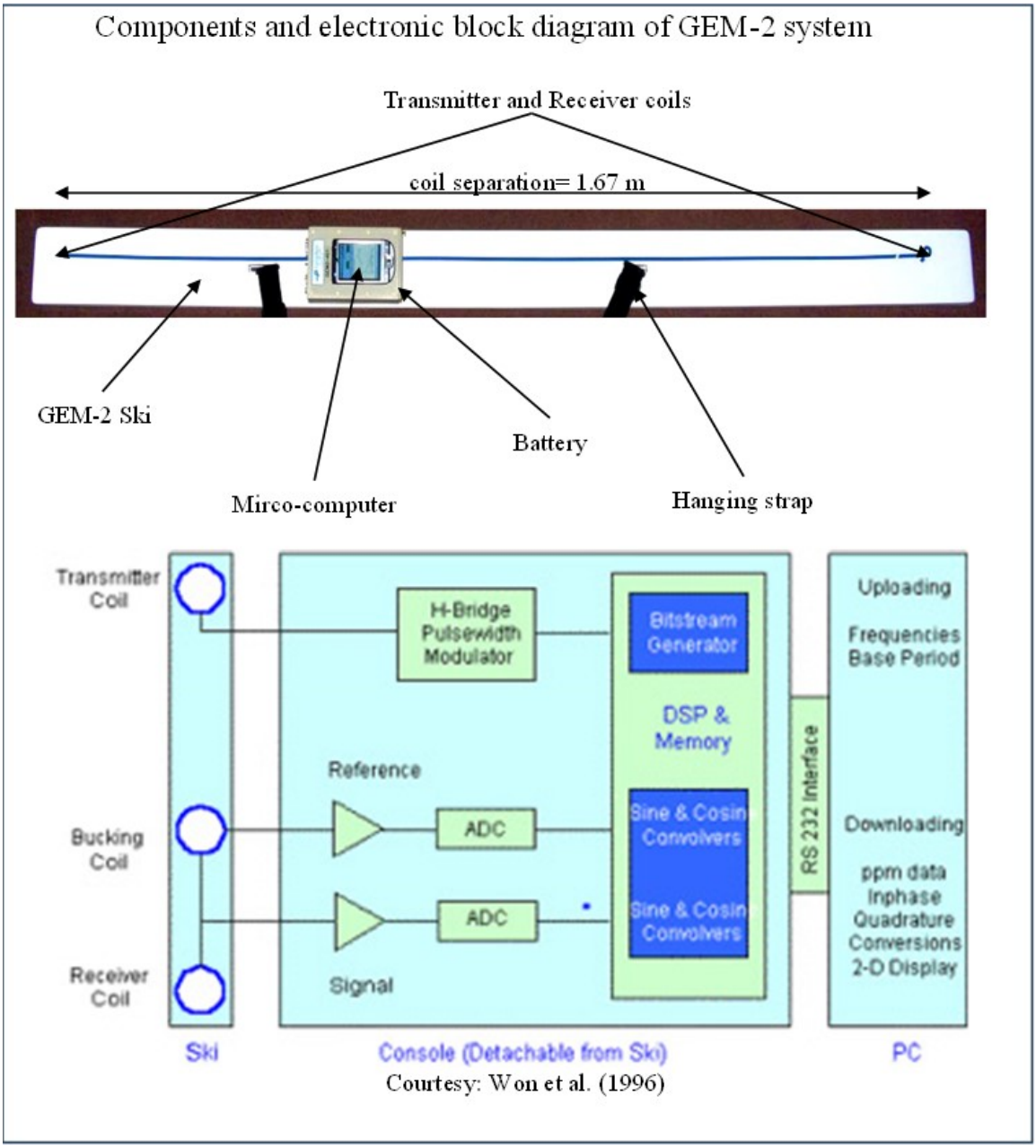

Figure C.1: Details of the GEM-2 systems and its internal components.

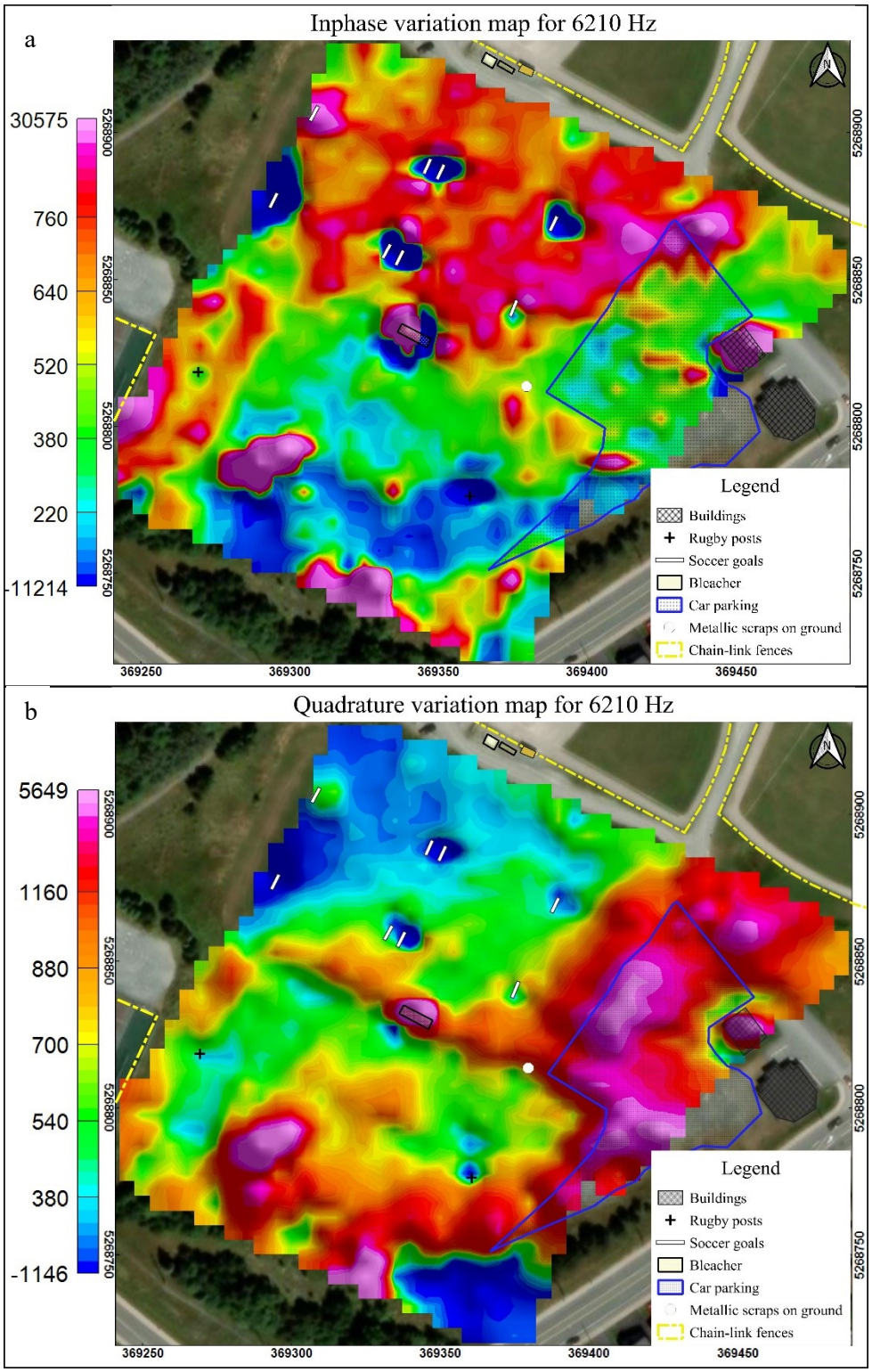

Figure C.2: The raw inphase (a) and quadrature (b) data for 6210 Hz gridded in Oasis Montaj.

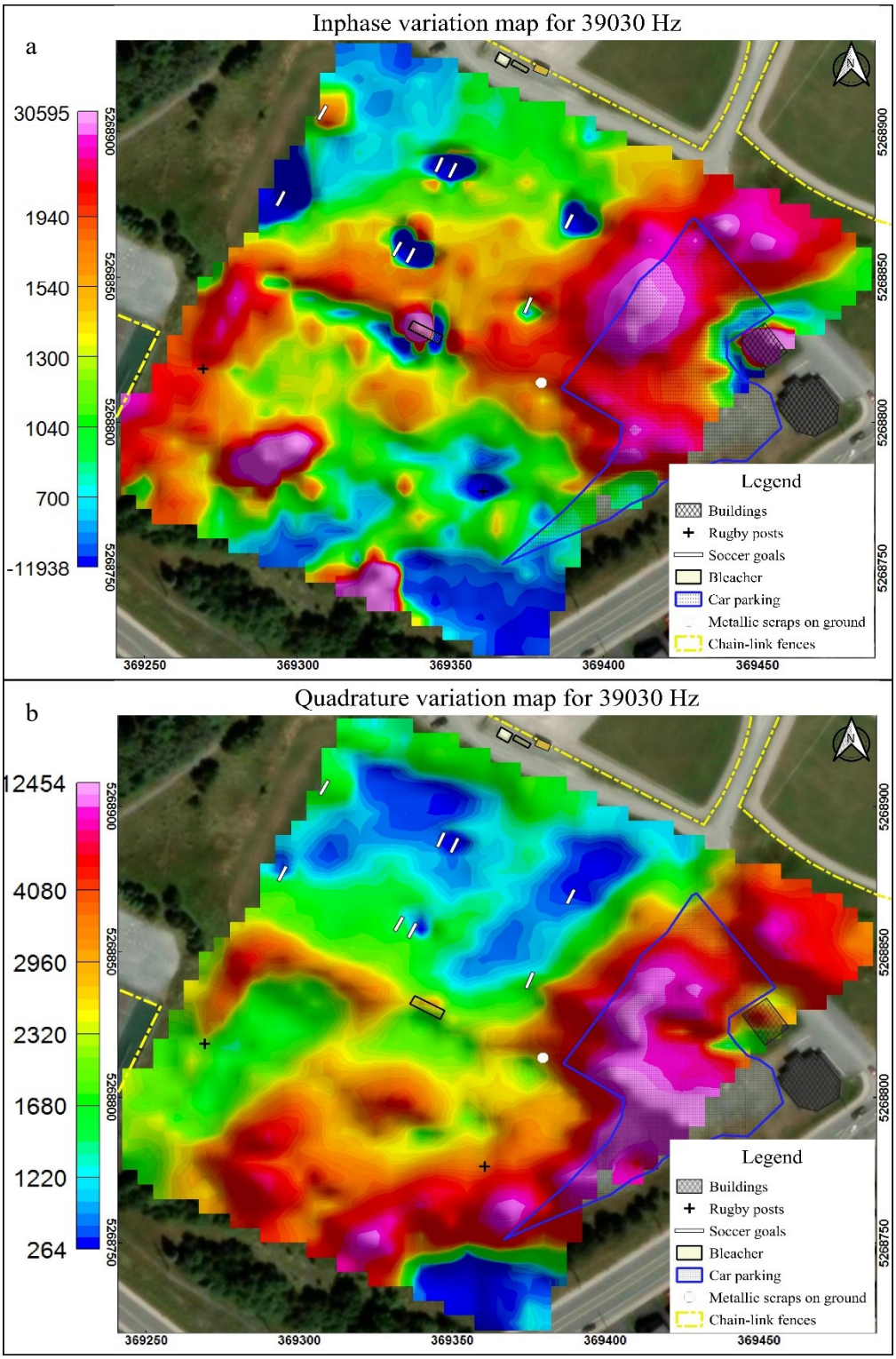

Figure C.3: The raw inphase (a) and quadrature (b) data for 39030 Hz gridded in Oasis Montaj.

Appendix D: Ground Penetrating Radar Survey

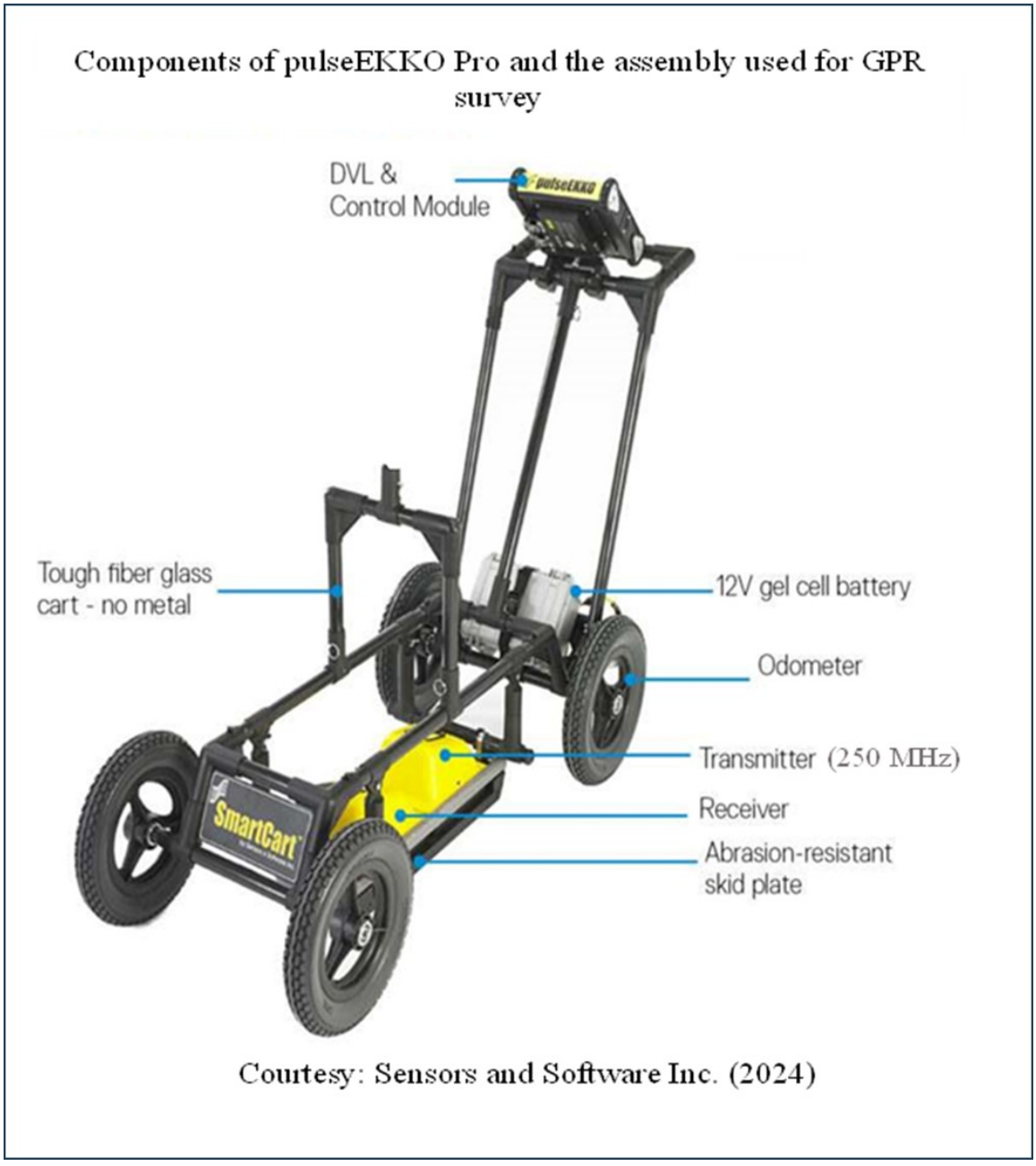

Figure D.1: The detail components of pulse-EKKO Pro system used for the work.

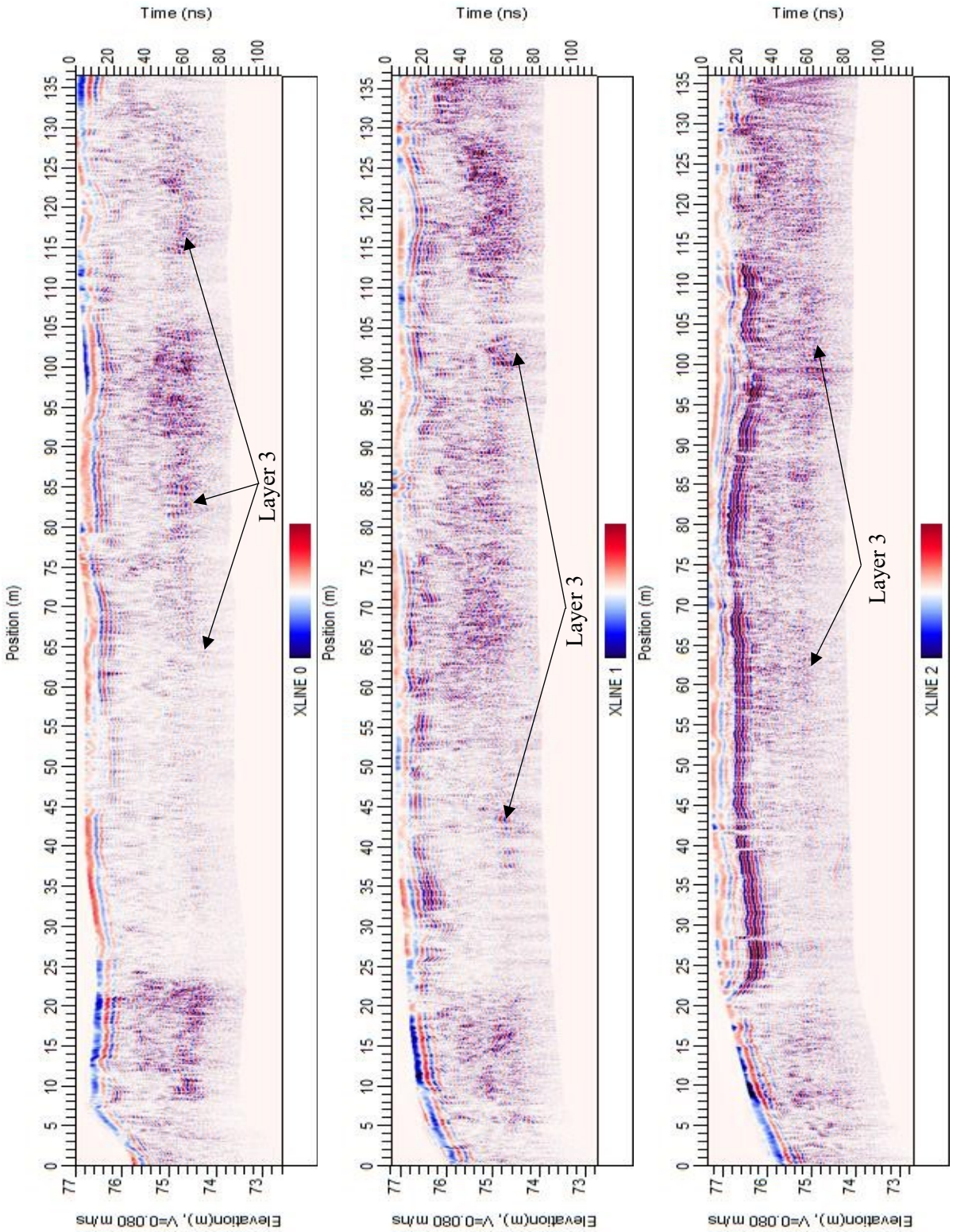

Figure D.2: GPR profiles for XLINE 0, XLINE 1 and XLINE 2.

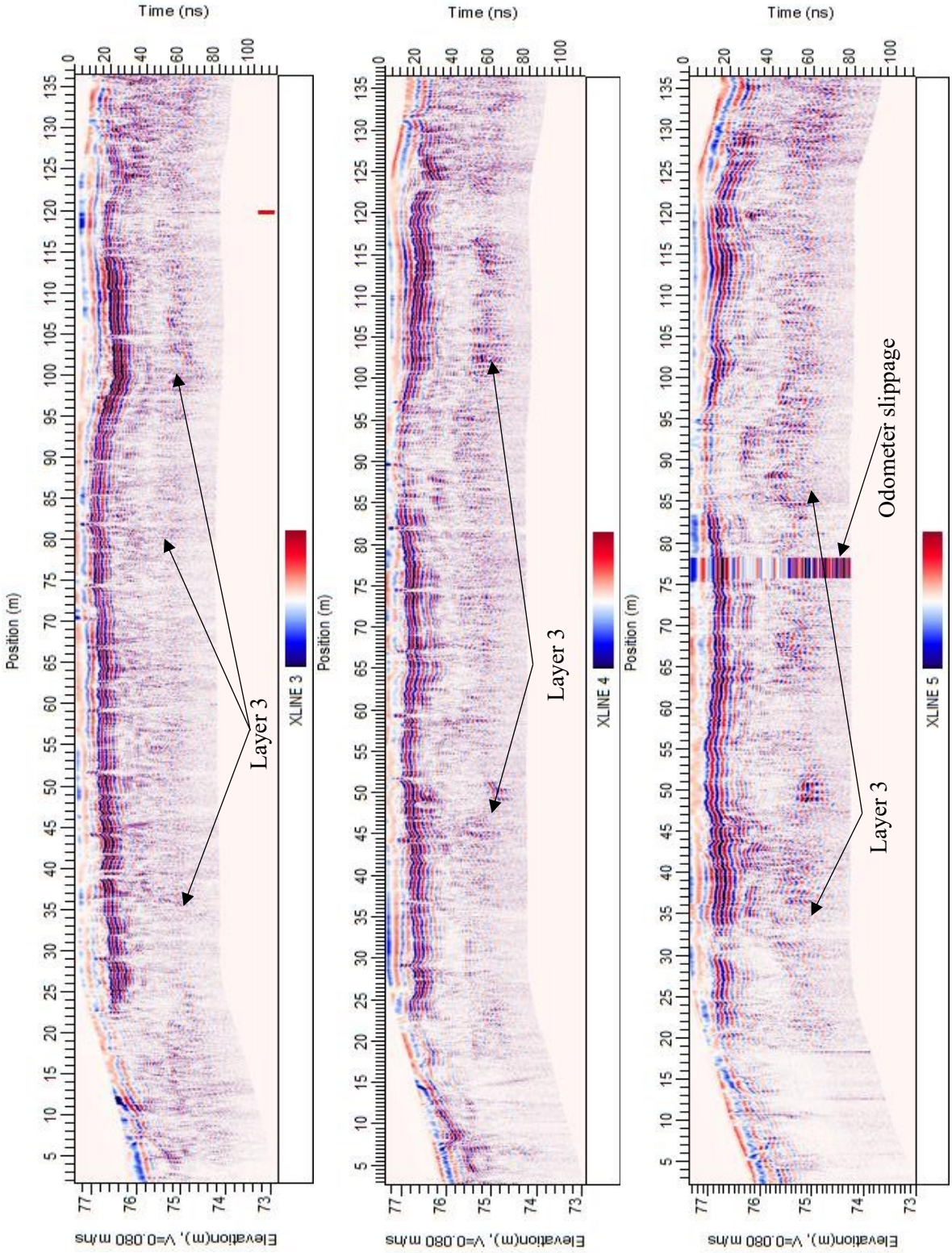

Figure D.3: GPR profiles for XLINE 3, XLINE 4 and XLINE 5.

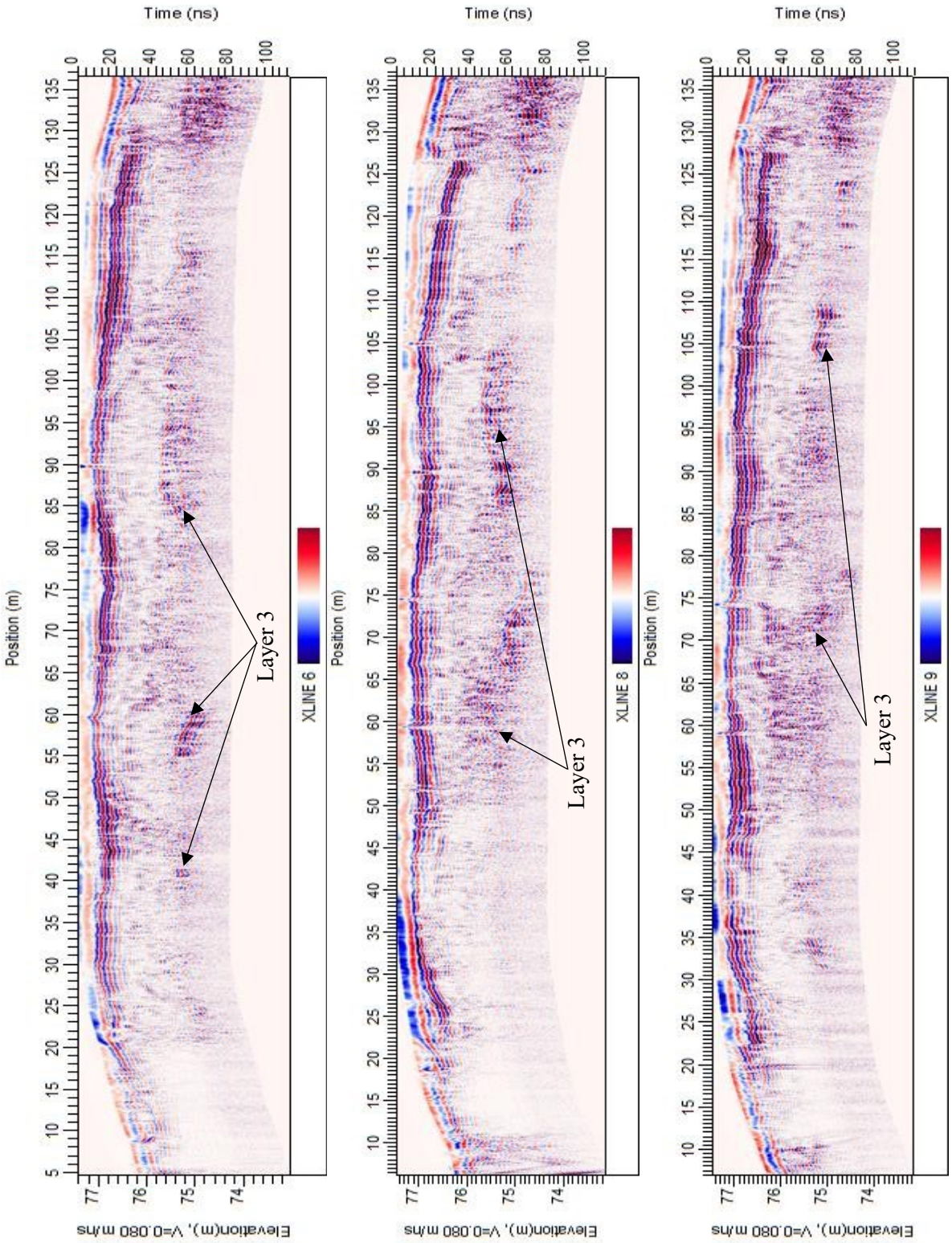

Figure D.4: GPR profiles for XLINE 6, XLINE 8 and XLINE 9.

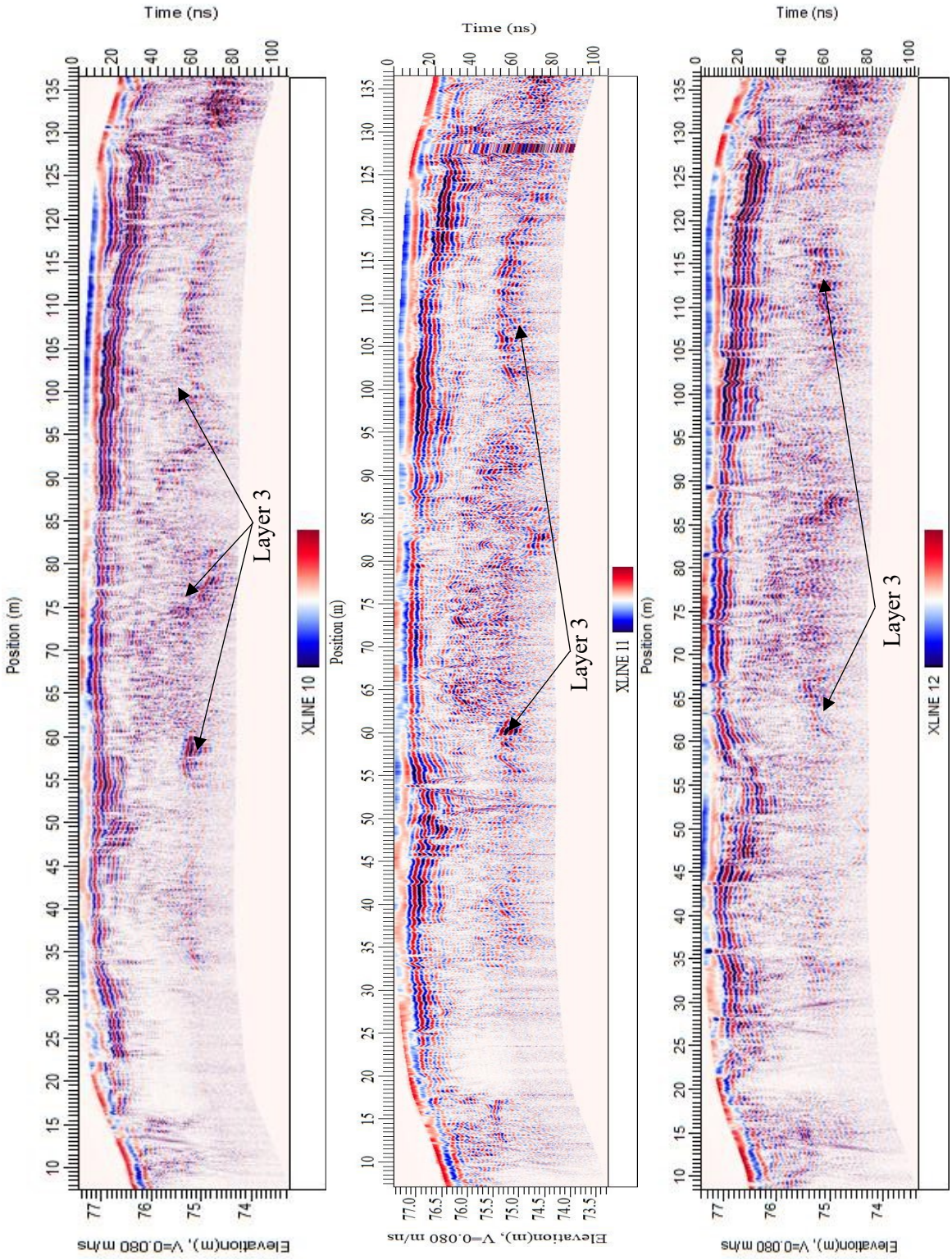

Figure D.5: GPR profiles for XLINE 10, XLINE 11 and XLINE 12.

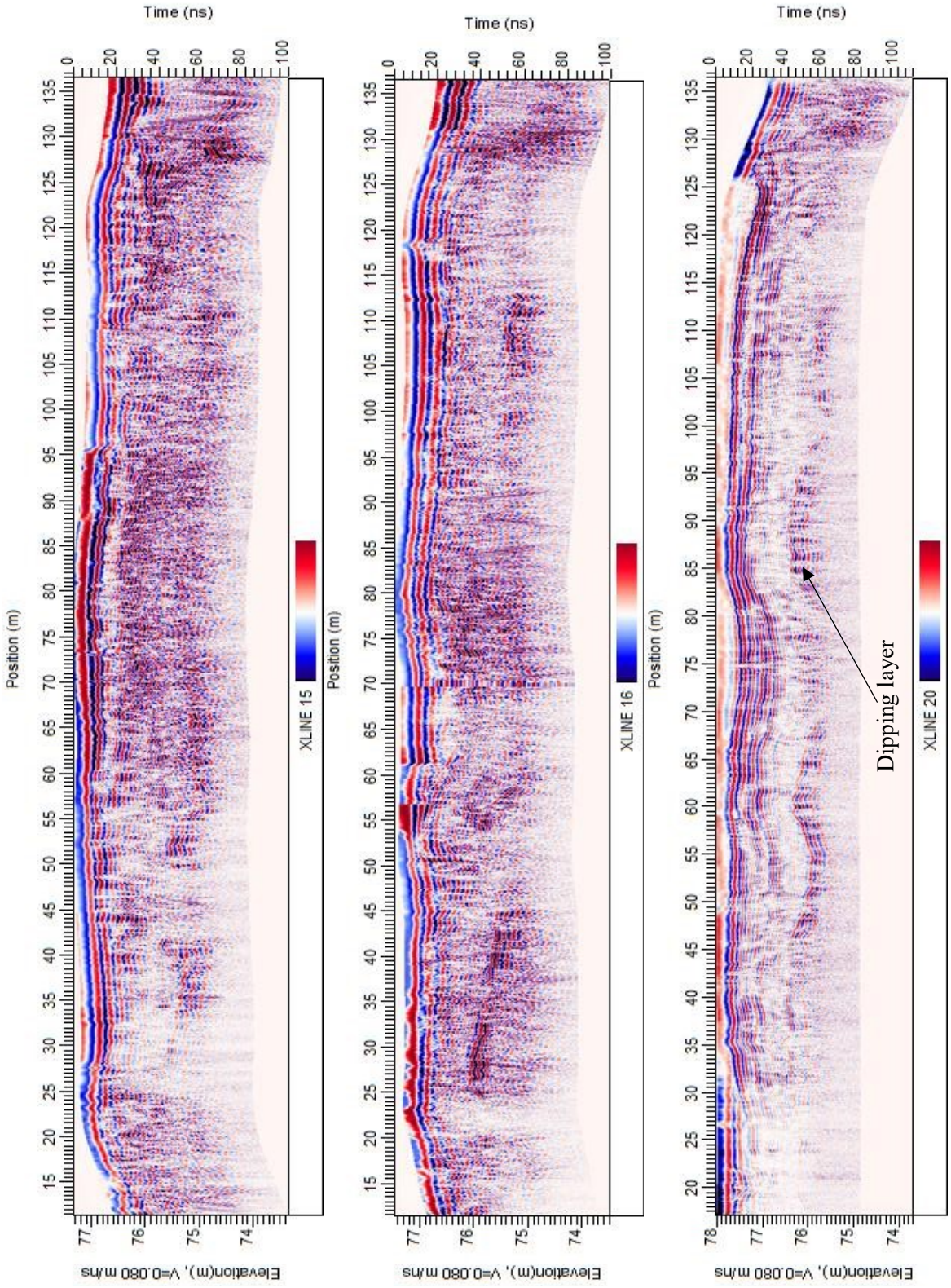

Figure D.6: GPR profiles for XLINE 15, XLINE 16 and XLINE 20.

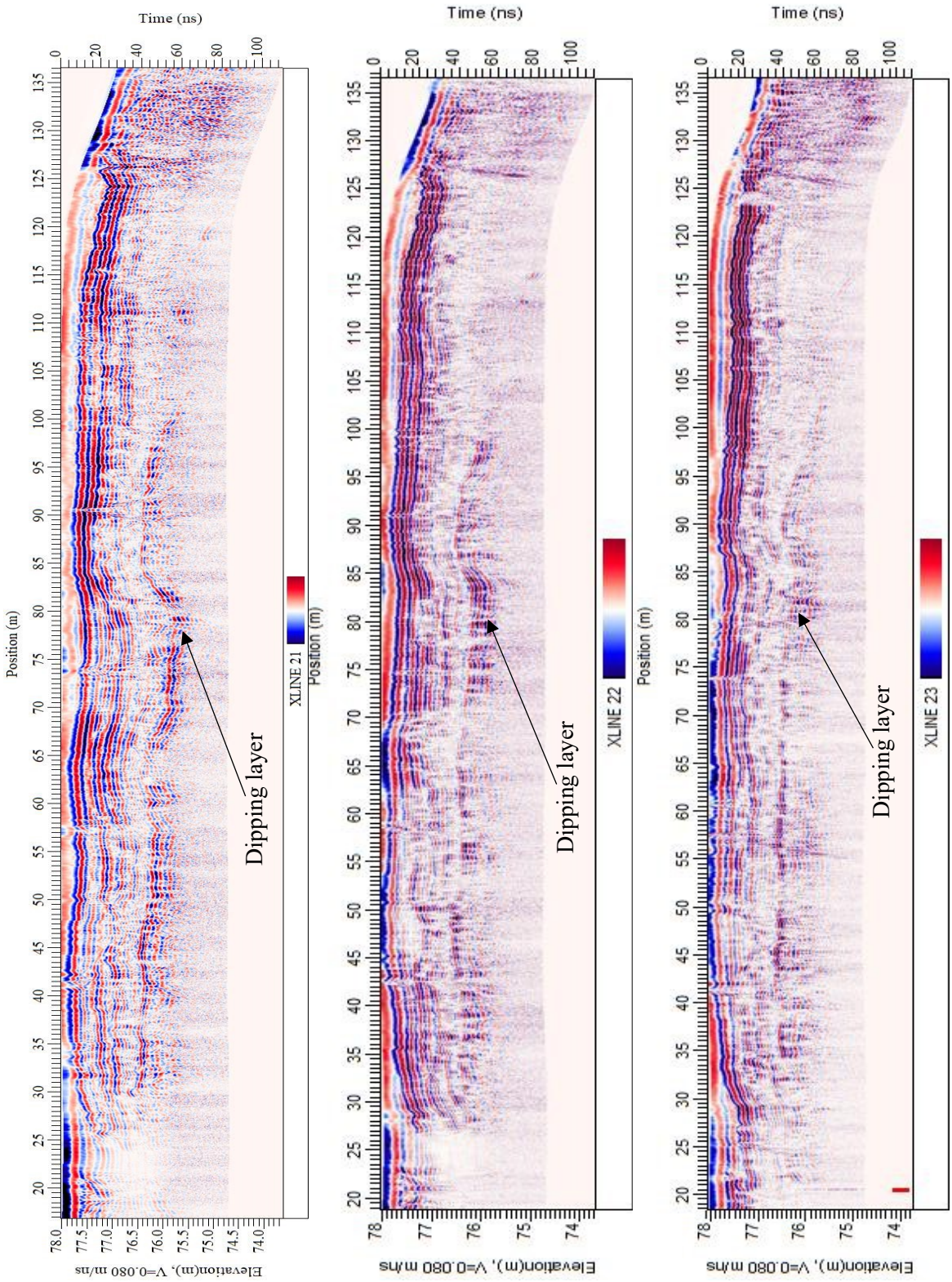

Figure D.7: GPR profiles for XLINE 21, XLINE 22 and XLINE 23.

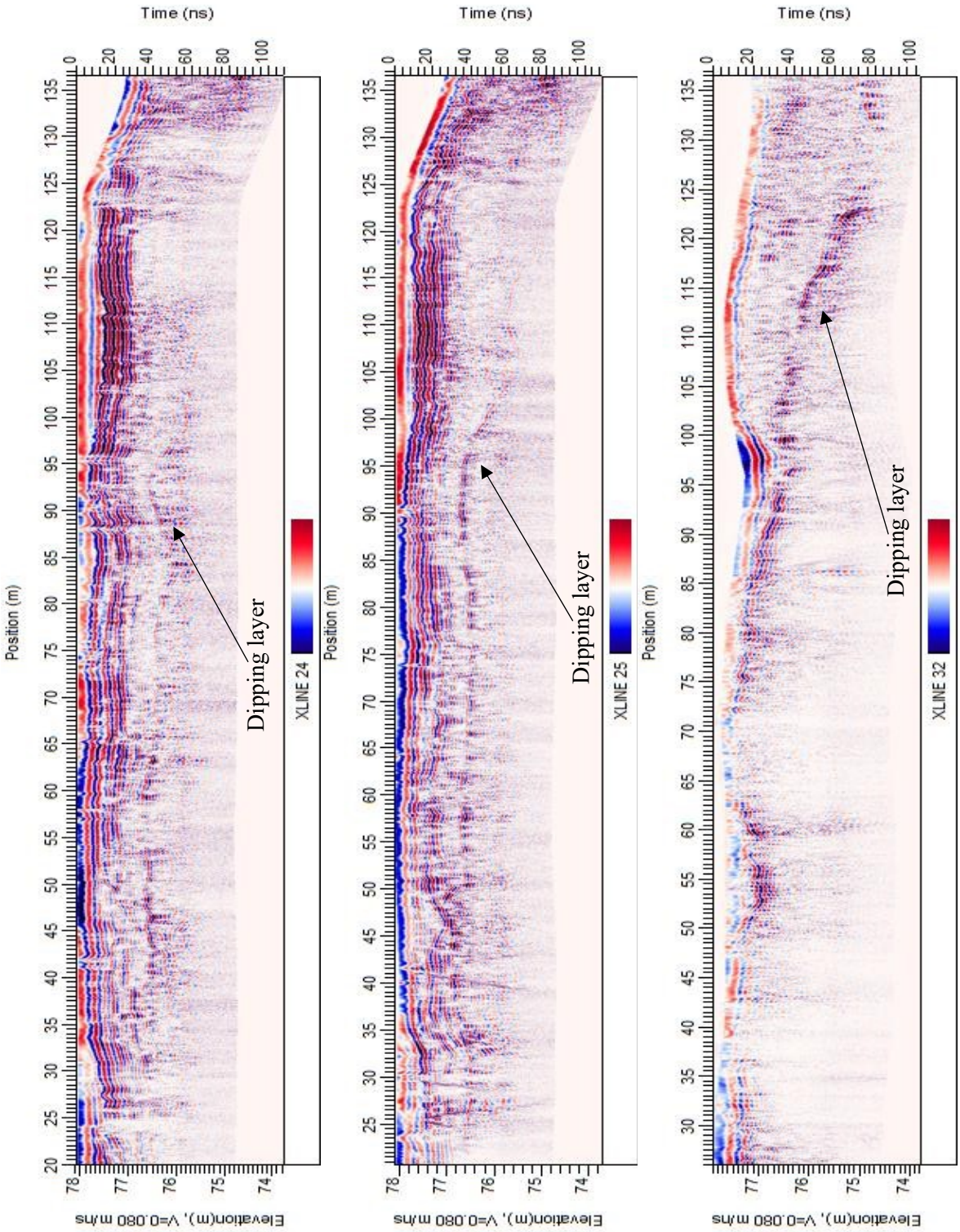

Figure D.8: GPR profiles for XLINE 24, XLINE 25 and XLINE 32.

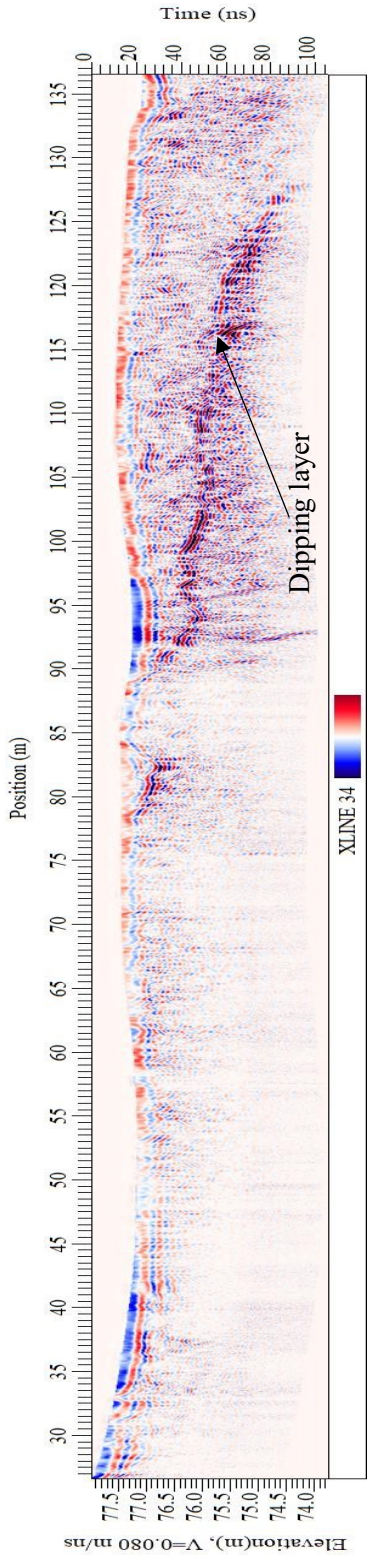

Figure D.9: GPR profile for XLINE 34.

Appendix E: Topographic Survey

Wishingwell Park has relatively flat surface with several playing fields (soccer, rugby and baseball). However, these playing fields have appreciable differences in elevations relative to surrounding area and within themselves as well. Thus, a detailed topographic survey was conducted on 12th May, 2023. The topographic survey was done using the Topcon HiPer V Real Time Kinematic (RTK) differential GPS, using a stationary base and a roving receiver. The survey has an accuracy of a few centimetres (Topcon Corp., 2024).

During the survey, the base was positioned, in Universal Transverse Mercator (UTM) system, at 369442.068 (easting, m), 5268826.330 (northing, m) and elevation of 74.610 m above mean sea level. It was used to collect precise static data for the entire duration of roving. The static data retrieved from the Canadian Geodetic Survey has the difference of +1.307 m in easting, +1.799 m in northing and +2.115 m in elevation when compared with the actual base location data (given above).

The rover was mounted on a staff, whose height can be adjusted, and the assembly was carried all over the area. At every position, the assembly was made as vertical as possible using a water bubble attached to the staff and allowed it to rest until a reading stabilizes and then take measurements using FC-500 Topcon system. This operation was repeated by moving at least a step or two each time along lines, approximately 5 m apart, roughly parallel to the soccer and the rugby field. All the location data (eastings, northings and heights also known as ENH) were accordingly corrected for the static. Figure E.1 depicts overall coverage of the topographic survey in the area. The elevation data were gridded in Oasis Montaj, using a grid size of 2.5 m and the minimum curvature method, and contoured as shown in Figure E.2.

Figure E.1: Topographic survey layout showing measurement points (white dots). (Scale= 1:855)

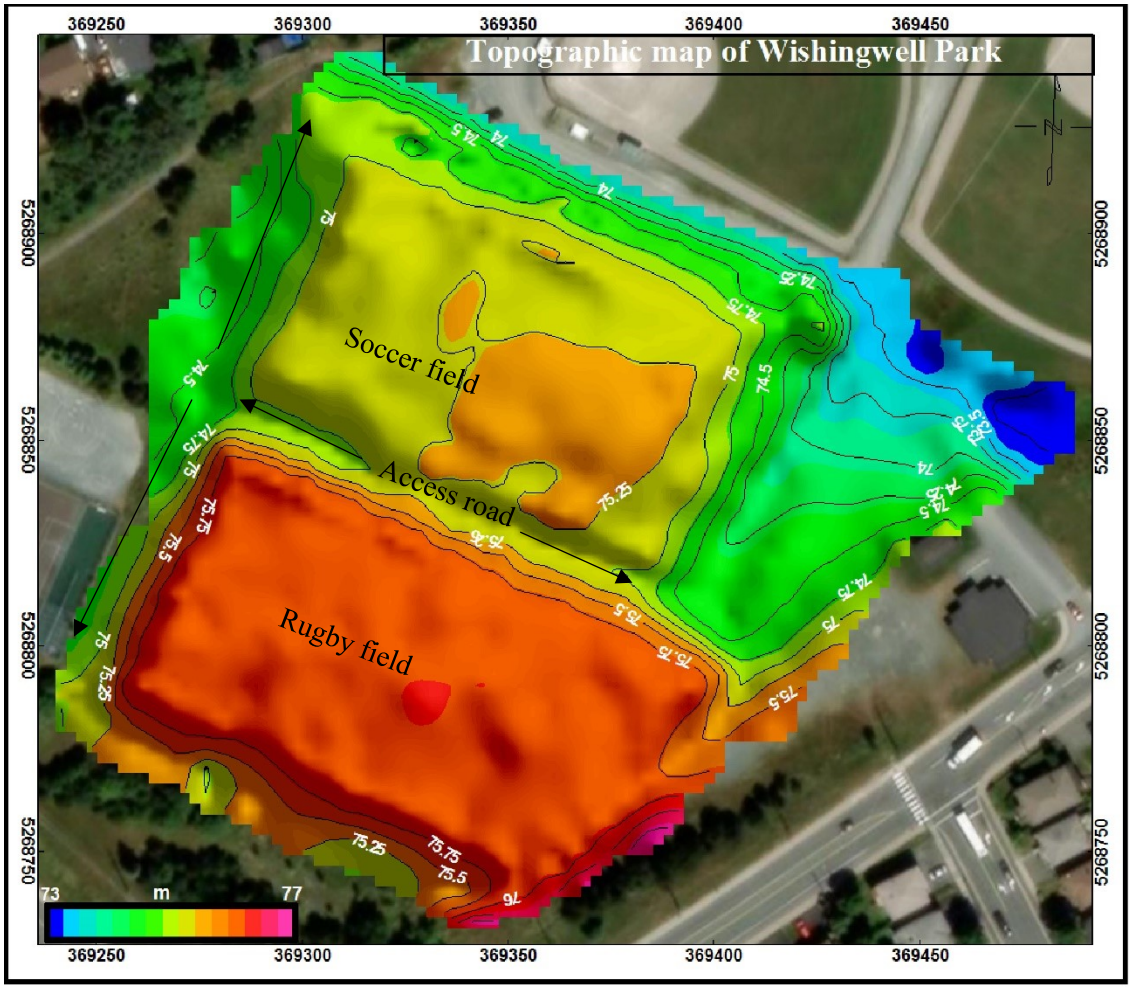

Figure E.2: Topographic map of the study area (Colour Scale=linear, elevation above mean sea level). (Scale= 1:855, Black arrow shows access road).

Figure E.2 clearly shows that the two playing fields are elevated by about 1.5-2.5 m relative to the surrounding area using soil layers. The rugby field is elevated even higher than the soccer fields by about a metre. There are access roads (pathways) surrounding the playing fields as shown. Moreover, the lumpy nature of the ground surface is observed significantly in the field as well. It may be due to uneven settlement of the top layer of soil. This can arguably be due to the long-term compaction of incompletely or unevenly compacted heterogeneous waste underlying the load from the overlying embanked soil layer in the area.